POLITECNICO DI MILANO
Department of Chemistry, Materials and Chemical Engineering
“Giulio Natta”
Ph.D. in Materials Engineering - Year XXIV
2012

STABILITY AND EFFICIENCY OF ORGANIC MATERIALS AND DEVICES FOR THE PHOTOVOLTAIC TECHNOLOGY

Author:	Gianmarco GRIFFINI (738544)
Supervisor:	Prof. Stefano TURRI
Tutor:	Prof. Marinella LEVI
Coordinator:	Prof. Chiara CASTIGLIONI

cover image:

details from M. K. Č*iurlionis "Creation of the World (II)", 1905-1906*.

ABSTRACT

New materials and technologies have been explored in the past decades in the attempt to meet the demand of energy production from clean, renewable sources. In particular, organic materials and conjugated polymers have been investigated for use in polymer-based organic photovoltaics (PSCs) and in organic luminescent solar concentrators (OLSC).

Long-term stability of materials and devices together with power conversion efficiency (PCE) have been recognized as central research areas, both in academia and industry.

In the work presented in this PhD thesis, PSC and OLSC technologies were examined and aspects related to their environmental stability and efficiency were studied, with the aim of achieving a greater understanding of the criticalities characteristic of these two research fields.

A first study was carried out on the photo-chemical stability of a model PSC polymer (poly(3-hexyl-thiophene) - P3HT) in the solid state. The results obtained from this study underlined a substantial instability of P3HT to photo-oxidation following exposure to simulated sunlight. In particular a degradation mechanism for the polymer was proposed and potential strategies for lengthening its photo-stability were examined, including the use of multi-walled carbon nanotubes.

Together with photo-chemical stability, morphological stability of PSC polymers and devices was also examined. To this end, a series of photocrosslinkable low band-gap polymers was prepared and tested in PSC devices during long-term high-temperature annealing. Photocrosslinking allowed the formation and preservation of an optimal bulk-heterojunction (BHJ) morphology, and highly-efficient PSC devices could be fabricated. Atomic force microscopy (AFM) studies on the photoactive layer of devices evidenced a good correlation between surface morphology of the photoactive layer and photovoltaic behavior of devices.

The analysis on PSC technology was extended to the evaluation of the power conversion efficiency (PCE) of devices, employing new isothianaphthene (ITN)-based low band-gap polymers with various electron-withdrawing substituents as active layer materials. BHJ PSC devices were fabricated with PCEs up to 3.0% and the electron-withdrawing character of functional groups was shown to strongly influence the polymer electronic behavior.

In the attempt to explore novel processing techniques compatible with large-scale production of PSC devices, a preliminary study on inverted PSCs was carried-out. As alternative to thermal evaporation, the metallic back-electrode was deposited onto the device by blade-coating an Ag paste. Both device fabrication and testing were completely performed in ambient air and PCEs in the order of 0.5% were achieved on large area (3.6 cm^2) PSC devices. These results demonstrated the possibility of producing working PSC devices in air with no need of vacuum processing steps.

The work carried out on OLSC technology firstly addressed the study of the

photo-chemical stability of the materials constituting the thin-film luminescent concentrator, namely an organic luminescent dye dissolved into a polymer matrix (PMMA). The behavior of each material constituting the OLSC device was monitored (PMMA alone, luminescent dye alone and combination of the two) during exposure in air to high-energy UV-light and a degradation mechanism for the dye molecule was proposed. In addition, the role of the organic dye molecule in the degradation of PMMA was elucidated and the effect of the state of aggregation of the organic dye on its photo-stability was clarified.

The stability study on OLSC materials was followed by a parametric study on the efficiency of a working OLSC device coupled to a c-Si solar cell, tested under simulated sunlight. A number of device parameters were analyzed and successively optimized, including the organic dye concentration and the thickness of the thin-film OLSC. A maximum efficiency gain of over 40% was achieved after the integration of the c-Si solar cell with the OLSC thin-film. These results give important guidelines for the fabrication of efficient OLSC devices.

IV

Stability and Efficiency of Organic Materials and Devices for PVs

>>
ACKNOWLEDGMENTS

I wish to thank my supervisors, Prof. Stefano Turri and Prof. Marinella Levi, for their invaluable guidance throughout this Ph.D. work and for their continuous support and help. Thank you for giving me the opportunity to work with you on such an amazing and interesting topic and for making ChIP*lab* a pleasant and stimulating place.

I would also like to thank Prof. Jean M. J. Fréchet for giving me the chance to spend eight months of my Ph.D. in his research group at the University of California, Berkeley, where I could learn so much about organic photovoltaics.

My deep thanks also go to all the people who shared these past three years of work and laboratory life with me: Gilly for her precious help in the everyday laboratory life and for always being there with a smile; Diego for living with me practically side-by-side every single day of these three years, for the long chats on science and science-fiction and for the enormous help in and out of the lab: I whish you all the best for your future; Raffaella for all the time spent together discussing about science and life, and for helping me to widen my perspective on things; Giuseppe for introducing me to the wonderful world of design and for becoming the good friend I know today; Frapic for the long chats in the lab and in the office; Carmela for the interesting discussions on potential and hopefully viable bridges between our two research lines; Francesca and Massimo for the great collaboration we have just started, which will hopefully lead us to a real integration of design and engineering; Serena and Barbara who just entered our group and brought with them enthusiasm and professionalism; Stefano for his passion. Many thanks to Pedro, Antonio, Sara, Cristina and Antonio for their amazing work in the lab.

I thank Prof. M. Del Zoppo and Dr. L. Brambilla for their help with the interpretation of the spectroscopic results, and Luca for helping me with the NMR analysis.

I am grateful to all the people in the Fréchet group at UC Berkeley, who made my stay there enjoyable and fruitful. In particular, I would like to thank Justin, for the support, the guidance and the long and pleasant chats smoking cigars; Claudia, a master device engineer and a wonderful person; Jessica, one of the best synthetic chemists I have ever met; Tom, for the interesting and stimulating discussions on polymers, chemistry and American culture; Jill and Claire, for the inspiring and very helpful suggestions on my work.

I would like to thank my parents Anita and Antonio, who have supported my decision of going back to research and are now becoming wonderful grandparents.

The most genuine and heartfelt thanks go to Camilla, the very special person with whom I have decided to live and share my life. Thank you for making my everyday life easy and stimulating, and for the constant encouragement and help you can always give me: you are a wonderful woman and an amazing mother.

Finally, the most special thanks go to the little Elia, who just landed in this world: you have beautifully changed my life. Thank you for all your patience and for teaching me everyday with your big smiles how to be a good father.

>>

TABLE OF CONTENTS

1 Aims and structure of the work 3
1.1 Aims of the work 4
1.2 Structure of the work 5

2 Energy from the sun: the photovoltaic technology 7
2.1 Understanding solar cell operation 9
2.2 Photovoltaic devices: from silicon to organic materials 20
2.3 Polymer solar cells 24
2.4 Concentrating solar light: from imaging to non-imaging devices 34
2.5 Luminescent solar concentrators 36
2.6 References 46

3 Study of photo-degradation mechanisms in π–conjugated polymers for polymer solar cells 57
3.1 Introduction 58
3.2 Experimental 61
3.3 Results and discussion 62
3.4 Conclusions and future work 76
3.5 References 77

4 New low-bandgap photocrosslinkable polymers for improved morphological stability in high-efficiency polymer solar cells 83
4.1 Introduction 84
4.2 Experimental 87
4.3 Results and discussion 93
4.4 Conclusions and future work 114
4.5 References 115

5 Characterization of new low-bandgap donor-acceptor polymers for efficient polymer solar cells 121
5.1 Introduction 122
5.2 Experimental 125
5.3 Results and discussion 128
5.4 Conclusions and future work 144
5.5 References 145

6 Study of stability and degradation of materials for organic luminescent solar concentrators 151
6.1 Introduction 152
6.2 Experimental 155
6.3 Results and discussion 157
6.4 Conclusions and future work 189
6.5 References 190

7 Fabrication and testing of working devices: an overview of materials and methods 193
7.1 Introduction 194
7.2 Bulk-heterojunction polymer solar cells 195
7.3 Thin-film organic luminescent solar concentrators 209
7.4 References 222

8 Conclusions and future work 225
8.1 Polymer solar cells 226
8.2 Organic luminescent solar concentrators 229

Appendix A: List of symbols and abbreviations 231
Appendix B: List of publications and communications 235

FOREWORD

The steady increase in energy consumption currently experienced by most world economies accompanied by the urge of reducing the environmental impact of fossil-fuel energy calls for new routes for energy production from clean and renewable sources.

Photovoltaics, the direct conversion of sunlight into electricity, represent one of the simplest and most promising technologies to address these issues. Owing to its modular nature, the photovoltaic technology is potentially suitable for a large variety of applications. In addition, their silent operation and the absence of moving parts associated with their function make photovoltaic devices a potentially disruptive technology that may significantly contribute to the world's future electrical energy needs.

The photovoltaic market is currently largely dominated by silicon-based devices, although several technologies exist, that make use of different materials, device architectures and manufacturing processes. Among these, polymer-based organic photovoltaics (PSC) and organic luminescent solar concentrators (OLSC) have recently gained increasing attention because of the many advantages they can provide: low-cost production, solution processability, device flexibility, and light-weight.

Although intense research efforts have been made in the past decades leading to a rapid development of these two new technologies, the road to their commercial deployment is still long, mainly because of many issues related to the stability and the efficiency of the actual devices that are yet to be solved.

In the attempt to tackle some of these open issues, this work critically analyzes both PSC and OLSC technologies and specifically addresses aspects related to their efficiency and their photo-chemical and morphological stability, in the attempt to give guidelines for improved device performance.

Part of this work was carried-out during an eight-month research stage at the University of California, Berkeley within the group of Prof. J. M. J. Fréchet.

image in next page:
details from M. K. Čiurlionis "The Sun is Passing in the Sign of Sagittarius", 1906-1907.

>1

AIMS AND STRUCTURE OF THE WORK

1.1 AIMS OF THE WORK

Photovoltaic technology (PV) represents nowadays one of the most promising means to produce energy from clean and renewable sources.

Although the PV market is currently largely dominated by silicon-based PV devices, new materials and technologies have started to gain increasing attention in the past decades, both from academia and industry. In particular, organic materials and conjugated polymers have been recently investigated for use in polymer-based organic photovoltaics and in organic luminescent solar concentrators.

The intense research efforts in these two fields have allowed a rapid development of these technologies in the last twenty-to-thirty years. Nevertheless, the road to their commercial deployment is still long, mainly because of many issues related to the stability and the efficiency of the actual devices that are yet to be solved.

Especially, a clear understanding of the degradation mechanisms of the materials constituting the actual working devices is still lacking, and effective strategies to improve device lifetime are needed. In addition, the role of materials design and processing on device efficiency needs to be further investigated to optimize device performance. These issues represent central milestones in view of a potential future commercialization of these technologies.

In this Ph.D. work, different aspects related to the stability and the efficiency of polymer-based organic photovoltaics and organic luminescent solar concentrators were investigated with the aim of proposing potential strategies to improve device performance and lifetime. For each technology, both materials properties and device operation were analyzed in detail so that a deeper understanding of the criticalities associated with these research areas could be achieved.

1.2 STRUCTURE OF THE WORK

This Ph.D. thesis is structured as follows:

Chapter 1 highlights the aims of this Ph.D. work.

Chapter 2 presents an overview on the general mechanisms underlying solar cell operation and on the specific differences in the photocurrent generation between inorganic and organic photovoltaics. The most common device parameters to describe solar cell performance are derived theoretically from the equivalent electrical circuit and represented on the experimental current-voltage curve. The inorganic photovoltaic market is briefly reviewed and the main technological achievements are highlighted, before discussing in full detail the principles of operation of polymer-based organic photovoltaics and organic luminescent solar concentrators. For these two technologies, a critical analysis on recent achievements in materials and device engineering is presented with particular emphasis on long-term stability and efficiency of devices, these two aspects being the main focus of this thesis.

Chapter 3 presents a study on the photo-oxidative degradation of a model p-conjugated polymer used in polymer-based photovoltaics, namely poly(3-hexylthiophene) - P3HT. By irradiating the solid-state polymer in ambient air under simulated sunlight, a degradation mechanism is proposed. In addition, the effect of polymer regioregularity on the rate of P3HT degradation is also examined in detail. Finally, potential strategies to improve P3HT photo-stability are proposed, including the use of hindered amine light stabilizers and multi-walled carbon nanotubes.

Chapter 4 describes the results obtained from a study on long-term thermal stability of polymer solar cells based on low-bandgap copolymers. The synthesis of a series of novel photocrosslinkable low-bandgap copolymers based on the thieno[3,4-c] pyrrole-4,6-dione acceptor monomer is presented and the effect of the amount of photocrosslinkable moiety on device performance is investigated. Optimization of photocrosslinking conditions and device parameters is also described, followed by evaluation of their morphological and photovoltaic stability at high temperature. In addition, the influence of n-type material on morphological stability is also examined, by studying blends incorporating $PC_{61}BM$ or $PC_{71}BM$.

Chapter 5 presents a study on the characterization and device performance of novel donor-acceptor co-polymers containing isothianaphthene (ITN) acceptor monomers with different electron-withdrawing functionalities, namely ester, imide and nitrile. An extensive optimization of different device parameters is presented on each polymer system, where characteristic quantities such as polymer:fullerene ratio, active layer blend concentration, solvent system and thermal annealing are systematically examined in order to yield optimal device performance. The effects of the electron-withdrawing substituents on the optical and electronic properties of the resulting polymers are discussed in detail.

Chapter 6 reports on a study on the photo-degradation of a thin-film organic luminescent solar concentrator consisting of a model organic luminescent perylene-based dye dissolved in a poly(methyl-methacrylate) (PMMA) matrix, deposited onto a glass slide. By exposing the device in air to high-energy UV-light, its photo-stability is characterized by means of FTIR, UV-vis and photoluminescence spectroscopy during irradiation time. The behavior of each material constituting the OLSC device is monitored and a degradation mechanism for the dye molecule is proposed. Finally, the role of the organic dye molecule in the degradation of PMMA is analyzed and the effect of the state of aggregation of the organic dye on its photo-stability is clarified

Chapter 7 presents a comprehensive overview on the main experimental methods followed in this work to fabricate working devices. In particular, details are given on all materials, fabrication procedures and electrical characterization methods employed for standard bulk-heterojunction polymer solar cells, inverted-type bulk heterojunction polymer solar cells and thin-film organic luminescent solar concentrators. In addition, preliminary results on novel processing techniques compatible with large-scale production of polymer-based photovoltaics are discussed. Finally, a study on the effect of luminescent dye concentration and thin-film thickness on the photovoltaic response of organic luminescent solar concentrators is presented.

Chapter 8 gives a detailed summary of all the main experimental results obtained in this Ph.D. work and presents an outlook on possible future research lines. Finally, Appendix A presents a list of symbols and acronyms used in this thesis and Appendix B gives a list of publications in international journals and communications in national and international conferences.

image in next page:

details from M. K. Čiurlionis "Creation of the World (XIII)", 1905-1906.

>2

ENERGY FROM THE SUN: THE PHOTOVOLTAIC TECHNOLOGY

In one of his most famous quotes, Thomas A. Edison stated:[1] "*We are like tenant farmers chopping down the fence around our house for fuel when we should be using nature's inexhaustible sources of energy - sun, wind and tide [...] I'd put my money on the sun and solar energy. What a source of power! I hope we don't have to wait until oil and coal run out before we tackle that.*"

After almost a century since this visionary statement, solar energy has become a reality in today's world.

With its average 105 terawatts (TW) of power hitting the exposed surface of Earth continuously, the sun is theoretically able to supply approximately 10000 times more power than the 19 TW expected to be consumed by the population on the planet in 2015.[1] An efficient way to harness this enormous amount of energy from the sun to make it readily available for consumption is by means of photovoltaic (PV) devices (also known as solar cells), which employ the photovoltaic effect[2] to directly convert sunlight into electricity. In general, this implies the emergence of an electric voltage between two electrodes attached to the PV device upon shining light onto it.

Owing to its modular nature, PV technology is potentially suitable for a large variety of applications. In addition, with their silent operation and absence of moving parts associated with their function, PV devices can potentially contribute to a great portion of the world's future electrical energy needs.

Although the photovoltaic effect was first observed in the 19th century, modern solar cell prototypes appeared only in the 1950's and 1960's as electricity generators, thanks to the progresses in the early silicon semiconductor technology for electronic applications.[3]

Nowadays, several PV technologies exist, that make use of different materials, device architectures and manufacturing processes.

The multidisciplinary approach to this field, which requires skills from different areas such as chemistry, physics, materials science and engineering, and electrical engineering, to name but a few, has allowed a rapid development of this technology in the last twenty-to-thirty years, making it one of the most promising alternatives to fossil-fuel energy sources.

---

[1] In conversation with Henry Ford and Harvey Firestone (1931); as quoted in "Uncommon Friends: Life with Thomas Edison, Henry Ford, Harvey Firestone, Alexis Carrel & Charles Lindbergh" by James Newton - Houghton Mifflin Harcourt Publisher, 1989.

2.1 UNDERSTANDING SOLAR CELL OPERATION

A large variety of PV technologies are available nowadays for the conversion of solar energy into electricity, each characterized by a different material constituting the photoactive layer in the PV device. As shown in Figure 2.1, impressive improvements have been reported over the past thirty years in the performance of PV devices. In particular, different technologies have experienced different increases in power conversion efficiency, leading to record values that can vary significantly depending on the photoactive material employed in the PV device.

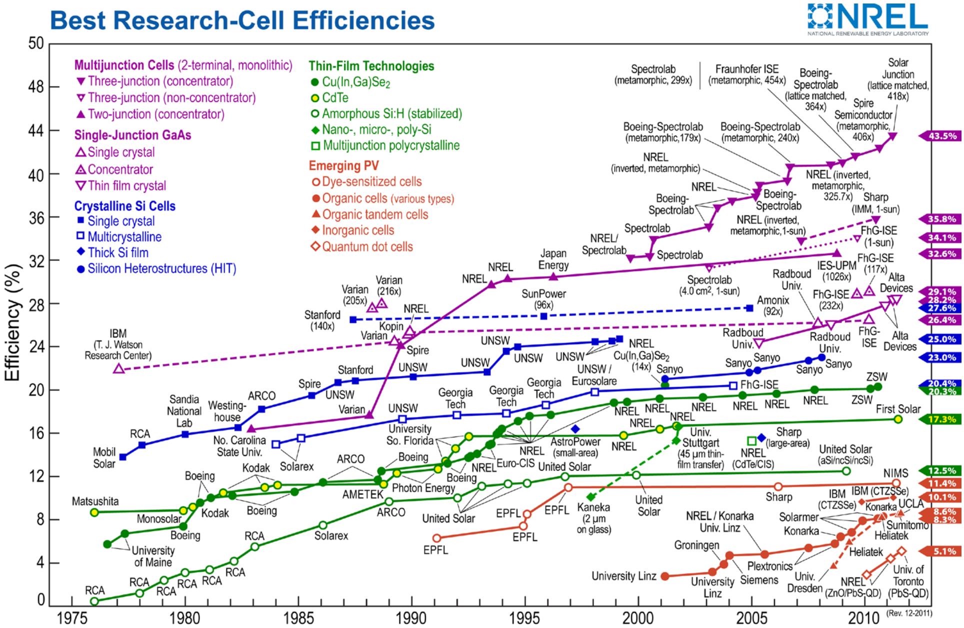

Figure 2.1. Evolution of the best laboratory solar cell efficiencies for different PV cell technologies (source: National Renewable Energy Laboratory – USA, 2011).

In order to comprehend the origin of these performance differences, a full understanding of the general principles underlying solar cell operation is required. As regards this aspect, it is important to examine the physical phenomena occurring within the photoactive materials and in particular to determine the driving forces responsible for the emergence of a photogenerated current flux in both organic (OPV) and inorganic PV devices.

The general kinetic expression for the current density of electrons $J_n(x)$ through any solar cell generated by electrical and chemical potential energy gradients can be written as:[4]

$$J_n(x) = n(x)\mu_n \nabla U(x) + kT\mu_n \nabla n(x) \qquad \text{(Equation 2.1a)}$$

where n(x) is the concentration of electrons, μ_n is the electron mobility and k and T are Boltzmann's constant and the absolute temperature, respectively. Similarly, the flux of holes $J_h(x)$ can be described by:

$$J_h(x) = h(x)\mu_h \nabla U(x) + kT\mu_h \nabla h(x) \qquad \text{(Equation 2.1b)}$$

where h(x) and μ_n similarly represent concentration and mobility of holes, respectively.

These two expressions are valid both at equilibrium and at non-equilibrium, both in the dark and under illumination.[4]

If the quasi-Fermi level E_{Fn} (i.e. the non-equilibrium Fermi level, under illumination) for electrons (or similarly for holes) is considered:

$$E_{Fn}(x) = E_{CB}(x) + kT \ln\{n(x)/N_C\} \qquad \text{(Equation 2.2)}$$

where $E_{CB}(x)$ is the electrical potential energy at the conduction-band edge and N_C is the density of electronic states at the bottom of the conduction-band, simpler expressions of $J_n(x)$ and $J_h(x)$ can be obtained:

$$J_n(x) = n(x)\mu_n \nabla E_{Fn}(x) \qquad \text{(Equation 2.3a)}$$

$$J_h(x) = h(x)\mu_h \nabla E_{Fh}(x) \qquad \text{(Equation 2.3b)}$$

Therefore, any process causing a change in the photo-electrochemical force (i.e., $\nabla E_{Fn} \neq 0$ or $\nabla E_{Fh} \neq 0$) will yield photovoltaic effect and thus a current flow through the device. Such a change can be achieved either by a variation $\nabla\mu$ of the chemical potential from its equilibrium value or by a change of the electrical potential ∇U. It is therefore useful to split Equation 2.1a into two independent electron fluxes, each driven by one of the non-equilibrium forces $\nabla\mu$ and ∇U. In particular, the current density due to the electrical potential gradient can be written as:

$$J_n(x) = n(x)\mu_n \nabla U(x) \qquad \text{(Equation 2.4a)}$$

while the current density due to the chemical potential gradient as:

$$J_n(x) = n(x)\mu_n \nabla \mu(x) \qquad \text{(Equation 2.4b)}$$

where, $\nabla\mu(x) = kT/(n(x)\nabla n(x))$.

The two equations presented above (Equations 2.4a and 2.4b) show that the electrical potential energy gradient ∇U and the chemical potential energy gradient $\nabla\mu$ are equivalent driving forces for the current density to be generated, although they originate from totally different physical phenomena.

This consideration is very important when comparing inorganic to organic solar cells. While the conventional inorganic PV devices mainly rely on the action of an electric potential gradient ∇U across a p-n junction, in OPV devices $\nabla \mu$ is often predominant, as it will be described in the next Sections.

2.1.1 Inorganic solar cells

Inorganic PV devices are essentially constituted by interfaces between semiconducting layers, or a semiconductor layer and a metal, that create a potential difference between the layers by virtue of the difference in their physical properties, namely the nature of doping, the doping level and the atomic composition of each layer. Accordingly, inorganic solar cells can be based on simple p-n homojunctions, more complex heterojunctions, common Schottky barriers or p-i-n junctions.[5] In the following, a brief description of the physics behind the simple p-n homojunction is presented, which can typically be exemplified by a junction between p-doped and n-doped silicon.

When a p-n junction is formed between doped inorganic semiconductors, the interactions occurring at the interface between the materials and with the electrodes determine the carrier distributions and concentrations in the materials under equilibrium conditions.[5,6] In order to describe these interactions, it is convenient to consider a conventional band-energy diagram for the p-n junction where valence band and conduction bands at the interface between p-doped and n-doped materials are represented (see Figure 2.2)

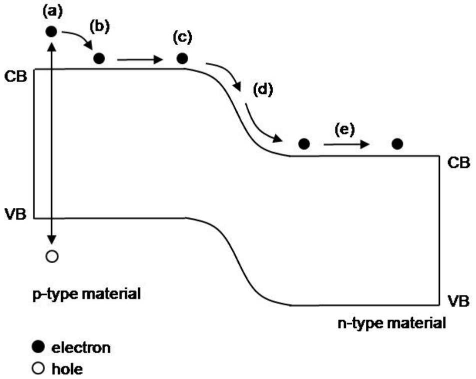

Figure 2.2 Absorption of photons with an average photon energy larger than the bandgap on either side of the junction (a) is followed by thermalization and formation of holes and electrons near the top of the valence (VB) and conduction (CB) bands, respectively (b). Minority carriers (electrons in the p-type semiconductor; holes in the n-type semiconductor) diffuse to the junction (c) where they are swept across as a result of a drift process (d) and accumulate on the other side of the junction where they can diffuse and become majority carriers (e). For the sake of simplicity, these steps have been represented for electrons, but the same applies to holes.

At the interface between the p-type and n-type materials, where the so-called depletion region is present, the free charge redistribution leads to an equilibrium condition characterized by the formation of a potential difference and an electric field confined across the junction, which vanish outside the depletion region. The presence of this potential difference, also known as the built-in potential, causes the energy bands to bend within the depletion region.

Illumination of the materials and absorption of photons with sufficient energy to overcome the bandgap of the material lead to the formation of free charges (holes and electrons) near the top of the valence (holes) and conduction (electrons) bands in both sides of the p-n junction.

The additional electrons formed in the n-part of the junction and holes formed in the p- part of the junction upon illumination is negligible compared to the density of the majority carriers in both sides at thermal equilibrium (i.e., holes in the p-doped material and electrons in the n-doped material). On the other hand, the density of photogenerated minority carriers (i.e., electrons in the p-doped material and holes in the n-doped material) is large proportionate to the density of minority carriers at equilibrium in the dark. These photogenerated minority carriers are responsible for the charge transport occurring upon illumination, through a process that is mainly governed by a combination of drift and diffusion. The minority carriers approaching the depletion region by a diffusion process are swept across it as a result of a drift process caused by the presence of the built-in potential at the junction (the electric potential gradient ∇U). In this way, they accumulate on the other side of the junction where they become majority carriers and can diffuse away from it, generating the electrical current flow.

Therefore, in inorganic solar cells electrons can efficiently be separated from holes only by the action of the electrical potential-energy gradient ∇U across the cell.

2.1.2 Organic solar cells

The basic mechanisms underlying the operation of organic solar cells present several differences compared with inorganic PV devices.

One of the main differences is related to the interfacial processes occurring upon device illumination, which are closely associated with the mechanisms of charge generation. In inorganic solar cells, light absorption immediately yields free electron-hole pairs throughout the bulk of the material. Conversely, light absorption in OPV devices generally results in the formation of mobile excited states.[7,8] This difference is intimately related to the dielectric constant and the non-covalent electronic interactions characteristic of organic materials. The dielectric constant of organic materials is usually low compared to inorganic semiconductors, thus causing the attractive Coulomb potential well around the developing electron-hole pair to extend over a larger volume compared to inorganic semiconductors. On the other side, the non-covalent electronic interactions between organic molecules being weak (narrow band-width) compared to the strong inter-atomic electronic interactions of covalently bonded inorganic semiconductor materials (e.g., silicon), the electron's (hole's) wave function is spatially restricted and localized in the Coulomb potential well of its corresponding hole (electron). As a result of these two phenomena, a tightly bound electron/hole pair (Frenkel-type exciton or excited state) is the usual product of light absorption in organic semiconductors.[9-11] Such an exciton is a mobile, electrically neutral species which is virtually unaffected by electric fields and that needs to be dissociated in order to form free charge carriers. In fact, the most important process occurring in most OPV cells during operation is the interfacial dissociation of excitons into a free electron and a free hole. This process mainly takes place at the hetero-interface between two different organic materials,[12] which are in most cases non-doped semiconductors. Generally, these two materials are referred to as n-type (electron-acceptor or electron-conducting) and p-type (electron-donor or hole-conducting) materials, where these terms denote the majority type of carriers in each semiconductor. Such a hetero-interface may for instance be created by an intimate mixture of a p-type conjugated polymer and an n-type organic molecule in a so-called bulk heterojunction (BHJ). Because no free charge carriers are available in the non-illuminated device, when the two materials are brought into intimate contact no depletion region is formed. Therefore, no built-in potential is formed and no band-bending is observed (unlike in the inorganic counterpart). Instead, a band offset is observed at the interface between p-type and n-type materials.

In most OPV devices, excitons created upon light absorption in either side of the hetero-interface do not possess enough energy to dissociate in the bulk. For this reason, they first must diffuse to the hetero-interface where they can find sufficient energy for their dissociation.[9,10] This dissociation energy is provided by the band offset between p-type and n-type materials (Figure 2.3), which yields electrons in the n-type material already separated from holes in the p-type material. Therefore, already separated free charge carriers are formed across the hetero-interface, resulting in a chemical potential gradient $\nabla\mu$ that provides the necessary driving force to further separate the charges and generate the current flow.

It is worth noticing that the energy of a free electron/hole pair (corresponding to the electrical bandgap of the material) is larger than the energy of a thermalized[2] exciton (which corresponds to the optical band gap of the material) and their difference is the exciton binding energy (Figure 2.3).[4] Therefore, the thermodynamic requirement for interfacial exciton dissociation to occur is that the

---

[2] After an electron is photo-promoted to an excited state, its potential energy decreases until it reaches the lowest lying level in the conduction band - the so-called Lowest Unoccupied Molecular Orbital (LUMO). Since this energy decrease takes place by heat dissipation, this processed is known as thermalisation.

band offset between p-type and n-type materials (Δ in Figure 2.3) has to be greater than the exciton binding energy (0.3-0.5 eV).[13-17]

Finally, because of their usually low carrier densities at equilibrium, OPVs under illumination are almost always majority carrier devices, contrary to most inorganic solar cells which are minority carrier devices.

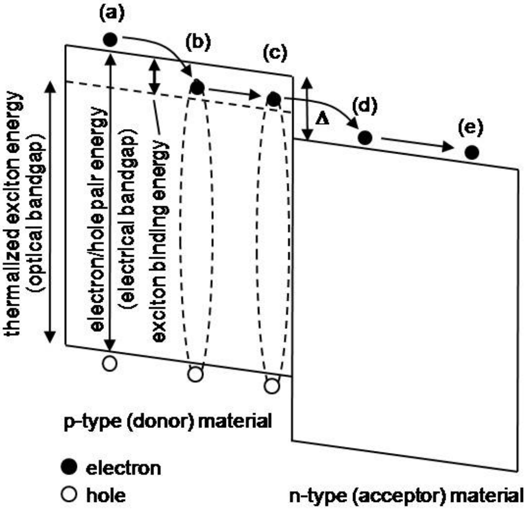

Figure 2.3 Absorption of photons with an average energy larger than the optical bandgap on either side of the heterojunction (a) is followed by thermalization and formation of excitons (b). Excitons diffuse to the p-n heterojunction (c) where they dissociate and transfer an electron (hole) into the n-type (p-type) material (d); the charge carrier is then transported via diffusion to the respective electrode (e); Δ denotes the band energy offset between the p-type and n-type material. For the sake of simplicity, these steps have been represented only for electrons, but the same applies to holes.

2.1.3 Characterizing solar cell performance: the I-V curve

In general, the performance of PV devices can be measured in terms of how efficiently they are able to convert light energy into electrical energy.

One of the first studies on the theoretical maximum efficiency of a solar cell was presented by Shockley and Queisser[18] who calculated the maximum power conversion efficiency as a function of the semiconductor bandgap through a detailed balance of the different particle fluxes in the solar cell. It was found that a maximum efficiency of about 30% can be theoretically obtained with semiconducting materials presenting a bandgap between 1.3 eV and 1.5 eV (Figure 2.4).

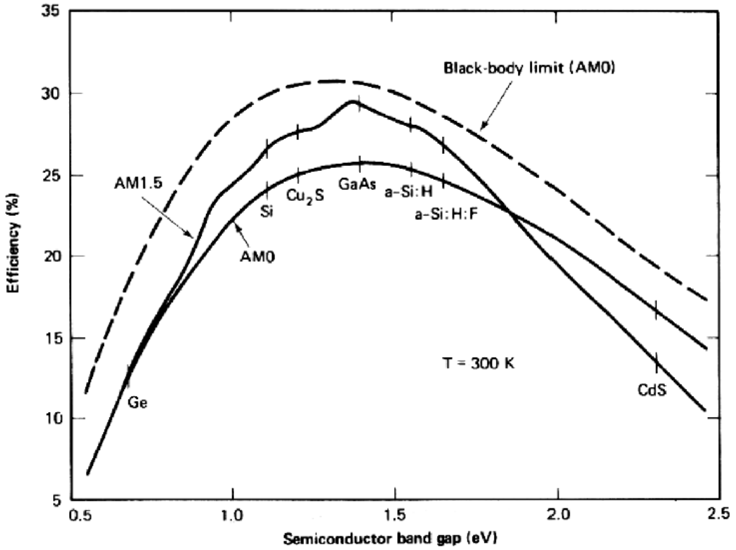

Figure 2.4 Dependence of the solar cell power conversion efficiency on the semiconductor band-gap. The solid lines represent semi-empirical limits assuming space(AM0) and terrestrial (AM1.5) solar radiation; the dashed line is purely based on thermodynamic considerations for blackbody solar cells under AM0 radiation.[18,19]

A simple way to describe the behavior of PV devices and to evaluate their power conversion efficiency is by means of an equivalent circuit, as the one shown in Figure 2.5.

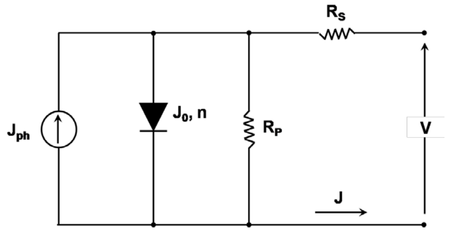

Figure 2.5 Equivalent circuit of a PV cell: R_S and R_P are the series and shunt resistances, respecively; J_{ph} is the generated photocurrent density; J_0 reverse saturation current-density of the diode with ideality factor n; J is the current-density flowing through the circuit; V is the voltage.

Since a solar cell in the dark behaves as a diode, a diode with reverse saturation current density J_0 (current density in the dark at reverse bias) and ideality factor n is included in the equivalent circuit. In addition, a current source J_{ph} is present, which corresponds to the photocurrent generated upon solar cell illumination. Finally series (R_S) and shunt (R_P) resistances are considered. On one hand, R_S has to be minimized in order to achieve optimal PV performance and takes into account the finite conductivity of the semiconducting material, the contact resistance between the semiconductors and the adjacent electrodes, and the resistance associated with electrodes and interconnections. On the other hand, R_P needs to be maximized and takes into account the loss of carriers via possible leakage paths, including structural defects such as pinholes in the film, or recombination centers introduced by impurities.

The solution of this equivalent circuit provides an analytical expression for the total current density produced by the PV device, known as the Shockley equation:[20]

$$J = \frac{1}{1 + R_S/R_P}\left\{J_0\left[\exp\left(\frac{V - JR_S}{nk_BT/q}\right) - 1\right] - \left[J_{ph} - \frac{V}{R_P}\right]\right\} \qquad \text{(Equation 2.5)}$$

where V is the voltage, q is the elementary charge and k_BT the thermal energy. When $J_{ph} = 0$, Equation 2.5 gives the dark current density.

This equation describes the produced photocurrent density as a function of the applied voltage. Accordingly, the J-V (current density-voltage) characteristic curve of the solar cell can be plotted for dark and illuminated PV devices (Figure 2.6). From the J-V plot, different characteristic parameters can be highlighted.

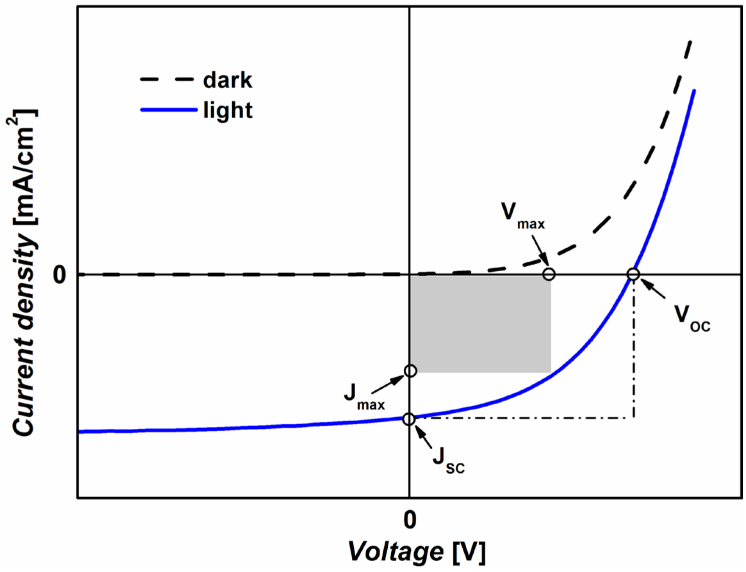

Figure 2.6 Current-density voltage (J-V) characteristic curves of a solar cell in the dark and under illumination. The meaning of each parameter is explained in the text. The shaded area represents the maximum power output of the solar cell.

For V = 0 (no voltage applied), the short-circuit current density J_{SC} is obtained, whose expression can be derived from Equation 1.5 as follows:

$$J_{SC} = -\frac{1}{1+R_S/R_P}\left\{J_{ph} - J_0\left[\exp\left(\frac{|J_{SC}|R_s}{nk_BT/q}\right)-1\right]\right\} \qquad \text{(Equation 2.6)}$$

Conversely, when no current is flowing through the device (J = 0, open-circuit conditions) the open-circuit voltage V_{OC} is found, obtained from Equation 1.5 as follows:

$$V_{OC} = n\frac{k_BT}{q}\ln\left\{1+\frac{J_{ph}}{J_0}\left[1-\frac{V_{OC}}{J_{ph}R_P}\right]\right\} \qquad \text{(Equation 2.7)}$$

For sufficiently small series resistance and sufficiently large shunts, the effects of R_S or R_P can be neglected and approximate expressions for J_{SC} and V_{OC} can be written:[20]

$$J_{SC} \approx -J_{ph} \qquad \text{(Equation 2.8)}$$

$$V_{OC} \approx n\frac{k_BT}{q}\ln\left\{1+\frac{J_{ph}}{J_0}\right\} \qquad \text{(Equation 2.9)}$$

The value of the J_{SC} is mainly controlled by the intrinsic current generation process due to light absorption and by the charge recombination events occurring within the device. Conversely, V_{OC} is strictly related to the quality of the diode and to its reverse saturation current density, as apparent from Equation 1.9.

Both J_{SC} and V_{OC} can be determined experimentally upon device illumination as intersects of the experimental J-V curve with the vertical and horizontal axes, respectively. For any point on the J-V curve between J_{SC} and V_{OC} in the fourth quadrant ($J_{SC} < 0$ and $V_{OC} > 0$), the PV device delivers electrical power density, given as the product between voltage and current density. The maximum value of power density P_{max} is obtained when the product between current-density and voltage is maximized,

$$P_{max} = J_{max} \cdot V_{max} \qquad \text{(Equation 2.10)}$$

with J_{max} and V_{max} being the current-density and voltage, respectively, at the maximum power density.

The power conversion efficiency (PCE) of the solar cell is then defined as the ratio between the maximum power produced by the solar cell P_{max} and the incident power density P_{in}, as follows:

$$PCE = \frac{P_{max}}{P_{in}} = \frac{I_{max} \cdot V_{max}}{P_{in}} = FF\frac{I_{SC} \cdot V_{OC}}{P_{in}} \qquad \text{(Equation 2.11)}$$

where FF is the fill factor of the solar cell, defined as:

$$FF = \frac{I_{max} \cdot V_{max}}{I_{SC} \cdot V_{OC}} \qquad \text{(Equation 2.12)}$$

which is a measure of the quality of the operating diode (i.e., the PV device) under illumination.

The quantitative characterization of the performance of solar cells in laboratory research is generally performed by employing standardized illumination conditions, in which the spectrum of the source simulates the solar spectrum on the earth (AM 1.5G) and has an intensity of approximately 100 mW/cm^2 (Figure 2.7). This value corresponds to the average intensity of sunlight with an angle of incidence $\theta = 48°$ relative to the normal to the earth's surface. The prefix AM denotes the air mass value, that practically indicates how much air mass the sunlight has been transmitted through ($AM = 1/\cos\theta$). The letter G stands for "global" and indicates that the incident light includes components of both light diffused and light reflected from the soil.

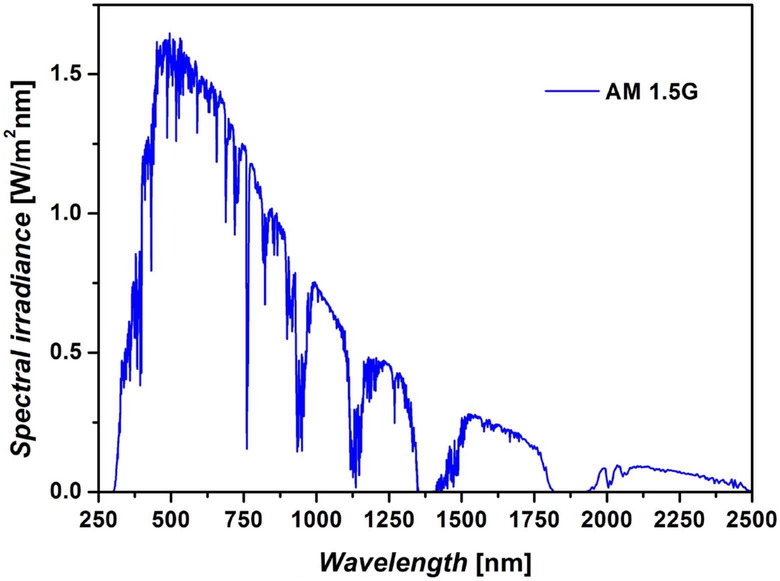

Figure 2.7 AM 1.5G sunlight emission spectrum in the 250 – 2500 nm region.

The power conversion efficiency PCE, the fill factor FF, the short-circuit current density J_{SC} and the open-circuit voltage V_{OC} represent the key parameters for the characterization of any type of PV device.

2.2 PHOTOVOLTAIC DEVICES: FROM SILICON TO ORGANIC MATERIALS

The current photovoltaic market is largely dominated by silicon (Si)-based devices, as illustrated in the diagram shown in Figure 2.8 depicting the market shares of different PV technologies in 2008.[21]

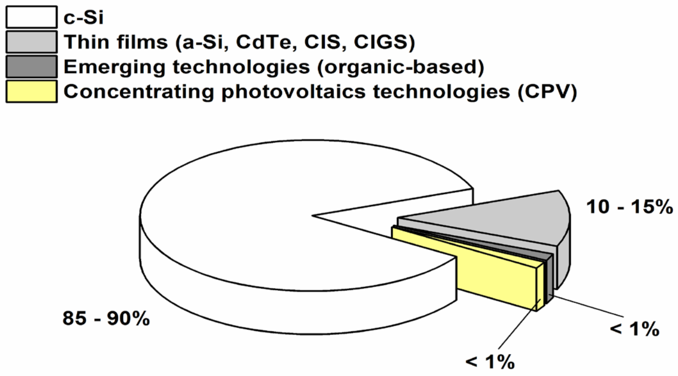

Figure 2.8 Percent share of 2008 photovoltaics market.

Despite not being the ideal material for solar cells (non-optimal band-gap value, indirect band-gap semiconductor, poor absorption coefficient), Si-based technologies account for approximately 90% of the current photovoltaic market, making Si the leading material for solar cell construction. There are several technical and economic factors leading to the dominance of Si in the solar cell industry.[19] Among them, the most dominant are probably the technical knowhow developed by the Si-based semiconductor industry by the 1970s (which the solar industry took advantage of in its infancy) together with the availability of large quantities of high quality Si material coming from the microelectronics market.

As we have seen in Section 2.1.1, the working mechanisms of Si-based PV devices rely on photon absorption throughout the bulk of the semiconducting material, further extending out of the depletion region. As a result, in order for the charges to be separated and collected to the respective electrodes, diffusion of the photo-excited free charge carriers towards the depletion region must occur. This highlights the importance of the manufacturing quality of the entire semiconducting material to be incorporated in the PV device, which needs to be pure enough to guarantee long minority carrier lifetime and high carrier mobility, so that optimal device efficiency can be attained.

Although an in-depth description of the production methods employed to

fabricate Si-based PV devices is out of the scope of this Ph.D. work, the leading role of Si in the photovoltaic market calls for an at least brief overview on the standard architecture of a Si-based solar cell and on the most common method for fabricating it.
A schematic of the typical Si solar cell architecture commonly used in production up to present[22] is shown in Figure 2.9.

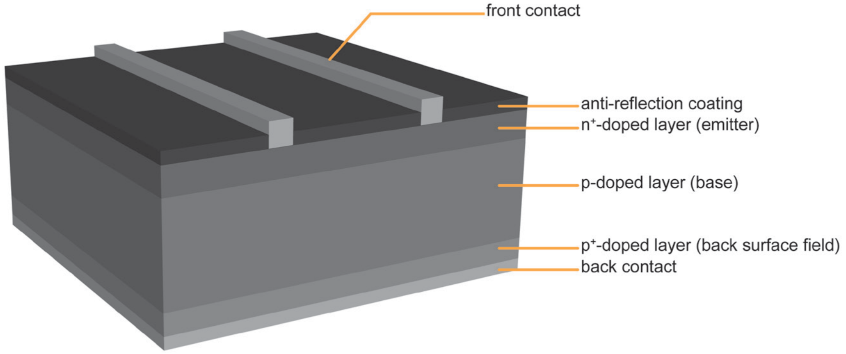

Figure 2.9 Device architecture of a typical Si-based solar cell.

Standard monocrystalline-Si solar cells are fabricated starting from Si wafers obtained via the Czochralski method, where p-doped (usually boron-doped) mono-crystalline Si rods are slowly withdrawn from a Si melt starting from a rotating Si seed crystal. The obtained crystal rods are cut into wafers having a typical thickness ranging from 200 mm to 500 mm. Such a large wafer thickness (> 200 mm) is required in order to absorb most of the light incident onto the device because of the low optical absorption coefficienct of monocrystalline (and multicrystalline) Si that results from its indirect energy bandgap structure. The wafer surfaces are micro-textured by etching with a solution of NaOH and isopropyl alcohol so as to minimize reflection losses and refract light entering the Si to high angles of refraction, thus enhancing the optical path length within the Si. A p-n junction is formed by diffusing an n-type dopant (usually phosphorus) into the wafer as an impurity into the front side of the wafer for a typical depth of 0.5 mm (the n$^+$-doped emitter layer). Screen-printed Ag contact fingers are used on the front n-type surface to make electrical contact while also allowing light to be transmitted to the junction region. The typical width of the contact fingers is 200 μm and the separation between two fingers is 3 mm, for a balance between minimum resistance and minimum light shadowing. The backside electrical contact is formed by screen-printing an Al film onto the Si wafer. Upon annealing this Al layer, a p$^+$-doped region is formed at the back of the cell which lowers the contact resistance and supplies a back surface field that reflects minority carriers back towards the junction.[22] Finally, a transparent antireflective coating (usually silicon nitride SiN_X or TiO_2) is deposited by plasma-enhance chemical vapor deposition (PECVD) over the top surface to complete the device.

Despite representing the standard for Si-based solar cells, this architecture has been shown to present a number of limitations mainly ascribable to the use of screen-printed contacts. In order to overcome these limitations, solar cells have been developed in which the contacts are defined either using photolithography or laser scribing.[23]

At present, the highest efficiency reported on small-scale laboratory monocrystalline-Si solar cells is the "passivated emitter rear locally diffused" solar cell, which achieved a certified PCE of 25% thanks to improvements in the surface texturing of the Si wafer and to inclusion of a SiO_2 layer at the back of the device to passivate its back surface.[24]

Although high device efficiencies can be attained with crystalline-Si solar cells, this technology still presents some disadvantages, essentially related to the high thermal and capital costs needed for wafer production. In an attempt to overcome some of these limits, various thin-film technologies have been developed that offer lower costs both in terms of material supply and thermal budget. Amongst these, amorphous silicon (which is actually hydrogenated amorphous silicon, aSi:H) presents some advantages due to the possibility of depositing layers on both rigid and flexible substrates and to the reduction of layer thickness (only a few microns) needed to absorb most of the incident light due to direct optical bandgap structure of aSi:H coupled to a high absorption coefficient for photons with energies higher than the bandgap energy. One main disadvantage of this technology is that aSi:H solar cells suffer of severe degradation under illumination, because of the well-known Staebler-Wronski effect and record efficiencies of only 10% have been reported.[25-28]

Other thin-film technologies include cadmium-telluride (CdTe) solar cells, copper indium-gallium diselenide [Cu(In,Ga)Se2] solar cells and gallium arsenide (GaAs) solar cells. Even though these technologies present some disadvantages mainly related to the fabrication costs and the potential toxicity of some of the materials employed,[22] much work has been done to improve their performance and device efficiencies challenging those of silicon have been reported, with record laboratory-scale PCEs of 16.7%, 19.6% and 28.3%, respectively.[29]

Alongside inorganic-based solar cells, organic and polymeric materials have been explored and developed in the past twenty years to be employed as photoactive materials in different types of organic-based PV technologies. Among these, dye-sensitized solar cells (DSSC) or Grätzel cells[30] present nowadays the highest efficiency, with a certified PCE of 11%.[29] In this type of solar cells, light is absorbed by a dye molecule (typically a ruthenium-based dye)[31] adsorbed onto the surface of a mesoporous film of semiconducting metal-oxide nanoparticles, filled with a liquid electrolyte containing a redox couple. After photoexcitation, the dye molecule injects an electron into the metal-oxide semiconductor (typically mesoporous TiO_2 particles), which is responsible for the transport of this electron to the anode. The presence of the redox couple (typically iodide/triiodide) in the electrolyte ensures the oxidized dye to be reduced back to its neutral state. As a result of their basic working principles, in DSSCs two different materials, the dye molecule and the metal-oxide nanoparticles, are distinctively responsible for charge generation and charge transport, respectively.[32] Because of potential problems arising from solvent leakage and corrosion from the iodide/triiodide redox couple, solid-state DSSC have been recently presented, where an organic hole-transporter replaces the liquid electrolyte. Although this strategy has proven to be promising and advances are being reported, efficiencies still remain lower than those of devices based on liquid electrolytes.[32]

A relatively new class of organic-based PV devices makes use of semiconducting conjugated polymers as photoactive p-type materials employed in conjunction with an organic small molecule acting as the n-type material. These so-called polymer solar cells (PSC) have recently attracted considerable attention because of the many advantages they can provide: low-cost solution-based processability, flexible devices, and light-weight construction. The PSC technology has experienced enormous improvements in the past decade in terms of both materials and device engineering, recently leading to a few demonstrations of middle-to-large-scale device production.[33,34] A detailed overview on these advances will be presented in the next Section.

2.3 POLYMER SOLAR CELLS

A schematic representation of a typical single junction PSC is shown in Figure 2.10. The architecture of the device is characterized by a layered structure, in which the main component is the photoactive layer, generally constituted by a p-type electron-donor and an n-type electron-acceptor material. In PSCs, both donor and acceptor materials are p-conjugated organic materials and one of them (or both) is a semiconducting polymer. The photoactive layer is sandwiched between two electrodes, one of which is transparent to allow light transmission to the photoactive layer. Additionally, electron-transporting (typically LiF or TiO_X) and/or hole-transporting (typically poly(3,4-ethylenedioxythiophene):poly(styrenesulfonate) PEDOT:PSS) layers may be present.

Different refined models exist in the literature to describe the photoinduced charge transfer at the origin of free charge carrier generation in PSC devices,[14,16] however their description is not within the scope of this work and will therefore be neglected herein. On the contrary, a more simplified mechanism is invoked to describe the process of converting light into electrical current in a PSC, essentially consisting in the following five consecutive steps:[35]

- Absorption of a photon, that leads to photoexcitation of the absorbing materials with consequent promotion of electrons from the ground state (the highest occupied molecular orbital - HOMO) to the excited state (the lowest unoccupied molecular orbital - LUMO), and formation of an excited state (the electron-hole pair or exciton);
- Diffusion of the exciton towards the donor-acceptor interface, if the excited state is photogenerated within a diffusion length from it;
- Dissociation of the excited state at the donor-acceptor interface to form free charge carriers. This step can be accomplished if the energy offset between donor and acceptor materials is higher than the exciton binding energy. In particular, excitons photogenerated in the donor side of the interface will dissociate by transferring the electron to the LUMO level of the acceptor while retaining the positive charge. Conversely, excitons created in the other side of the donor-acceptor interface will transfer the hole to the HOMO of the donor while retaining the negative charge;
- Transport of the free charge carriers to the respective electrodes (electrons are transported in the acceptor material, holes are transported in the donor material);
- Collection of the free charges at the electrodes.

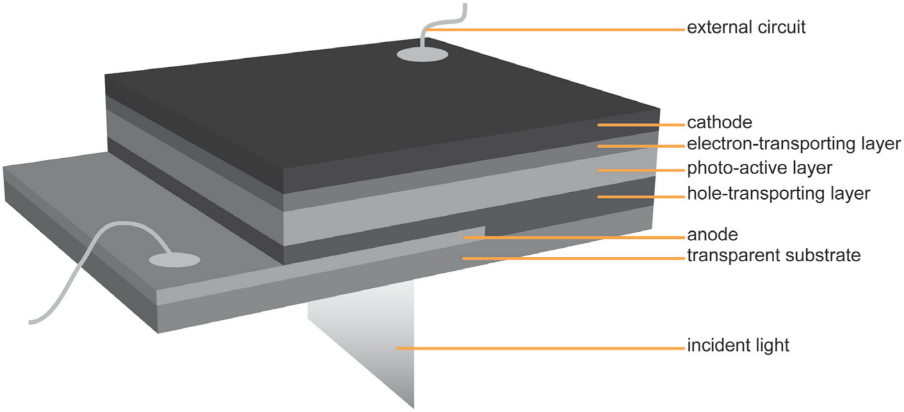

Figure 2.10. Device architecture of a typical single-junction polymer solar cell.

As apparent from this simple mechanism, the overall performance of a PSC device is controlled by the relative efficiency of each step contributing to the generation of an electrical current. Therefore, the optimization of each of these steps is critical in order to extract as much energy as possible from the device to achieve maximum PCE. This optimization encompasses the development of improved approaches in materials design and in device architecture and engineering, as will be shown in the following Sections.

2.3.1 Efficiency of polymer solar cells: the role of materials and device engineering

The parameters determining the PCE of polymer solar cells are the open-circuit voltage V_{OC}, the short-circuit current density J_{SC} and the fill factor FF (Section 2.1.3). While the FF strongly depends on the nanomorphology of the photoactive layer (as will be discussed later in this Section), V_{OC} and J_{SC} are closely related to the intrinsic properties of the photoactive materials.

We have seen in Section 2.1.2 that a driving force greater than the Coulombic attraction of the electron-hole pair (the exciton) is needed for exciton dissociation. Such a driving force can be obtained by tuning the energy levels of the donor and acceptor materials during synthesis so that sufficient energy offsets $|\mathrm{HOMO}_{acceptor} - \mathrm{HOMO}_{donor}|$ and $|\mathrm{LUMO}_{donor} - \mathrm{LUMO}_{acceptor}|$ can be ensured and the exciton binding energy can be overcome. In addition, to increase the portion of the light absorbed by the PSC device (number of photons contributing to the J_{SC} of the PSC device), donor materials (typically p-conjugated polymers) with a broad absorption spectrum are required. As opposed to that, in order to improve the V_{OC} of the device, a high-energy band-gap donor material is more desirable, as V_{OC} appears to be directly proportional to the $\mathrm{LUMO}_{acceptor} - \mathrm{HOMO}_{donor}$ difference.[36-39] Therefore, synthetic efforts are needed in order to produce low band-gap polymers with deep HOMO level that can profit of the low-energy component of the solar emission spectrum to improve the current output while maximizing the V_{OC} of the device.

In the attempt to meet the above requirements, several donor polymers have been synthesized and tested in the past few years in PSC devices, mainly used in conjunction with a fullerene derivative (either [6,6]-phenyl-C_{61}-butyric acid methyl ester – $PC_{61}BM$ or [6,6]-phenyl-C_{71}-butyric acid methyl ester – $PC_{71}BM$)[40,41] as the n-type molecule. This choice of acceptor molecule stems from the unique characteristics of fullerenes which make them the best n-type molecules employed so far in PSC devices: the occurrence of ultrafast (~50 fs) photoinduced charge transfer between the donor polymer and fullerenes,[42-45] their high electron mobility (1 cm^2 V^{-1} s^{-1} for $PC_{61}BM$ as measured by field effect transistor measurements),[46] their ability to phase-segregate in the active layer film.

The first polymers that were developed for the PSC technology were poly(1,4-phenylene-vinylene)s (PPVs), especially the extensively studied poly[2-methoxy-5-(3,7-dimethyloctyloxy)1-4-phenylene-vinylene] (MDMO-PPV), and regioregular poly(3-hexyl-thiophene) (P3HT) (Figure 2.11).[47]

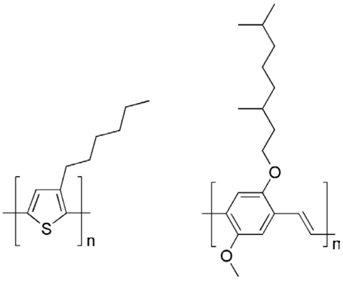

Figure 2.11 Molecular structure of poly(3-hexyl-thiophene) - P3HT and poly[2-methoxy-5-(3,7-dimethyloctyloxy)1-4-phenylene-vinylene] - MDMO-PPV.

In particular, the good charge carrier mobility of regioregular P3HT has made it the most-studied conjugated polymer in organic field-effect transistors (OFETs) and later on the most popular p-type polymer in PSC technology. Devices containing P3HT in blend with PC61BM have now reached PCE as high as 5.1% after systematic optimization of device parameters and application of appropriate post-processing treatments such as thermal annealing.[48,49] Although research on this polymer is still underway with the aim of further improving device performance through modification of the morphology, the device architecture and the electron acceptor, no significant steps ahead in power conversion efficiency have appeared in the literature in past five years. The main issue with P3HT is its quite large band-gap (1.9-2.0 eV), which limits light absorption to only about 46% of the solar spectrum.[47]

One way to overcome this problem is to design low band-gap polymers that are able to absorb low-energy light and simultaneously ensure optimal energy level alignment with the acceptor molecule. To date, the most interesting and effective synthetic approach used to obtain such materials is via the copolymerization of electron-rich (donor) and electron-poor (acceptor) monomers to yield low bandgap copolymers with optical and electronic properties that can be easily tuned by synthetic control of the electron-rich and electron-poor units. The resulting low bandgap materials are known as donor-acceptor (or push-pull) copolymers.

Different building blocks have been explored to be used in such copolymers, with the most common being fluorene, carbazole, dibenzosilole and benzodithiophene as electron-rich units, and benzodiathiazole, diketopyrrolopyrrole, thienopyrroledione as electron-poor units.[47] Although excellent reviews on the synthesis, characterization, and device performance of these new copolymers have recently appeared in the literature,[47,50-52] it is worth mentioning some of the most interesting examples of PSC devices including this type of materials.

In two independent works by Leclerc et al.[53] and Fréchet et al.[54] the electron-poor thieno[3,4-c]pyrrole-4,6-dione (TPD) unit was copolymerized with the benzodithiophene (BDT) electron-rich unit and the resulting low band-gap copolymer was tested in PSC devices in conjunction with fullerene derivatives. By synthetic control of the alkyl solubilizing pattern in the copolymer and after thorough optimization of device parameters (including the use of high boiling point solvent additives), a maximum PCE as high as 6.8% could be achieved.

The same electron-rich unit (BDT) was employed in a later work by Yu et al.[55] copolymerized with an ester-substituted fluorine-containing thieno[3,4-b] thiophene, to give a copolymer (PTB7) with a low band-gap of about 1.6 eV, showing efficient absorption around the region with the highest photon flux of the solar spectrum (about 700 nm). By carefully controlling the morphology of the active layer by means of high boiling point solvent additives, fully optimized PSC devices containing this copolymer in conjunction with $PC_{71}BM$ exhibited a very high value of FF (68.97%) and a remarkable 7.4% maximum PCE.

In a very recent work by Chen et al.[56] a novel alcohol/water-soluble conjugated polymer, poly[(9,9-bis(3′-(N,N-dimethylamino)propyl)-2,7-fluorene)-alt-2,7-(9,9-dioctylfluorene)] (PFN) was presented, to be used as cathode interlayer in PSC devices based on $PC_{71}BM$ and the previously reported PTB7 copolymer. The incorporation of this PFN interlayer allowed significant and simultaneous enhancement in J_{SC}, V_{OC}, and FF, leading to an outstanding certified PCE of 8.37%, which is to date the best reported value in the literature for PSCs.

As noticeable from the studies on low bandgap copolymers presented so far, an important factor that significantly affects the performance of PSC devices is the nano-scale morphology of the photoactive layer.

The exciton diffusion length in organic materials is only about 10-20 nm[57] due to the short lifetime of the photoexcited electron-hole pair. This implies that the exciton must reach the donor-acceptor interface to yield charge transfer without undergoing radiative or non-radiative decay. Therefore, the donor and acceptor phases should self-organize to form nano-scale domains on the same length-scale of the exciton diffusion length, so that efficient exciton harvesting can be facilitated.[58] To increase the probability of exciton splitting, the interfacial area between the electron-donor and the electron-acceptor materials should be as large as possible. In addition, once the exciton is formed and dissociated, the free charge carriers (holes and electrons) must drift to the electrodes within their lifetimes. For this reason, a 3D morphology characterized by a bicontinuous percolated network of the donor and acceptor materials is necessary for productive charge extraction from the device.[48,59]

Following these considerations, the structure of the active layer and the architecture of devices have evolved in the past few years in an attempt to meet the above-mentioned requirements.

The immediate evolution of the single layer device architecture, in which an organic semiconductor is sandwiched between two metal electrodes with different workfunctions to yield rather poor photovoltaic performance, is the bilayer heterojunction architecture, which was pioneered by Tang in 1986.[60] In this device structure, the photoactive layer is formed by depositing the electron-donor and the electron-acceptor on top of each other to yield a planar (or corrugate, in the case of diffused bilayer heterojunction devices) interface where exciton separation may occur. The bilayer is sandwiched between two electrodes matching the donor HOMO and the acceptor LUMO, for efficient extraction of the corresponding charge carriers. While monomolecular charge transport can be ensured with this device architecture (after the excitons are dissociated at the donor-acceptor interface, the electrons travels within the n-type acceptor and the holes travels within the p-type donor material), the probability of charge separation is relatively low because the region for exciton splitting is only limited to the planar (corrugated) donor-acceptor interface.

In order to overcome this drawback, the so-called bulk heterojunction (BHJ) structure was proposed[7,61] and still represents the state-of-the-art in PSC technology. In a BHJ, the photoactive layer is composed of a blend of a donor (a p-type conjugated polymer) and an acceptor (an n-type fullerene derivative) material intimately mixed to form an interpenetrating phase network at the nanoscale level in which each donor-acceptor interface is ideally within a distance shorter than the exciton diffusion length from each photogeneration site. The main advantage of this structure is that the interfacial area where charge separation can occur is largely increased. In addition, because the interface is dispersed throughout the bulk, a great reduction of losses due to short exciton diffusion length is achieved, as ideally all excitons will be dissociated within their lifetime. Furthermore, the charges are separated within different phases hence recombination is reduced to a large extent.

In order to guarantee efficient charge transport and collection to the respective electrodes, the donor and acceptor phases must form a bicontinuous percolated network of interpenetrated domains. Therefore, the nano-scale control of the morphology of the photoactive layer in BHJ devices becomes extremely important to guarantee optimal device performance, as witnessed by the numerous processing techniques available today for optimization of the BHJ morphology.[62,63]

The same BHJ concept presented above is nowadays found in almost every high performing PSC device, although some differences in device architectures can be found. In the most studied PSCs, devices are typically fabricated by simple solution processing of the active layers followed by evaporation of metallic back electrodes, to produce devices with a so-called “standard” architecture where electrons flow from the transparent electrode (anode) to the back metallic electrode (cathode) (Figure 2.11).

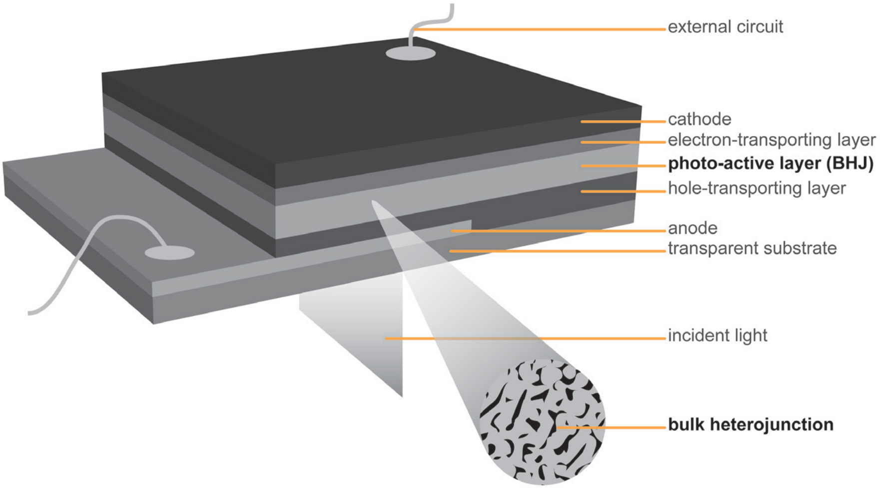

Figure 2.11 Schematization of a standard-type bulk-heterojunction PSC device architecture.

A standard geometry is extremely convenient when devices are to be prepared on a laboratory scale, as it represents a suitable standardized platform to investigate materials properties and efficiency. However, such a device architecture may present some drawbacks when large-scale production is considered mainly due to the vacuum processing steps required for back electrode deposition.

As a way to overcome these problems, the so-called “inverted” device geometry was introduced, allowing the use of solution-processed rather than vacuum-processed metallic back electrodes.[64,65] As shown in Figure 2.12, in this device architecture the transparent electrode works as a cathode, where electron collection takes place. Conversely, the back electrode is responsible for the extraction of holes, thus behaving as anode.

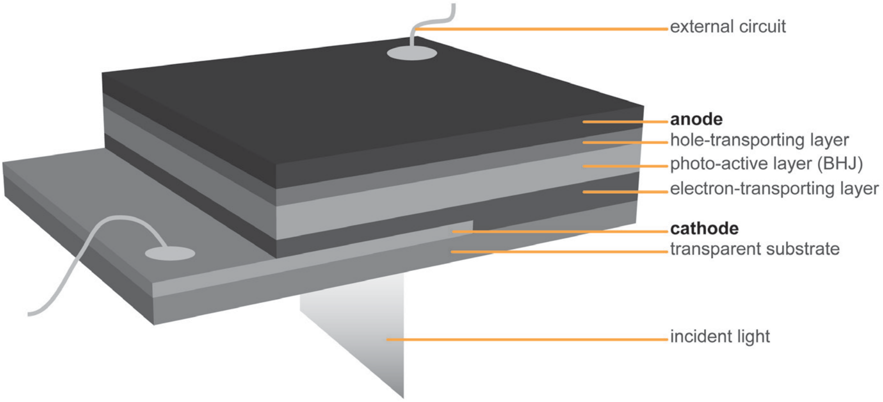

Figure 2.12 Schematization of an inverted-type bulk-heterojunction PSC device architecture.

Alongside large-scale processability, the inverted architecture has shown some advantages compared to the standard geometry also in terms of device stability.[62] Standard BHJ devices can suffer from degradation of the top electrode, which is normally made of a low-work-function metal (typically Al) that is highly reactive and oxidizes easily in air, thus increasing the series resistance at the metal/BHJ interface and decreasing device performance.[62] In addition the PEDOT:PSS layer is potentially detrimental to the polymer active layer due to its acidic nature, which etches the ITO electrode and causes interface instability via indium diffusion into the polymer active layer. In the inverted device geometry, the potential interfacial instability is overcome by replacing the hole conducting PEDOT:PSS layer with other functional buffer layers which are able to lower the workfunction of ITO and prevent the ITO layer from etching.[66,67] In addition, the back electrode is substituted with PEDOT:PSS (typically) covered by a stable, high workfunction metal such as Au or Ag. The inverted device architecture represents therefore an attractive concept to improve device stability and lifetime.

The importance of guaranteeing a long-term stability of PSC devices represents a critical issue in view of a future potential commercialization of this technology. Accordingly, a more detailed discussion on this topic is presented in the next Section.

2.3.2 Stability of polymer solar cells

The primary focus in PSC research has been the optimization of device performance by developing new high-performing materials, novel device architectures and efficient ways to control the nano-scale morphology of the photoactive layer to improve the photovoltaic response of the device. It was shown in the previous Section that efficiencies exceeding 8% are now possible, with appropriate choice of device components and processing treatments. One of the major challenges for widespread diffusion and commercialization of this technology is the relatively short lifetime of the devices, leading to decline of photovoltaic performance over time. As opposed to inorganic silicon-based PV technologies, where lifetimes in the order of 25 years are commonly guaranteed, the intrinsically less stable nature of organic and polymeric materials (especially to chemical degradation from oxygen and water) calls for tremendous improvements in device stability.

Many degradation pathways have been identified in PSC devices (see Figure 2.13), the most common of which comprise diffusion of oxygen and water into the device and consequent reaction with the active materials, photodegradation of the active components, corrosion at electrode interfaces, interlayer diffusion of material and reaction with the active components, formation of particles within the device.[68]

Since the degradation behavior of PSC devices is rather complex and the degradation mechanisms are interrelated with each other, it is often difficult to directly determine to what extent a particular degradation pathway contributes to the overall decline of the photovoltaic response of the PSC device. Therefore, a full understanding of each identified mechanism is essential in order to minimize or prevent degradation.[69] This can be typically accomplished by means of systematic experiments that require the use of physical and chemical characterization techniques on the materials employed in the PSC device as well as convenient testing apparatuses for device characterization.[70-72]

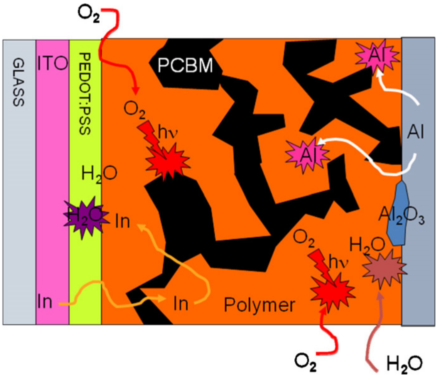

Figure 2.13 Graphical overview of the main degradation mechanisms occurring in a typical PSC device.[68]

The use of time-of-flight secondary ion mass spectrometry (TOF-SIMS) methodologies allowed Krebs et al.[73,74] to describe oxygen diffusion through a bilayer PSC device. It was shown that diffusion was originated by the introduction of oxygen into the Al back-electrode through microscopic pinholes on the Al film. Once inside the PSC device, oxygen was shown to continually diffuse through the lateral and vertical planes of the device until the counter electrode (ITO) was reached. Another significant degradation pathway was found to be the diffusion of ITO material into the devices (Al/C_{60}/P3CT/ITO, where P3CT is poly(3-carboxydithiophene)) and its consequent reaction with the photoactive layer.

The role of the hole-conducting PEDOT:PSS interlayer in the degradation of PSC devices was also investigated.[75] By means of photovoltaic tests on MDMO-PPV:PC_{61}BM devices with and without the PEDOT:PSS interlayer, it was demonstrated that the degradation was associated with the hygroscopic nature of the PEDOT:PSS layer. Charge transport measurements showed that the effect of water on PEDOT:PSS was to increase the resistivity of the PEDOT:PSS/blend layer interface, but not to affect the charge mobilities of the active layer.

More recently,[76] P3HT:PC_{61}BM and MDMO-PPV:PC_{61}BM bulk heterojunction solar cells were fabricated with different configurations to examine the effect of ITO and PEDOT:PSS on PSC stability and degradation. The V_{OC} of solar cells was shown to be kept constant during aging in atmosphere if the ITO electrode was avoided. However, absence of ITO led to high series resistances and low values of photocurrent. This indicated that use of more conductive films than PEDOT:PSS could lead to ITO-free PSCs that would exhibit lower costs and longer lifetimes.

Another important contribution to the relatively poor stability of PSC devices operating in ambient atmosphere is given by the photochemical degradation of the conjugated polymer constituting the p-type material in the photoactive layer. In particular, photo-oxidation of the conjugated polymer still represents a challenge, although progresses have been made in the selection of polymeric materials with desirable optical and electronic properties that also show improved photochemical stability. In particular, polythiophenes have demonstrated to exhibit rather good stability to light compared with other polymeric systems, as will be shown more in detail in Chapter 3.

In the attempt to fabricate air-stable PSC devices, thermocleavable polymers have been introduced, in which insoluble solid films are obtained upon heat treatment thanks to the presence of thermocleavable side chains appended to the polymer. In particular, an inverted device architecture was employed to fabricate PSCs where the active layers comprised a transparent cathode based on solution processed zinc oxide, a photoactive layer based on a BHJ of zinc oxide nanoparticles and thermocleaved poly-(3-carboxydithiophene) (P3CT), a PEDOT:PSS layer and finally a printed silver based anode.[77] It was shown that unencapsulated devices were robust and not sensitive to mechanical handling of the active layer and back electrode. In addition, 80% of the initial performance at continuous illumination could be retained for about 100 h of operation. In the dark and under ambient conditions, the PSC devices could be stored for more than six months without noticeable degradation in performance.

In a later study,[78] the stability of the PSC devices based on similar thermocleavable low band-gap polymers bearing different thermocleavable ester groups was investigated in four different atmospheres, namely dry nitrogen, dry oxygen, humid nitrogen and ambient atmosphere. The photovoltaic properties of the PSCs were tested in the glass/ITO/PEDOT:PSS/polymer:PC61BM/Al configuration and were found to be very stable in dry oxygen atmosphere, where the device decay was similar to inert conditions (dry nitrogen). This was in stark contrast to conjugated materials containing vinylene bonds that are very sensitive towards oxygen. A rapid performance decay was however observed in the presence of water (with and without oxygen present) and removal of water was deemed to be necessary to achieve devices with stability exceeding hundreds of hours.

In addition to chemical degradation pathways, the preservation of an optimal BHJ morphology within the photoactive layer is critical for sustaining long-term high PSC performance. Most BHJ systems show poor stability and often undergo macrophase segregation of the blend components, especially after prolonged exposure to heat.[79-82]

Several studies have focused on the morphological evolution of the active layer of standard BHJ systems incorporating P3HT or MDMO-PPV as donor materials and potential approaches to improve the stability of such BHJ have also been examined, especially at high temperature. A thorough discussion on this aspect will be the topic of Chapter 4, where strategies to improve the thermal stability of high performing PSCs will also be presented.

2.4 CONCENTRATING SOLAR LIGHT: FROM IMAGING TO NON-IMAGING DEVICES

Solar cells based on inorganic semiconductors such as mono- and poly-crystalline silicon largely dominate the PV market nowadays (see Section 2.2). These devices have found applications mainly as small-scale devices in solar panels on building roofs, pocket calculators, water pumps and portable electronics.

These conventional PV technologies allow for as much as 25%[29] of the incoming solar energy to be harvested and converted into electricity, a value that is very close to the theoretically predicted upper limit of 30%[18] for this type of materials. One major drawback that characterizes the Si-based PV technology is associated with the high production costs of the actual solar cells that still require many energy intensive processes at high temperatures (400-1400 °C). This adds to the increasingly high cost of poly-crystalline silicon, the starting material for solar cell production. According to the these figures, it is clear that PV technologies with low fabrication costs would be now highly desirable, even at the expense of further improvements in power conversion efficiency.

One strategy to meet this requirement would be to reduce the amount of silicon necessary for solar cell fabrication by using concentrating systems to collect sunlight over a large area and re-direct it onto small-area solar cells.[83] This approach would reduce material (Si) consumption while preserving and potentially improving the electrical power output from the PV device, because of the increased illumination intensity experienced by the solar cells.

To date, two main types of concentrating technologies have been presented in the literature, namely imaging and non-imaging solar concentrators.[84]

The first category comprises the so-called concentrated photovoltaics (CPV) where Fresnel lenses, parabolic dish collectors or a combination of both are employed to collect sunlight and focus it onto very small units of high-cost high-efficiency solar cells.[85] Although very high concentrations can be achieved with these devices (hundreds suns) resulting in improved solar cell performance, they present some significant drawbacks: high sunlight concentration may lead to excessive heating of the solar cell, therefore cooling systems are needed to alleviate high temperature effects and prolong solar cell lifetime;[85] these devices are only able to capture direct solar radiation, therefore precise solar tracking systems (typically two-axis systems) are required to keep the solar cell under illumination; finally, to avoid shadowing from neighbor collectors, large areas for CPV installation are required.

As alternative to CPV technology, non-imaging concentrators have been proposed. Among these, luminescent solar concentrators (LSCs), first introduced in the late 1970s as one of the simplest methods to concentrate sunlight in thin polymeric slabs,[86] have gained increasing attention in the past few years as a result of the recent advances in materials science and nano-optics.[87]

As will be shown more in detail in the next Section, this technology makes use of a sheet of luminescent material to collect and trap both direct and diffuse solar radiation, convert it and transfer it to smaller areas of silicon solar cells mounted on the edges to generate electricity.

2.5 LUMINESCENT SOLAR CONCENTRATORS

A schematic cross-sectional view of an LSC device is presented in Figure 1.14, where the main operating mechanisms are also depicted.

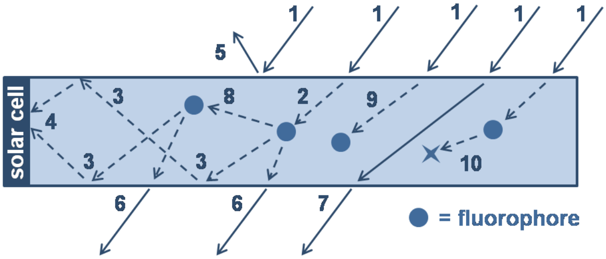

Figure 2.14 Cross-sectional view of a typical LSC device, in which the operating mechanisms are shown: incoming sunlight incident on the top surface of the LSC 1), absorption of the light by a fluorophore molecule 2), light re-emitted by the fluorophore is trapped within the matrix by total internal reflection (TIR) 3), re-emitted light reaches solar cells mounted at the edges of the LSC 4). Common loss mechanisms are: top surface reflection 5), escape-cone losses for light re-emitted within the Brewster (critical) angle 6), transmission of unabsorbed sunlight 7), re-absorption of emitted light 8), non-radiative fluorescence decay 9), and absorption of emitted light by the host matrix 10).

The LSC consists of a transparent matrix containing luminescent species (typically organic dyes or quantum dots) that absorb part of the incident solar spectrum and re-emit it at a longer wavelength. Part of the light emitted by the luminescent species is guided (in a waveguide mode) towards the edges of the transparent matrix by total internal reflection (TIR), where high efficiency solar cells can collect it. When the materials constituting the LSC device are all organic-based, the LSC is often referred to as organic luminescent solar concentrator (OLSC).

The presence of different loss mechanisms can reduce the amount of photons re-emitted by the fluorophore and directed towards the solar cells. In particular, reflection of the incident light from the top surface (Fresnel reflection) is responsible for about 4% loss of incident photons.[88] In addition, only the light re-emitted by the fluorophore within an emission angle larger than the critical angle Θ_C (see Equation 2.20) can be trapped within the LSC. For angles of incidence with the LSC surface smaller than Θ_C, the light will exit the LSC in the so-called escape-cone and will be lost. Furthermore, a fraction of the incident sunlight can be transmitted through the LSC without being absorbed by the fluorophore, due to the limited absorption spectrum of the fluorescent species. Additionally, re-absorption phenomena can occur, where fluorescence emission of a fluorophore is re-absorbed by another fluorophore molecule. This may happen if the absorption spectrum of the fluorophore overlaps (even partially) the emission spectrum. As a result, the fluorescence can again be re-emitted and transported to the edges of the LSC or leave the LSC through the escape-cone and then lost. Non-radiative decay of the fluorescence may also take place as fluorophores may exhibit non-unity fluorescence quantum yield (FQY, ratio of the number of photons emitted by fluorescence to the number of photons absorbed), causing the absorbed photons to be lost. Finally, parasitic absorption in the host matrix may occur, leading to further losses.

Two typical device configurations are commonly used in LSC technology: the bulk-plate LSC and the thin-film LSC. In both cases, a planar arrangement is normally employed, though cylindrical,[89] bent[90] or flexible[91,92] configurations have recently appeared in the literature as promising LSC architectures.

In the bulk-plate configuration, a sheet (plate) of transparent host matrix (a polymer such as PMMA or an inorganic material such as glass) is doped with one or more luminescent species, with solar cells optically matched to the plate edges (Figure 2.15).

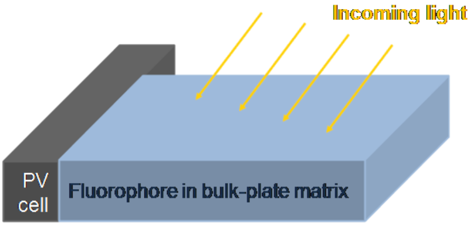

Figure 2.15 Schematic representation of a “bulk-plate” LSC configuration.

Conversely, in the thin-film design a transparent carrier matrix (polymeric or inorganic) doped with one or more luminescent species is deposited as a thin-film onto a transparent substrate (typically glass) at the edges of which solar cells are placed (Figure 2.16).

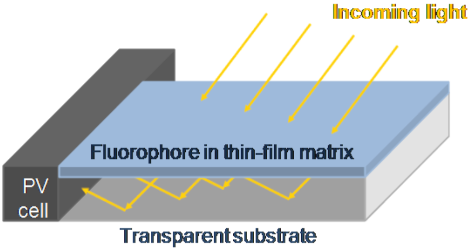

Figure 2.16 Schematic representation of a “thin-film” LSC configuration.

The advantage of doped thin-films having optical contact with the transparent substrate is that the luminescence emitted from the thin-film is trapped in the substrate while parasitic losses due to self-absorption and scattering from impurities can be greatly reduced as compared to bulk doped plates.[93]

2.5.1 Efficiency of luminescent solar concentrators

The first publications on LSCs appeared in the late 1970s[93] followed by extensive studies going on throughout the 1980s, until the limitations of the fluorescent organic dyes available at that time hindered further development[94]. In recent years, novel luminescent materials such as new organic dyes, quantum dots and rare-earth materials have been proposed,[94] and techniques to reduce the losses within the devices have been presented, such as the use of liquid crystals[95-97] or photonic crystals[93,98,99]. These new developments have motivated a renewed interest in the LSC technology, followed by an increasing amount of research papers appeared on this topic in the last ten years.[94]

The performance of an LSC is measured in terms of effective concentration ratio C, given by the product of the geometrical concentration factor G (also known as geometric gain) and the optical efficiency η_{opt} of the device:

$$C = G \cdot \eta_{opt} \qquad \text{(Equation 2.13)}$$

The geometrical factor G is define as:

$$G = \frac{A^{(LSC)}}{A^{(CELL)}} \qquad \text{(Equation 2.14)}$$

where $A^{(LSC)}$ is the top surface area of the LSC plate (or thin-film) and $A^{(CELL)}$ is the active area of the solar cell(s) (which corresponds to the area of the LSC edge(s)).

The optical efficiency of the LSC plate (or thin-film) can be defined as the ratio of the energy delivered from the LSC edges to the energy incident onto the LSC surface:

$$\eta_{opt} = \frac{P_{OUT}^{LSC}}{P_{IN}} \qquad \text{(Equation 2.15)}$$

where P_{IN} is the total solar power incident on the LSC and P_{OUT}^{LSC} is the power delivered from the LSC edges.

As shown in the previous Section (Figure 2.14), different loss mechanisms may occur in an LSC device, each specifically contributing to the overall optical efficiency η_{opt}. In order to highlight these contributions, η_{opt} can be expressed by the product of the efficiencies of the different processes taking place in the LSC, as shown in the following equation:[93]

$$\eta_{opt} = (1-R)\eta_{abs}\eta_{LQY}\eta_{Stokes}\eta_{trap}\eta_{self}\eta_{mat} \qquad \text{(Equation 2.16)}$$

In particular, 1 - R represents the fraction of light transmitted into the LSC plate (or thin-film), with R being the Fresnel reflection coefficient of the LSC surface:

$$R = \frac{(n-1)^2}{(n+1)^2} \qquad \text{(Equation 2.17)}$$

where n is the refractive index of the material (typically 4% for n = 1.5).
The fraction of photons absorbed by the LSC η_{abs} (also called absorption efficiency) must be maximized for optimum LSC performance. In particular, the LSC should ideally absorb the largest possible portion of the incident photons having energies greater than the bandgap of the solar cells attached to the edges of the LSC. In the case of LSC coupled to Si solar cells, all wavelengths shorter than 950 nm should be ideally absorbed and re-emitted in the 950 – 1000 nm range, where the Si solar cell exhibit a maximum spectral response.
The luminescence quantum yield η_{LQY} determines the fraction of photons emitted to the number of photons absorbed by the fluorescent molecule:

$$\eta_{LQY} = \frac{\text{number of emitted photons}}{\text{number of absorbed photons}} \qquad \text{(Equation 2.18)}$$

Practically, it indicates the probability that an excited fluorescent molecule decays by fluorescent photon emission. Near-unity values of η_{LQY} are required for optimal LSC performance.
Because the fluorescence process intrinsically implies a photon energy loss (the emitted photon has a longer wavelength/lower energy than the absorbed photon), it is important to quantify such energy loss by means of the so-called Stokes efficiency η_{Stokes}. In particular, η_{Stokes} is defined as:

$$\eta_{Stokes} = \frac{\nu_{emitted}}{\nu_{absorbed}} \qquad \text{(Equation 2.19)}$$

where $n_{emitted}$ and $n_{absorbed}$ are the energies of emitted and absorbed photons, respectively.
The efficiency of waveguide trapping η_{trap} determines the fraction of the light emitted by the fluorophore that can be confined within the LSC in waveguide mode.[100,101] Practically, this indicates the fraction of light emitted by the fluorophore at an angle larger than the critical angle Θ_C:

$$\Theta_C = \sin^{-1}\left(\frac{1}{n}\right) \qquad \text{(Equation 2.20)}$$

and can be obtained by the following equation:[102]

$$\eta_{trap} = \sqrt{1 - \frac{n_{clad}^2}{n_{core}^2}} \qquad \text{(Equation 2.21)}$$

where the waveguide core and cladding refractive indices are η_{core} and η_{clad}, respectively. For air cladding ($\eta_{clad} = 1$) and an organic thin film refractive index of $\eta_{core} = 1.7$, $\eta_{trap} = 80\%$ (20% of the fluorescence photons will be emitted within either the front or the rear escape-cone and will be lost from the LSC).

As a way to increase η_{trap}, the application of photonic structures to the LSC was proposed recently. In particular, it was shown[99] that by employing a commercially available photonic band-stop reflection filter for the light emitted from the luminescent dyes in bulk-plate LSCs, the relative efficiency of the LSC system increased by 20%, thanks to the reduction of escape-cone losses.

Another approach to reduce surface losses in LSC thus enhancing the waveguide trapping efficiency htrap made use of organic wavelength selective mirrors applied onto the LSC surface.[103] It was shown that by adding selectively reflective cholesteric liquid crystal layers to the top of the LSC using an air gap both reduced the loss of light from the surface of the waveguide and increased the light output at the edge of the LSC up to 12%.

Dye alignment by means of liquid crystals was also proven to be a successful strategy to reduce the escape-cone losses and improve LSC device performance. [95-97]

The efficiency η_{self} (self absorption efficiency) takes into account losses due to re-absorption of the emitted photons by neighbor fluorophores.[104] These re-absorption events may occur in fluorophores that exhibit overlapping absorption and emission spectra, such as organic dyes. Re-absorption may lead to a reduction in LSC optical efficiency in the cases where trapped photons that would have reached the edge of the LSC are re-directed out of the device and lost. Photons in an LSC can experience multiple re-absorption events, each one increasing the chance of the photon being lost. The self absorption efficiency for an LSC containing an organic dye is typically on the order of 40-80 %, although this depends greatly on concentration and LQY.[104,105]

As a way to reduce re-absorption losses, patterned dye structures were employed in thin-film LSCs.[106] It was shown that by engineering the dye coating into regular line patterns via standard photolithography, the surface coverage of the dye molecules was reduced, thus decreasing the probability of the re-emitted light to encounter another dye molecule and hence the probability of re-absorption.

Recently,[107] the re-absorption problem was overcome by employing resonance-shifting, in which sharply directed emission from a bilayer cavity into the glass substrate returns to interact with the cavity off-resonance at each subsequent bounce. In this way, re-absorption losses occurring during photon travelling towards the LSC edges could be significantly reduced and a more than two-fold increase in concentration ratio C could be obtained with respect to conventional LSCs.

The carrier matrix can also contribute to losses in the LSC under operation, as absorption of trapped fluorescence by the host matrix may occur. The fraction of emitted photons absorbed or scattered by the host matrix is $1 - \eta_{mat}$, where η_{mat} is the host matrix absorption efficiency, i.e. the fraction of fluorescence transmitted by the host). These absorption events can normally be neglected in the visible range ($\eta_{mat} > 95\%$), where most host materials are highly transparent, but they may gain increasing importance in regions where absorption of the host material may be observed.

The absolute power conversion efficiency $\eta_{ABS}^{(LSC)}$ of an LSC connected to photovoltaic cells at a given wavelength λ is given by the product between the overall optical efficiency η_{opt} of the LSC and the power conversion efficiency of the solar cell at that specific wavelength $\eta(\lambda)^{(CELL)}$, as described by the following equation:[93]

$$\eta_{ABS}^{(LSC)} = \frac{P_{OUT}}{P_{IN}} = \eta_{opt} \cdot \eta(\lambda)^{(CELL)} \qquad \text{(Equation 2.22)}$$

where P_{OUT} is the power delivered by the solar cells coupled to the LSC plate.

For practical reasons, when electrical measurements on the operating LSC/solar cell system are performed in standard illumination conditions (AM 1.5G, see Figure 2.7), $\eta_{ABS}^{(LSC)}$ is often expressed in terms of the electrical parameters of the photovoltaic cell as follows:[108]

$$\eta_{ABS}^{(LSC)} = FF^{(LSC)} \frac{(I_{SC}^{(LSC)} / A^{(LSC)}) V_{OC}^{(LSC)}}{P_{IN}} \qquad \text{(Equation 2.23)}$$

where $FF^{(LSC)}$, $I_{SC}^{(LSC)}$ and $V_{OC}^{(LSC)}$ are the fill factor, the short-circuit current and the open-circuit voltage measured from the solar cell coupled to the LSC and $A^{(LSC)}$ is the illuminated top surface area of the LSC plate (thin-film).

The theoretical thermodynamic limits of such power conversion efficiency were recently examined by means of Monte Carlo ray-tracing simulations.[109] It was shown that the maximum efficiency of an LSC system resulting from the thermodynamic theory of LSC[84] may be described by the detailed balance model of Shockley-Queisser for non concentrating solar cells with a single band gap energy (see Section 2.1.3), provided that photonic structures at LSC surface are considered, acting as an omnidirectional spectral band stop filter.

In one of the first noteworthy experimental studies on LSC power conversion efficiency, Goetzberger et al,[110] reported a significant $\eta_{ABS}^{(LSC)}$ = 4.0% for a large-area (40 cm x 40 cm x 0.3 cm) two-sheet stack system consisting of a short-wavelength emitting plate coupled to gallium arsenide (GaAs) solar cells placed above a long-wavelength emitting plate coupled to Si solar cells with an air gap between the plates. In a later work by Friedman,[111] a thin-film LSC module (14 cm x 14 cm x 0.3 cm) with a mixture of dyes was fabricated and tested to yield $\eta_{ABS}^{(LSC)}$ = 3.2% with Si solar cells and $\eta_{ABS}^{(LSC)}$ = 4.5% with GaAs solar cells. The higher efficiency resulting from the system with GaAs solar cells resulted from the higher open-circuit voltage of this type of solar cell. More recently, Baldo et al.[102] reported *calculated* power conversion efficiencies of up to 5.9% for single plate LSCs (thin-film deposited on 25 mm x 25 mm x 2 mm glass substrate) and up to 6.8% for tandem LSCs, by exploiting Förster resonance energy transfer (FRET), solid-state salvation and phosphorescence via a combination of fluorescent and phosphorescent dyes doped into a hybrid host matrix. Concurrently, Slooff et. al.[108] achieved a remarkable $\eta_{ABS}^{(LSC)}$ = 7.1% with four GaAs solar cells coupled to the edges of a bulk-plate LSC (50 mm x 50 mm x 5 mm) and Goldschmidt et. al.[99] obtained $\eta_{ABS}^{(LSC)}$ = 6.7% with four gallium indium phosphide (GaInP) solar cells coupled to a multi-dye stack of two 20 mm x 20 mm x 3 mm bulk-plate LSCs.

As apparent from the results presented above, it is often difficult to directly compare measured efficiencies of LSC devices as $\eta_{ABS}^{(LSC)}$ strongly depends on LSC dimensions, number of solar cells attached, type of the solar cells employed and use of diffuse reflectors or selective mirrors at the sides or at the front/rear faces. For this reason, it is sometimes convenient to evaluate a relative efficiency increment which gives a measure of the increase in efficiently experienced by the solar cell when coupled to the LSC plate (thin-film) (see Chapter 7).

2.5.2 Degradation of luminescent solar concentrators

The stability of LSC devices, and of OLSC in particular, still represents a key issue for commercial deployment of this technology. Indeed, no commercialization will be viable unless lifetimes longer than at least ten years are achieved.[94]

Among the potential routes for OLSC performance degradation, the instability of the materials constituting the OLSC device to light exposure appears to be the most critical factor. In particular, the photodegradation of the host matrix and the luminescent species represent the most common degradation pathways.

In one of the first studies on performance evaluation,[112] OLSCs were prepared by dissolving commercial organic dyes in MMA and subsequently thermally polymerizing the material to obtain OLSCs to the edge of which silicon solar cells were attached. The optical efficiency and the current output of each OLSC were measured during prolonged exposure to sunlight (one year on field) and a decrease in optical band-gap of the dye upon light exposure was observed. Such a decrease was attributed to an increase in the degree of disorder of the amorphous phase and photochemical decomposition of the dyes. In particular, it was suggested that a high optical band-gap energy luminescent dye would result in better stability.

In a later study from the same group,[113] the optical absorption of perylene-based dye-doped PMMA prepared by both thermal polymerization and casting methods was measured before and after exposure to filtered or unfiltered light using xenon arc-lamp or direct sunlight. It was shown that the optical band-gap of thermally polymerized PMMA was reduced by doping with perylene dye or after exposure to UV-radiation. In addition, samples prepared by thermal polymerization exhibited better photostability than solvent-cast samples, as observed from FTIR and calorimetric analyses.

The role of polymer matrix composition was also examined,[114] by preparing copolymers of styrene and methyl-methacrylate (MMA) to fabricate the OLSC carrier matrix. It was shown that by incorporating commercial fluorescent dyes into poly(styrene-co-methyl methacrylate) matrixes, a better photo-stability was observed compared with PMMA alone. In particular, the half-life of the dye in the copolymer matrix was proven to be more than five times longer than in the PMMA matrix as observed by field performance tests.

The photodegradation of perylene di-imide dye molecules dispersed in polyester or PMMA films and solutions was studied by monitoring the fluorescence and absorption intensity of the dye upon irradiation with increasing 532 nm laser pulses.[115] Photo-oxidation was shown to be the main mechanism responsible for the photo-degradation of the OLSC device, while samples exposed to laser pulses in anaerobic conditions underwent partially reversible photo-reduction.

The effect of light source on the stability of OLSC plates was evaluated by exposing OLSCs containing different dye molecules to continuous (~ 200 days) white light illumination (solar simulator), outdoor conditions and high intensity (15 suns) monochromatic light (470 nm).[116] It was observed that OLSC lifetime strongly depends on the organic luminescent species employed, where the best tested materials exhibited an initial decrease in performance (measured in terms of device J_{SC} and EQE) followed by a plateau. On these systems, monochromatic light soaking experiments showed that bleaching of the best performing material was caused by excitation within its absorption band.

In the attempt to evaluate the performance of new fluorescent materials, OLSCs based on PMMA doped with phthalocyanine, nickel-phthalocyanine or hematoporphyrin laser dyes were prepared by casting method.[117] Optical absorption measurements were carried-out at room temperature in the 200–900 nm wavelength region both before and after sample irradiation with sunlight for two weeks. The degradation of PMMA–dye samples, measured by absorption, was found to obey a first-order kinetic equation. The photodegradation studies revealed that the phthalocyanine dye systems were the most stable, as well as being the most efficient in terms of Stokes shift and fluorescence quantum yield.

In a study of potential application of OLSCs as photoselective films to increase irradiance level for photosynthesis in greenhouses, PMMA-doped films embedded with commercial coumarin dyes were prepared on polyethylene substrates.[118] Their photostability was studied by irradiating the samples with artificial sunlight from a Xenon arc lamp for 24 h and recording the change in optical density of the thin film. A second order kinetics two-step photodegradation mechanism was observed resulting in only an 8% decrease of optical density after 24 h exposure to simulated sunlight. In addition, the OLSC thin-films (~ 1 mm) also exhibited good thermal stability, as no major thermal effects were observed on the dye molecules for temperatures below the glass transition temperature of the PMMA matrix.

In a recent work by Kinderman et al.,[119] the performance and stability of different luminescent organic dyes incorporated in OLSC devices based on PMMA as host matrix was evaluated upon exposure to simulated sunlight in terms of modifications of the electrical and optical properties of the OLSC system (thin-films or bulk plates coupled to mc-Si solar cells). Screening of the stability of the dyes in different matrix materials indicated that the stability is strongly dependent on the type of dye, additives, monomer residues in the polymer matrix and purity. Better stability was achieved in pure PMMA coatings on glass plates compared with bulk PMMA samples. It was thought that this was caused by additives in the bulk PMMA samples but may also be a result of the bulk samples being cured with UV light, which can cause photodegradation of the dyes The most stable dyes exhibited a 10% lost of their initial absorption after four weeks of continuous illumination. Guidelines were given by the authors on possible strategies to lengthen OLSC lifetime, including the use of inorganic quantum dots.

In a later work by van Sark et al.[120] OLSC thin-films and bulk plates were exposed to continuous illumination under a sulphur lamp as well as in outdoor conditions. The plate samples were fabricated by polymerization of a dye-doped solution of MMA, while the thin-films were produced by depositing a solution of PMMA and organic dye on glass substrates. Electrical (I-V) characterization on complete OLSC devices was performed in order to track the degradation effects on device performance. Both types of OLSC devices (thin-films and bulk plates) showed a decline in device current output upon illumination, irrespective of the light source employed. OLSC lifetime was found to depend strongly on the dye molecule employed. In addition, performance degradation of OLSC devices was shown to occur also for samples stored in the dark, suggesting that light exposure is not the only responsible for device degradation.

As evidenced by the literature review presented above, most of the studies on OLSCs addressing stability issues have mainly been devoted to the evaluation of modifications occurring to the photovoltaic response and optical efficiency of devices during prolonged exposure to outdoor light or during laboratory tests (laser or UV light). However, very little is known about the molecular degradation mechanisms of the actual materials constituting the OLSC device, and in particular on the modifications occurring to the luminescent species upon irradiation.

Although a number of organic dyes showing high fluorescence quantum yield combined with relatively good photo-stability have been presented in the literature,[117,121,122] the reduction of absorption intensity and the fluorescence quenching of the dye molecule following interaction with light remains a critical aspect and a clear understanding of the degradation mechanisms of light-exposed dye molecules at molecular level is needed to develop successful strategies to effectively lengthen OLSC lifetime. This topic will be discussed in full detail in Chapter 6.

2.6 REFERENCES

1. "International Energy Outlook 2011", DOE/EIA-0484(2011), U.S. Energy Information Administration (EIA), September 2011.
2. A.E. Becquerel "Memoire sur les effects electriques produits sous l'influence des rayons solaires." C. R. Acad. Sci. 1839, 9, 561-567.
3. D.M. Chapin, C.S. Fuller, and G.L. Pearson "A New Silicon p-n Junction Photocell for Converting Solar Radiation into Electrical Power." J. Appl. Phys. 1954, 25, 676-677.
4. B.A. Gregg and M.C. Hanna "Comparing organic to inorganic photovoltaic cells: Theory, experiment, and simulation." J. Appl. Phys. 2003, 93, 3605-3614.
5. S.M.Sze and K.K.Ng "Physics of semiconductor devices.", Third edition, Wiley Interscience, Hoboken, New Jersey 2007.
6. R.F.Pierret "Semiconductor Device Fundamentals.", Addison-Wesley Publishing Company, Inc., Reading, Massachussetts 1996.
7. G. Yu, J. Gao, J.C. Hummelen, F. Wudl, and A.J. Heeger "Polymer Photovoltaic Cells - Enhanced Efficiencies Via A Network of Internal Donor-Acceptor Heterojunctions." Science 1995, 270, 1789-1791.
8. B.A. Gregg "Bilayer molecular solar cells on spin-coated TiO2 substrates." Chem. Phys. Lett. 1996, 258, 376-380.
9. B. Kippelen and J.L. Bredas "Organic photovoltaics." Energy Environ. Sci. 2009, 2, 251-261.
10. B.C. Thompson and J.M.J. Fréchet "Organic photovoltaics - Polymer-fullerene composite solar cells." Angew. Chem. Int. Ed. 2008, 47, 58-77.
11. B.A. Gregg, S.G. Chen, and R.A. Cormier "Coulomb forces and doping in organic semiconductors." Chem. Mater. 2004, 16, 4586-4599.
12. J.J.M. Halls, C.A. Walsh, N.C. Greenham, E.A. Marseglia, R.H. Friend, S.C. Moratti, and A.B. Holmes "Efficient Photodiodes from Interpenetrating Polymer Networks." Nature 1995, 376, 498-500.
13. D. Beljonne, J. Cornil, L. Muccioli, C. Zannoni, J.L. Bredas, and F. Castet "Electronic Processes at Organic-Organic Interfaces: Insight from Modeling and Implications for Opto-electronic Devices." Chem. Mater. 2011, 23, 591-609.
14. J.L. Bredas, J.E. Norton, J. Cornil, and V. Coropceanu "Molecular Understanding of Organic Solar Cells: The Challenges." Acc. Chem. Res.

2009, 42, 1691-1699.

15. M.D. McGehee "Overcoming recombination." Nat. Photonics 2009, 3, 250-252.

16. T.M. Clarke and J.R. Durrant "Charge Photogeneration in Organic Solar Cells." Chem. Rev. 2010, 110, 6736-6767.

17. T.W. Holcombe, J.E. Norton, J. Rivnay, C.H. Woo, L. Goris, C. Piliego, G. Griffini, A. Sellinger, J.L. Bredas, A. Salleo, and J.M.J. Frechet "Steric Control of the Donor/Acceptor Interface: Implications in Organic Photovoltaic Charge Generation." J. Am. Chem. Soc. 2011, 133, 12106-12114.

18. W. Shockley and H.J. Queisser "Detailed Balance Limit of Efficiency of p-n Junction Solar Cells." J. Appl. Phys. 1961, 32, 510-519.

19. A.Goetzberger and V.U.Hoffmann "Photovoltaic Solar Energy Generation.", Springer-Verlag, Berlin Heidelberg 2005.

20. B.P. Rand, J. Genoe, P. Heremans, and J. Poortmans "Solar cells utilizing small molecular weight organic semiconductors." Progr. Photovolt.: Res. Appl. 2007, 15, 659-676.

21. "Technology Roadmaps - Solar photovoltaic energy", International Energy Agency (iea), 2010.

22. R.W. Miles, G. Zoppi, and I. Forbes "Inorganic photovoltaic cells." Mater. Today 2007, 10, 20-27.

23. S. Wenham "Buried-contact silicon solar cells." Prog. Photovolt: Res. Appl. 1993, 1, 3-10.

24. J.H. Zhao, A.H. Wang, M.A. Green, and F. Ferrazza "19.8% efficient "honeycomb'' textured multicrystalline and 24.4% monocrystalline silicon solar cells." Appl. Phys. Lett. 1998, 73, 1991-1993.

25. A. Kolodziej "Staebler-Wronski effect in amorphous silicon and its alloys." Opto-Electron. Rev. 2004, 12, 21-32.

26. 26. E. Spanakis, E. Stratakis, P. Tzanetakis, H. Fritzsche, S. Guha, and J. Yang "Light induced stress in a-Si1-xGex : H alloys and its correlation with the Staebler-Wronski effect." Non-Cryst. Solids 2002, 299, 521-524.

27. P. Tzanetakis "Metastable volume changes of hydrogenated amorphous silicon and silicon-germanium alloys produced by exposure to light." Sol. Energy Mater. Sol. Cells 2003, 78, 369-389.

28. B. Schroder "Thin-Film Technology Based on Hydrogenated Amorphous-Silicon." Mater. Sci. Eng. A 1991, 139, 319-333.

29. M.A. Green, K. Emery, Y. Hishikawa, W. Warta, and E.D. Dunlop "Solar cell efficiency tables (version 39)." Prog. Photovolt: Res. Appl. 2012, 20, 12-20.

30. M. Gratzel "Photoelectrochemical cells." Nature 2001, 414, 338-344.

31. G.t. Michael "Dye-sensitized solar cells." Photochem. Photobiol. C: 2003, 4, 145-153.

32. H.â.J. Snaith and L. Schmidt-Mende "Advances in Liquid-Electrolyte and Solid-State Dye-Sensitized Solar Cells." Adv. Mater. 2007, 19, 3187-3200.

33. F.C. Krebs, M. Jorgensen, K. Norrman, O. Hagemann, J. Alstrup, T.D. Nielsen, J. Fyenbo, K. Larsen, and J. Kristensen "A complete process for production of flexible large area polymer solar cells entirely using screen printing-First public demonstration." Sol. Energy Mater. Sol. Cells 2009, 93, 422-441.

34. M. Manceau, D. Angmo, M. Jorgensen, and F.C. Krebs "ITO-free flexible polymer solar cells: From small model devices to roll-to-roll processed large modules." Org. Electron. 2011, 12, 566-574.

35. R. Po, M. Maggini, and N. Camaioni "Polymer Solar Cells: Recent Approaches and Achievements." J. Phys. Chem. C 2010, 114, 695-706.

36. M.D. Perez, C. Borek, S.R. Forrest, and M.E. Thompson "Molecular and Morphological Influences on the Open Circuit Voltages of Organic Photovoltaic Devices." J. Am. Chem. Soc. 2009, 131, 9281-9286.

37. K. Vandewal, K. Tvingstedt, A. Gadisa, O. Inganas, and J.V. Manca "Relating the open-circuit voltage to interface molecular properties of donor:acceptor bulk heterojunction solar cells." Phys. Rev. B: Condens. Matter Mater. Phys. 2010, 81, 125204.

38. M.C. Scharber, D. Wuhlbacher, M. Koppe, P. Denk, C. Waldauf, A.J. Heeger, and C.L. Brabec "Design rules for donors in bulk-heterojunction solar cells - Towards 10 % energy-conversion efficiency." Adv. Mater. 2006, 18, 789-794.

39. S. Yamamoto, A. Orimo, H. Ohkita, H. Benten, and S. Ito "Molecular Understanding of the Open-Circuit Voltage of Polymer:Fullerene Solar Cells." Adv. Energy Mater. 2011, Early View, DOI: 10.1002/aenm.201100549.

40. J.C. Hummelen, B.W. Knight, F. Lepeq, F. Wudl, J. Yao, and C.L. Wilkins "Preparation and Characterization of Fulleroid and Methanofullerene Derivatives." Journal of Organic Chemistry 1995, 60, 532-538.

41. M.M. Wienk, J.M. Kroon, W.J.H. Verhees, J. Knol, J.C. Hummelen, P.A. van Hal, and R.A.J. Janssen "Efficient Methano[70]fullerene/MDMO-PPV Bulk Heterojunction Photovoltaic Cells." Angew. Chem. Int. Ed. 2003, 42, 3371-3375.

42. N.S. Sariciftci, L. Smilowitz, A.J. Heeger, and F. Wudl "Photoinduced Electron-Transfer from A Conducting Polymer to Buckminsterfullerene." Science 1992, 258, 1474-1476.

43. N.S. Sariciftci, L. Smilowitz, D. Braun, G. Srdanov, V. Srdanov, F. Wudl, and A.J. Heeger "Observation of A Photoinduced Electron-Transfer from A Conducting Polymer (Mehppv) Onto C60." Synth. Met. 1993, 56, 3125-3130.

44. N.S. Sariciftci and A.J. Heeger "Reversible, Metastable, Ultrafast Photoinduced Electron-Transfer in Conjugated Polymer and Buckminsterfullerene Composites and Heterojunctions." Mol. Cryst. Liq. Cryst. 1994, 256, 317-326.

45. N.S. Sariciftci and A.J. Heeger "Reversible, Metastable, Ultrafast Photoinduced Electron-Transfer from Semiconducting Polymers to Buckminsterfullerene and in the Corresponding Donor-Acceptor Heterojunctions." Int. J. Mod. Phys. B 1994, 8, 237-274.

46. T.B. Singh, N. Marjanovic, G.J. Matt, S. Gunes, N.S. Sariciftci, A.M. Ramil, A. Andreev, H. Sitter, R. Schwodiauer, and S. Bauer "High-mobility n-channel organic field-effect transistors based on epitaxially grown C-60 films." Org. Electron. 2005, 6, 105-110.

47. P.L.T. Boudreault, A. Najari, and M. Leclerc "Processable Low-Bandgap Polymers for Photovoltaic Applications." Chem. Mater. 2011, 23, 456-469.

48. W.L. Ma, C.Y. Yang, X. Gong, K. Lee, and A.J. Heeger "Thermally stable, efficient polymer solar cells with nanoscale control of the interpenetrating network morphology." Adv. Funct. Mater. 2005, 15, 1617-1622.

49. J.Y. Kim, S.H. Kim, H.H. Lee, K. Lee, W.L. Ma, X. Gong, and A.J. Heeger "New architecture for high-efficiency polymer photovoltaic cells using solution-based titanium oxide as an optical spacer." Adv. Mater. 2006, 18, 572-576.

50. E. Bundgaard and F.C. Krebs "Low band gap polymers for organic photovoltaics." Sol. Energy Mater. Sol. Cells 2007, 91, 954-985.

51. W.Z. Cai, X. Gong, and Y. Cao "Polymer solar cells: Recent development and possible routes for improvement in the performance." Sol. Energy Mater. Sol. Cells 2010, 94, 114-127.

52. A. Facchetti "pi-Conjugated Polymers for Organic Electronics and Photovoltaic Cell Applications." Chem. Mater. 2011, 23, 733-758.

53. Y.P. Zou, A. Najari, P. Berrouard, S. Beaupre, B.R. Aich, Y. Tao, and M. Leclerc "A Thieno[3,4-c]pyrrole-4,6-dione-Based Copolymer for Efficient Solar Cells." J. Am. Chem. Soc. 2010, 132, 5330-5331.

54. C. Piliego, T.W. Holcombe, J.D. Douglas, C.H. Woo, P.M. Beaujuge, and J.M.J. Fréchet “Synthetic Control of Structural Order in N-Alkylthieno[3,4-c]pyrrole-4,6-dione-Based Polymers for Efficient Solar Cells.” J. Am. Chem. Soc. 2010, 132, 7595-7597.
55. Y.Y. Liang, Z. Xu, J.B. Xia, S.T. Tsai, Y. Wu, G. Li, C. Ray, and L.P. Yu “For the Bright Future-Bulk Heterojunction Polymer Solar Cells with Power Conversion Efficiency of 7.4%.” Adv. Mater. 2010, 22, E135-E138.
56. Z. He, C. Zhong, X. Huang, W.Y. Wong, H. Wu, L. Chen, S. Su, and Y. Cao “Simultaneous Enhancement of Open-Circuit Voltage, Short-Circuit Current Density, and Fill Factor in Polymer Solar Cells.” Adv. Mater. 2011, 23, 4636-4643.
57. N. Jean-Michel “Organic photovoltaic materials and devices.” C. R. Phys. 2002, 3, 523-542.
58. S.K. Pal, T. Kesti, M. Maiti, F.L. Zhang, O. Inganas, S. Hellstrom, M.R. Andersson, F. Oswald, F. Langa, T. Osterman, T. Pascher, A. Yartsev, and V. Sundstrom “Geminate Charge Recombination in Polymer/Fullerene Bulk Heterojunction Films and Implications for Solar Cell Function.” J. Am. Chem. Soc. 2010, 132, 12440-12451.
59. X. Yang and J. Loos “Toward high-performance polymer solar cells: The importance of morphology control.” Macromolecules 2007, 40, 1353-1362.
60. C.W. Tang “Two-layer organic photovoltaic cell.” Appl. Phys. Lett. 1986, 48, 183-185.
61. G. Yu and A.J. Heeger “Charge Separation and Photovoltaic Conversion in Polymer Composites with Internal Donor-Acceptor Heterojunctions.” J. Appl. Phys. 1995, 78, 4510-4515.
62. L.M. Chen, Z.R. Hong, G. Li, and Y. Yang “Recent Progress in Polymer Solar Cells: Manipulation of Polymer: Fullerene Morphology and the Formation of Efficient Inverted Polymer Solar Cells.” Adv. Mater. 2009, 21, 1434-1449.
63. J. Peet, M.L. Senatore, A.J. Heeger, and G.C. Bazan “The Role of Processing in the Fabrication and Optimization of Plastic Solar Cells.” Adv. Mater. 2009, 21, 1521-1527.
64. F.C. Krebs “Polymer solar cell modules prepared using roll-to-roll methods: Knife-over-edge coating, slot-die coating and screen printing.” Sol. Energy Mater. Sol. Cells 2009, 93, 465-475.
65. F.C. Krebs, J. Fyenbo, and M. Jorgensen “Product integration of compact roll-to-roll processed polymer solar cell modules: methods and manufacture

using flexographic printing, slot-die coating and rotary screen printing." J. Mater. Chem. 2010, 20, 8994-9001.

66. J.S. Huang, G. Li, and Y. Yang "A semi-transparent plastic solar cell fabricated by a lamination process." Adv. Mater. 2008, 20, 415-419.

67. G. Li, C.W. Chu, V. Shrotriya, J. Huang, and Y. Yang "Efficient inverted polymer solar cells." Appl. Phys. Lett. 2006, 88, 253503-253503.

68. M. Jorgensen, K. Norrman, and F.C. Krebs "Stability/degradation of polymer solar cells." Sol. Energy Mater. Sol. Cells 2008, 92, 686-714.

69. F.C. Krebs "Polymer photovoltaics: a practical approach.", SPIE, Bellingham, Washington 2008.

70. S.A. Gevorgyan, M. Jorgensen, and F.C. Krebs "A setup for studying stability and degradation of polymer solar cells." Sol. Energy Mater. Sol. Cells 2008, 92, 736-745.

71. M.O. Reese, A.K. Sigdel, J.J. Berry, D.S. Ginley, and S.E. Shaheen "A simple miniature controlled-atmosphere chamber for optoelectronic characterizations." Sol. Energy Mater. Sol. Cells 2010, 94, 1254-1258.

72. S.A. Gevorgyan, M. Jorgensen, F.C. Krebs, and K.O. Sylvester-Hvid "A compact multi-chamber setup for degradation and lifetime studies of organic solar cells." Sol. Energy Mater. Sol. Cells 2011, 95, 1389-1397.

73. F.C. Krebs and K. Norrman "Analysis of the failure mechanism for a stable organic photovoltaic during 10000 h of testing." Progr. Photovolt.:Res. Appl. 2007, 15, 697-712.

74. K. Norrman and F.C. Krebs "Lifetimes of organic photovoltaics: Using TOF-SIMS and O-18(2) isotopic labelling to characterise chemical degradation mechanisms." Sol. Energy Mater. Sol. Cells 2006, 90, 213-227.

75. K. Kawano, R. Pacios, D. Poplavskyy, J. Nelson, D.D.C. Bradley, and J.R. Durrant "Degradation of organic solar cells due to air exposure." Sol. Energy Mater. Sol. Cells 2006, 90, 3520-3530.

76. M. Girtan and M. Rusu "Role of ITO and PEDOT:PSS in stability/degradation of polymer: fullerene bulk heterojunctions solar cells." Sol. Energy Mater. Sol. Cells 2010, 94, 446-450.

77. F.C. Krebs "Air stable polymer photovoltaics based on a process free from vacuum steps and fullerenes." Sol. Energy Mater. Sol. Cells 2008, 92, 715-726.

78. M.H. Petersen, S.A. Gevorgyan, and F.C. Krebs "Thermocleavable Low Band Gap Polymers and Solar Cells Therefrom with Remarkable Stability toward Oxygen." Macromolecules 2008, 41, 8986-8994.

79. B. Paci, A. Generosi, D. Bailo, V.R. Albertini, and R. de Bettignies "Discriminating bulk, surface and interface aging effects in polymer-based active materials for efficient photovoltaic devices." Chem. Phys. Lett. 2010, 494, 69-74.

80. B. Paci, A. Generosi, V.R. Albertini, R. Generosi, P. Perfetti, R. de Bettignies, and C. Sentein "Time-resolved morphological study of bulk heterojunction films for efficient organic solar devices." J. Phys. Chem. C 2008, 112, 9931-9936.

81. S. Bertho, G. Janssen, T.J. Cleij, B. Conings, W. Moons, A. Gadisa, J. D'Haen, E. Goovaerts, L. Lutsen, J. Manca, and D. Vanderzande "Effect of temperature on the morphological and photovoltaic stability of bulk heterojunction polymer: fullerene solar cells." Sol. Energy Mater. Sol. Cells 2008, 92, 753-760.

82. E. Verploegen, R. Mondal, C.J. Bettinger, S. Sok, M.F. Toney, and Z.A. Bao "Effects of Thermal Annealing Upon the Morphology of Polymer-Fullerene Blends." Adv. Funct. Mater. 2010, 20, 3519-3529.

83. I. Anton, D. Pachon, and G. Sala "Characterization of optical collectors for concentration photovoltaic applications." Progr. in Photovolt.:Res. Appl. 2003, 11, 387-405.

84. G. Smestad, H. Ries, R. Winston, and E. Yablonovitch "The Thermodynamic Limits of Light Concentrators." Sol. Energy Mater. 1990, 21, 99-111.

85. D. Barlev, R. Vidu, and P. Stroeve "Innovation in concentrated solar power." Sol. Energy Mater. Sol. Cells 2011, 95, 2703-2725.

86. J.S. Batchelder, A.H. Zewail, and Cole T. "Luminescent solar concentrators. 1: theory of operation and techniques for performance evaluation." Appl. Optics 1979, 18, 3090-3110.

87. P.F. Scudo, L. Abbondanza, R. Fusco, and L. Caccianotti "Spectral converters and luminescent solar concentrators." Sol. Energy Mater. Sol. Cells 2010, 94, 1241-1246.

88. R. Reisfeld, D. Shamrakov, and C. Jorgensen "Photostable Solar Concentrators Based on Fluorescent Glass-Films." Sol. Energy Mater. Sol. Cells 1994, 33, 417-427.

89. K.R. McIntosh, N. Yamada, and B.S. Richards "Theoretical comparison of cylindrical and square-planar luminescent solar concentrators." App. Phys. B-Lasers O. 2007, 88, 285-290.

90. M.G. El Shaarawy, S.M. El Bashir, M. Hammam, and M.K. El Mansy "Bent

fluorescent solar concentrators (BFSCs): Spectroscopy, stability and outdoor performance." Curr. Appl. Phys. 2007, 7, 643-649.

91. J. Yoon, L.F. Li, A.V. Semichaevsky, J.H. Ryu, H.T. Johnson, R.G. Nuzzo, and J.A. Rogers "Flexible concentrator photovoltaics based on microscale silicon solar cells embedded in luminescent waveguides." Nat. Commun. 2011, 2, 343.

92. J. Yoon, A.J. Baca, S.I. Park, P. Elvikis, J.B. Geddes, L.F. Li, R.H. Kim, J.L. Xiao, S.D. Wang, T.H. Kim, M.J. Motala, B.Y. Ahn, E.B. Duoss, J.A. Lewis, R.G. Nuzzo, P.M. Ferreira, Y.G. Huang, A. Rockett, and J.A. Rogers "Ultrathin silicon solar microcells for semitransparent, mechanically flexible and microconcentrator module designs." Nat. Mater. 2008, 7, 907-915.

93. R. Reisfeld "New developments in luminescence for solar energy utilization." Opt. Mater. 2010, 32, 850-856.

94. B.C. Rowan, L.R. Wilson, and B.S. Richards "Advanced Material Concepts for Luminescent Solar Concentrators." Ieee J. Sel. Top. Quant. Electron. 2008, 14, 1312-1322.

95. C.L. Mulder, P.D. Reusswig, A.M. Velazquez, H. Kim, C. Rotschild, and M.A. Baldo "Dye alignment in luminescent solar concentrators: I. Vertical alignment for improved waveguide coupling." Opt. Express 2010, 18, A79-A90.

96. C.L. Mulder, P.D. Reusswig, A.P. Beyler, H. Kim, C. Rotschild, and M.A. Baldo "Dye alignment in luminescent solar concentrators: II. Horizontal alignment for energy harvesting in linear polarizers." Opt. Express 2010, 18, A91-A99.

97. P.P.C. Verbunt, A. Kaiser, K. Hermans, C.W.M. Bastiaansen, D.J. Broer, and M.G. Debije "Controlling Light Emission in Luminescent Solar Concentrators Through Use of Dye Molecules Aligned in a Planar Manner by Liquid Crystals." Adv. Funct. Mater. 2009, 19, 2714-2719.

98. A. Gombert and A. Luque "Photonics in photovoltaic systems." Phys. Status Solidi A 2008, 205, 2757-2765.

99. J.C. Goldschmidt, M. Peters, A. Bosch, H. Helmers, F. Dimroth, S.W. Glunz, and G. Willeke "Increasing the efficiency of fluorescent concentrator systems." Sol. Energy Mater. Sol. Cells 2009, 93, 176-182.

100. J.C. Goldschmidt, M. Peters, M. Hermle, and S.W. Glunz "Characterizing the light guiding of fluorescent concentrators." J. Appl. Phys. 2009, 105,

101. M.G. Debije, P.P.C. Verbunt, B.C. Rowan, B.S. Richards, and T.L. Hoeks

"Measured surface loss from luminescent solar concentrator waveguides." Appl. Opt. 2008, 47, 6763-6768.

102. M.J. Currie, J.K. Mapel, T.D. Heidel, S. Goffri, and M.A. Baldo "High-efficiency organic solar concentrators for photovoltaics." Science 2008, 321, 226-228.

103. M.G. Debije, M.P. Van, P.P.C. Verbunt, M.J. Kastelijn, R.H.L. van der Blom, D.J. Broer, and C.W.M. Bastiaansen "Effect on the output of a luminescent solar concentrator on application of organic wavelength-selective mirrors." Appl. Opt. 2010, 49, 745-751.

104. L.R. Wilson, B.C. Rowan, N. Robertson, O. Moudam, A.C. Jones, and B.S. Richards "Characterization and reduction of reabsorption losses in luminescent solar concentrators." Appl. Opt. 2010, 49, 1651-1661.

105. R. Soti, E. Farkas, M. Hilbert, Z. Farkas, and I. Ketskemety "Photon transport in luminescent solar concentrators." J. Lumin. 1996, 68, 105-114.

106. S. Tsoi, D.J. Broer, C.W.M. Bastiaansen, and M.G. Debije "Patterned dye structures limit reabsorption in luminescent solar concentrators." Opt. Express 2010, 18, A536-A543.

107. N.C. Giebink, G.P. Wiederrecht, and M.R. Wasielewski "Resonance-shifting to circumvent reabsorption loss in luminescent solar concentrators." Nat. Photonics 2011, 5, 695-702.

108. L.H. Slooff, E.E. Bende, A.R. Burgers, T. Budel, M. Pravettoni, R.P. Kenny, E.D. Dunlop, and A. Buchtemann "A luminescent solar concentrator with 7.1% power conversion efficiency." Phys. Status Solidi RRL 2008, 2, 257-259.

109. U. Rau, F. Einsele, and G.C. Glaeser "Efficiency limits of photovoltaic fluorescent collectors." Appl. Phys. Lett. 2005, 87, 171101.

110. V. Wittwer, W. Stahl, and A. Goetzberger "Fluorescent planar concentrators." Sol. Energy Mater. 1984, 11, 187-197.

111. Friedman P.S. "Progress on the development of luminescent solar concentrators." In Proc. SPIE Role of electro-optics in photovoltaic conversion technology 1980, 248, 98-104.

112. A.F. Mansour "Optical efficiency and optical properties of luminescent solar concentrators." Polym. Test. 1998, 17, 333-343.

113. A.F. Mansour, M.G. El Shaarawy, S.M. El Bashir, M.K. El Mansy, and M. Hammam "Optical study of perylene dye doped poly(methyl methacrylate) as fluorescent solar collector." Polym. Int. 2002, 51, 393-397.

114. A.F. Mansour, H.M.A. Killa, S.A. El Wanees, and M.Y. El Sayed "Laser dyes

doped with poly(ST-Co-MMA) as fluorescent solar collectors and their field performance." Polymer Testing 2005, 24, 519-525.

115. N. Tanaka, N. Barashkov, J. Heath, and W.N. Sisk "Photodegradation of polymer-dispersed perylene di-imide dyes." Appl. Opt. 2006, 45, 3846-3851.

116. L.H. Slooff, A.R. Burgers, N.J. Bakker, T. Budel, A. Büchtemann, R. Danz, T. Meyer, A. Meyer, and T.H. Wadman "The luminescent concentrator: stability issues." Proc. of 22nd European Photovoltaic Solar Energy Conference (22nd EUPVSEC), Milan 2007

117. S.M. Reda "Stability and photodegradation of phthalocyanines and hematoporphyrin doped PMMA as solar concentrators." Sol. Energy 2007, 81, 755-760.

118. M. Hammam, M.K. El Mansy, S.M. El Bashir, and M.G. El Shaarawy "Performance evaluation of thin-film solar concentrators for greenhouse applications." Desalination 2007, 209, 244-250.

119. R. Kinderman, L.H. Slooff, A.R. Burgers, N.J. Bakker, A. Buchtemann, R. Danz, and J.A.M. van Roosmalen "I-V performance and stability study of dyes for luminescent plate concentrators." J. Sol. Energy Eng.-T. ASME 2007, 129, 277-282.

120. W.G.J.H. van Sark, K.W.J. Barnham, L.H. Slooff, A.J. Chatten, A. Buchtemann, A. Meyer, S.J. McCormack, R. Koole, D.J. Farrell, R. Bose, E.E. Bende, A.R. Burgers, T. Budel, J. Quilitz, M. Kennedy, T. Meyer, C.D.M. Donega, A. Meijerink, and D. Vanmaekelbergh "Luminescent Solar Concentrators - A review of recent results." Opt. Express 2008, 16, 21773-21792.

121. G. Seybold and G. Wagenblast "New Perylene and Violanthrone Dyestuffs for Fluorescent Collectors." Dyes Pigm. 1989, 11, 303-317.

122. P.A. Cahill "Toward red-emitting, radiation tolerant chromophores." Radiat. Phys. Chem. 1993, 41, 351-363.

image in next page:

details from M. K. Č*iurlionis "Allegro (Sonata II - Sonata of the Spring)", 1907.*

>3

STUDY OF PHOTO-DEGRADATION MECHANISMS IN π-CONJUGATED POLYMERS FOR POLYMER SOLAR CELLS

3.1 INTRODUCTION

As we have shown in Chapter 2, considerable efforts have been made by the PSC research community in the last few years in order to improve power conversion efficiencies of devices. In particular, extensive research has been carried out with the aim of developing novel p-type materials for the photoactive layer and significant advances have been made in the field of device processing and engineering, leading to power conversion efficiencies exceeding 7%.[1-3]

Although PSC device efficiency represents a central milestone for the commercial deployment of this technology, environmental stability/degradation of devices is another crucial area in which scientific and technological efforts are needed for the development of successful PSC systems. Due to the complex multilayer architecture of BHJ devices, multiple degradation pathways may occur when the illuminated PSC device is exposed to oxygen and water (i.e. ambient air). Therefore a comprehensive knowledge of the degradation mechanisms occurring in the finished device is of paramount importance to explore strategies to improve device lifetime.

The formation of corrosion products at the electrodes following exposure to air and their interaction with the photoactive layer were shown to represent a potential cause of decline in device performance.[4-7] In addition, stability of working devices may be affected by morphological degradation of the photoactive layer. As will be discussed in detail in Chapter 4, most BHJ systems show poor stability and often undergo macrophase segregation of the blend components with time, as the peak-performance BHJ morphology in an optimized PSC device only represents a metastable state, which is not usually maintained over long operation times.[8-13]

Another aspect affecting the stability of PSC devices is the diffusion of water into the device and its reaction with the active materials in the PSC leading to a decay of the photovoltaic performance over time.[14-17]

A major contribution to poor stability of PSC devices operating in ambient atmosphere is given by the photo-chemical degradation of the conjugated polymer constituting the p-type material in the photoactive layer. In particular, photo-oxidation of the conjugated polymer still represents a challenge, although progresses have been made in the selection of polymeric materials with desirable optical and electronic properties that also exhibit improved photochemical stability.

In the highest performing standard PSC devices the photoactive layer consists of a bulk heterojunction (BHJ) of a p-type conjugated polymer blended with an n-type soluble fullerene derivative such as [6,6]-phenyl-C_{61}-butyric acid methyl ester ($PC_{61}BM$) or [6,6]-phenyl-C_{71}-butyric acid methyl ester ($PC_{71}BM$). Among the most commonly employed p-type materials, poly(3-hexylthiophene) (P3HT) has received a great deal of attention due to its good electrical and mechanical properties as well as its ability to be easily solution-processed in common organic solvents.[18] Standard devices based on the P3HT:PC$_{61}$BM BHJ system have shown encouraging results in terms of power conversion efficiency, achieving values of up to 5.6%.[19,20] Although P3HT appears to be more environmentally stable than other semiconducting conjugated polymers such as MEH-PPV or MDMO-PPV, also devices based on this material are susceptible to chemical degradation. In particular, P3HT stability towards light still appears to be poor and the mechanisms underlying its degradation have to be fully clarified, especially in the solid state. In addition, no effective stabilization strategies have been proposed to counteract P3HT photo-oxidative degradation.

One of the first studies on the stability of P3HT towards light was carried out by Abdou and Holdcroft.[21] In their work, P3HT in chloroform solution containing dissolved molecular oxygen was irradiated by UV and visible light. Degradation of the polymer was observed and two degradation pathways were proposed. The first involved the photosensitized formation of singlet oxygen $O_2(^1\Delta_g)$ by the triplet state of P3HT causing formation of endoperoxide species which would lead in turn to reduction of π-conjugation and polymer photo-bleaching. The second involved free-radical attack of photosensitized trace amounts of transition-metal salts to the lateral alkyl chain leading to chain scission and formation of carbonyl and hydroxyl adducts as well as crosslinking. Based on these observations, in a later work by the same group[22] a mechanism accounting for the solid state behaviour of P3HT was subsequently proposed. However, no suggestions were given on possible ways to reduce the degradation rate. A similar free-radical mechanism was suggested for the thermo-oxidative degradation of poly(3-octylthiophene) (P3OT) in the solid state[23] with formation of a ketonic group in the α-carbon position of the alkyl side chain of the polymer. The effect of stabilizers on the degradation of P3OT was also studied, by employing different classes of stabilizers, namely primary antioxidants, secondary antioxidants, antioxidants reacting with non-oxygenated radicals, metal deactivators, and light stabilizers in the form of radical scavengers. However, no clear positive effects on the degradation rate of P3OT were observed by FTIR and SEC analyses. This was attributed to the high sensitivity of hydrogen abstraction from the α-carbon position of P3OT which could lead to a radical site in every alkyl group of the polymer. In the work by Caronna et al.[24] the photo-degradation of poly(3-butylthiophene) (P3BT) in the solid state was studied in different environmental conditions, namely air, nitrogen and oxygen. No degradation was observed in nitrogen atmosphere while two degradation products were isolated and identified after irradiation in air. Their formation was attributed to the reaction of singlet oxygen with the polymer conjugated chain, the former generated by energy transfer from the excited state of the polymer to molecular oxygen. In addition two compounds were found to decrease the rate of polymer oxidation, namely N-hexadecyl-N-methylaniline and 1-phenyldodecan-1-one.

Their stabilizing action was attributed to their ability to act as light screen thereby protecting the polymer from photo-oxidation. The poly[2-methoxy-5-(3′,7′-dimethyloctyloxy)-1,4-phenylenevinylene] (MDMO-PPV) system in solid state was studied by Chambon et al.[25,26] through photo- and thermal-oxidation. Infrared spectroscopy allowed to monitor the formation of ester, formate and carboxylic acid species and a degradation route was suggested involving radical oxidation of the polymer. The study was extended to the blend constituted by methanofullerene $PC_{61}BM$ and MDMO-PPV. It was found that the addition of $PC_{61}BM$ to MDMO-PPV results in a decrease of degradation rate of MDMO-PPV in blended film. This effect was attributed to radical scavenging properties of $PC_{61}BM$. In two recent works by Manceau et al.[27,28] the photo-oxidative degradation of P3HT in the solid state was studied in the presence of air under accelerated conditions. On the basis of infrared spectroscopy, X-ray photoelectron spectroscopy and chemical derivatisation, a degradation mechanism was proposed involving the radical oxidation of the hexyl side-chain and the sulphur atom of thiophene ring. Based on a previous work by the same group,[29] it was also confirmed that singlet oxygen does not appear to be the main intermediate in the degradation process of P3HT. However, no suggestions were made on possible ways to decrease the degradation rate of the polymeric system.

Although accelerated aging tests represent a relatively rapid way to obtain important information on the photo-chemical response of polymeric systems, degradation mechanisms proposed on the basis of this type of studies may differ significantly from the behaviour of the polymer in actual operating conditions, namely under sunlight. A suitable way to evaluate the photo-oxidative degradation of polymeric systems for photovoltaic applications in conditions similar to environmental is to perform tests under simulated sunlight.

In this section, we present a study on the photo-oxidative degradation of solid-state P3HT in ambient air and under simulated sunlight. A degradation mechanism is proposed confirming what reported in the literature for accelerated experiments.[28] The effect of polymer regioregularity on the rate of P3HT degradation is also examined in details. Finally, the effect of the addition of two compounds to P3HT is studied, namely a Hindered Amine Light Stabilizer (HALS) and Multi-Walled Carbon Nanotubes (MWCNT), with the aim of improving the stability of pure P3HT towards light.

3.2 EXPERIMENTAL

Regioregular poly(3-hexylthiophene) (P3HT-RR) was purchased from Rieke Metals Inc. (type 4002, regioregularity 90-93% - data given by supplier). Highly-regioregular poly(3-hexylthiophene) (P3HT-hRR) was purchased from BASF (type P200 Sepiolid, regioregularity > 98% - data given by the supplier). Both P3HT types were used as received. Chloroform (Sigma-Aldrich) was used as solvent in all tests. Multi-walled carbon nanotubes (MWCNT – average diameter 9.5 nm, average length 1.5 μm, purity > 95%) were purchased from NanoCyl and used as received, without any further purification. The Hindered Amine Light Stabilizer additive (TINUVIN®292) was purchased from CIBA Chemicals and used as received.

Infrared spectroscopy and UV-Vis spectroscopy were performed on thin film samples (~ 200 nm) deposited onto NaCl, KBr and glass substrates by spin-coating (WS-400B-NPP Spin-Processor, Laurell Technologies Corp.). The thickness of the samples was measured by profilometry. Infrared spectra were recorded in transmission mode on a Nicolet 760 – FTIR Spectrophotometer controlled by OMNIC software. Spectra were obtained using 32 scans and a 4 cm^{-1} resolution. UV-VIS absorption spectra were recorded in transmission mode by means of a Jasco V-570 UV-VIS-NIR Spectrophotometer on solid state samples deposited onto quartz substrates.

All samples were irradiated in air by means of a Class A solar simulator (Xenon short arc lamp 150 W, Abet Technologies) with AM1.5G (ASTM 927-91) spectral distribution and a power output of about 2200 W/m^2 (approximately 2 suns). The solar simulator power output was monitored by means of a power-meter with thermopile sensor (Ophir). Samples were collected at different irradiation times.

The molecular weight of the samples was determined through Gel Permeation Chromatography (GPC – Waters 410) using THF as eluent and polystyrene standards.

Proton nuclear magnetic resonance (^{1}H-NMR) spectra were recorded on a Bruker AC 300 NMR Spectrometer. All samples for ^{1}H-NMR analysis were dissolved in $CDCl_3$.

Differential scanning calorimetry (DSC) analyses were performed on solid state samples using a DSC/823e-Mettler Toledo differential scanning calorimeter. Scan rate was 20 K/min.

3.3 RESULTS AND DISCUSSION

3.3.1 Photo-degradation of poly(3-hexylthiophene) in the solid state

3.3.1.1 Gel Permeation Chromatography

The molecular weight of P3HT-RR samples was measured by gel permeation chromatography (GPC). The molecular weight of the polymer was measured at different light exposure times in order to monitor modifications of the macromolecular chain length. The pristine polymer gave values of Mn and Mw of 30 KDa and 70 KDa, respectively. By increasing the exposure time of the cast polymer films, no significant variation of Mn and Mw was observed even after 200 h of exposure to simulated sunlight. On the other hand, a progressively higher amount of insoluble material was formed with increasing exposure time. This trend reflects the fact that the GPC analysis is limited to soluble material as it is carried out in solution. Insoluble moieties containing degradation products, which were not found in the pristine polymer but only in degraded samples, are filtered out before elution of the sample into the GPC and are thus excluded from the analysis.

3.3.2 1H-NMR Spectroscopy

Solution ^{1}H-NMR spectroscopy was performed on all P3HT-RR samples. The pristine material showed one sharp band centred at δ 6.98 in the 1H-NMR which can be attributed to the thiophene proton and denotes the HT-HT regioregular structure of the polymer. This regioregular structure was confirmed by the ^{1}H-NMR spectrum in the α- and β-methylene proton region, where the signals corresponding to HT linkages gave a HT-HT regioregularity of 89.8% (Figure 3.1a).

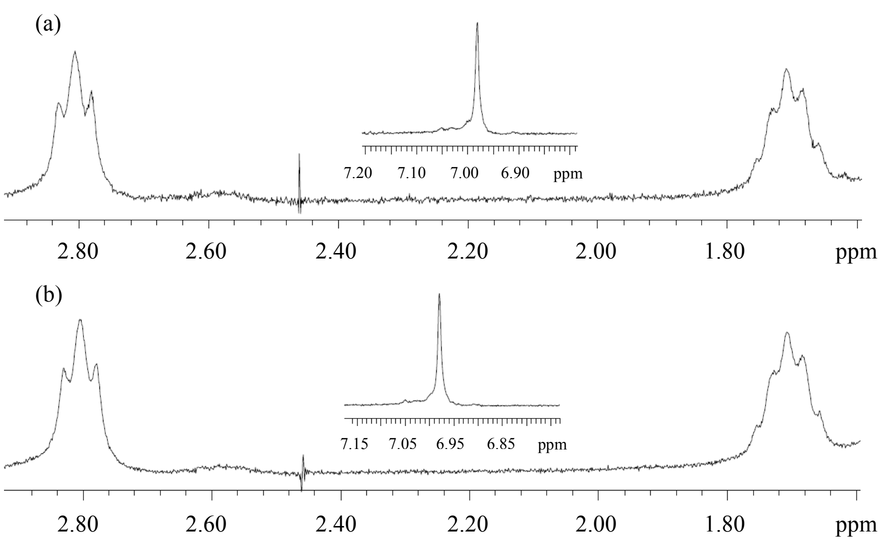

Figure 3.1 Expanded ^{1}H-NMR spectra in the methylene region for pristine P3HT-RR (a) and 100 h irradiated P3HT-RR (b). Aromatic region is also shown in the insets.

When considering the spectra of irradiated samples, no modifications to the P3HT ^{1}H-NMR spectrum were found even after 100 h of exposure (Figure 3.1b). The reason for that might be the fact that also in this case the analysis is carried out on polymer solution, thus insoluble moieties formed during irradiation are excluded from the analysis.

3.3.3 UV-Vis absorption spectroscopy

The solid-state UV-Vis absorption spectrum of the pristine P3HT-RR is shown in Figure 3.2, where also the spectrum of 24 hours irradiated P3HT-RR is presented. The pristine polymer shows a maximum peak at 520 nm and two shoulders at 550 nm and 600 nm, respectively. After irradiation, a progressive decrease of the absorption intensity of the polymer was observed associated to a 15 nm blue shift of the maximum absorption wavelength lmax. These modifications can be attributed to the photo-bleaching of the polymer resulting from a reduction of the conjugation length. These observations are consistent with recent literature reports[28] on accelerated aging tests on the same polymer system at longer exposure times.

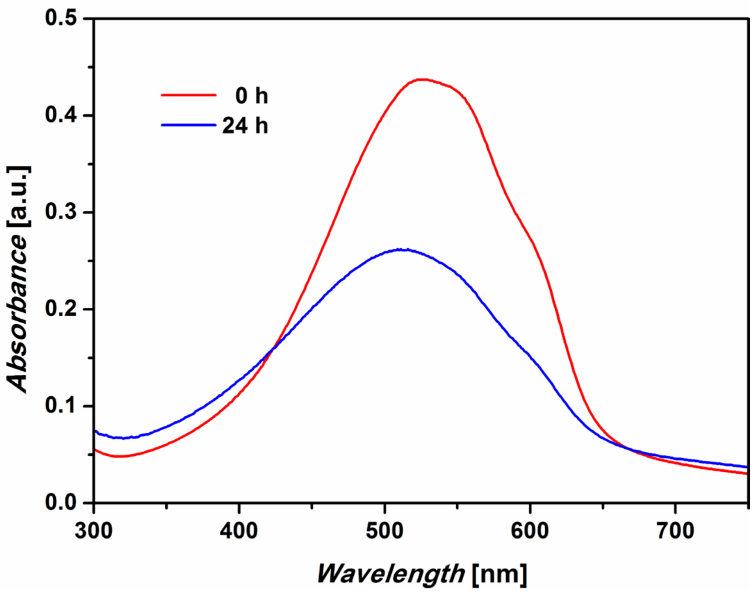

Figure 3.2 UV-Vis absorption spectra of P3HT-RR as a function of irradiation time (0 h, 24 h).

3.3.4 Fourier-transform infrared spectroscopy

FTIR spectroscopy was used to monitor the rate of the photo-oxidation process. After prolonged exposure to simulated sunlight, significant modifications to the IR spectrum of the polymer were observed. In order to identify the changes occurring during irradiation, the main IR absorption bands for the pristine polymer were identified and are reported in Table 3.1.[30]

Table 3.1 Frequencies and assignments of main IR bands for pristine P3HT-RR.

Wavenumber [cm^{-1}]	Assignment
3055	C-H (aromatic) str
2955	CH_3 asym str
2925	CH_2 asym str
2855	CH_2 sym str
1510 1454	thiophene ring str
820	C-H bend thiophene ring

A progressive decrease of absorption intensity was observed for various functional groups. In particular, the intensity of the absorption bands related to alkyl groups, aromatic C-H and thiophene ring rapidly decreased. As an example, Figure 3.3 shows the progressive disappearance of the characteristic bands assigned to alkyl groups. After approximately 50 h of exposure to simulated sunlight, the intensity of the peaks is decreased down to less than 50% of its original value.

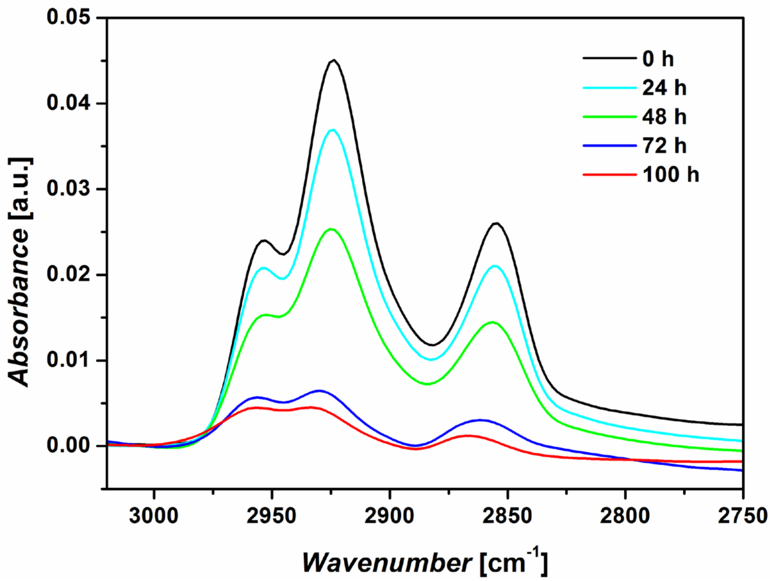

Figure 3.3 Variation of FTIR spectra of P3HT-RR spin-coated films in the C-H aliphatic region as a function of irradiation time (a: 0 h; b: 6 h; c: 24 h; d: 48 h; e: 72 h; f: 100 h)

In addition, the simultaneous formation of other characteristic absorption bands was observed. In particular, several features appeared in the carbonyl region (Figure 3.4) where the development of different maxima could be distinguished upon irradiation. Furthermore, the emergence of a sharp band in the sulfoxide region was observed (1050 cm^{-1} – 1150 cm^{-1}) at increasing exposure times (Figure 3.4 - inset). The progressive decrease of absorption intensity of the band assigned to the thiophene ring (Table 3.1) can also be seen in Figure 3.4 at 1510 cm^{-1}.

Figure 3.5 shows the time-dependent evolution of absorption intensity of different characteristic IR bands during light exposure. In order to make comparisons easier, normalized absorption intensities are presented (the normalized absorption intensity for a given peak is the ratio between the absorption intensity of that peak at a given exposure time and the maximum absorption intensity found for the same peak during the entire exposure time). As shown in the plot, a decrease of intensity for signals attributed to alkyl groups and thiophene ring is observed accompanied by the appearance of new bands. As also suggested in the literature,[28] these new bands may be assigned to carbonyl species and thioesters.

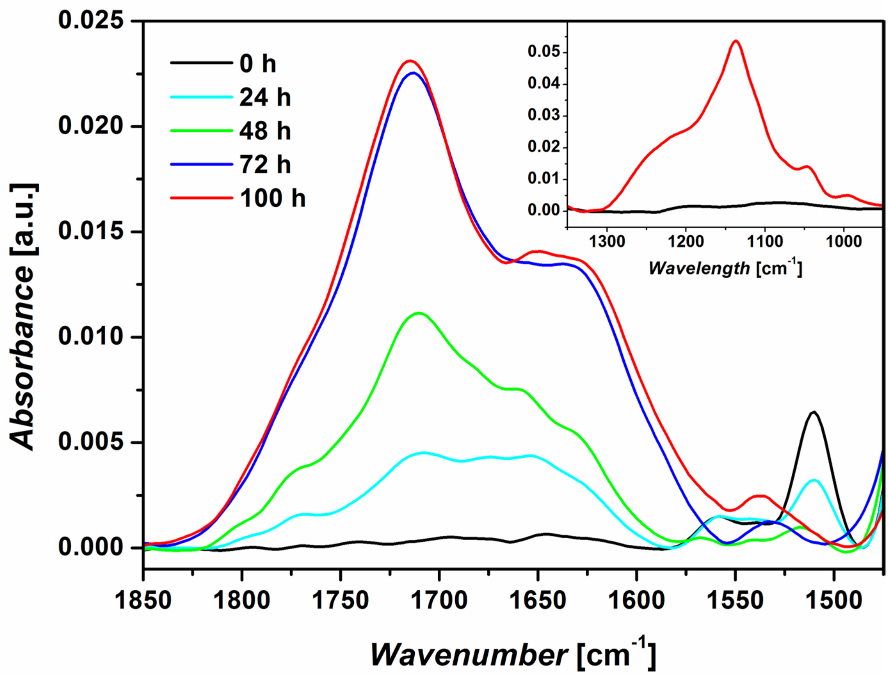

Figure 3.4 Variation of FTIR spectra of P3HT-RR spin-coated films in the carbonyl region as a function of irradiation time (a: 0 h; b: 6 h; c: 24 h; d: 48 h; e: 72 h; f: 100 h). The inset shows the formation of characteristic bands in the sulfoxide region (1050 cm^{-1} – 1150 cm^{-1}).

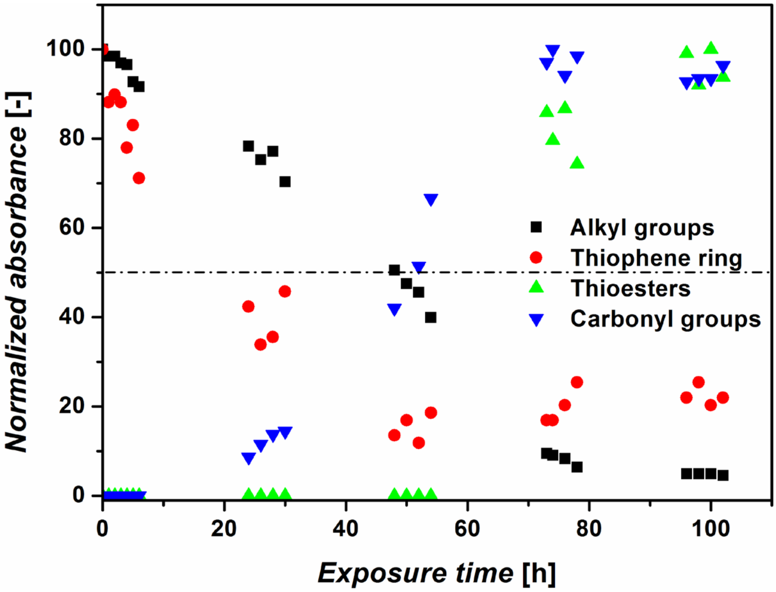

Figure 3.5 Variation of normalized absorbance for characteristic groups in P3HT -RR as a function of exposure time.

After about 50 h of exposure to simulated sunlight, the original absorption intensity is reduced by almost 50% in the case of both alkyl groups and thiophene ring. Concurrently, signals assigned to C=O stretching of carbonyl species and S=O stretching of thioesters progressively appear with a similar rate of formation. These trends suggest that disruption of the macromolecular chain during exposure to simulated sunlight is accompanied by formation of new degradation products. This aspect is discussed more in detail in the next paragraph.

It is interesting to note that the entire FTIR spectrum of the polymer underwent significant modifications during the degradation process. In particular, no FTIR signals appeared to remain constant during light exposure, making it impossible to determine an actual degradation kinetic (variation of concentration of molecular species over time) for the polymer.

In addition, partial loss of the irradiated material may have occurred during the degradation process. Therefore, the decrease of intensity found for FTIR signals associated with alkyl groups and thiophene ring may have also partially been caused by decrease of the optical path length. These considerations may suggest that the rate of disappearance observed for these characteristic groups may have actually appeared faster in the FTIR degradation study than in a real-case scenario (overestimate of the rate of disappearance). Conversely, the formation of new degradation species observed upon light exposure may have appeared slower from the FTIR study than in the real case (underestimate of the rate of formation of new degraded species).

3.3.5 Degradation mechanism of poly(3-hexylthiophene) thin films

The results found so far underline a substantial instability of P3HT to photo-oxidation and suggest that significant modifications may occur to the structure of the polymer upon exposure to simulated sunlight. These modifications can be described by invoking a two-fold photo-oxidative degradation mechanism for the polymer. On one side (Scheme 3.1), oxidation may occur on the alkyl side-chain resulting from the attack of oxygen to the carbon in α-position to the thiophene ring. It is known from the literature[31] that the carbon atom of a methylene in α-position is characterized by reduced C-H bond energy and therefore it represents a preferential site for radical attack. This radical attack may lead to the formation of carbonyl species on the side chain, as inferred from the signal observed at 1715 cm-1 in the FITR spectrum of the polymer forming upon light exposure.

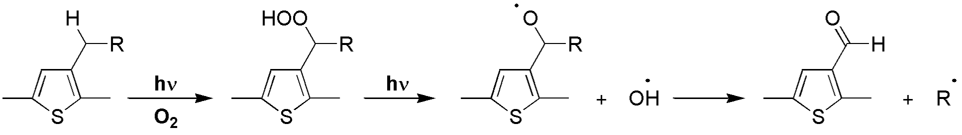

Scheme 3.1 Proposed mechanism of photo-oxidation of lateral alkyl chain in P3HT-RR.

On the other side (Scheme 3.2), photo-oxidation of the polymer backbone may ultimately lead to the opening of the thiophene ring with the formation of thio-species. In particular, degradation products such as thioesters, sulfoxides, dialkyl sulphones and sulphones seem to form, as evidenced by the appearance of their FTIR signals observed in the spectra of light exposed polymer samples (620 cm^{-1}, 1050 cm^{-1}, 1150 cm^{-1}, 1190 cm^{-1}, respectively).

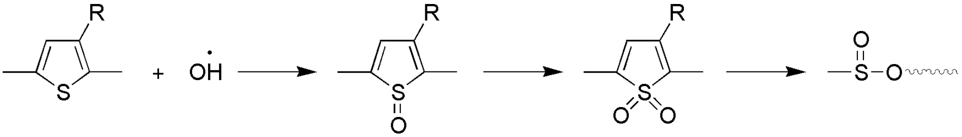

Scheme 3.2 Proposed mechanism of photo-oxidation of polymer backbone in P3HT-RR.

3.3.6 Effect of regio-regularity on photo-degradation of poly(3-hexylthiophene) in the solid state

As known from the literature,[30] four triad regioisomers are found for P3HT polymer chain: the HT-HT triad, the HT-HH triad, the TT-HT triad and the TT-HH triad – see Figure 3.6.

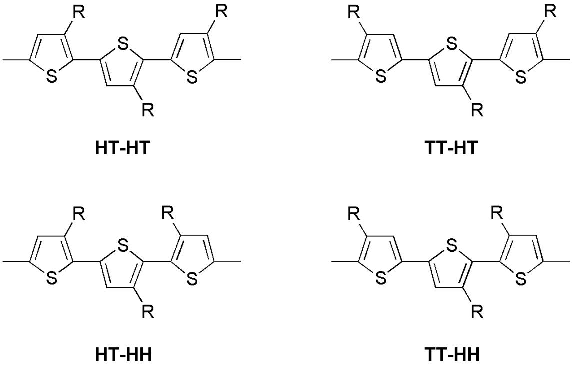

Figure 3.6 Triad regioisomers of P3HT.

Regioregular HT-HT P3HT appears to give better electro-optical properties compared to the regiorandom polymer, mainly due to the steric hindrance induced by the presence of HH linkages that can lead to defects in the conjugated chain. [32-39]

In addition to yield improved power conversion efficiency in PSC devices,[40] P3HT regioregularity may also have an effect on the degradation rate of the polymer. In order to examine this effect, P3HT samples with different HT regioregularity were considered, namely P3HT-RR (lower regioregularity) and P3HT-hRR (higher regioregularity), and their photochemical behaviour was studied during exposure to simulated sunlight.

3.3.6.1 1H-NMR spectroscopy

In order to evaluate the degree of HT regioregularity in the polymers under study, solution ^{1}H-NMR spectroscopy was performed on all samples and their characteristic features in the a-methylene proton region of the spectrum were examined, as this region may give useful information on the extent of HT linkages in the polymer chain.

From the expanded ^{1}H-NMR spectrum in the a-methylene proton region, an 89.8% HT linkage regioregularity was found for P3HT-RR (lower-regioregularity polymer). In contrast, P3HT-hRR (higher-regioregularity polymer) yielded a 93.5% HT regioregularity. These results are consistent with the values given by the material suppliers (see Section 3.2).

3.3.6.2 Differential scanning calorimetry

Calorimetric measurements were carried out by means of differential scanning calorimetry (DSC) on all pristine polymer samples, in order to study the influence of regioregularity on melting point and degree of crystallinity. An endothermic transition was observed from a crystalline to a liquid crystalline state at a temperature of 210 °C - 240 °C (peak maximum 220 °C) for pristine P3HT-RR. In contrast, pristine P3HT-hRR exhibited a higher melting temperature (232 °C). Both values are consistent with literature reports.[41]

By means of DSC analysis, enthalpy of fusion and degree of crystallinity c = $\Delta H/\Delta H^0$ were also evaluated, being ΔH the actual enthalpy of fusion of the polymer and ΔH^0 the enthalpy of fusion of the ideal crystal, taken as 99 J/g.[42] As presented in Table 3.2, a larger enthalpy of fusion and a higher degree of crystallinity are found for P3HT-hRR compared with P3HT-RR.

Table 3.2 Enthalpy of fusion and degree of crystallinity for P3HT-RR and P3HT-hRR, obtained by integration of the melting peak in the third DSC scan.

	P3HT-RR	P3HT-hRR
Enthalpy of fusion ΔH [J/g]	13.38	20.80
Degree of crystallinity χ [ΔH/ΔH°]	13.4	21.0

As known from the literature,[43] the solubility of gases is larger in amorphous regions than in crystalline regions of polymeric materials, making the crystalline core of polymers nearly inaccessible to species such as molecular oxygen. In addition, the mobility of radical species has been found to be larger in amorphous regions than in crystalline regions. These observations suggest that the rate of bulk oxidation is greater in amorphous than in crystalline polymers.

Due to the presence of a higher portion of amorphous phase as inferred from DSC measurements, the rate of the photo-oxidative degradation process in lower-regioregularity P3HT-RR could appear faster than in higher-regioregularity P3HT-hRR. In order to examine this effect, spectroscopic studies on polymer samples exposed to light are presented in the following sections.

3.3.6.3 UV-Vis spectroscopy

The normalized UV-Vis absorption spectra of solid state P3HT-RR and P3HT-hRR are shown in Figure 3.7. The appearance of a more defined vibronic structure is observed for P3HT-hRR compared to P3HT-RR, accompanied by a slightly red shifted λ_{max} (520 nm vs 522 nm for P3HT-RR and P3HT-hRR, respectively). The finer vibronic structure of P3HT-hRR may be associated to better planarization and stacking of P3HT-hRR polymer chains with respect to P3HT-RR[44] resulting from the higher degree of order in the polymer.[45]

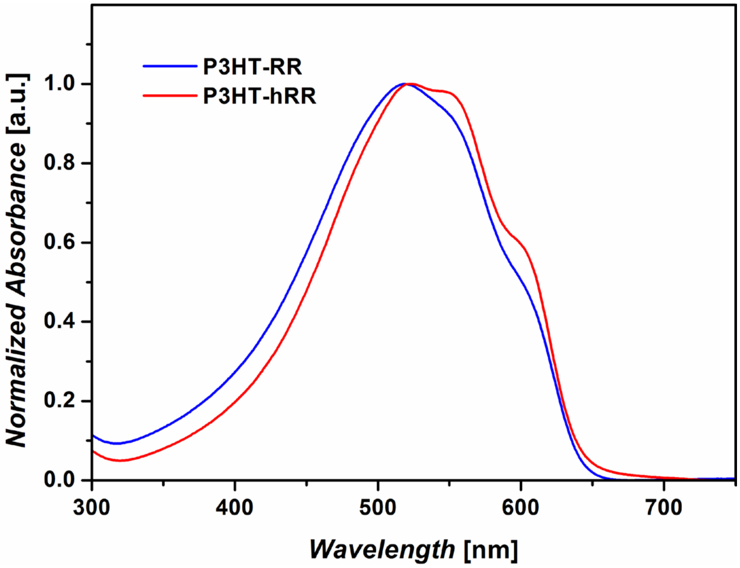

Figure 3.7 Normalized UV-Vis absorption spectra of solid state P3HT-RR and P3HT-hRR.

The modifications in the optical properties of P3HT-RR and P3HT-hRR upon light exposure were monitored by irradiating polymer thin films at increasing time with a high-power (500 W) UV-lamp and recording the evolution of the respective UV-Vis absorption spectra. A UV-light source was chosen in this case in order to swiftly highlight trends that were then explored more in detail with

FTIR studies under simulated sunlight. For both polymers, a significant decrease in the absorbance (35% decrease) is observed after a UV-exposure time of only 4 h accompanied by a blue shift of lmax and a noticeable decolouration of the polymer films (photo-bleaching). Interestingly, the extent of this blue shift after 4 h of UV-exposure was found to be higher for P3HT-RR (9 nm) than for P3HT-hRR (5 nm). This result may explained by considering the lower degree of crystallinity (higher portion of amorphous phase) in P3HT-RR than in P3HT-hRR, which may lead to faster degradation processes, as already pointed out in Section 3.3.2.2.

In order to validate these trends, FTIR studies on P3HT-RR and P3HT-hRR samples exposed to simulated sunlight were carried out and the results are presented in the next paragraph.

3.3.6.4 Fourier-transform infrared spectroscopy

The evolution of FTIR absorption spectra of P3HT-RR and P3HT-hRR during exposure to simulated sunlight was examined by monitoring characteristic absorption bands in the polymer FTIR spectra (see Section 3.3.1.5 for details). The decrease of the intensity of bands assigned to alkyl groups in the range 3000 ÷ 2800 cm^{-1} for both P3HT-RR and P3HT-hRR is shown in Figure 3.8 as a function of exposure time. During the first 24 h of exposure to light, the absorption intensity in the two polymer systems appears to decrease at a similar rate. After about 30 h, nearly 20% of the initial absorbance is lost for both P3HT-RR and P3HT-hRR. However, some significant differences in the kinetics of the degradation process for the two polymers emerge after about 48 h of exposure to light. In particular, the absorption intensity in the P3HT-RR system starts to rapidly drop, falling below 20% of its initial value after only 70 h of irradiation. In contrast, the rate of absorbance decrease maintains a constant value for P3HT-hRR, resulting in a 50% drop compared with its initial value after 100 h of exposure to simulated sunlight. A similar trend was observed for the disappearance of FTIR signals assigned to vibrations of thiophene ring (1510 cm^{-1}) and aromatic groups (820 cm^{-1}), highlighting a faster degradation process for P3HT-RR than for P3HT-hRR.

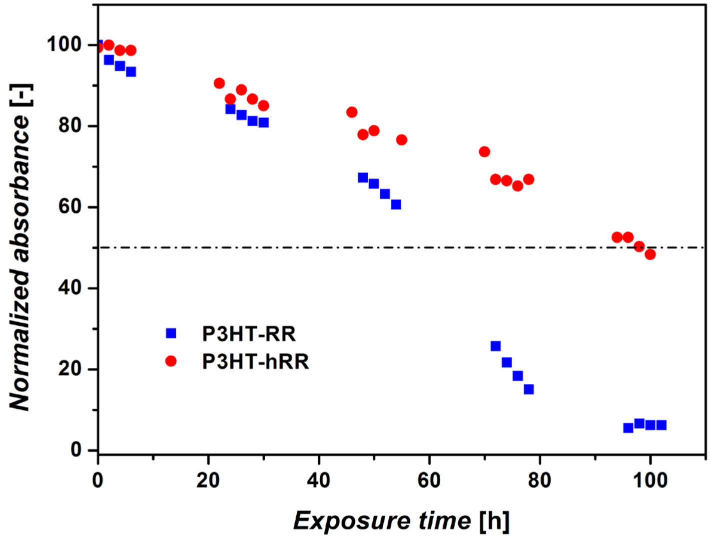

Figure 3.8 Variation of normalized absorption intensity of alkyl groups (3000 ÷ 2800 cm^{-1}) as a function of irradiation time in P3HT-RR and P3HT-hRR.

The emergence of new absorption bands in the carbonyl region (1715 cm^{-1}) for both polymer systems is shown in Figure 3.9 as a function of light exposure time. Similarly to what found previously, the modifications in P3HT-RR are characterized by a two-step process, where a constant increase in the intensity of the 1715 cm^{-1} absorption band in the first 24 h of exposure to light is followed by a sharp increase after 48 h of irradiation. An 80% increase of the absorption intensity of the carbonyl band is observed after less than 80 h of light exposure. As opposed to this trend, a less sharp increase is found for P3HT-hRR, where only a 60% increase in absorbance is found after 80 h of light exposure. Similar trends were also reported for the emergence of FTIR signals assigned to sulphones (1150 cm^{-1}) and thioesters (620 cm^{-1}).

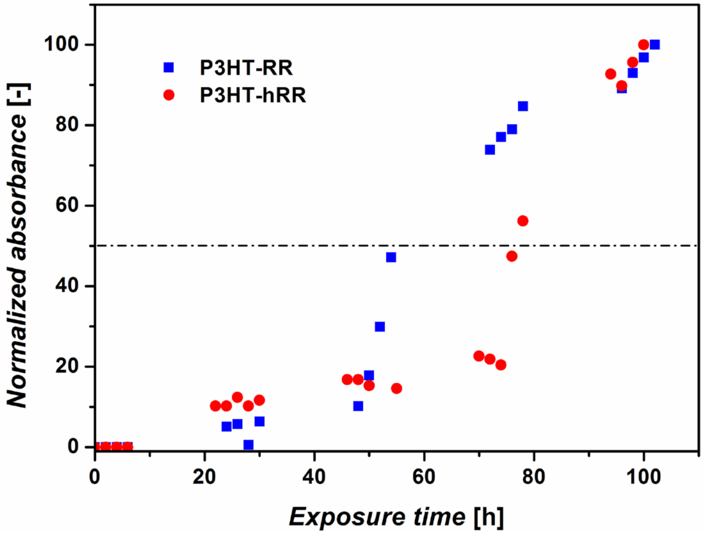

Figure 3.9 Variation of normalized absorption intensity of carbonyl species (1715 cm-1) as a function of irradiation time in P3HT-RR and P3HT-hRR.

As shown by the FTIR analysis, considerable differences appear in the rate of degradation of P3HT-RR and P3HT-hRR. In particular, significantly faster modifications of the polymer structure (disappearance of FTIR signals assigned to vibrations of alkyl groups, thiophene ring and aromatic groups) and formation of degradation products (appearance of FTIR signals assigned to vibrations of carbonyl species, thioesters and sulphones) are observed for P3HT-RR compared with P3HT-hRR (see Section 3.3.1.5 for details on the polymer degradation mechanism).

These results are in line with the trends observed in the UV-Vis analysis (Section 3.3.2.3), again suggesting that a higher degree of crystallinity in the polymer may result in a slower degradation process. As necessary condition to achieve crystallinity, polymer regioregularity represents therefore a critical parameter to be looked at not only to achieve high PSC performance,[40] but also to enhance polymer stability to photo-degradation.

3.3.7 Stabilization strategies for poly(3-hexylthiophene) thin films

Considering the results shown so far, P3HT-RR seems to show a remarkable instability towards photo-oxidation under simulated sunlight. In order to assess the possibility to reduce the degradation rate of the polymer, potential stabilizing additives were therefore tested. In particular two substances were chosen, one belonging to the class of Hindered Amine Light Stabilizers (HALS) and the other being Multi-Walled Carbon Nanotubes (MWCNT). The former was chosen because of its known ability to act as a radical scavenger in plastics and coating technology. The latter was selected because it may act both as a radical scavenger[26] and quencher of excited states, and has the potential to be employed as an efficient electron-acceptor photovoltaic component.[46-49] The HALS (5% wt.) was added to a solution of P3HT-RR in chloroform (20 mg/ml), dissolved by magnetic stirring and then spin-coated onto NaCl, KBr and CaF_2 substrates for FTIR analysis. For the MWCNT system, a homogeneous dispersion was prepared by ultrasonicating MWCNT in chloroform for 90 min. The desired volume of the MWCNT dispersion was then added to a P3HT-RR chloroform solution (20 mg/ml) and a further 60 min ultrasonication was performed. The final concentration of the P3HT-RR/MWCNT dispersion (20 mg/ml P3HT-RR in chloroform – 1% wt. MWCNT) was prepared by distillation of chloroform under vacuum and magnetic stirring. The dispersion was then spin-coated onto NaCl, KBr and CaF_2 substrates for FTIR analysis.

3.3.7.1 Fourier-transform infrared spectroscopy

The stabilizing effects of the two additives were monitored by means of FTIR. Figure 3.10 shows the changes of normalized absorption intensity of FTIR bands in the alkyl group region as a function of irradiation time. The behaviour of pure P3HT-RR is also reported, for reference.

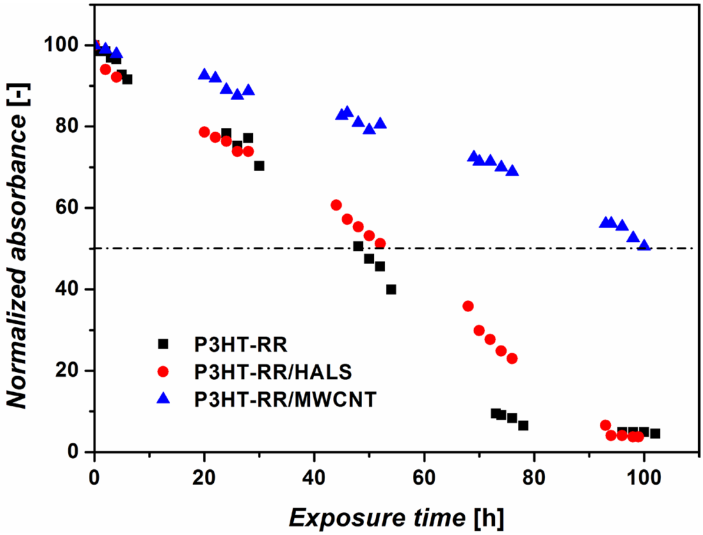

Figure 3.10 Variation of normalized absorption intensity of the alkyl group FTIR signals as a function of irradiation time for pure P3HT-RR, P3HT-RR/HALS system and P3HT-RR/MWCNT system.

No significant effects on the degradation rate of P3HT are found after the addition of HALS to P3HT. In contrast, a clear reduction in the degradation rate is observed when MWCNT are added. In particular, after about 100 h of exposure to simulated sunlight, a decrease of only 50% of the absorption intensity is reported for the P3HT-RR/MWCNT blend. As shown in the plot, the same value of absorption intensity is reached after only 50 h of irradiation for pure P3HT and P3HT-HALS system.

The time-dependent variation of normalized absorption intensity of FTIR bands related to carbonyl groups (1715 cm^{-1}) during irradiation is reported in Figure 3.11.

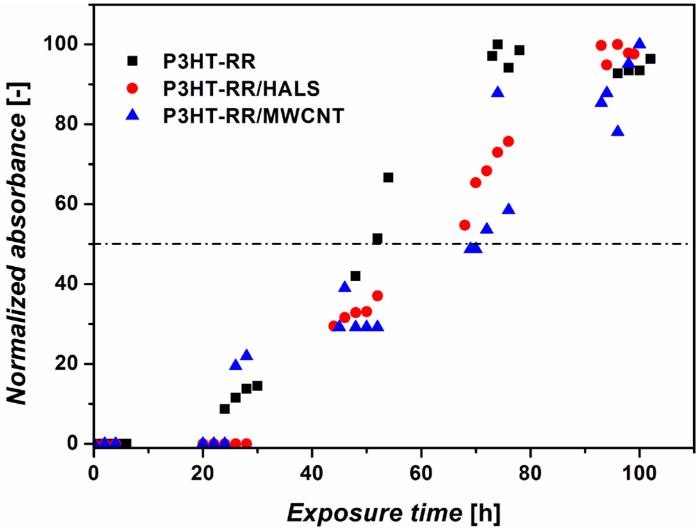

Figure 3.11 Variation of normalized absorption intensity of FTIR signals related to carbonyl groups as a function of irradiation time for pure P3HT, P3HT-HALS system and P3HT-MWCNT system.

In this case both the presence of HALS and MWCNT appear to slightly slow down the degradation rate of P3HT. Moreover the formation of carbonyl species appears to be slower for the P3HT-RR/MWCNT than for the P3HT-RR/HALS system, according to the trend reported in Figure 3.10. Similar trends were observed for the disappearance of FTIR signals assigned to vibrations of the thiophene ring (1510 cm^{-1}) and for the formation of the band assigned to vibrations of sulphone and thioester groups (1150 cm^{-1} and 620 cm^{-1}).

An explanation of the stabilizing effect of carbon nanotubes observed through FTIR in the P3HT-RR/MWCNT blend may be given by considering the radical scavenging properties of MWCNT which allow for a reduction of the degradation rate of P3HT-RR. Similar results were observed on another system, namely MDMO-PPV blended with methano-fullerene $PC_{61}BM$, suggesting that also $PC_{61}BM$ can act as radical scavenger when mixed with P3HT and exposed to light.[26] The reduced stabilizing effect reported in the P3HT-RR/HALS system could be attributed to the induction time needed by HALS molecules to activate and act as photo-stabilizers. Clearly, this induction time appears to be longer than the degradation rate of the pure polymer.

3.4 CONCLUSIONS AND FUTURE WORK

According to the results presented in this Section, P3HT appears to be substantially unstable to photo-oxidative degradation when exposed to simulated sunlight in ambient air. Significant modifications of the chemical structure of the polymer were observed and a degradation mechanism was proposed, involving side-chain scission with formation of carbonyl species and aperture of the thiophene ring with formation of thioesters. This mechanism confirms recent literature findings on the same system, exposed to accelerated aging test conditions.[27,28]

Higher polymer regioregularity was found to have an impact on polymer photo-stability. The rate photo-degradation appeared to decrease by increasing polymer regioregularity, mainly due to the presence of a higher degree of crystallinity in the polymer. This result highlights the importance of this parameter not only to achieve high PSC performance, but also to allow enhanced polymer photo-stability.

In an attempt to improve the stability towards photo-oxidative degradation of the pure polymer, the addition of two substances to P3HT was investigated. In particular, a HALS and MWCNT were individually added to pure P3HT and the photo-chemical behaviour of each of these new systems was studied through FTIR. While no significant modifications were observed in the P3HT/HALS blend, the addition of MWCNT to P3HT appeared to slow down considerably the degradation rate of the polymer. This stabilizing effect was attributed to the radical scavenging properties of MWCNT. These results suggest that MWCNT may represent a promising material for improved photo-stability in organic solar cells. Further studies will be needed in order to clarify this aspect and to explore the potential use of MWCNT as alternative n-type material in BHJ organic photovoltaics.

3.5 REFERENCES

1. Y.Y. Liang, Z. Xu, J.B. Xia, S.T. Tsai, Y. Wu, G. Li, C. Ray, and L.P. Yu "For the Bright Future-Bulk Heterojunction Polymer Solar Cells with Power Conversion Efficiency of 7.4%." Adv. Mater. 2010, 22, E135-E138.
2. Z. He, C. Zhong, X. Huang, W.Y. Wong, H. Wu, L. Chen, S. Su, and Y. Cao "Simultaneous Enhancement of Open-Circuit Voltage, Short-Circuit Current Density, and Fill Factor in Polymer Solar Cells." Adv. Mater. 2011, 23, 4636-4643.
3. H.Y. Chen, J.H. Hou, S.Q. Zhang, Y.Y. Liang, G.W. Yang, Y. Yang, L.P. Yu, Y. Wu, and G. Li "Polymer solar cells with enhanced open-circuit voltage and efficiency." Nat. Photonics 2009, 3, 649-653.
4. M. Logdlund and J.L. Bredas "Theoretical-Studies of the Interaction Between Aluminum and Poly(P-Phenylenevinylene) and Derivatives." J. Chem. Phys. 1994, 101, 4357-4364.
5. K. Kawano, R. Pacios, D. Poplavskyy, J. Nelson, D.D.C. Bradley, and J.R. Durrant "Degradation of organic solar cells due to air exposure." Sol. Energy Mater. Sol. Cells 2006, 90, 3520-3530.
6. R. Pacios, A.J. Chatten, K. Kawano, J.R. Durrant, D.D.C. Bradley, and J. Nelson "Effects of photo-oxidation on the performance of poly[2-methoxy-5-(3 ',7 '-dimethyloctyloxy)-1,4-phenylene vinylene]:[6,6]-phenyl C(61)-butyric acid methyl ester solar cells." Adv. Funct. Mater. 2006, 16, 2117-2126.
7. F.C. Krebs and K. Norrman "Analysis of the failure mechanism for a stable organic photovoltaic during 10000 h of testing." Progr. Photovolt.: Res. Appl. 2007, 15, 697-712.
8. J. Jo, S.S. Kim, S.I. Na, B.K. Yu, and D.Y. Kim "Time-Dependent Morphology Evolution by Annealing Processes on Polymer:Fullerene Blend Solar Cells." Adv. Funct. Mater. 2009, 19, 866-874.
9. M.A. Ruderer and P. Muller-Buschbaum "Morphology of polymer-based bulk heterojunction films for organic photovoltaics." Soft Matter 2011, 7, 5482-5493.
10. X. Yang and J. Loos "Toward high-performance polymer solar cells: The importance of morphology control." Macromolecules 2007, 40, 1353-1362.
11. X.N. Yang, J. Loos, S.C. Veenstra, W.J.H. Verhees, M.M. Wienk, J.M. Kroon, M.A.J. Michels, and R.A.J. Janssen "Nanoscale morphology of high-performance polymer solar cells." Nano Lett. 2005, 5, 579-583.
12. D. Di Nuzzo, A. Aguirre, M. Shahid, V.S. Gevaerts, S.C.J. Meskers, and

R.A.J. Janssen "Improved Film Morphology Reduces Charge Carrier Recombination into the Triplet Excited State in a Small Bandgap Polymer-Fullerene Photovoltaic Cell." Adv. Mater. 2010, 22, 4321-4324.

13. M. Helgesen, M. Bjerring, N.C. Nielsen, and F.C. Krebs "Influence of the Annealing Temperature on the Photovoltaic Performance and Film Morphology Applying Novel Thermocleavable Materials." Chem. Mater. 2010, 22, 5617-5624.

14. K. Norrman, M.V. Madsen, S.A. Gevorgyan, and F.C. Krebs "Degradation Patterns in Water and Oxygen of an Inverted Polymer Solar Cell." J. Am. Chem. Soc. 2010, 132, 16883-16892.

15. K. Norrman, S.A. Gevorgyan, and F.C. Krebs "Water-Induced Degradation of Polymer Solar Cells Studied by H(2)(18)O Labeling." ACS Appl. Mater. Interfaces 2009, 1, 102-112.

16. K. Norrman, N.B. Larsen, and F.C. Krebs "Lifetimes of organic photovoltaics: Combining chemical and physical characterisation techniques to study degradation mechanisms." Sol. Energy Mater. Sol. Cells 2006, 90, 2793-2814.

17. K. Norrman and F.C. Krebs "Lifetimes of organic photovoltaics: Using TOF-SIMS and O-18(2) isotopic labelling to characterise chemical degradation mechanisms." Sol. Energy Mater. Sol. Cells 2006, 90, 213-227.

18. J. Roncali "Conjugated Poly(Thiophenes) - Synthesis, Functionalization, and Applications." Chem. Rev. 1992, 92, 711-738.

19. R. Gaudiana and C. Brabec "Organic materials - Fantastic plastic." Nat. Photonics 2008, 2, 287-289.

20. G. Dennler, M.C. Scharber, and C.J. Brabec "Polymer-Fullerene Bulk-Heterojunction Solar Cells." Adv. Mater. 2009, 21, 1323-1338.

21. M.S.A. Abdou and S. Holdcroft "Mechanisms of Photodegradation of Poly(3-Alkylthiophenes) in Solution." Macromolecules 1993, 26, 2954-2962.

22. M.S.A. Abdou and S. Holdcroft "Solid-state photochemistry of pi-conjugated poly(3-alkylthiophenes)." Can. J. Chem. 1995, 73, 1893-1901.

23. N. Ljungqvist and T. Hjertberg "Oxidative-Degradation of Poly(3-Octylthiophene)." Macromolecules 1995, 28, 5993-5999.

24. T. Caronna, M. Forte, M. Catellani, and S.V. Meille "Photodegradation and photostabilization studies of poly(3-butylthiophene) in the solid state." Chem. Mater. 1997, 9, 991-995.

25. S. Chambon, A. Rivaton, J.L. Gardette, M. Firon, and L. Lutsen "Aging of a donor conjugated polymer: Photochemical studies of the degradation of

poly[2-methoxy-5-(3 ‘,7 ‘-dimethyloctyloxy)-1,4-phenylenevinylene].” J. Polym. Sci., Part A-Polym. Chem. 2007, 45, 317-331.

26. S. Chambon, A. Rivaton, J.L. Gardette, and M. Firon “Photo- and thermal degradation of MDMO-PPV : PCBM blends.” Sol. Energy Mater. Sol. Cells 2007, 91, 394-398.
27. M. Manceau, J. Gaume, A. Rivaton, J.L. Gardette, G. Monier, and L. Bideux “Further insights into the photodegradation of poly(3-hexylthiophene) by means of X-ray photoelectron spectroscopy.” Thin Solid Films 2010, 518, 7113-7118.
28. M. Manceau, A. Rivaton, J.L. Gardette, S. Guillerez, and N. Lemaitre “The mechanism of photo- and thermooxidation of poly(3-hexylthiophene) (P3HT) reconsidered.” Polym. Degrad. Stab. 2009, 94, 898-907.
29. M. Manceau, A. Rivaton, and J.L. Gardette “Involvement of Singlet Oxygen in the Solid-State Photochemistry of P3HT.” Macromol. Rapid Commun. 2008, 29, 1823-1827.
30. T.A. Chen, X.M. Wu, and R.D. Rieke “Regiocontrolled Synthesis of Poly(3-Alkylthiophenes) Mediated by Rieke Zinc - Their Characterization and Solid-State Properties.” J. Am. Chem. Soc. 1995, 117, 233-244.
31. J. Berkowitz, G.B. Ellison, and D. Gutman “3 Methods to Measure Rh Bond-Energies.” J. Phys. Chem. 1994, 98, 2744-2765.
32. R.D. Mccullough and R.D. Lowe “Enhanced Electrical-Conductivity in Regioselectively Synthesized Poly(3-Alkylthiophenes).” J. Chem. Soc.-Chem. Commun. 1992 70-72.
33. R.D. Mccullough, R.D. Lowe, M. Jayaraman, and D.L. Anderson “Design, Synthesis, and Control of Conducting Polymer Architectures - Structurally Homogeneous Poly(3-Alkylthiophenes).” J. Org. Chem. 1993, 58, 904-912.
34. R.D. Mccullough, S. Tristramnagle, S.P. Williams, R.D. Lowe, and M. Jayaraman “Self-Orienting Head-To-Tail Poly(3-Alkylthiophenes) - New Insights on Structure-Property Relationships in Conducting Polymers.” J. Am. Chem. Soc. 1993, 115, 4910-4911.
35. R.D. Mccullough and S.P. Williams “Toward Tuning Electrical and Optical-Properties in Conjugated Polymers Using Side-Chains - Highly Conductive Head-To-Tail Heteroatom-Functionalized Polythiophenes.” J. Am. Chem. Soc. 1993, 115, 11608-11609.
36. H.Y. Mao and S. Holdcroft “Grignard Synthesis of Pi-Conjugated Poly(3-Alkylthiophenes) - Controlling Molecular-Weights and the Nature of

Terminal Units." Macromolecules 1992, 25, 554-558.

37. H.Y. Mao, B. Xu, and S. Holdcroft "Synthesis and Structure Property Relationships of Regioirregular Poly(3-Hexylthiophenes)." Macromolecules 1993, 26, 1163-1169.

38. R.M.S. Maior, K. Hinkelmann, H. Eckert, and F. Wudl "Synthesis and Characterization of 2 Regiochemically Defined Poly(Dialkylbithiophenes) - A Comparative-Study." Macromolecules 1990, 23, 1268-1279.

39. W. Yen, C.C. Chan, T. Jing, G.W. Jang, and K.F. Hsueh "Electrochemical Polymerization of Thiophenes in the Presence of Bithiophene Or Terthiophene - Kinetics and Mechanism of the Polymerization." Chem. Mater. 1991, 3, 888-897.

40. Y. Kim, S. Cook, S.M. Tuladhar, S.A. Choulis, J. Nelson, J.R. Durrant, D.D.C. Bradley, M. Giles, I. Mcculloch, C.S. Ha, and M. Ree "A strong regioregularity effect in self-organizing conjugated polymer films and high-efficiency polythiophene: fullerene solar cells." Nat. Mater. 2006, 5, 197-203.

41. S. Hugger, R. Thomann, T. Heinzel, and T. Thurn-Albrecht "Semicrystalline morphology in thin films of poly(3-hexylthiophene)." Colloid Polym. Sci. 2004, 282, 932-938.

42. S. Malik and A.K. Nandi "Crystallization mechanism of regioregular poly(3-alkyl thiophene)s." J. Polym. Sci., Part B-Polym. Phys. 2002, 40, 2073-2085.

43. Y. Kamiya and E. Niki "Oxidative degradation." In: "Aspects of degradation and stabilization of polymers", Editors: H.H.G. Jellinek, Elsevier Scientific Publishing Company, Amsterdam, p. 79-147.

44. J. Cornil, J.P. Calbert, D. Beljonne, R. Silbey, and J.L. Bredas "Interchain interactions in pi-conjugated oligomers and polymers: a primer." Synth. Met. 2001, 119, 1-6.

45. P.J. Brown, D.S. Thomas, A. Kohler, J.S. Wilson, J.S. Kim, C.M. Ramsdale, H. Sirringhaus, and R.H. Friend "Effect of interchain interactions on the absorption and emission of poly(3-hexylthiophene)." Phys. Rev. B: Condens. Matter Mater. Phys. 2003, 67, 064203.

46. E. Kymakis, N. Kornilios, and E. Koudoumas "Carbon nanotube doping of P3HT: PCBM photovoltaic devices." J. Phys. D: Appl. Phys. 2008, 41, 165110.

47. E. Kymakis, E. Stratakis, and E. Koudoumas "Integration of carbon nanotubes as hole transport electrode in polymer/fullerene bulk heterojunction solar cells." Thin Solid Films 2007, 515, 8598-8600.

48. E. Kymakis, I. Alexandrou, and G.A.J. Amaratunga "High open-circuit

voltage photovoltaic devices from carbon-nanotube-polymer composites." J. Appl. Phys. 2003, 93, 1764-1768.

49. M.M. Stylianakis, J.A. Mikroyannidis, and E. Kymakis "A facile, covalent modification of single-wall carbon nanotubes by thiophene for use in organic photovoltaic cells." Sol. Energy Mater. Sol. Cells 2010, 94, 267-274.

image in next page:

details from M. K. Čiurlionis "Sparks (III)", 1906.

>4

NEW LOW-BANDGAP PHOTOCROSSLINKABLE POLYMERS FOR IMPROVED MORPHOLOGICAL STABILITY IN HIGH-EFFICIENCY POLYMER SOLAR CELLS

4.1 INTRODUCTION

Together with power conversion efficiency, long-term stability of devices has been recently recognized as a central area in which research efforts are needed for PSC technology to hit the market.[1,2]

As we have seen in the previous Chapter, several studies have demonstrated the detrimental effects that oxygen and moisture may have on device operation[3-6] and attempts have been made to elucidate the effects of their interaction with the photoactive organic layer.[7-9] In addition to chemical degradation pathways, achieving and maintaining an optimal BHJ morphology within the active layer is critical for sustaining high PSC performance. In optimized BHJs, phase separation of the electron donor and the electron acceptor domains should be on the same length-scale as the exciton diffusion length, so that efficient exciton harvesting can be facilitated.[10] Furthermore, a three-dimensional bicontinuous network of the p-type and n-type materials is required for productive charge extraction from the device.[11,12]

Although several processing techniques can be employed to achieve an optimized BHJ morphology,[13] the peak-performance morphology only represents a metastable state, which cannot usually be maintained over long operation times. Most BHJ systems show poor stability and often undergo macrophase segregation of the blend components, especially after prolonged exposure to heat.[14-17] Considering that during normal operation the active layer in PSC devices may be subjected to large temperature fluctuations, improving the robustness of the BHJ with respect to thermal stability is critical.[18,19]

Several studies have focused on the morphological evolution of the active layer of standard BHJ systems incorporating P3HT or poly[2-methoxy-5-(3′,7′-dimethyloctyloxy)-1,4-phenylenevinylene] (MDMO-PPV) as donor materials.[16,17,20-23] In addition, potential approaches to improve the thermal stability of such PSC devices have also been examined. Polymer regioregularity was shown to have a partially detrimental effect on morphological stability of devices. In particular, it was shown that polymerization of 3-hexylthiophene in the presence of small amounts of dihexylthiophene monomer leads to a reduction of effective copolymer regioregularity as a result of an increase in the content of non-HT linkages in the copolymer. Devices fabricated from this copolymer blended with $PC_{61}BM$ in the active layer showed enhanced thermal stability compared with devices containing higher-regioregularity P3HT. This effect was attributed to a reduction of the driving force for polymer crystallization upon annealing given by the lower polymer regioregularity, that allows to prevent exclusion of $PC_{61}BM$ from the ordered P3HT domains and therefore phase segregation of the BHJ.[24] These findings are partially in contrast with the results previously presented on photostability of conjugated polymers. Indeed, in Chapter 3 we showed by means of FTIR analysis that an increase in P3HT regioregularity may result in improved polymer photostability. This suggests that a balance should be sought between photostability and thermal stability.

Another approach to increase the thermal stability of P3HT:PC$_{61}$BM-based PSC systems made use of di-block copolymers as compatibilizers. It was shown that by adding to the P3HT:PC$_{61}$BM system an appropriate amphiphilic di-block copolymer incorporating fullerene and P3HT macromonomers, a reduction of the interfacial energy between donor and acceptor materials could be obtained. This resulted in a decrease in the rate of phase segregation in the blend and ultimately in increased thermal stability over time with respect to standard P3HT:PC$_{61}$BM devices.[25]

An alternative method to control and improve morphological stability of the active layer involved the use of a poly-(3-alkylthiophene)-based di-block copolymer containing a fullerene-functionalized block, employed as single active layer component in PSC devices. Although characterized by a significantly lower starting efficiency, PSC systems containing the fullerene-functionalized block copolymer exhibited better photovoltaic performance after prolonged high temperature annealing compared with control P3HT:PC$_{61}$BM devices. This result was attributed to the micro-phase separated structure of the di-block copolymer that is able to stabilize the film morphology upon annealing.[26]

The use of thermally crosslinkable fullerene derivatives containing glycidyl functionalities in the photoactive layer was found to effectively prevent phase segregation of PC$_{61}$BM and therefore allow the formation of a stable morphology of the active layer. However, the photovoltaic performance of the cells after crosslinking was significantly reduced with respect to the control system.[27] The same thermal crosslinking concept was employed more recently[28] for the synthesis of a poly(3-(5-hexenyl)thiophene) (P3HNT). Upon heating, the vinyl group of the polymer side chain was shown to undergo crosslinking thereby preventing the formation of large PC$_{61}$BM aggregates during prolonged high temperature annealing. Devices containing crosslinked P3HNT blended with PC$_{61}$BM showed slightly enhanced stability after annealing compared with standard P3HT:PC$_{61}$BM devices.

In the work by Kim et al.[29], a library of photocrosslinkable P3HT copolymers containing some light-sensitive bromoalkyl substituents was synthesized and used as p-type materials in BHJ devices. It was shown that after two days of annealing at an elevated temperature of 150 °C, devices containing the photocrosslinked polymer within the active layer were able to retain their initial power conversion efficiency (PCE). This result was attributed to the stabilizing effect of the photocrosslinked polymer on the nanoscale morphology of the active layer. In contrast to thermal crosslinking, photocrosslinking does not interfere with the thermal treatments that are often needed during device optimization;

thus, this process allows for morphology optimization with independent control of crosslinking and thermal annealing.

Although BHJ devices based on the P3HT:$PC_{61}BM$ blend still represent a benchmark for the PSC research community, new p-type polymers have recently been synthesized in an effort to improve device efficiency.[30,31] In particular, the target p-type polymer should ideally exhibit a broad absorption in the solar emission spectrum[32,33] and suitable energy levels to match those of the n-type molecule so as to maximize open circuit voltage and ensure efficient charge separation.[34-38] One strategy towards increasing low energy light absorption and modulating energy level alignment with the n-type material takes advantage of the donor-acceptor (D-A) approach, in which copolymerization of electron-rich and electron-poor monomers leads to the formation of low-bandgap polymers with optical and electronic properties that can be tuned via synthetic control of the electron-rich and electron-poor units. Using this concept, reports have demonstrated PCEs exceeding 7-8% after systematic optimization of the active layer morphology and appropriate device parameters.[39-44] Although an optimal active layer morphology is necessary to achieve such record PSC performance, its evolution during device operation is rarely considered. In particular, the morphological stability of PSCs based on D-A polymers at high temperatures still needs to be investigated in details and no examples of long-term thermally stable devices based on this class of high efficiency p-type polymers have been reported in the literature.

In this Section we report a study on long-term thermal stability of PSC devices based on D-A copolymers.[45] Through a new synthetic pathway, we have developed a photocrosslinkable derivative of the thieno[3,4-c]pyrrole-4,6-dione (TPD)-based polymer that was recently reported in the literature.[39,41] Different copolymers were prepared containing increasing amounts of photocrosslinkable moiety in order to study their effect on device performance. After thorough optimization of device parameters, photocrosslinked and non-photocrosslinked PSC devices were subjected to high-temperature (150 °C) annealing and their morphological and photovoltaic stability was investigated. In addition, the influence of n-type material on long-term thermal stability was also examined, by studying blends incorporating $PC_{61}BM$ or $PC_{71}BM$.

4.2 EXPERIMENTAL

4.2.1 Materials

All air-sensitive and moisture-sensitive reactions were performed under inert atmosphere with glassware that was oven and flame dried prior to use. All organic extracts were dried over powdered $MgSO_4$ and concentrated under reduced pressure with a rotary evaporator. Flash chromatography was performed using Merck Kieselgel 60 (230 - 400 mesh) silica. Dry tetrahydrofuran (THF) and N,N-dimethylmethanamide (DMF) were purchased from Fisher Scientific and passed through two packed columns of neutral alumina, under N_2 pressure. All reagents from commercial sources were used without further purification.

4.2.2 Instrumentation

All ^{1}H NMR and ^{13}C NMR spectra were obtained with a Bruker AVQ-400, AVB-400 or AV-600 instrument. ^{13}C spectra were measured with a proton-decoupling pulse program. Data from high-resolution mass spectrometry (HRMS) using electron impact (EI) were obtained by the UC Berkeley mass spectrometry facility.

For polymer molecular weight determination, polymer solutions (1 mg/mL) were prepared using HPLC grade chloroform ($CHCl_3$). Samples were briefly heated and then allowed to return to room temperature prior to filtering through a 0.45 μm PVDF filter. Size exclusion chromatography (SEC) was performed with HPLC grade $CHCl_3$ eluent at 1.0 mL/min by using three PLgel columns (7.5 x 300 mm) with pore sizes of 105, 103, and 500 Å, respectively. The particle size in columns was 5 μm and the columns were thermostated at 35 °C. The SEC system consisted of a Waters 510 pump, a Waters 717 autosampler, a Waters 486 UV-Vis detector, and a Wyatt Optilab DSP differential refractive index detector. The apparent molecular weights and polydispersities (Mw/Mn) were determined with a calibration based on linear polystyrene standards using Empower software from Waters.

UV–Vis absorption spectra were recorded on polymer thin films at room temperature using a Varian Cary 50 Conc UV-Visible spectrophotometer. The polymers were spin-coated on ITO-coated glass substrates from o-DCB solutions (15 mg/ml). The thickness of the thin films was measured by profilometry (Veeco Dektat 150) and determined to be 90 ±10 nm. A blank ITO-coated glass substrate was used as reference.

Tapping-mode atomic force microscopy (AFM) was performed on a Veeco Nanoscope V scanning probe microscope using RTESP tips.

4.2.3 Synthetic procedure

4.2.3.1 Synthesis of monomers

Monomers 2,6-bis(trimethyltin)-4,8-bis((2-ethylhexyl)oxy)benzo[1,2-b:4,5-b‘] dithiophene (BDT-EH) and 1,3-dibromo-5-octyl-4H-thieno[3,4-c]pyrrole-4,6(5H)-dione (TPD-O) (Figure 4.1) were synthesized and characterized as previously reported.[39]

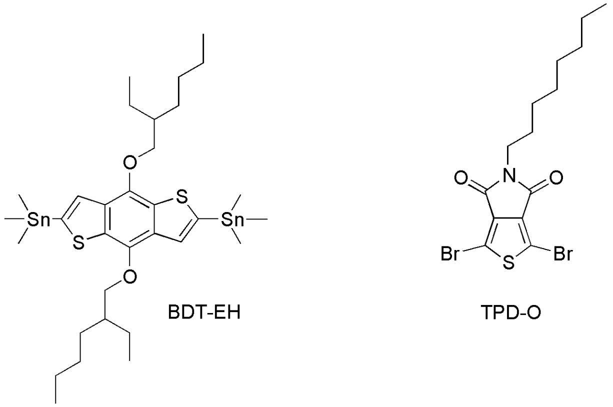

Figure 4.1 Monomers 2,6-bis(trimethyltin)-4,8-bis((2-ethylhexyl)oxy)benzo[1,2-b:4,5-b‘] dithiophene (BDT-EH, left) and 1,3-dibromo-5-octyl-4H-thieno[3,4-c]pyrrole-4,6(5H)-dione (TPD-O, right).

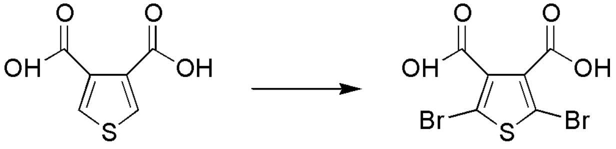

(1)

Scheme 4.1 Synthesis of 2,5-Dibromothiophene-3,4-dicarboxylic acid (1) from Thiophene-3,4-dicarboxylic acid.

2,5-Dibromothiophene-3,4-dicarboxylic acid (1) (Scheme 4.1).

Thiophene-3,4-dicarboxylic acid (20.0 g, 116 mmol), glacial acetic acid (120 mL) and bromine (23.9 mL, 74.3 g, 465 mmol) were combined and heated to 55 °C for 96 h. After cooling the reaction mixture to almost room temperature (RT), excess bromine was quenched with saturated $NaHSO_3$, until the reaction contents became nearly clear. The mixture was cooled to 4 °C and flakey beige solids crystallized from solution. The crystals were crushed during filtration and were washed with ice water to yield 2,5-dibromothiophene-3,4-dicarboxylic acid as a beige powder (22.0 g, 57 %). ^{13}C NMR (100 MHz, acetone-*d6*): δ (ppm) = 162.5, 135.9, 115.3. HRMS (EI, *m*/*z*): calculated for $C_6H_2Br_2O_4S$ [M]+: 329.8020; found, 329.7987.

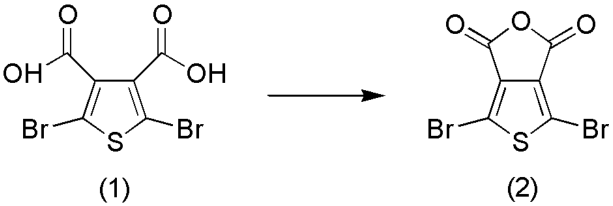

Scheme 4.2 Synthesis of 4,6-dibromothieno[3,4-c]furan-1,3-dione (2) from 2,5-Dibromothiophene-3,4-dicarboxylic acid.

4,6-dibromothieno[3,4-c]furan-1,3-dione (2) (Scheme 4.2).

2,5-Dibromothiophene-3,4-dicarboxylic acid (13.3 g, 40.3 mmol) was combined with acetic anhydride (110 mL) and stirred at 110 °C for 1 h. After cooling the reaction flask to RT, crystallization occurred. Pure crystals were obtained by filtration and washing with hexanes to yield 4,6-dibromothieno[3,4-c]furan-1,3-dione as off-white needles (10.9 g, 87 %). ^{13}C NMR (100 MHz, acetone-*d6*): δ (ppm) = 161.7, 135.0, 114.7. HRMS (EI, *m*/*z*): calculated for $C_6Br_2O_3S$ [M]+: 311.7914; found, 311.7919.

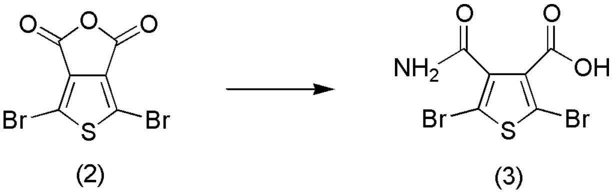

Scheme 4.3 Synthesis of 2,5-dibromo-4-carbamoylthiophene-3-carboxylic acid (3) from 4,6-dibromothieno[3,4-c]furan-1,3-dione.

2,5-dibromo-4-carbamoylthiophene-3-carboxylic acid (3) (Scheme 4.3).

4,6-dibromothieno[3,4-c]furan-1,3-dione (4.00 g, 12.8 mmol) was dissolved in dry THF (12 mL). Ammonia (7.54 mL of a 5.1 M solution in methanol, 38.5 mmol) was added to the flask and the reaction mixture was stirred at RT for 5 min. After removing volatile species in vacuo, water was added to the flask until the organic residue completely dissolved. The organic species was precipitated by dropwise addition of concentrated hydrochloric acid (3 mL) and then filtered to yield 2,5-dibromo-4-carbamoylthiophene-3-carboxylic acid as a white powder (3.68 g, 87%). ^{1}H NMR (400 MHz, DMSO-*d6*): δ (ppm) = 13.46 (s, 1 H), 7.86 (s, 1 H), 7.62 (s, 1 H). ^{13}C NMR (100 MHz, DMSO-*d6*): δ (ppm) = 163.7, 161.9, 140.9, 133.3, 116.2, 109.8. HRMS (EI, *m*/*z*): calculated for $C_6H_3Br_2NO_3S$ [M]+: 328.8180; found, 328.8179.

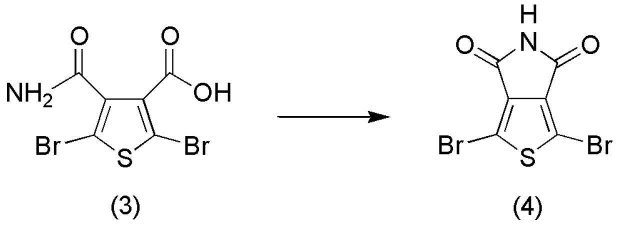

Scheme 4.4 Synthesis of 1,3-Dibromo-4H-thieno[3,4-c]pyrrole-4,6(5H)-dione (4) from 2,5-dibromo-4-carbamoylthiophene-3-carboxylic acid.

1,3-Dibromo-4H-thieno[3,4-c]pyrrole-4,6(5H)-dione (4) (Scheme 4.4).
Triethylamine (2.23 mL, 1.62 g, 16.0 mmol) and then carbonyldiimidazole (2.72 g, 16.8 mmol) were slowly added to a solution of 2,5-dibromo-4-carbamoylthiophene-3-carboxylic acid (5.26 g, 16.0 mmol) in dry THF (200 mL). After stirring for 12 h at RT, the reaction mixture was extracted with ethyl acetate (150 mL) and washed with 1.0 M aqueous $NaHSO_4$ (3 x 200 mL). The organic layer was dried, filtered and concentrated to yield 1,3-dibromo-4H-thieno[3,4-c]pyrrole-4,6(5H)-dione as a fine white solid (4.62 g, 93%). ^{1}H NMR (500 MHz, DMSO-*d6*): δ (ppm) = 11.57 (s, 1 H). ^{13}C NMR (125 MHz, DMSO-*d6*): δ (ppm) = 161.0, 136.0, 112.5. HRMS (EI, *m*/*z*): calculated for $C_6HBr_2NO_2S$ [M]+: 310.8074; found, 310.8080.

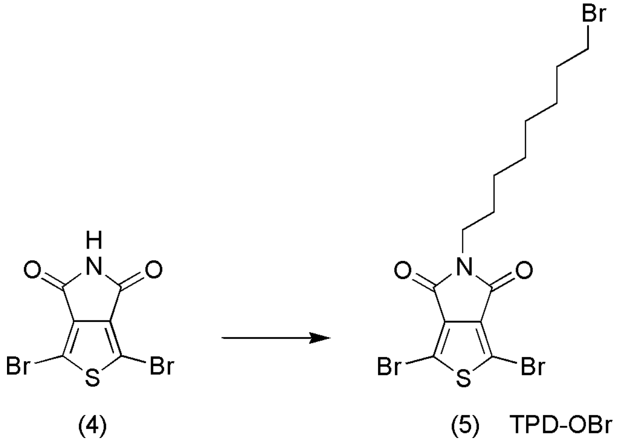

Scheme 4.5 Sinthesis of 1,3-dibromo-5-(8-bromooctyl)-4H-thieno[3,4-c]pyrrole-4,6(5H)-dione (5, TPD-OBr) from 1,3-Dibromo-4H-thieno[3,4-c]pyrrole-4,6(5H)-dione.

1,3-dibromo-5-(8-bromooctyl)-4H-thieno[3,4-c]pyrrole-4,6(5H)-dione (5) (Scheme 4.5).
1,3-Dibromo-4H-thieno[3,4-c]pyrrole-4,6(5H)-dione (1.00 g, 3.22 mmol) was dissolved in dry DMF (6 mL) and combined with sodium hydride (0.100 g, 4.18 mmol). The reaction contents were stirred at RT for 1 h and then added dropwise to a 50 °C solution of 1,8-dibromooctane (2.62 g, 9.65 mmol) in dry DMF (10 mL). After stirring for 12 h at RT, the reaction mixture was extracted with ether (50 mL) and washed with water (3 x 50 mL). The organic layer was dried, filtered,

concentrated and purified by column chromatography on silica gel with a mixed mobile phase of $CHCl_3$ and hexanes (80:20). Further purification of the organic extract by recrystallization in methanol and $CHCl_3$ yielded 1,3-dibromo-5-(8-bromooctyl)-4H-thieno[3,4-c]pyrrole-4,6(5H)-dione (TPD-OBr) as flakey, light yellow crystals (0.534 g, 33%). ^{1}H NMR (400 MHz, $CDCl_3$): δ (ppm) = 3.59 (t, J = 7.25 Hz, 2 H), 3.39 (t, J = 6.84 Hz, 2 H), 1.83 (m, 2 H), 1.62 (m, 2 H), 1.41 (m, 2 H), 1.32 (m, 6 H). ^{13}C NMR (100 MHz, $CDCl_3$): δ (ppm) = 160.5, 134.9, 113.1, 38.9, 34.2, 32.8, 29.0, 28.7, 28.3, 28.2, 26.8. HRMS (EI, *m/z*): calculated for $C_{14}H_{16}Br_3NO_2S$ [M]+: 500.8431; found, 500.8438.

4.2.3.2 Representative synthesis of copolymers

BDT-EH (200 mg, 259 μmol), TPD-O (91.3 mg, 216 μmol), TPD-OBr (21.7 mg, 43.2 μmol), tris(dibenzylideneacetone)dipalladium(0) (7.11 mg, 7.77 μmol) and tri-o-tolylphosphine (9.46 mg, 31.1 μmol) were combined and then cycled 3 times with vacuum and nitrogen. The reagents were dissolved in dry chlorobenzene (6.0 mL) and stirred at 110 °C for 36 h. A strong complexing ligand (N,N-diethyl-2-phenyldiazenecarbothioamide, 17.0 mg, 76.8 μmol mmol) was added to the reaction mixture to remove residual catalyst before precipitating the reaction contents into methanol (200 mL). The precipitate was filtered through a Soxhlet thimble and purified via Soxhlet extraction for 2 h with methanol, 2 h with methylene chloride and was finally collected in chlorobenzene. The chlorobenzene solution was then purified by column chromatography on mixed column of silica gel, Celite and neutral alumina with a mobile phase of warm chloroform. The eluted purple solution was finally concentrated in vacuo, precipitated into methanol (200 mL) and filtered to yield p(BDT/TPD-Br16) (from here on referred to as TPD-Br16) as a dark purple solid (179 mg, 96 %). SEC analysis: Mn = 30.3 kDa, Mw = 71.1 kDa, PDI = 2.35.

4.2.4 Polymer photocrosslinking

Photocrosslinking was carried out in a nitrogen-filled glove box by irradiating the polymer films with UV light (λ = 254 nm) from a low-power lamp (2.1 - 2.4 mW cm^{-2}) with exposure times ranging from 0 to 45 min. To evaluate the extent of photocrosslinking, the irradiated polymer films were immersed into chlorobenzene for 5 min, followed by rinsing with acetone for 3 minutes and then dried under a stream of nitrogen. UV-Vis absorption spectra of the polymer films were then recorded after irradiation and solvent washing, and compared to the UV-Vis absorption spectra of the same polymer films prior to irradiation.

4.2.5 Device fabrication and testing

All devices were fabricated on ITO-coated glass substrates (pre-patterned,R = 20 $\Omega\square^{-1}$, Thin Film Devices, Inc.). The substrates were firstly ultrasonicated in 2% Hellmanex soap water for 20 min, and then subjected to successive ultrasonication in de-ionized water (20 min), acetone (20 min) and isopropyl alcohol (20 min). The substrates were then dried under a stream of nitrogen. A thin-layer (40 nm) of filtered PEDOT:PSS (Baytron PH) was spin-coated onto UV-ozone treated ITO substrates at 4000 RPM for 40 s followed by baking at 140 °C for 15 min in air. All substrates were then moved to a nitrogen-filled glove box to perform all the following fabrication steps. Solutions of the polymers (p(BDT/TPD-Br0) - from here on referred to as TPD-Br0, TPD-Br16 or p(BDT/TPD-Br33) - from here on referred to as TPD-Br33, 15 mg/mL) and fullerene molecules ($PC_{61}BM$ or $PC_{71}BM$, 40 mg/mL) in o-dichlorobenzene (o-DCB) were prepared separately and stirred overnight at 110 °C. The solutions were passed through a 0.45 μm polytetrafluoroethylene filter, prior to the preparation of the blend solutions. The polymer:fullerene blend solutions were spin-coated onto the substrate for 40 sec at 1200 RPM followed by 4 sec at 2000 RPM to produce films with thickness of 90-100 nm. UV-mediated photocrosslinking was then performed on the TPD-Br16:fullerene and TPD-Br33:fullerene cast films, by irradiating them with a low-power UV lamp at 254 nm (UV light intensity: 2.1 - 2.4 mW cm^{-2}). The cathode, consisting of Ca (20nm) and Al (100 nm), was then deposited by thermal evaporation under vacuum (~ 10^{-7} torr) through a shadow mask defining an active device area of 0.03 cm2. The layout of the shadow mask afforded eight independent devices on each substrate. In order to carry out the thermal stability tests, thermal annealing was performed on complete devices on a temperature-controlled hot plate at 150 °C. Devices were left to cool down to room temperature before testing. The current-voltage (J-V) curves were measured using a Keithley 2400 source-measure unit under AM 1.5G solar illumination at 100 mW cm^{-2} (1 sun) using a Thermal-Oriel 150 W solar simulator. During device optimization, different concentrations for the blend solutions and different polymer:acceptor ratios were tested in order to obtain the optimized process conditions, and the experiments were repeated multiple times to ensure data reproducibility.

4.3 RESULTS AND DISCUSSION

The structure of the newly synthesized polymers employed in this study is presented in Figure 4.2. The polymers contain TPD repeat units with a terminal, primary bromine functionality appended to the octyl solubilizing group, that allows photocrosslinking of the polymer in the PSC devices. By selectively varying the amount of bromine-functionalized TPD units (TPD-OBr) during polymer synthesis, different polymers were prepared: 0% TPD-OBr units (TPD-Br0), 16% TPD-OBr units (TPD-Br16), and 33% TPD-OBr units (TPD-Br33).

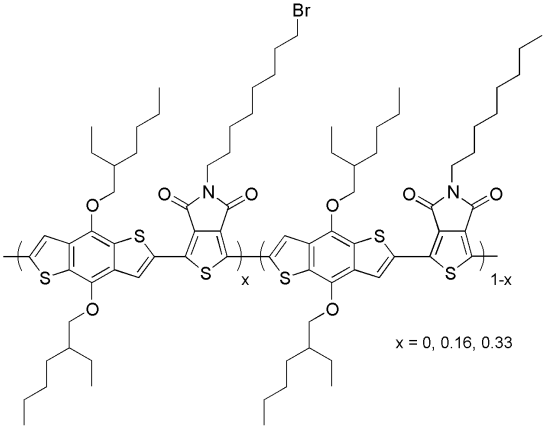

Figure 4. 2 Molecular structure of the polymers presented in this Chapter.

After optimization of the photocrosslinking conditions, each polymer was incorporated in BHJ with an n-type fullerene derivative (either $PC_{61}BM$ or $PC_{71}BM$) and the PSC devices fabricated thereafter were tested against long-term thermal stability with and without photocrosslinking of the active layer.

4.3.1 UV-Vis absorption spectroscopy

The normalized UV-Vis absorption spectra of the as-cast TPD-Br0, TPD-Br16 and TPD-Br33 polymers are shown in Figure 4.3. All polymers exhibit three maxima between 400 nm and 700 nm, in accordance with previous reports.[39,41] Furthermore, no major differences can be observed between the absorption spectra of the three polymers, indicating that their optical properties are not significantly affected by the addition of Br-units to the polymer.

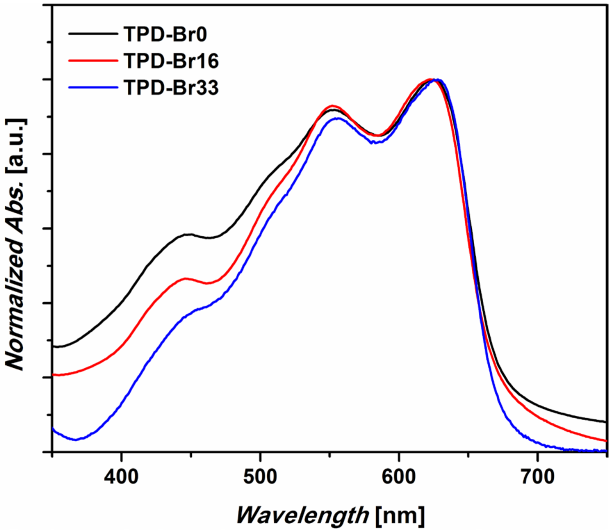

Figure 4.3 Normalized absorption spectra of polymer films without Br substituents (TPD-Br0), and with 16% (TPD-Br16) and 33% (TPD-Br33) Br substituents in the polymer chain.

4.3.2 UV-mediated photocrosslinking of polymer thin films

Figure 4.4 shows the UV-Vis absorption spectra of TPD-Br16 films as-cast and after UV-mediated photocrosslinking at increasing UV-irradiation times.

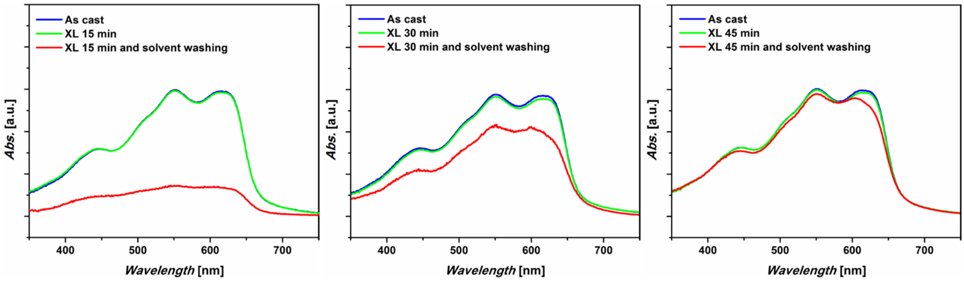

Figure 4.4 Absorption spectra of TPD-Br16 polymer films pristine (as cast), after UV-irradiation (photocrosslinking (XL)), and after UV-irradiation and solvent washing (XL and solvent washing): a) 15 min of UV-exposure, b) 30 min of UV-exposure, c) 45 min of UV-exposure.

By increasing the UV-exposure time, the solvent resistance of the polymer film is progressively improved. After 45 min of UV irradiation, the polymer film appears fully resistant to solvent washing (Figure 4.4c). The absorption intensity at 550 nm after UV-irradiation and washing with solvent differs by less than 4% from the absorption intensity of the as-cast film, indicating that photocrosslinking has occurred. In addition no major differences in the absorption spectra of as-cast and photocrosslinked films are observed, indicating that the photocrosslinking process does not significantly affect the optical properties of the solid state polymer.

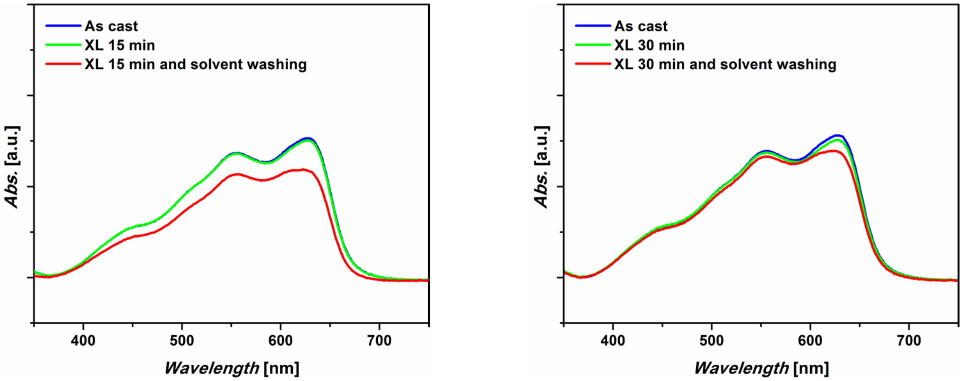

Figure 4.5 Absorption spectra of TPD-Br33 polymer films pristine (as cast), after UV-irradiation (photocrosslinking (XL)), and after UV-irradiation and solvent washing (XL and solvent washing): a) 15 min of UV-exposure, b) 30 min of UV-exposure.

As evidenced in Figure 4.5, a similar trend is observed for the TPD-Br33 polymer films. However in this case the same level of solvent resistance is achieved after a shorter UV exposure time (30 min), suggesting that a higher density of photocrosslinking moiety in the polymer structure enables a faster photocrosslinking process to occur.

Neither TPD-Br16 nor TPD-Br33 showed any resistance to solvent washing after thermal annealing only, indicating that thermal crosslinking does not take place in these systems.

The control polymer TPD-Br0 containing no Br units did not undergo photocrosslinking when irradiated with UV light, as evidenced by the poor resistance to solvent washing even after prolonged exposure to a UV light source.

4.3.3 Optimization of photocrosslinked PSC devices

The performance of the PSC devices incorporating the photocrosslinkable polymers was investigated using the indium tin oxide (ITO)/poly(3,4-ethylenedioxythiophene) (PEDOT):poly(styrenesulfonate) (PSS)/polymer:fullerene/Ca/Al device architecture. Optimization of device parameters is presented in this Section.

4.3.3.1 Photocrosslinked TPD-Br16:$PC_{61}BM$ devices

A systematic study on different device parameters was carried out on photocrosslinked devices (45 min UV-exposure, see Section 4.3.2) in order to achieve optimal PV performance. Figure 4.6 shows the J-V characteristics of TPD-Br16:$PC_{61}BM$ devices at varying polymer:$PC_{61}BM$ weight ratio. By increasing the amount of fullerene acceptor in the active layer blend, an increase in power conversion efficiency is observed (from 2.44% in the 1:1.5 blend to 3.31% in the 1:2.5 blend), mainly resulting from an increase in fill factor and current density. This trend may be related to the intercalation of the fullerene molecules in the available spaces between the polymer side chains.[46-48] When intercalation occurs, a high level of fullerene-loading in the active blend is necessary to create a pure electron-transporting fullerene phase that yields the phase separation needed for efficient BHJ devices. Therefore, in systems where intercalation is expected to occur, optimum blend ratios close to 1:3 polymer:fullerene are generally found, in contrast to an optimum near 1:1 in systems where intercalation cannot occur.

A further increase in fullerene content was found to cause a decrease in PCE, likely due to the proportional decrease in the amount of light-absorbing phase (the conjugated polymer) where exciton generation occurs.

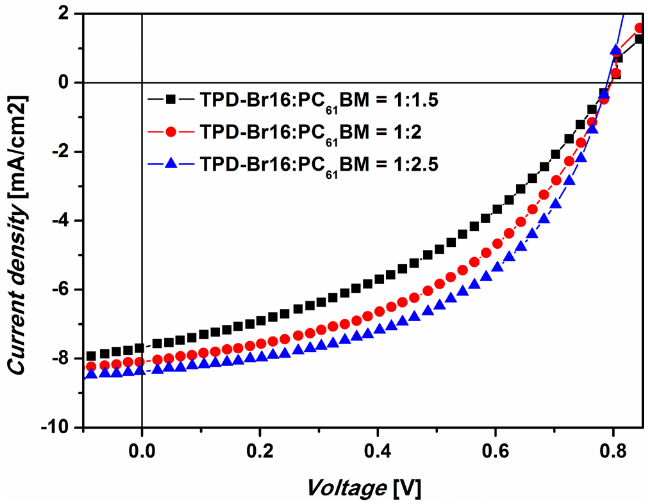

Figure 4.6 Current-voltage (J-V) curves of TPD-Br16:$PC_{61}BM$ devices at varying polymer:$PC_{61}BM$ ratio. The active layer blend concentration is 24 mg/mL for all devices.

The effect of active layer thickness on device performance was explored by varying the active layer blend concentration (see Figure 4.7). After an increase in concentration from 24 mg/mL to 26 mg/mL a slight reduction of PCE is observed (down to 2.92%), likely due to the emergence of resistances within the active layer that are detrimental to charge transport.

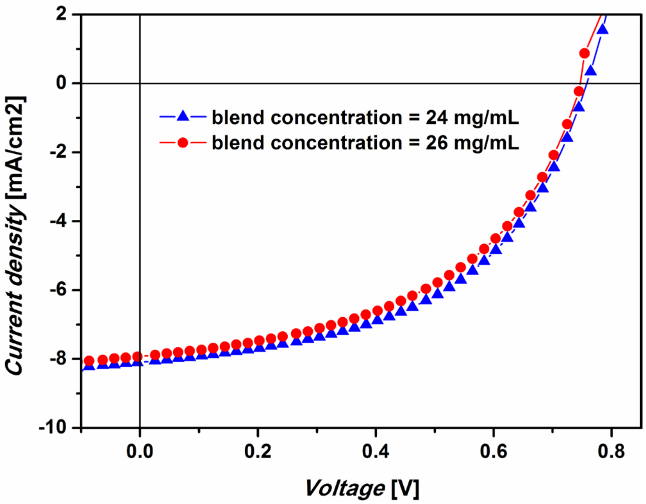

Figure 4.7 J-V curves of TPD-Br16:PC$_{61}$BM devices at varying active layer blend concentration. The polymer:PC$_{61}$BM ratio is 1:2.5 for all devices.

In order to optimize the active layer morphology, several processing techniques have been reported.[13] Among these techniques, the incorporation of high boiling-point solvent additives into the polymer:fullerene solution has shown promising results.[49-51]

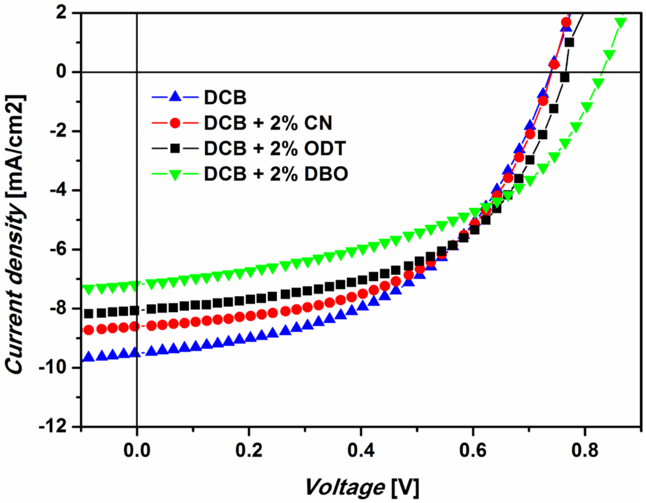

Figure 4.8 J-V curves of TPD-Br16:PC$_{61}$BM devices with active layer processed from different solvent systems.

To test this approach on our system, different high boiling-point solvents were considered in conjunction with o-dichlorobenzene (DCB), namely chloronaphthalene (CN), octane-di-thiol (ODT) and di-bromo-octane (DBO).

As shown in Figure 4.8, no significant improvements in PCE were obtained by employing solvent additives in the active layer blend solution. In particular, the best PV performance was found for devices containing DCB only, suggesting that neither the selective solubility of the fullerene component in the specific solvent additive (in the case of ODT and DBO) nor the reduction of evaporation kinetics (in the case of CN) can effectively act on the nanoscale phase segregation of the active layer to lead control of film morphology and enhanced device performance. Therefore, no solvent additives were employed in the optimized devices during thermal annealing studies.

In summary, optimization of photocrosslinked TPD-Br16:$PC_{61}BM$ devices led to an optimal polymer:$PC_{61}BM$ ratio of 1:2.5 and an active layer blend concentration of 24 mg/mL.

4.3.3.2 Photocrosslinked TPD-Br33:$PC_{61}BM$ devices

Following the methodology used for TPD-Br16:$PC_{61}BM$ devices, optimization of device parameters for the photocrosslinked TPD-Br33:$PC_{61}BM$ blend was also carried out.

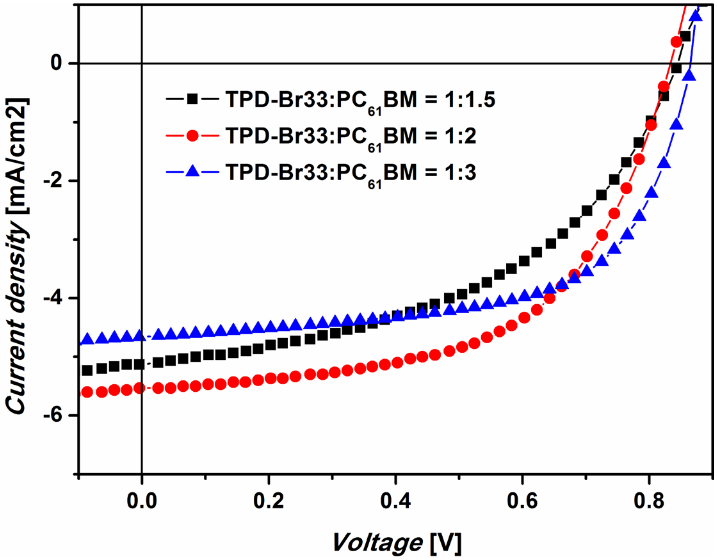

Figure 4.9 J-V curves of TPD-Br33:$PC_{61}BM$ devices at varying polymer:$PC_{61}BM$ ratio. The active layer blend concentration is 20 mg/mL for all devices.

As inferred from Figure 4.9 and Figure 4.10, an optimal polymer:$PC_{61}BM$ ratio of 1:2 was found for TPD-Br33:$PC_{61}BM$ devices with an optimal active layer blend concentration of 24 mg/mL. As for TPD-Br16:$PC_{61}BM$ devices, the use of solvent additives did not give any efficiency improvement also in the case of the TPD-Br33:$PC_{61}BM$ blend.

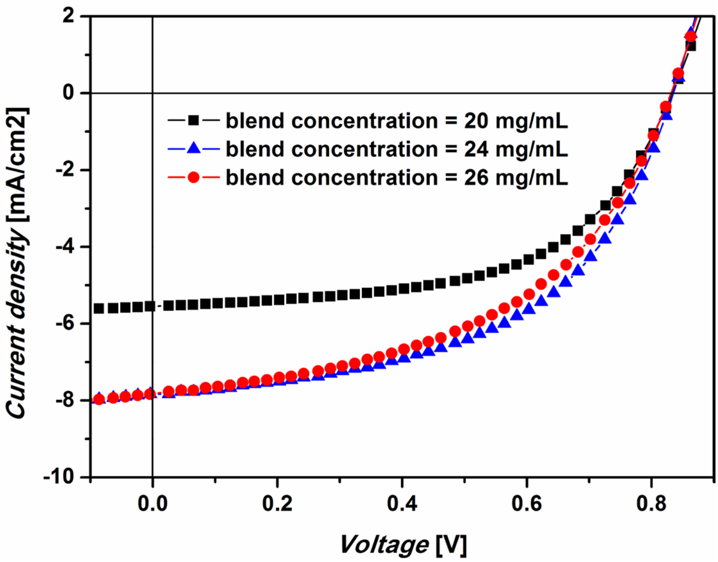

Figure 4.10 J-V curves of TPD-Br33:$PC_{61}BM$ devices at varying active layer blend concentration. The polymer:PC61BM ratio is 1:2 for all devices.

4.3.3.3 TPD-Br0:$PC_{61}BM$ devices

The optimal device parameters for the control polymer TPD-Br0 in BHJ with $PC_{61}BM$ were taken from recent literature reports[39] and yielded a PCE of 5.7%. No high boiling point solvent additives were employed in TPD-Br0:$PC_{61}BM$ control devices in order to ensure the same fabrication conditions for all polymers under test.

4.3.3.4 Photocrosslinked TPD-Br16:$PC_{71}BM$ devices

In order to evaluate the effect of fullerene acceptor on device efficiency and ultimately on thermal stability, the device optimization process was extended to blends constituted by photocrosslinked polymers and $PC_{71}BM$.Therefore, TPD-Br16:$PC_{71}BM$ ratio and active layer blend concentration were varied in order to achieve the best performance in photocrosslinked devices.

Figure 4.11 shows that an optimal ratio of 1:2 is found for the TPD-Br16:$PC_{71}BM$ system. Similarly to what observed for the TPD-Br16:$PC_{61}BM$ blend, an optimal active layer blend concentration of 24 mg/mL is found for TPD-Br16:$PC_{71}BM$ devices (see Figure 4.12), suggesting that the optimal active layer thickness is in this case independent of fullerene acceptor type.

No high boiling-point solvent additives were used in optimized devices, as they did not yield any improvement to device performance.

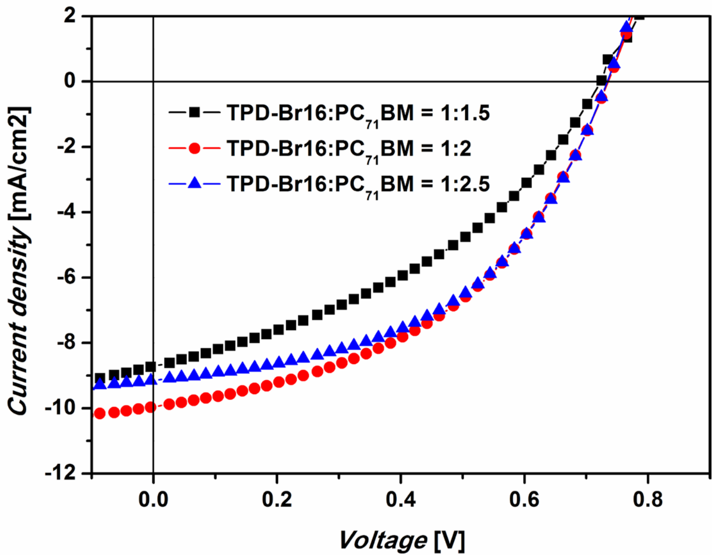

Figure 4.11 J-V curves of TPD-Br16:$PC_{71}BM$ devices at varying polymer:$PC_{71}BM$ ratio. The active layer blend concentration is 24 mg/mL for all devices.

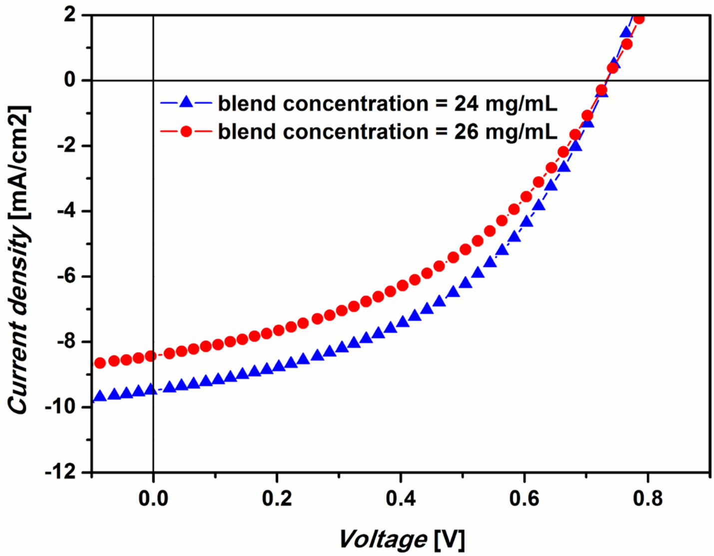

Figure 4.12 J-V curves of TPD-Br16:$PC_{71}BM$ devices at varying active layer blend concentration. The polymer:$PC_{71}BM$ ratio is 1:2 for all devices.

4.3.3.5 Photocrosslinked TPD-Br33:$PC_{71}BM$ devices

The same optimization procedure shown earlier was also employed for photocrosslinked TPD-Br33:$PC_{71}BM$ devices and the results are shown in Figure 4.13 and Figure 4.14.

The best device performance was found for a polymer:PC$_{71}$BM ratio of 1:2.5 and an active layer blend concentration of 24 mg/mL. Also in this case, no solvent additives were employed in the active layer blend as they did not give any efficiency improvement.

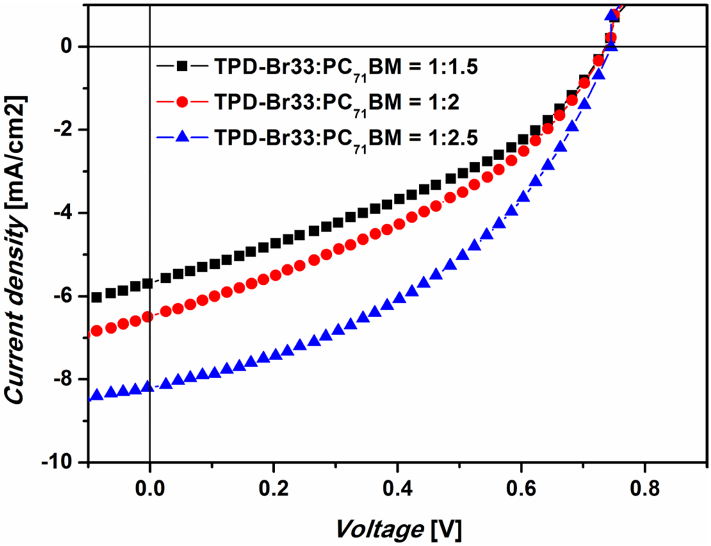

Figure 4.13 J-V curves of TPD-Br33:PC$_{71}$BM devices at varying polymer:PC$_{71}$BM ratio. The active layer blend concentration is 24 mg/mL for all devices.

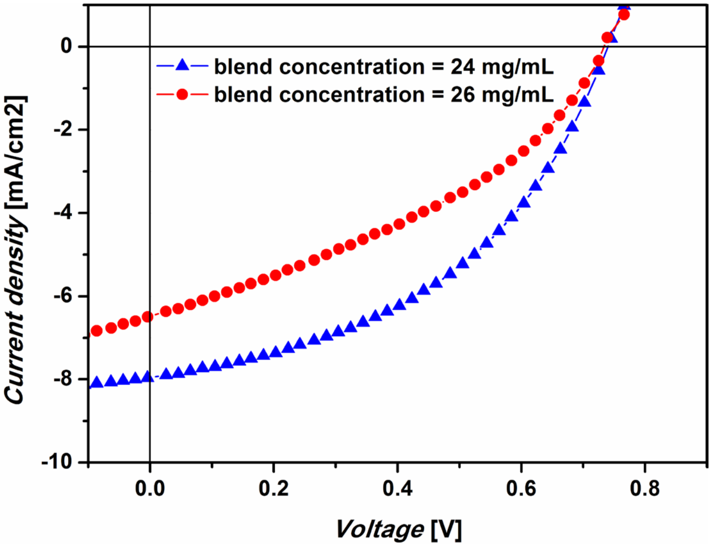

Figure 4.14 J-V curves of TPD-Br33:PC$_{71}$BM devices at varying active layer blend concentration. The polymer:PC$_{71}$BM ratio is 1:2.5 for all devices.

4.3.3.6 TPD-Br0:$PC_{71}BM$ devices

The optimal parameters for the control TPD-Br0:$PC_{71}BM$ devices were taken from recent literature reports[41] and yielded a PCE of 5.3%. No solvent additives were employed in TPD-Br0:$PC_{71}BM$ control devices in order to ensure the same fabrication conditions for all polymers under test.

4.3.4 Thermal stability of polymer:$PC_{61}BM$ devices

The thermal stability of TPD-Br16:$PC_{61}BM$ devices is shown in Figure 4.15, where the performance of both photocrosslinked (TPD-Br16 XL) and non-photocrosslinked (TPD-Br16 no XL) devices are shown. For comparison, the thermal stability of control devices TPD-Br0 is also shown. The average device parameters at 0 h and 72 h annealing are listed in Table 4.1. The initial performance of TPD-Br16 no XL devices (4.1% PCE) is slightly lower than TPD-Br0 devices (5.7% PCE), suggesting that the introduction of a terminal alkyl-bromine functionality on the solubilizing group of TPD affects the PV performance of the PSC devices at this incorporation ratio. Furthermore, TPD-Br16 XL devices show an even lower initial PCE (2.5%) with respect to both TPD-Br0 and TPD-Br16 no XL. This can be attributed to the effect of crosslinking on the π-stacking of the polymer chains, affecting the electronic properties of the polymer and the PSC device performance.[39]

However, large differences are observed in the PV response of devices upon exposure to heat: while both TPD-Br0 and TPD-Br16 no XL show a sharp decrease in performance upon thermal annealing over time, devices containing the photocrosslinked polymer (TPD-Br16 XL) show a peak PCE after 30 min of annealing followed by a rather stable PCE throughout the entire annealing time. This behaviour may be explained by considering the ability of $PC_{61}BM$ molecules to diffuse within the crosslinked polymer network during the annealing process.

Their motion can initially provide favourable conditions for charge separation and transport leading to a substantial increase in PCE in the first 30 min of annealing. Longer annealing times may lead to the formation of aggregates in the active layer that are detrimental to charge transport and cause a decrease in PCE. However, the crosslinked polymer network in TPD-Br16 XL devices prevents complete disruption of the active layer morphology during annealing thus allowing a relatively constant PCE to be maintained over the annealing time. These observations will be further clarified in the next section (see Section 4.3.9), where characterization the surface morphology of active layer in TPD-Br16 devices will be presented.

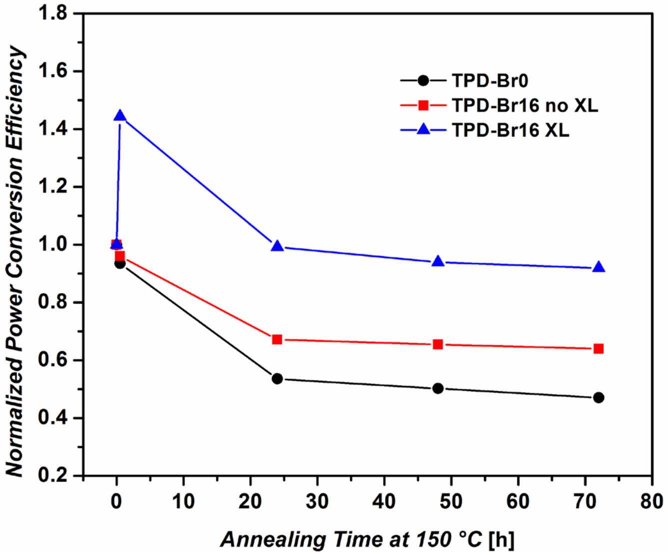

Figure 4.15 Normalized power conversion efficiencies of TPD-Br0, non-photocrosslinked TPD-Br16 and photocrosslinked TPD-Br16 devices during long-term thermal annealing at 150 °C with $PC_{61}BM$ as n-type material. The efficiency of each device was normalized to its initial efficiency (at annealing time 0 h). The same blend concentration (24 mg/mL in dichlorobenzene) was used for all devices. The polymer:$PC_{61}BM$ ratio was 1:2 for TPD-Br0 devices and 1:2.5 for both non-photocrosslinked and photocrosslinked TPD-Br16 devices.

Table 4.1 Characteristic photovoltaic parameters for TPD-Br0:$PC_{61}BM$ and TPD-Br16:$PC_{61}BM$ devices.

	XL[a)]	Annealing Time t_A [h]	J_{SC} [mA/ cm^2]	V_{OC} [V]	FF [%]	PCE (PCEmax) [%]
TPD_Br0	-	0	-10.6	0.79	67	5.7 (5.7)
TPD_Br0	-	72	-6.7	0.91	44	2.7 (2.7)
TPD_BR16	-	0	-9.6	0.72	59	4.1 (4.2)
TPD_Br16	-	72	-6.5	0.91	44	2.6 (2.6)
TPD_Br16	+	0	-7.2	0.77	45	2.5 (2.6)
TPD_Br16	+	72	-5.2	0.95	46	2.3 (2.3)

[a)] Active layers not subjected (-) and subjected (+) to crosslinking under UV-irradiation prior to cathode deposition.

The evolution of device performance with annealing time for the three systems reported in Figure 4.15 can be better understood by analyzing the J-V output characteristics recorded at annealing times 0 h and 72 h at 150 °C (see Figure 4.16).

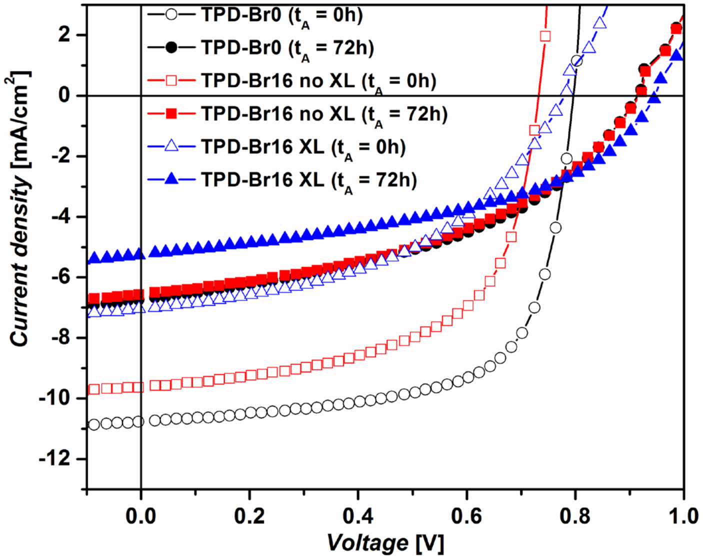

Figure 4.16 J-V curves of the best TPD-Br16:$PC_{61}BM$ PSC devices before (hollow symbols, t_A = 0 h) and after (full symbols, t_A = 72 h) long-term thermal annealing (t_A).

An increase in the V_{OC} is observed for all devices after 72 h of annealing at high temperature. This increase may be related to a change in the energy of the interfacial charge-transfer states between polymer and fullerene caused by morphological rearrangement of the fullerene molecules adjacent to the polymer chains after annealing.[37,52] In opposition, a significant decrease in the short-circuit current density (approximately 35% decrease) and fill factor during annealing is observed for both TPD-Br0 and TPD-Br16 no XL devices, which yields a strong drop of PCE with respect to the initial values. Instead, TPD-Br16 XL devices show a less sharp decrease of J_{SC} after 72 h of annealing at 150 °C (25% drop), while the fill factor increases slightly compared to its initial value. This suggests that photocrosslinking allows the preservation of a favourable active layer morphology throughout the annealing process, that ultimately leads to thermally stable PSC devices.

As shown in Figure 4.17 and Figure 4.18, similar trends were observed for the TPD-Br33:$PC_{61}BM$ system. A summary of the characteristic PV parameters for TPD-Br33:$PC_{61}BM$ devices is given in Table 4. 2.

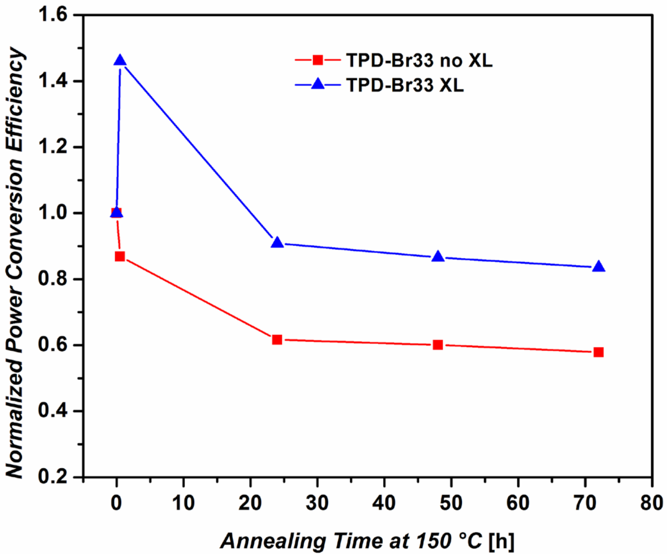

Figure 4.17 Normalized power conversion efficiencies of non-photocrosslinked TPD-Br33 and photocrosslinked TPD-Br33 devices during long-term thermal annealing at 150 °C with $PC_{61}BM$ as n-type material. The efficiency of each device was normalized to its initial efficiency (at annealing time 0 h). The same blend concentration (24 mg/mL in dichlorobenzene) was used for all devices. The polymer:$PC_{61}BM$ ratio was 1:2 for all devices.

Table 4.2 Characteristic photovoltaic parameters for TPD-Br33:$PC_{61}BM$ devices.

	XL[a)]	Annealing Time t_A [h]	J_{SC} [mA/cm^2]	V_{OC} [V]	FF [%]	PCE (PCEmax) [%]
TPD-Br33	-	0	-9.4	0.73	66	4.5 (4.6)
TPD-Br33	-	72	-6.2	0.92	46	2.6 (2.7)
TPD-Br33	+	0	-7.3	0.77	46	2.6 (2.8)
TPD-Br33	+	72	-5.6	0.91	43	2.2 (2.3)

[a)] Active layers not subjected (-) and subjected (+) to crosslinking under UV-irradiation prior to cathode deposition.

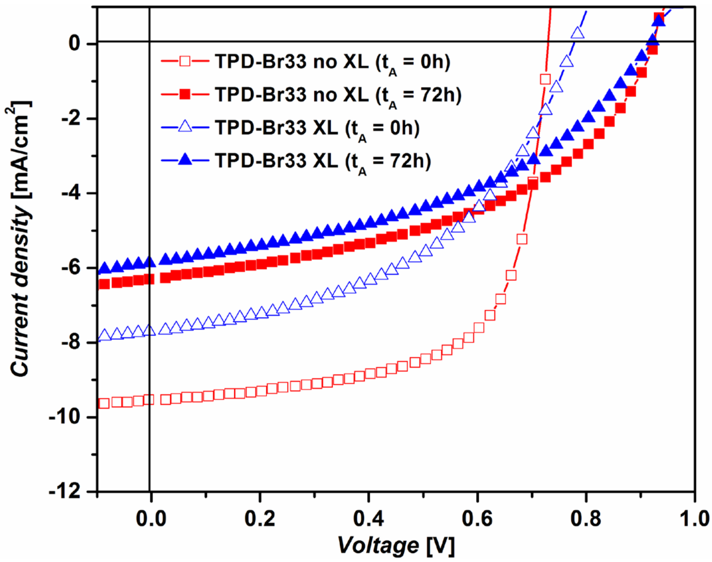

Figure 4.18 J-V curves of the best TPD-Br33:$PC_{61}BM$ PSC devices before (hollow symbols, t_A = 0 h) and after (full symbols, t_A = 72 h) long-term thermal annealing (t_A).

4.3.5 Thermal stability of polymer:PC71BM devices

Figure 4.19 shows the normalized power conversion efficiency of photocrosslinked TPD-Br16 devices (TPD-Br16 XL), compared with the performances of both non-photocrosslinked (TPD-Br16 no XL) and control (TPD-Br0) devices, with $PC_{71}BM$ as electron acceptor. The average device parameters at 0 h and 72 h annealing are listed in Table 4.3. The initial performance of TPD-Br16 no XL devices (5.6% PCE) is comparable to that of TPD-Br0 devices (5.2% PCE), suggesting that the improved light absorption given by $PC_{71}BM$ compared with $PC_{61}BM$ positively counteracts the detrimental effects on device performance resulting from the introduction of a bromine functionality on the solubilizing chain of the TPD group. On the other hand, TPD-Br16 XL devices show a significantly lower initial PCE (3.3%) with respect to both TPD-Br0 and TPD-Br16 no XL. The same effect was observed in $PC_{61}BM$ devices and it was attributed to a disruption of the π-stacking of the polymer chains due to polymer crosslinking.[39] However, a striking difference is observed between TPD-Br16 XL and the other two devices upon exposure to heat: while both TPD-Br0 and TPD-Br16 no XL devices undergo a sharp decrease in performance upon thermal annealing over time, TPD-Br16 XL devices show an increase in PCE, which stabilizes after 24 h of annealing. A maximum PCE as high as 4.7% is obtained for the crosslinked polymer after 72 h of annealing at 150 °C. As opposed to BHJs containing photocrosslinked polymer and $PC_{61}BM$, the high PCE achieved during the first annealing hours in $PC_{71}BM$ devices is maintained over the entire annealing time.

The J-V curves recorded at annealing times 0 h and 72 h at 150 °C for the three systems reported in Figure 4.19 are presented in Figure 4.20. Similarly to what found for $PC_{61}BM$ devices, an increase in the V_{OC} is observed for all devices after 72 h of annealing at high temperature. In addition, both TPD-Br0 and TPD-Br16 no XL devices undergo a significant decrease in their short-circuit current density and fill factor during annealing, which results in a sharp decrease of PCE with respect to the initial values. Conversely, the J_{SC} of TPD-Br16 XL devices remains constant, even after 72 h of annealing at 150 °C, while the fill factor increases about 18% compared to its initial value. This indicates that photocrosslinking has allowed for an optimal morphology of the active layer to be preserved throughout the entire annealing process, thus leading to remarkable long-term thermal stability of these devices.

In order to better clarify the different behaviour found for polymer:$PC_{61}BM$ blends compared to polymer:$PC_{71}BM$ blends, surface analysis on the active layer morphology was carried out and will be presented in Section 4.3.9.

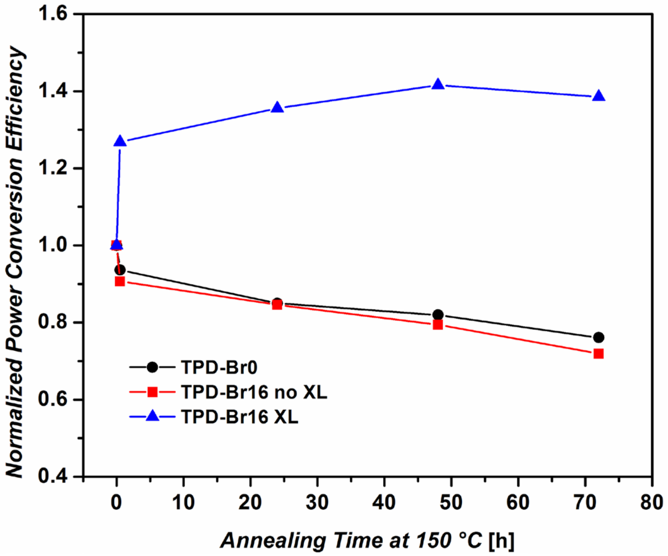

Figure 4.19 Normalized power conversion efficiencies of TPD-Br0, non-photocrosslinked TPD-Br16 and photocrosslinked TPD-Br16 devices during long-term thermal annealing at 150 °C with $PC_{71}BM$ as n-type material. The efficiency of each device was normalized to its initial efficiency (at annealing time 0 h). The same blend concentration (24 mg/mL in dichlorobenzene) and polymer:$PC_{71}BM$ ratio was used for all devices.

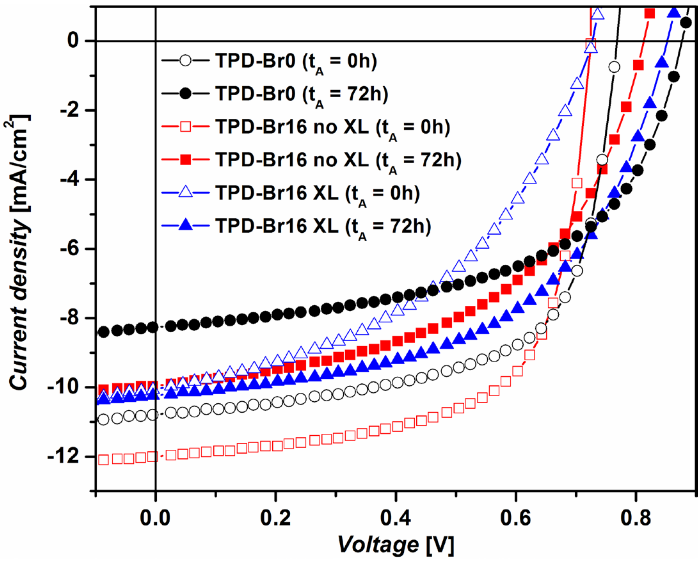

Figure 4.20 J-V curves of the best TPD-Br16:$PC_{71}BM$ PSC devices before (hollow symbols, t_A = 0 h) and after (full symbols, t_A = 72 h) long-term thermal annealing (t_A).

Table 4.3 Characteristic photovoltaic parameters for TPD-Br0:$PC_{71}BM$ and TPD-Br16:$PC_{71}BM$ devices.

	XL a)	Annealing Time t_A [h]	J_{SC} [mA/cm^2]	V_{OC} [V]	FF [%]	PCE (max) [%]
TPD_Br0	-	0	-10.6	0.76	64	5.2 (5.3)
TPD-Br0	-	72	-8.2	0.87	55	3.9 (4.1)
TPD-BR16	-	0	-11.7	0.73	66	5.6 (5.7)
TPD-Br16	-	72	-9.6	0.81	51	4.0 (4.2)
TPD-Br16	+	0	-10.0	0.73	45	3.3 (3.3)
TPD-Br16	+	72	-10.1	0.85	53	4.6 (4.7)

a)Active layers not subjected (-) and subjected (+) to crosslinking under UV-irradiation prior to cathode deposition.

Similar trends were found for TPD-Br33 devices, although lower PCEs with respect to TPD-Br16 were observed for both the non-photocrosslinked and the photocrosslinked systems (see Figure 4.21, Figure 4.22 and Table 4.4). This indicates that, in the case of $PC_{71}BM$ blends, judicious control of photocrosslinkable moiety content in the polymer is necessary to ensure optimal PV performances.

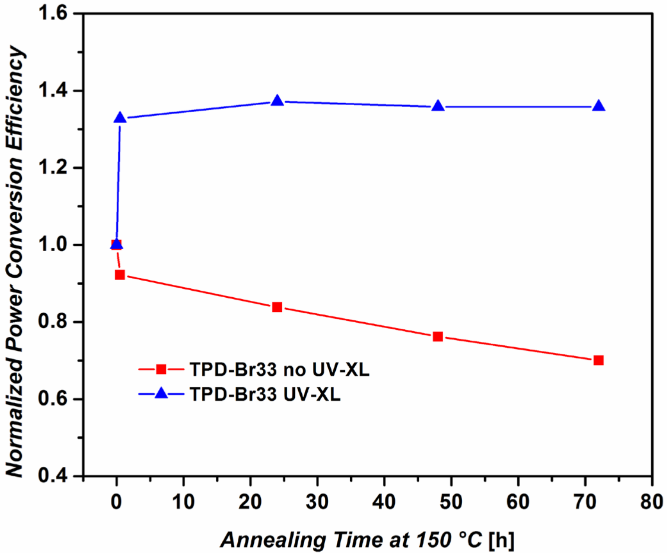

Figure 4.21 Normalized power conversion efficiencies of non-photocrosslinked TPD-Br33 and photocrosslinked TPD-Br33 devices during long-term thermal annealing at 150 °C with $PC_{71}BM$ as n-type material. The efficiency of each device was normalized to its initial efficiency (at annealing time 0 h). The same blend concentration (24 mg/mL in dichlorobenzene) was used for all devices. The polymer:$PC_{71}BM$ ratio was 1:2.5 for all devices.

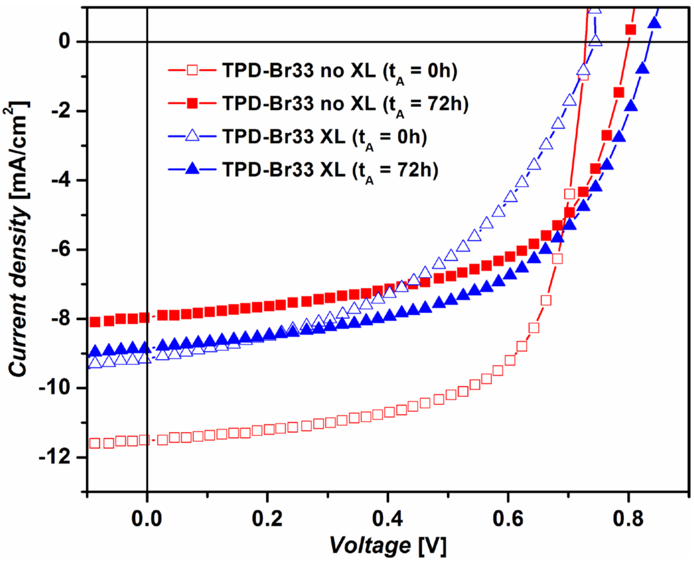

Figure 4.22 J-V curves of the best PTD-Br33:$PC_{71}BM$ PSC devices before (hollow symbols, t_A = 0 h) and after (full symbols, t_A = 72 h) long-term thermal annealing (t_A).

Table 4.4 Characteristic photovoltaic parameters for TPD-Br33:$PC_{71}BM$ devices.

	XL[a)]	Annealing Time t_A [h]	J_{SC} [mA/cm^2]	V_{OC} [V]	FF [%]	PCE (max) [%]
TPD-Br33	-	0	-11.6	0.72	66	5.5 (5.6)
TPD-BR33	-	72	-8.1	0.80	59	3.9 (3.9)
TPD-Br33	+	0	-8.8	0.74	45	3.0 (3.1)
TPD-Br33	+	72	-8.7	0.83	55	4.0 (4.1)

a)Active layers not subjected (-) and subjected (+) to crosslinking under UV-irradiation prior to cathode deposition.

4.3.6 Surface characterization of active layer morphology in TPD-Br16 devices

In order to clarify the effect of photocrosslinking and fullerene acceptor type on the morphology of the active layer, atomic force microscopy (AFM) analysis was performed on photocrosslinked and non photocrosslinked TPD-Br16 devices. Both polymer:$PC_{71}BM$ and polymer:$PC_{61}BM$ films were studied (Figure 4.23 and Figure 4.24 for TPD-Br16:$PC_{71}BM$ devices and TPD-Br16:$PC_{61}BM$ devices, respectively). Before thermal annealing, the non-photocrosslinked TPD-Br16:$PC_{71}BM$ active layer film (Figure 4.23a,b) shows a well developed interpenetrating network and a finer nanoscale morphology compared to the photocrosslinked film (Figure 4.23e,f). The surface root-mean-square (RMS) roughness before annealing is 2.5 nm and 2.1 nm for non-photocrosslinked and photocrosslinked films, respectively. After annealing at 150 °C for 72 h, a very rough surface morphology is observed on the non-photocrosslinked film (Figure 4.23c,d), resulting in a value of RMS roughness as high as 34.9 nm. This significant morphology change may yield poor contact between the active layer and the electrode, as well as unfavourable conditions for charge separation and transport. Accordingly, a significant decrease in device performance is observed for the TPD-Br16 no XL:$PC_{71}BM$ device after annealing. On the other hand, a finer morphology is observed for the photocrosslinked film after annealing (Figure 4.23g,h), which is correlated to the increase in device PCE. Only a slight increase of RMS roughness is observed for this film (up to 3.0 nm), suggesting that photocrosslinking allows the preservation of a well developed interpenetrating donor/acceptor network within the active layer that can be maintained, even after 72 h of annealing at 150 °C.

In contrast, AFM analysis on TPD-Br16:$PC_{61}BM$ devices revealed the formation of aggregates in both photocrosslinked and non-photocrosslinked active layers after 72 h of annealing at 150 °C. In particular, a rougher surface was found for non-photocrosslinked films (Figure 4.24c,d) compared with photocrosslinked films (Figure 4.24g,h), with RMS roughness values of 10.2 nm and 5.9 nm for TPD-Br16 no XL:$PC_{61}BM$ and TPD-Br16 XL:$PC_{61}BM$, respectively. These observations well correlate with the PV data reported in Section 4.3.4.

The different behaviour found for polymer:$PC_{61}BM$ blends compared to polymer:$PC_{71}BM$ blends may be related to the different sizes of these fullerene molecules (1.67 vs. 1.92 nm),[53] and their movement during the annealing process. Thermal annealing appears to allow the smaller $PC_{61}BM$ molecules to diffuse within the crosslinked polymer network, initially improving the performance but ultimately leading to formation of larger aggregates; whereas this effect is not observed with $PC_{71}BM$. Due to steric bulkiness, the larger $PC_{71}BM$ molecules may be confined into the polymer network, thus inhibiting the formation of large aggregates. This result may indicate that, in addition to increased light absorption with respect to $PC_{61}BM$, $PC_{71}BM$ is able to provide morphological stability of the active layer at high temperature.

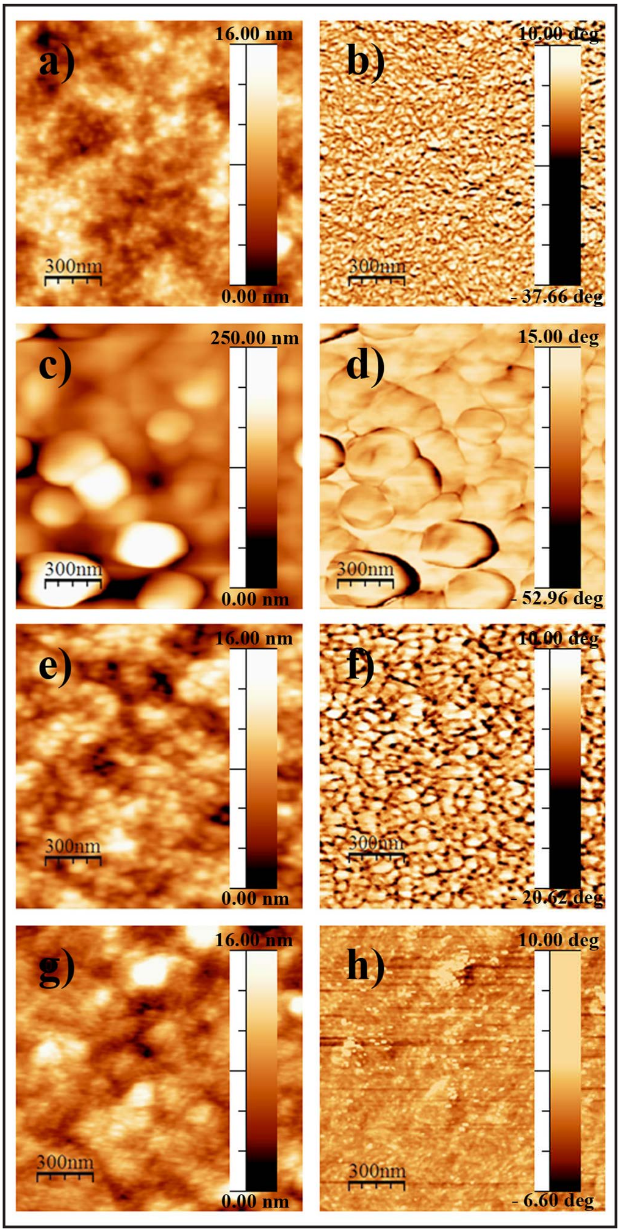

Figure 4.23 AFM (1.5 µm x 1.5 µm) topography (a, c, e, g) and phase (b, d, f, h) images of TPD-Br16:PC$_{71}$BM active layers. The top four images are for the non-crosslinked films (TPD-Br16 no XL), prior to (a, b) and after (c, d) 72 h of thermal annealing at 150 °C. The bottom four images are for the crosslinked devices (TPD-Br16 XL), prior to (e, f) and after (g, h) 72 h of thermal annealing at 150 °C.

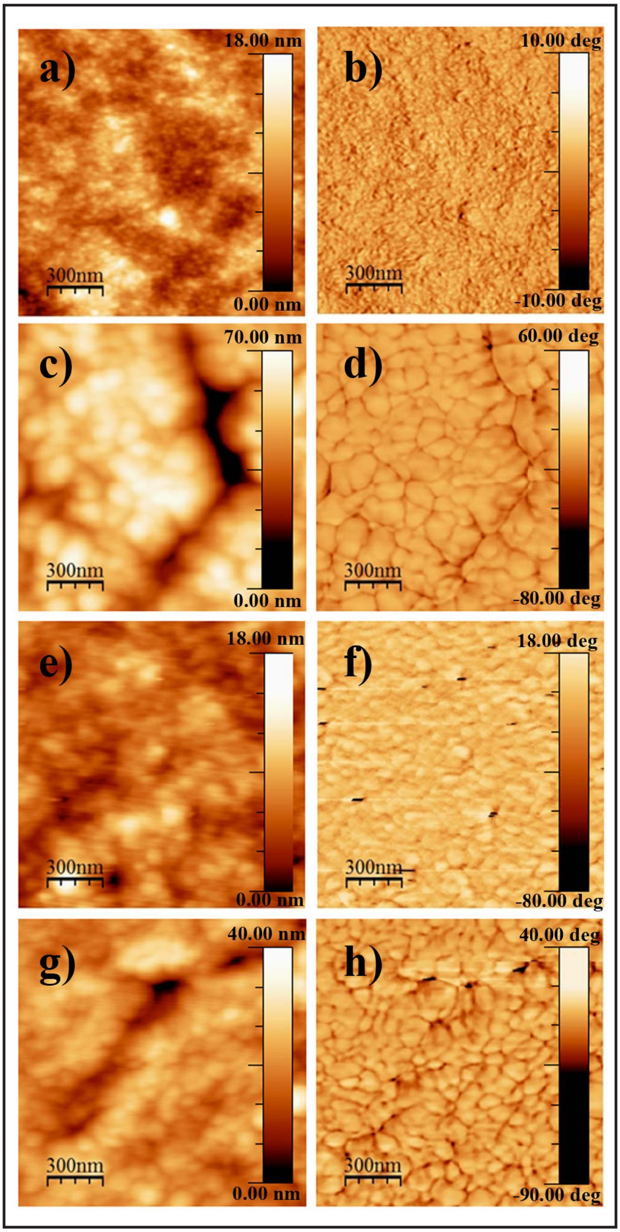

Figure 4.24 AFM (1.5 µm x 1.5 µm) topography (a, c, e, g) and phase (b, d, f, h) images of TPD-Br16:$PC_{61}BM$ active layers. The top four images are for the non-crosslinked films (TPD-Br16 no XL), prior to (a, b) and after (c, d) 72 h of thermal annealing at 150 °C. The bottom four images are for the crosslinked devices (TPD-Br16 XL), prior to (e, f) and after (g, h) 72 h of thermal annealing at 150 °C. The values of RMS roughness are as follows: 2.3 nm (prior to annealing) and 10.2 nm (after 72 h of annealing at 150 °C) for TPD-Br16 no XL; 2.1 nm (prior to annealing) and 5.9 nm (after 72 h of annealing at 150 °C) for TPD-Br16 XL.

4.4 CONCLUSIONS AND FUTURE WORK

The synthesis and characterization of a series of photocrosslinkable donor-acceptor conjugated polymers for use in BHJ organic solar cells was presented in this Chapter.

These polymers were incorporated with fullerene derivatives in BHJ devices and their thermal stability was tested at high temperature. It was demonstrated that after 72 h of thermal annealing at 150 °C, a stable PCE of 4.7% was obtained in devices containing photocrosslinked polymer and $PC_{71}BM$ in the active layer. This result represents the highest performance reported thus far for thermally stable PSC devices.

Careful control of the crosslinking moiety content in the polymer was found to be critical in order to achieve optimal device performance.

In addition, the type of fullerene molecule appeared to influence the thermal stability of the active layer. In particular, it was observed that photocrosslinked $PC_{71}BM$ devices outperform $PC_{61}BM$ devices both in efficiency and thermal stability. This suggests that in addition to increased light absorption with respect to $PC_{61}BM$, $PC_{71}BM$ may be able to provide morphological stability of the active layer at high temperature.

The results of our study provide important guidelines for the design and development of PSC materials with long-term thermal stability and high efficiency.

4.5 REFERENCES

1. M. Jorgensen, K. Norrman, and F.C. Krebs "Stability/degradation of polymer solar cells." Sol. Energy Mater. Sol. Cells 2008, 92, 686-714.
2. C.J. Brabec, S. Gowrisanker, J.J.M. Halls, D. Laird, S. Jia, and S.P. Williams "Polymer-Fullerene Bulk-Heterojunction Solar Cells." Adv. Mater. 2010, 22, 3839-3856.
3. F.C. Krebs and H. Spanggaard "Significant improvement of polymer solar cell stability." Chem. Mater. 2005, 17, 5235-5237.
4. F.C. Krebs and K. Norrman "Analysis of the failure mechanism for a stable organic photovoltaic during 10000 h of testing." Progr. Photovolt.: Res. Appl. 2007, 15, 697-712.
5. M.O. Reese, A.J. Morfa, M.S. White, N. Kopidakis, S.E. Shaheen, G. Rumbles, and D.S. Ginley "Pathways for the degradation of organic photovoltaic P3HT : PCBM based devices." Sol. Energy Mater. Sol. Cells 2008, 92, 746-752.
6. A. Seemann, H.J. Egelhaaf, C.J. Brabec, and J.A. Hauch "Influence of oxygen on semi-transparent organic solar cells with gas permeable electrodes." Org. Electron. 2009, 10, 1424-1428.
7. M. Manceau, S. Chambon, A. Rivaton, J.L. Gardette, S. Guillerez, and N. Lemaitre "Effects of long-term UV-visible light irradiation in the absence of oxygen on P3HT and P3HT:PCBM blend." Sol. Energy Mater. Sol. Cells 2010, 94, 1572-1577.
8. A. Rivaton, S. Chambon, M. Manceau, J.L. Gardette, N. Lamaitre, and S. Guillerez "Light-induced degradation of the active layer of polymer-based solar cells." Polym. Degrad. Stab. 2010, 95, 278-284.
9. M.O. Reese, A.M. Nardes, B.L. Rupert, R.E. Larsen, D.C. Olson, M.T. Lloyd, S.E. Shaheen, D.S. Ginley, G. Rumbles, and N. Kopidakis "Photoinduced Degradation of Polymer and Polymer-Fullerene Active Layers: Experiment and Theory." Adv. Funct. Mater. 2010, 20, 3476-3483.
10. S.K. Pal, T. Kesti, M. Maiti, F.L. Zhang, O. Inganas, S. Hellstrom, M.R. Andersson, F. Oswald, F. Langa, T. Osterman, T. Pascher, A. Yartsev, and V. Sundstrom "Geminate Charge Recombination in Polymer/Fullerene Bulk Heterojunction Films and Implications for Solar Cell Function." J. Am. Chem. Soc. 2010, 132, 12440-12451.
11. W.L. Ma, C.Y. Yang, X. Gong, K. Lee, and A.J. Heeger "Thermally stable, efficient polymer solar cells with nanoscale control of the interpenetrating network morphology." Adv. Funct. Mater. 2005, 15, 1617-1622.

12. X. Yang and J. Loos "Toward high-performance polymer solar cells: The importance of morphology control." Macromolecules 2007, 40, 1353-1362.

13. J. Peet, M.L. Senatore, A.J. Heeger, and G.C. Bazan "The Role of Processing in the Fabrication and Optimization of Plastic Solar Cells." Adv. Mater. 2009, 21, 1521-1527.

14. B. Paci, A. Generosi, D. Bailo, V.R. Albertini, and R. de Bettignies "Discriminating bulk, surface and interface aging effects in polymer-based active materials for efficient photovoltaic devices." Chem. Phys. Lett. 2010, 494, 69-74.

15. B. Paci, A. Generosi, V.R. Albertini, R. Generosi, P. Perfetti, R. de Bettignies, and C. Sentein "Time-resolved morphological study of bulk heterojunction films for efficient organic solar devices." J. Phys. Chem. C 2008, 112, 9931-9936.

16. S. Bertho, G. Janssen, T.J. Cleij, B. Conings, W. Moons, A. Gadisa, J. D'Haen, E. Goovaerts, L. Lutsen, J. Manca, and D. Vanderzande "Effect of temperature on the morphological and photovoltaic stability of bulk heterojunction polymer: fullerene solar cells." Sol. Energy Mater. Sol. Cells 2008, 92, 753-760.

17. E. Verploegen, R. Mondal, C.J. Bettinger, S. Sok, M.F. Toney, and Z.A. Bao "Effects of Thermal Annealing Upon the Morphology of Polymer-Fullerene Blends." Adv. Funct. Mater. 2010, 20, 3519-3529.

18. D. Di Nuzzo, A. Aguirre, M. Shahid, V.S. Gevaerts, S.C.J. Meskers, and R.A.J. Janssen "Improved Film Morphology Reduces Charge Carrier Recombination into the Triplet Excited State in a Small Bandgap Polymer-Fullerene Photovoltaic Cell." Adv. Mater. 2010, 22, 4321-4324.

19. M. Helgesen, M. Bjerring, N.C. Nielsen, and F.C. Krebs "Influence of the Annealing Temperature on the Photovoltaic Performance and Film Morphology Applying Novel Thermocleavable Materials." Chem. Mater. 2010, 22, 5617-5624.

20. B. Conings, S. Bertho, K. Vandewal, A. Senes, J. D'Haen, J. Manca, and R.A.J. Janssen "Modeling the temperature induced degradation kinetics of the short circuit current in organic bulk heterojunction solar cells." Appl. Phys. Lett. 2010, 96, 163301.

21. X.N. Yang, J. Loos, S.C. Veenstra, W.J.H. Verhees, M.M. Wienk, J.M. Kroon, M.A.J. Michels, and R.A.J. Janssen "Nanoscale morphology of high-performance polymer solar cells." Nano Lett. 2005, 5, 579-583.

22. X.N. Yang, J.K.J. van Duren, R.A.J. Janssen, M.A.J. Michels, and J.

Loos "Morphology and thermal stability of the active layer in poly(p-phenylenevinylene)/methanofullerene plastic photovoltaic devices." Macromolecules 2004, 37, 2151-2158.

23. S. Rajaram, P.B. Armstrong, B.J. Kim, and J.M.J. Frechet "Effect of Addition of a Diblock Copolymer on Blend Morphology and Performance of Poly(3-hexylthiophene):Perylene Diimide Solar Cells." Chem. Mater. 2009, 21, 1775-1777.

24. K. Sivula, C.K. Luscombe, B.C. Thompson, and J.M.J. Fréchet "Enhancing the thermal stability of polythiophene: Fullerene solar cells by decreasing effective polymer regioregularity." J. Am. Chem. Soc. 2006, 128, 13988-13989.

25. K. Sivula, Z.T. Ball, N. Watanabe, and J.M.J. Fréchet "Amphiphilic diblock copolymer compatibilizers and their effect on the morphology and performance of polythiophene: Fullerene solar cells." Adv. Mater. 2006, 18, 206-210.

26. S. Miyanishi, Y. Zhang, K. Tajima, and K. Hashimoto "Fullerene attached all-semiconducting diblock copolymers for stable single-component polymer solar cells." Chem. Commun. 2010, 46, 6723-6725.

27. M. Drees, H. Hoppe, C. Winder, H. Neugebauer, N.S. Sariciftci, W. Schwinger, F. Schaffler, C. Topf, M.C. Scharber, Z.G. Zhu, and R. Gaudiana "Stabilization of the nanomorphology of polymer-fullerene "bulk heterojunction'' blends using a novel polymerizable fullerene derivative." J. Mater. Chem. 2005, 15, 5158-5163.

28. S. Miyanishi, K. Tajima, and K. Hashimoto "Morphological Stabilization of Polymer Photovoltaic Cells by Using Cross-Linkable Poly(3-(5-hexenyl) thiophene)." Macromolecules 2009, 42, 1610-1618.

29. B.J. Kim, Y. Miyamoto, B.W. Ma, and J.M.J. Fréchet "Photocrosslinkable Polythiophenes for Efficient, Thermally Stable, Organic Photovoltaics." Adv. Funct. Mater. 2009, 19, 2273-2281.

30. P.L.T. Boudreault, A. Najari, and M. Leclerc "Processable Low-Bandgap Polymers for Photovoltaic Applications." Chem. Mater. 2011, 23, 456-469.

31. A. Facchetti "pi-Conjugated Polymers for Organic Electronics and Photovoltaic Cell Applications." Chem. Mater. 2011, 23, 733-758.

32. E. Bundgaard and F.C. Krebs "Low band gap polymers for organic photovoltaics." Sol. Energy Mater. Sol. Cells 2007, 91, 954-985.

33. Y.F. Li and Y.P. Zou "Conjugated polymer photovoltaic materials with broad absorption band and high charge carrier mobility." Adv. Mater. 2008,

20, 2952-2958.

34. D. Beljonne, J. Cornil, L. Muccioli, C. Zannoni, J.L. Bredas, and F. Castet "Electronic Processes at Organic-Organic Interfaces: Insight from Modeling and Implications for Opto-electronic Devices." Chem. Mater. 2011, 23, 591-609.

35. J.L. Bredas, J.E. Norton, J. Cornil, and V. Coropceanu "Molecular Understanding of Organic Solar Cells: The Challenges." Acc. Chem. Res. 2009, 42, 1691-1699.

36. R.A. Marsh, J.M. Hodgkiss, and R.H. Friend "Direct Measurement of Electric Field-Assisted Charge Separation in Polymer: Fullerene Photovoltaic Diodes." Adv. Mater. 2010, 22, 3672-+.

37. K. Vandewal, K. Tvingstedt, A. Gadisa, O. Inganas, and J.V. Manca "Relating the open-circuit voltage to interface molecular properties of donor:acceptor bulk heterojunction solar cells." Phys. Rev. B: Condens. Matter Mater. Phys. 2010, 81, 125204.

38. D. Veldman, O. Ipek, S.C.J. Meskers, J. Sweelssen, M.M. Koetse, S.C. Veenstra, J.M. Kroon, S.S. van Bavel, J. Loos, and R.A.J. Janssen "Compositional and electric field dependence of the dissociation of charge transfer excitons in alternating polyfluorene copolymer/fullerene blends." J. Am. Chem. Soc. 2008, 130, 7721-7735.

39. C. Piliego, T.W. Holcombe, J.D. Douglas, C.H. Woo, P.M. Beaujuge, and J.M.J. Fréchet "Synthetic Control of Structural Order in N-Alkylthieno[3,4-c] pyrrole-4,6-dione-Based Polymers for Efficient Solar Cells." J. Am. Chem. Soc. 2010, 132, 7595-7597.

40. Y. Zhang, S.K. Hau, H.L. Yip, Y. Sun, O. Acton, and A.K.Y. Jen "Efficient Polymer Solar Cells Based on the Copolymers of Benzodithiophene and Thienopyrroledione." Chem. Mater. 2010, 22, 2696-2698.

41. Y.P. Zou, A. Najari, P. Berrouard, S. Beaupre, B.R. Aich, Y. Tao, and M. Leclerc "A Thieno[3,4-c]pyrrole-4,6-dione-Based Copolymer for Efficient Solar Cells." J. Am. Chem. Soc. 2010, 132, 5330-5331.

42. L.J. Huo, J.H. Hou, S.Q. Zhang, H.Y. Chen, and Y. Yang "A Polybenzo[1,2-b:4,5-b ']dithiophene Derivative with Deep HOMO Level and Its Application in High-Performance Polymer Solar Cells." Angew. Chem. Int. Ed. 2010, 49, 1500-1503.

43. Y.Y. Liang, Z. Xu, J.B. Xia, S.T. Tsai, Y. Wu, G. Li, C. Ray, and L.P. Yu "For the Bright Future-Bulk Heterojunction Polymer Solar Cells with Power Conversion Efficiency of 7.4%." Adv. Mater. 2010, 22, E135-138.

44. Z. He, C. Zhong, X. Huang, W.Y. Wong, H. Wu, L. Chen, S. Su, and Y. Cao "Simultaneous Enhancement of Open-Circuit Voltage, Short-Circuit Current Density, and Fill Factor in Polymer Solar Cells." Adv. Mater. 2011, 23, 4636-4643.

45. G. Griffini, J.D. Douglas, C. Piliego, T.W. Holcombe, S. Turri, J.M.J. Frechet, and J.L. Mynar "Long-Term Thermal Stability of High-Efficiency Polymer Solar Cells Based on Photocrosslinkable Donor-Acceptor Conjugated Polymers." Adv. Mater. 2011, 23, 1660-1664.

46. N.C. Cates, R. Gysel, J.E.P. Dahl, A. Sellinger, and M.D. McGehee "Effects of Intercalation on the Hole Mobility of Amorphous Semiconducting Polymer Blends." Chem. Mater. 2010, 22, 3543-3548.

47. N.C. Cates, R. Gysel, Z. Beiley, C.E. Miller, M.F. Toney, M. Heeney, I. Mcculloch, and M.D. McGehee "Tuning the Properties of Polymer Bulk Heterojunction Solar Cells by Adjusting Fullerene Size to Control Intercalation." Nano Lett. 2009, 9, 4153-4157.

48. A.C. Mayer, M.F. Toney, S.R. Scully, J. Rivnay, C.J. Brabec, M. Scharber, M. Koppe, M. Heeney, I. Mcculloch, and M.D. McGehee "Bimolecular Crystals of Fullerenes in Conjugated Polymers and the Implications of Molecular Mixing for Solar Cells." Adv. Funct. Mater. 2009, 19, 1173-1179.

49. J.K. Lee, W.L. Ma, C.J. Brabec, J. Yuen, J.S. Moon, J.Y. Kim, K. Lee, G.C. Bazan, and A.J. Heeger "Processing additives for improved efficiency from bulk heterojunction solar cells." J. Am. Chem. Soc. 2008, 130, 3619-3623.

50. J.S. Moon, C.J. Takacs, S. Cho, R.C. Coffin, H. Kim, G.C. Bazan, and A.J. Heeger "Effect of Processing Additive on the Nanomorphology of a Bulk Heterojunction MaterialGÇá." Nano Lett. 2010, 10, 4005-4008.

51. J. Peet, J.Y. Kim, N.E. Coates, W.L. Ma, D. Moses, A.J. Heeger, and G.C. Bazan "Efficiency enhancement in low-bandgap polymer solar cells by processing with alkane dithiols." Nat. Mater. 2007, 6, 497-500.

52. M.D. Perez, C. Borek, S.R. Forrest, and M.E. Thompson "Molecular and Morphological Influences on the Open Circuit Voltages of Organic Photovoltaic Devices." J. Am. Chem. Soc. 2009, 131, 9281-9286.

53. T. Kawauchi, J. Kumaki, A. Kitaura, K. Okoshi, H. Kusanagi, K. Kobayashi, T. Sugai, H. Shinohara, and E. Yashima "Encapsulation of fullerenes in a helical PMMA cavity leading to a robust processable complex with a macromolecular helicity memory." Angew. Chem. Int. Ed. 2008, 47, 515-519.

image in next page:

details from M. K. Čiurlionis "The Sun is Passing in the Sign of Libra", 1906-1907.

>5

CHARACTERIZATION OF NEW LOW-BANDGAP DONOR-ACCEPTOR POLYMERS FOR EFFICIENT POLYMER SOLAR CELLS

5.1 INTRODUCTION

As shown in Chapter 2, polymer solar cells (PSCs) have attracted considerable attention in the past few years due to their promise as a flexible and potentially low-cost alternative to commercial inorganic-based photovoltaic technology.[1-8] In particular, considerable efforts have been made by the PSC research community in an attempt to improve power conversion efficiencies of devices.

In the highest performing PSC devices, a p-type polymer is blended with an n-type soluble fullerene derivative and spun-cast from solution to form a bulk heterojunction (BHJ) with nanoscale phase domains. To-date, solution processed devices based on a polymer:fullerene active layer have reached power conversion efficiencies (PCEs) exceeding 7%.[9-11]

Although an optimal physical morphology of the active layer is necessary to achieve high PSC performance and its stability must be sought in order to ensure long-term high performance (see Chapter 4),[12-17] such an optimal active layer morphology does not ensure efficient charge transfer from the light-absorbing polymer to the electron transporting fullerene material.

For the charge to be effectively transferred from the polymer to the electron transporting fullerene material, the polymer and fullerene energy levels must be properly aligned. In particular, p-type polymers should be designed according to the following three criteria: they should possess energy levels such that an offset between the lowest unoccupied molecular orbitals (LUMOs) of the polymer and fullerene are a minimum of 0.3 eV, to ensure effective charge separation;[18-22] in addition the band gap of the polymer should be coupled with an absorption spectrum that matches the solar emission spectrum so as to optimize photocurrent generation;[23-27] finally, the polymer highest occupied molecular orbital (HOMO) should be sufficiently low in energy to create a large open circuit voltage (V_{OC}).[28-31] One approach towards increasing low energy light absorption and modulating the energy level alignment of the polymer with the n-type material is to design the polymer to have alternating electron-rich (donor) and electron-poor (acceptor) backbone components. Recently, many performance breakthroughs have occurred as a result of this donor-acceptor approach, and in particular, the development of new acceptor monomers has allowed for an increase in novel polymer backbone designs.

Acceptor monomers generally include one of two desirable structural design parameters: either a strong electron-withdrawing moiety or a functionality that promotes increased quinoidal character. By adding electron-withdrawing substituents to an acceptor monomer, the HOMO and LUMO energy levels of the resulting donor-acceptor copolymer are lowered, and the ideal V_{OC} of the polymer device should be increased.[26,28,29] Recently, electron-withdrawing functionalities such as esters, ketones, imides and fluorides have been incorporated into the acceptor monomer of some of the highest performing PSC polymers.[23,32-36] Alongside electron-withdrawing substituent effects, increasing the quinoidal character of an acceptor monomer can reduce bond length alternation and is beneficial for tuning the optical and electronic properties of the resulting copolymer. In addition, polymers with a stabilized quinoidal structure show better electron delocalization along their backbone and a narrower band gap.

One well-known polymer, polyisothianaphthene (PITN), has a chemical structure that intrinsically stabilizes its quinoidal state. The ITN monomer is a bicyclic compound that comprises a benzene ring fused to the 3,4 bond of thiophene, resulting in competing aromaticity between the two aromatic rings. In its aromatic form, PITN is stabilized by the aromatization of thiophene, and in its quinoidal form, the polymer is stabilized by the aromatization of benzene (Scheme 5.1).[37,38]

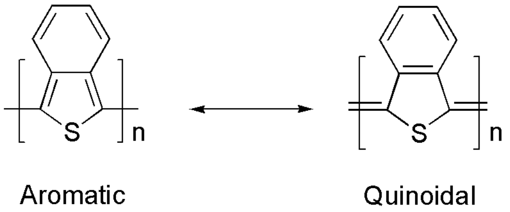

Scheme 5.1 Aromatic and quinoidal forms of poly(isothianaphthene) – PITN.

Since benzene possesses greater aromatic stabilization energy than thiophene (36 kcal/mol for benzene versus 29 kcal/mol for thiophene), the quinoidal structure of PITN is energetically favored and imparts a significant resonance contribution to the overall structure of PITN.[39,40] As an acceptor monomer, ITN is attractive not only because it has significant intrinsic quinoidal character, but also because it can be synthetically modified to include electron-withdrawing substituents.

In this Chapter we present a study on the characterization and the PSC device performance of novel donor-acceptor co-polymers containing ITN acceptor monomers with different electron-withdrawing functionalities, namely ester, imide and nitrile.

As a platform to study the effect of the different electron-withdrawing groups on the ITN-based donor-acceptor co-polymers, benzodithiophene (BDT) was employed as donor co-monomer. BDT is known to have a strong propensity to π-stack as a result of its large, planar structure, and it has been used in many of the highest performing PSC polymers.[24,34]

For each polymer presented in this work, the solubilizing alkyl side-chains on the BDT donor co-monomer were judiciously chosen to allow for a high level of solution-processability, without the addition of unnecessary side chain length and bulk.

An extensive optimization of different device parameters was performed on each polymer system. In particular, characteristic quantities such as polymer:fullerene ratio, active layer blend concentration, solvent system and thermal annealing were systematically examined in order to yield optimal device performance.

The results of this work show that the electron-withdrawing substituents appended to the ITN acceptor monomer can control the optical and electronic properties of the resulting polymers as well as the functionality of the polymers as p- and n-type materials in PSC devices. In addition, PSC devices were fabricated with PCEs of up to 3.0% for BHJ systems and PCEs of up to 0.3% for all-polymer bilayer devices.

5.2 EXPERIMENTAL

5.2.1 Materials

The molecular structures of the polymers studied in this Chapter are presented in Figure 5.1.

All these polymers were provided by the Fréchet group at the University of California, Berkeley.

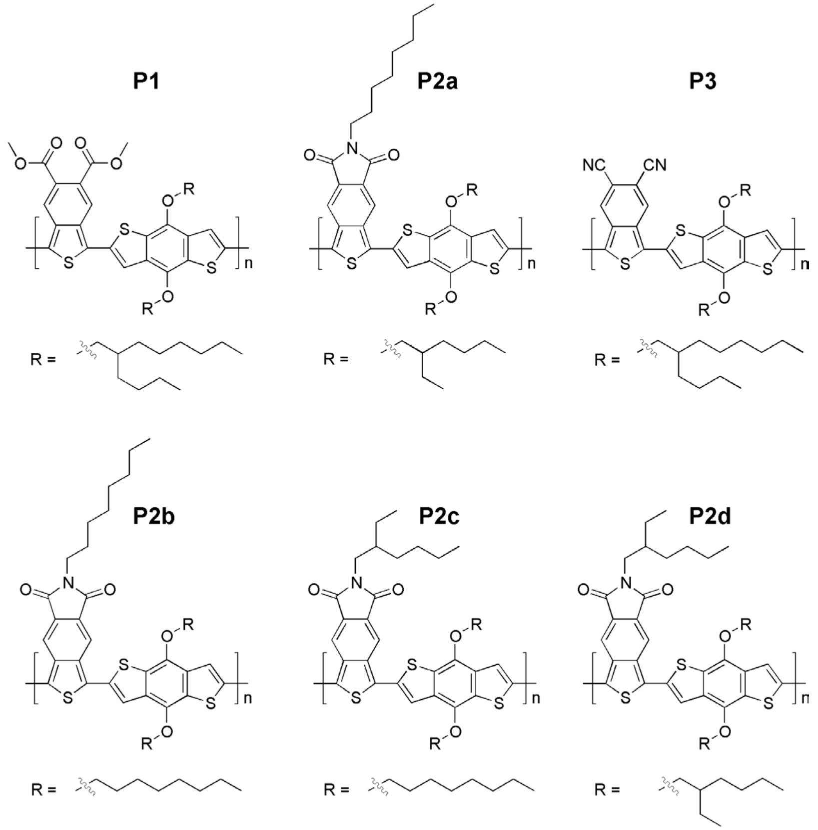

Figure 5.1 Molecular structure of the polymers studied in this Chapter: poly(dimethyl-benzo[c]thiophene-5,6-dicarboxylate-co-4,8-di(2-butyloctyloxy)benzo[1,2-b:4,5-b’] dithiophene) – ITN-DME/BDT-BO (P1); poly(6-octyl-5H-thieno[3,4-f]isoindole-5,7(6H)-dione -co-4,8-di(2-ethylhexyloxy)benzo[1,2-b:4,5-b’]dithiophene) - ITN-OI/BDT-EH (P2a); poly(benzo[c]thiophene-5,6-dicarbonitrile-co-4,8-di(2-butyloctyloxy)benzo[1,2-b:4,5-b’] dithiophene) – ITN-DCN/BDT-BO (P3); poly(6-octyl-5H-thieno[3,4-f]isoindole-5,7(6H)-dione -co-4,8-di(octyloxy)benzo[1,2-b:4,5-b’]dithiophene) - ITN-OI/BDT-O (P2b); poly(6-(2-ethylhexyl)-5H-thieno[3,4-f]isoindole-5,7(6H)-dione -co-4,8-di(octyloxy)benzo[1,2-b:4,5-b’]dithiophene) - ITN-EHI/BDT-O (P2c); poly(6-(2-ethylhexyl)-5H-thieno[3,4-f] isoindole-5,7(6H)-dione -co-4,8-di(2-ethylhexyloxy)benzo[1,2-b:4,5-b’]dithiophene) - ITN-EHI/BDT-EH (P2d).

For P1 and P3, the relatively large butyloctyl (BO) solubilizing group was chosen for BDT because ITN-DME and ITN-DCN possess limited solubilizing power. Conversely, for P2a, the smaller ethylhexyl (EH) side chain was chosen for BDT because ITN-I contains an aliphatic side chain that imparts solubility to the polymer. Additionally, because the size and placement of polymer side chains have been shown to affect PSC device performance,[41-43] four different ITN-I-co-BDT polymers were studied (P2a-d).

All solvents employed in this work (chloroform – $CHCl_3$, chlorobenzene – CB, 1,8-octanedithiol – ODT, 1,8-diodooctane – DIO, 1-chloronaphthalene - CN) were purchased from Sigma-Aldrich and used as received, without further purification.

5.2.2 Instrumtientation

All ^1H NMR spectra were obtained with a Bruker AVQ-400, AVB-400 or AV-600 instrument.

UV–Vis absorption spectra were recorded on polymer thin films at room temperature using a Varian Cary 50 Conc UV-Visible spectrophotometer. The polymers were spin-coated on ITO-coated glass substrates from chloroform solutions (15 mg/ml). The thickness of the thin films was measured by profilometry (Veeco Dektat 150) and determined to be 80 ±10 nm. A blank ITO-coated glass substrate was used as reference.

Cyclic voltammograms were collected using a Solartron 1285 potentiostat under the control of CorrWare II software. A standard three electrode cell based on a Pt wire working electrode, a silver wire pseudo reference electrode (calibrated vs. ferrocene(Fc)/ferrocenium(Fc+)), and a Pt wire counter electrode was purged with nitrogen and maintained under a nitrogen atmosphere during all measurements. Acetonitrile was purchased anhydrous from Aldrich and tetrabutylammonium hexafluorophosphate (0.1 M) was used as the supporting electrolyte. Polymer films were drop cast onto a Pt wire working electrode from a 1% (w/w) chloroform solution and dried under nitrogen prior to measurements.

5.2.3 Device fabrication and testing

All devices were fabricated on ITO-coated glass substrates (pre-patterned, R = 20 $\Omega\square^{-1}$, Thin Film Devices, Inc.). The substrates were firstly ultrasonicated in 2% Hellmanex soap water for 20 min, and then subjected to successive ultrasonication in de-ionized water (20 min), acetone (20 min) and isopropyl alcohol (20 min) before drying under a stream of nitrogen. After UV-ozone cleaning the substrates for 30 min, a thin-layer (40 nm) of filtered PEDOT:PSS (Clevios PH) was spin-coated onto each ITO substrate at 4000 RPM for 40 s followed by baking at 140 °C for 15 min in air. All substrates were then moved to a nitrogen-filled glove box to perform all the following fabrication steps.

Bulk heterojunction devices:

Solutions of P1 and P2a-d polymers (15 mg/mL) and PC61BM (40 mg/mL) in CB were prepared separately and stirred overnight at 110 °C. The solutions were passed through a 0.45 μm polytetrafluoroethylene syringe-filter prior to the preparation of the blend solutions. When employed, high boiling-point solvent additives (ODT, DIO and CN) were added to the respective CB blend solutions in varying volume concentrations and stirred overnight before spin-coating.

Bilayer devices:

Solutions of P3 polymer (4 mg/mL in THF) and poly(3-(4-n-octly)-phenylthiophene) (POPT) (4 mg/mL in CB) were prepared separately and stirred overnight at 50 °C and 110 °C, respectively. The solutions were passed through a 0.45 μm polytetrafluoroethylene syringe-filter prior to spin-coating.

The active layer solutions prepared as presented above were spin-coated at 1200 RPM for 40 sec followed by 1 sec at 2000 RPM, producing films with a thickness of 80-90 nm. The cathode, consisting of Ca (20nm) and Al (100 nm), was then deposited by thermal evaporation under vacuum (~ 10^{-7} torr) through a shadow mask defining an active device area of 0.03 cm^2. The layout of the shadow mask afforded eight independent devices on each substrate. When performed, thermal annealing was carried out by placing the complete device on a temperature controlled hot-plate in N_2 atmosphere with the active layer facing up. The current-voltage (J-V) curves were measured using a Keithley 2400 source-measure unit under AM 1.5G solar illumination at 100 mW cm^{-2} (1 sun) using a Thermal-Oriel 150 W solar simulator. During device optimization, different solution concentrations, polymer:$PC_{61}BM$ ratios and solvent systmes were tested in order to obtain the optimized process conditions, and the experiments were repeated multiple times to ensure data reproducibility. Eight distinct devices on each substrate were tested.

5.3 RESULTS AND DISCUSSION

The ester, imide and nitrile functionalities of ITN were selected to clarify the effect of different electron-withdrawing substituents on conjugated polymers.

A preliminary study on the electronic influence of substituents on the ITN molecules was performed by means of proton nuclear magnetic resonance (^{1}H-NMR) spectroscopy on the differently substituted ITN-monomers (see Figure 5.2).[44]

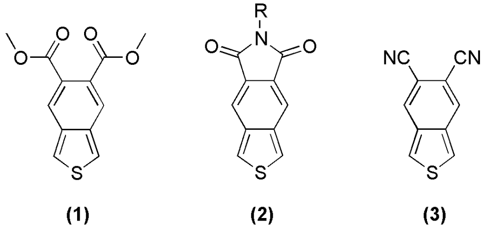

Figure 5.2 Differently substituted ITN monomers: dimethylester (1), imide (2) and dinitrile (3).

In the three molecule series (1, 2, 3), the two thiophene protons appeared at 7.82 ppm, 8.00 ppm and 8.55 ppm in the diester-based, imide-based and dinitrile-based monomers, respectively.

It was hypothesized that the most electron-deficient substituent would withdraw electron density away from the thiophene portion of ITN. Because electronegative atoms and electron-deficient functional groups generally promote the downfield (higher value) chemical shifts of adjacent atoms, the observed trend implies that the diester functionality on ITN is less electron-withdrawing than the imide, which in turn is less electron-deficient then the dinitrile.

5.3.1 Cyclic voltammetry

The impact of ester, imide and nitrile functional groups on the energy levels of the ITN co-polymers was examined and correlated with cyclic voltammetry (CV) measurements. As shown in Table 5.1, where values of HOMO and LUMO levels are reported for dimethylester, imide and dinitrile ITN polymers, P1 possesses the highest energy levels in the three polymer series (HOMO = - 5.58 eV, LUMO = - 3.46 eV). Slightly lower energy levels are observed for P2a (HOMO = - 5.65 eV, LUMO = - 3.62 eV), while P3 shows the lowest energy levels (HOMO = - 5.83 eV, LUMO = - 3. 91 eV).

The electron-withdrawing character is known to cause a decrease of the MO energy levels. Accordingly, P1 polymer shows the highest MO energy levels, the ester-functionality being the less electron-withdrawing among those studied in this work, as also inferred from the ^{1}H-NMR analysis.

It is worth noticing that while the HOMO levels of the co-polymers experience only a slight decrease in energy, a dramatic decrease is observed for the LUMO energy levels. This behavior indicates that the electronics of the acceptor has a greater influence on the LUMO of the polymer than on the HOMO.

Table 5.1 Electronic properties of the polymers studied in this work.

	Functional group	HOMO[a)] (eV)	LUMO[a)] (eV)	Eg[b)] (eV)
P1	di-methyl-ester	- 5.58	- 3.46	1.60
P2a	imide	- 5.65	- 3.62	1.54
P3	di-nitrile	- 5.83	- 3.91	1.51

[a)] HOMO and LUMO energy levels estimated from the onset oxidation and reduction potentials, respectively, in CV measurements assuming the absolute energy level of Fc/Fc+ at -5.12 eV; b) optical band-gap estimated from the onset edge of absorption spectra in solid films.

5.3.2 UV-vis absorption spectroscopy

The UV-vis absorption spectra of the three representative ITN co-polymers in thin-films are presented in Figure 5.3. All three co-polymers possess an absorption spectrum that shows favorable overlap with the visible region of the solar spectrum.

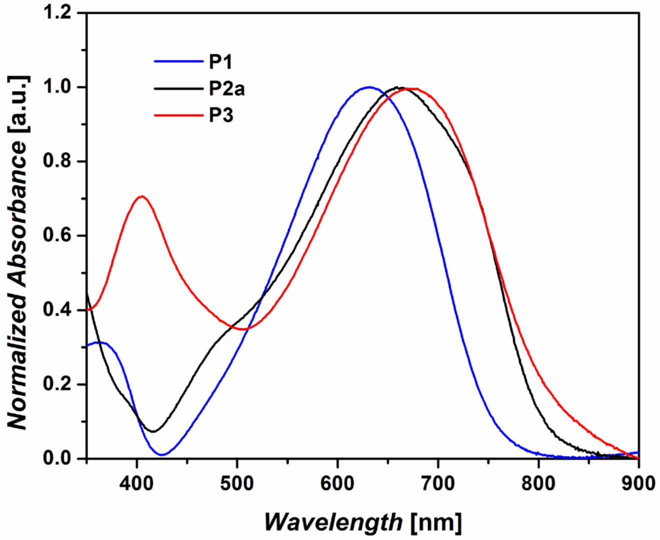

Figure 5.3 Normalized absorption spectra of the polymer thin-films considered in this work.

As expected, the weakly electron-withdrawing ester-containing polymer P1 presents an energy onset of absorption at about 750 nm, making it the largest band gap (E_g) material in this series (1.60 eV). Compared to P1, the more electron-deficient polymers, P2a and P3, have considerably red-shifted onsets of absorption and more narrow band gaps (1.54 and 1.51 eV, respectively). This band gap trend well correlates with the electronic trends of the three representative polymers, as found in the ^{1}H-NMR and CV analyses.

5.3.3 Optimization of BHJ PSC devices

In order to evaluate the performance of BHJ devices, P1 and P2a-d polymers were tested in individually optimized PSC devices using the standard indium-tin oxide (ITO)/poly(3,4-ethylenedioxythiophene) (PEDOT):poly(styrenesulfonate) (PSS)/polymer:fullerene/Ca/Al device architecture. This Section presents the complete optimization steps performed on each of these polymer systems so as to attain optimal PSC device performance.

The investigation on device performance of P3 polymer will be discussed in Section 5.3.5.

5.3.3.1 Optimization of P1:PC$_{61}$BM devices

A systematic study on different device parameters was carried out on P1 devices in BHJ with PC$_{61}$BM in order to achieve optimal photovoltaic (PV) performance. Figure 5.4 shows the J-V characteristics of P1:PC$_{61}$BM devices at varying polymer:PC$_{61}$BM ratio. By increasing the amount of fullerene acceptor in the active layer blend, an increase in power conversion efficiency is observed (from 0.83% in the 1:1 blend to 2.74% in the 1:2.5 blend), mainly resulting from an increase in fill factor and current density. As also observed in Chapter 4, this trend may be attributed to the intercalation of the fullerene molecules in the available spaces between the polymer side chains.[45,46]

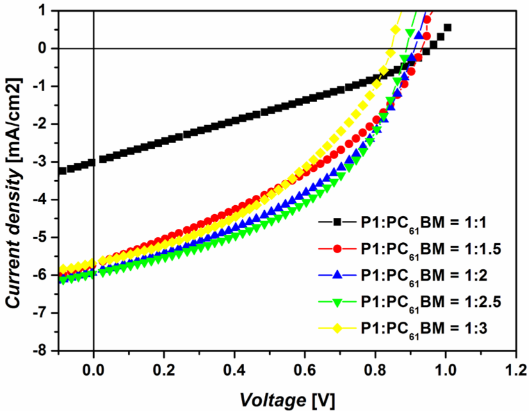

Figure 5.4 J-V curves of P1:PC$_{61}$BM devices at varying polymer:PC$_{61}$BM ratio. The active layer blend concentration is 20 mg/mL for all devices.

A further increase in fullerene content (P1:PC$_{61}$BM = 1:3) was found to cause a decrease in PCE (1.97%), likely resulting from the proportional decrease of the amount of light-absorbing phase (the conjugated polymer) where exciton generation occurs.

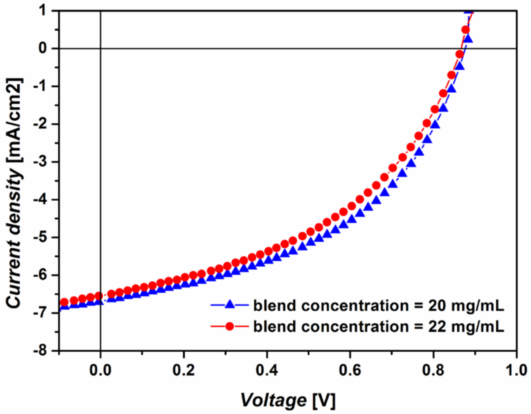

Figure 5.5 J-V curves of P1:PC$_{61}$BM devices at varying active layer blend concentration. The polymer:PC$_{61}$BM ratio is 1:2.5 for both devices.

The dependence of device performance on active layer thickness was investigated by varying the active layer blend concentration in CB (see Figure 5.5). After an increase in concentration from 20 mg/mL to 24 mg/mL a slight reduction of PCE is observed (down to 2.47%), likely due to the emergence of resistances within the active layer that are detrimental to charge transport.

The use of high boiling-point solvent additives[47-50] was also explored on the P1:PC$_{61}$BM BHJ system, but no significant improvements in PCE were reported. In particular, the best PV performance was found for active layers spun-cast from CB-only solutions, suggesting that solvent additives do not impart beneficial effects on the nanoscale morphology of the P1:PC$_{61}$BM active layer.

In summary, optimization of P1:PC$_{61}$BM devices led to an optimal polymer:PC$_{61}$BM ratio of 1:2.5 and an optimal active layer blend concentration of 20 mg/mL.

5.3.3.2 Optimization of P2a:PC$_{61}$BM devices

Following the same procedure used on P1 polymer, a thorough optimization of device parameters was also performed on P2a:PC$_{61}$BM devices.

In particular, the effect of active layer thickness on PSC performance was investigated by varying the concentration of the active layer blend in CB from 20 mg/mL to 24 mg/mL. As shown in Figure 5.6, the PCE of P2a:PC$_{61}$BM CHJ devices decreases at increasing blend concentration, reaching a maximum of 1.43% at 20 mg/mL.

The effect of polymer:PC$_{61}$BM ratio on device performance was also examined, as shown in Figure 5.7. An increase of fullerene content in the active layer appears to negatively affect the performance of P2a:PC$_{61}$BM devices, as evidenced by the decrease of PCE observed when moving from a 1:1.5 to a 1:3.5 polymer:PC$_{61}$BM ratio. This decrease is mainly resulting from a reduction of the J_{SC} of the device, thus suggesting that in this system light absorption and exciton generation in the polymer represent the key steps that control the PCE of the device.

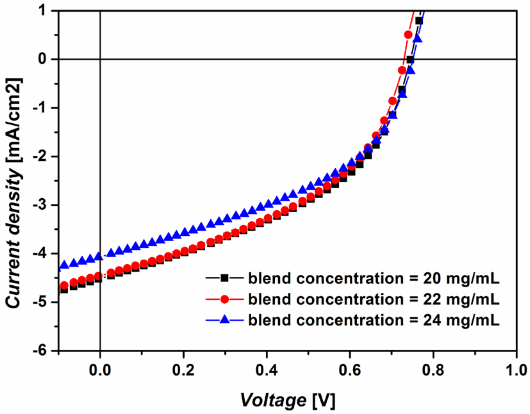

Figure 5.6 J-V curves of P2a:PC$_{61}$BM devices at varying active layer blend concentration. The polymer:PC$_{61}$BM ratio is 1:2 for all devices.

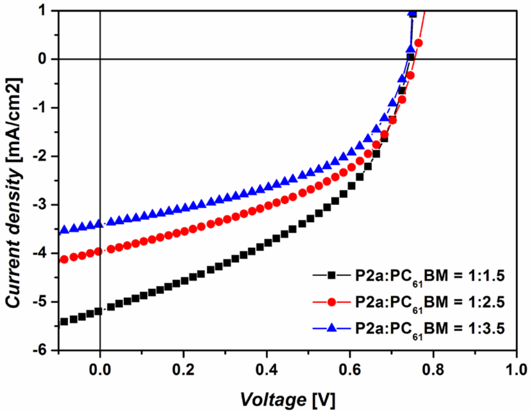

Figure 5.7 J-V curves of P2a:PC$_{61}$BM devices at varying polymer:PC61BM ratio. The active layer blend concentration is 20 mg/mL for all devices.

In order to further optimize the PSC performance of P2a:PC$_{61}$BM, different high boiling-point solvents were considered in conjunction with CB, namely 1-chloronaphthalene (CN), 1,8-diiodooctane (DIO), and 1,8-octanedithiol (ODT). As shown in Figure 5.8, all three solvent additives appear to improve device performance, although to different extents. While the addition of CN mainly yields a slight improvement of the fill factor of the device, DIO and ODT lead to a significant increase of J_{SC}, this effect being more evident with DIO.

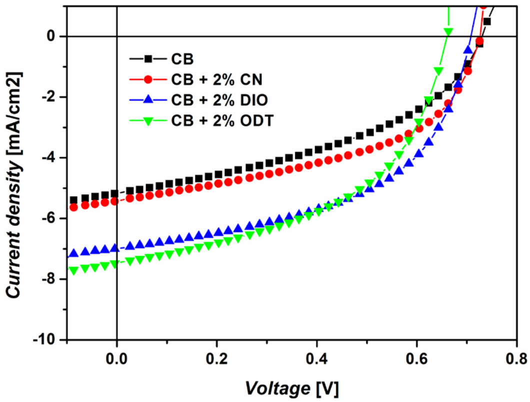

Figure 5.8 J-V curves of P2a:$PC_{61}BM$ devices with active layer processed from different solvent systems.

Therefore the effect of increasing concentrations of DIO (from 1% to 6%) on PSC performance was explored to optimize the PCE of the P2a:$PC_{61}BM$ device and the results are presented in Figure 5.9. The best PSC performance was found for devices containing CB with addition of 1% by vol. of DIO, with a maximum PCE of 2.94%. Indeed, a significant increase in J_{SC} (from -5.08 mA/cm2 for the CB only device to - 7.70 mA/cm2 for the CB + 1% DIO device) is achieved by the addition of DIO to the CB active layer blend solution, followed by an increase in fill factor (from 0.43 to 0.53 in the CB and CB +1% DIO, respectively).

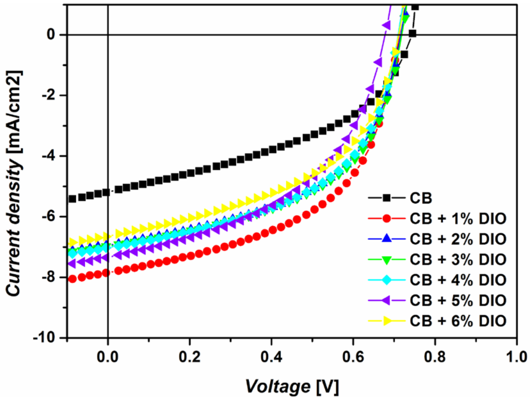

Figure 5.9 J-V curves of P2a:$PC_{61}BM$ devices with active layer processed from CB solutions containing increasing amount of DIO.

In summary, the best performance in P2a:$PC_{61}BM$ devices was found for a polymer:$PC_{61}BM$ ratio of 1:1.5, an active layer blend concentration of 20 mg/mL and an concentration of DIO in the CB active layer solution of 1% by vol.

5.3.3.3 Optimization of P2b:PC$_{61}$BM devices

A similar optimization methodology was employed on the P2b:PC$_{61}$BM system, in order to achieve optimal PSC device performance.

The effect of polymer:PC$_{61}$BM ratio on PSC performance in 18 mg/mL active layer blend solution concentration devices is shown in Figure 5.10.

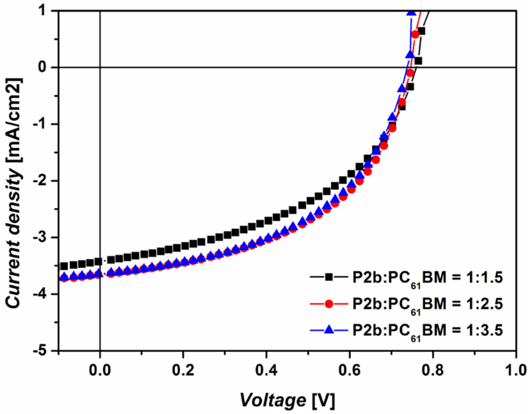

Figure 5.10 J-V curves of P2b:PC$_{61}$BM devices at varying polymer:PC$_{61}$BM ratio. The active layer blend concentration is 18 mg/mL for all devices.

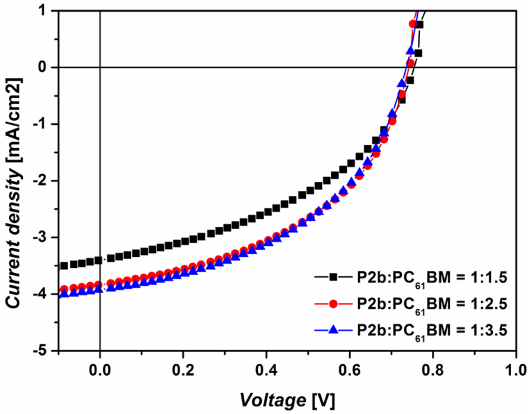

Figure 5.11 J-V curves of P2b:PC$_{61}$BM devices at varying polymer:PC$_{61}$BM ratio. The active layer blend concentration is 20 mg/mL for all devices.

A maximum is found for a 1:2.5 polymer:PC$_{61}$BM ratio with a PCE of 1.36%.

The same effect was also examined on 20 mg/mL active layer blends, and the results are shown in Figure 5.11. Also in this case, a maximum efficiency was found for 1:2.5 P2b:PC$_{61}$BM ratio, although with a slightly lower PCE than for 18 mg/mL blends (1.34% vs 1.36%). Such small effect of active layer blend concentration on device PCE (Figure 5.12) may indicate that the active layer thickness does not represent a severe limitation on the performance of P2b:PC$_{61}$BM devices in this range of film thickness (80 nm ± 10 nm).

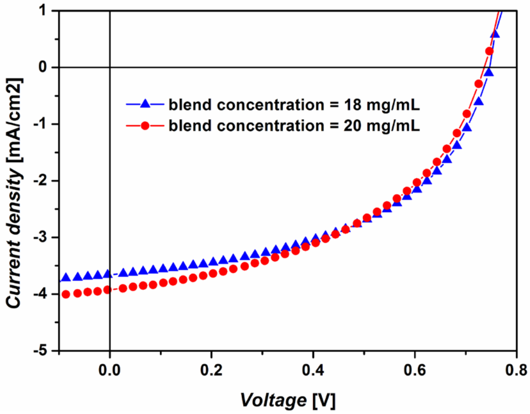

Figure 5.12 J-V curves of P2b:PC$_{61}$BM devices at varying active layer blend concentration. The polymer:PC$_{61}$BM ratio is 1:2.5 for both devices.

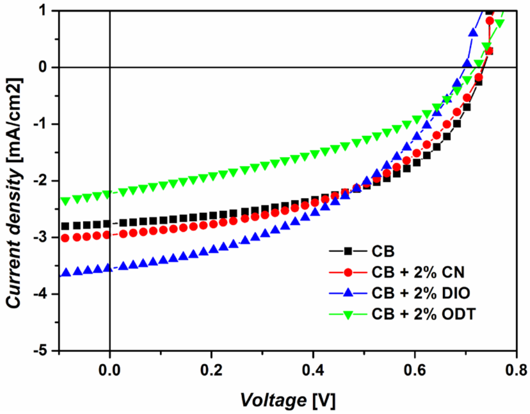

Figure 5.13 J-V curves of P2b:PC$_{61}$BM devices with active layer processed from different solvent systems.

The effect of solvent additives on PSC performance was tested also for the P2b:PC$_{61}$BM system, although no significant improvements were reported. As shown in Figure 5.13, only the addition of DIO appears to slightly improve the J_{SC} of the PSC device, but at the expense of a significant decrease in the fill factor and V_{OC} which lead to an overall decrease in PCE from 1.36% (CB only device) down to 1.00% (CB + 2% DIO). This behaviour suggests that neither the selective solubility of the fullerene component in the specific solvent additive (in the case of ODT and DIO) nor the reduction of evaporation kinetics (in the case of CN) can effectively act on the nanoscale phase segregation of the active layer to lead control of film morphology and enhanced device performance.

5.3.3.4 Optimization of P2c:$PC_{61}BM$ devices

The optimization of P2c:$PC_{61}BM$ devices was performed by firstly studying the effect of polymer:$PC_{61}BM$ ratio on PCE. As shown in Figure 5.14, an increase of fullerene content in the active layer blend yields a progressive decrease in PCE mainly due to a decrease in J_{SC}.

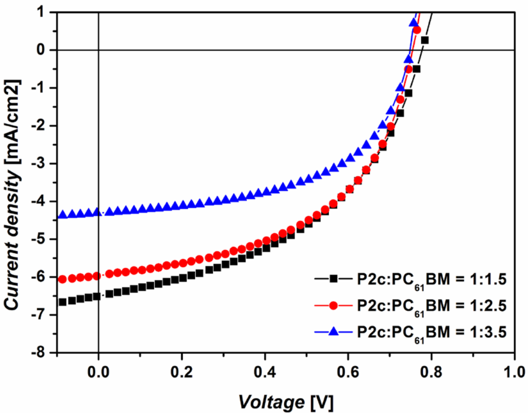

Figure 5.14 J-V curves of P2c:$PC_{61}BM$ devices at varying polymer:$PC_{61}BM$ ratio. The active layer blend concentration is 20 mg/mL for all devices.

An optimal polymer:fullerene ratio of 1:1.5 is found, similarly to what already observed in P2a:$PC_{61}BM$ devices (Section 5.3.3.2).

After investigating the effect of fullerene content in the active layer blend on device performance, the concentration of the active layer blend solution was systematically varied from 18 mg/mL to 22 mg/mL. As shown in Figure 5.15, an increase in J_{SC} is observed by decreasing the blend concentration from 22 mg/mL to 18 mg/mL, leading to a maximum PCE of 2.75%.

Finally, the effect of the presence of high boiling-point solvent additives on PSC performance was also studied, by testing solvent systems comprising CB only and CB with the addition of 2% by vol. of CN, DIO and ODT, respectively. As evidenced by the plots reported in Figure 5.16, the best PSC performance is obtained for active layers processed from CN-containing CB solutions, for which an increase of J_{SC} accompanied by a substantial improvement in fill factor is observed.

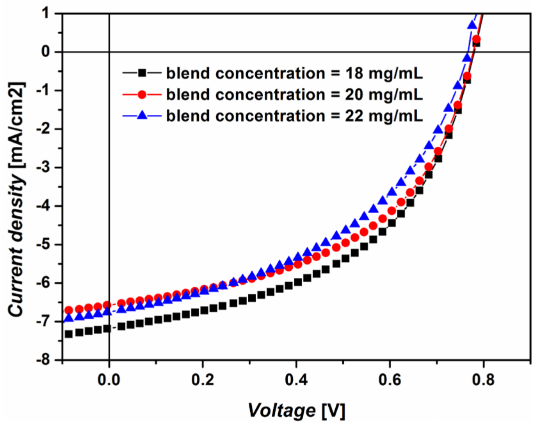

Figure 5.15 J-V curves of P2c:PC_{61}BM devices at varying active layer blend concentration. The polymer:PC_{61}BM ratio is 1:1.5 for all devices.

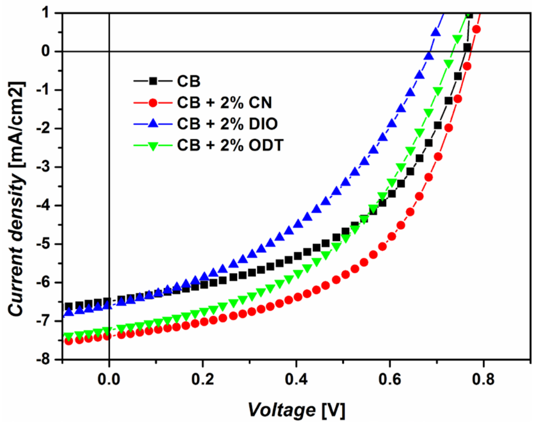

Figure 5.16 J-V curves of P2c:PC_{61}BM devices with active layer processed from different solvent systems.

In order to further optimize the PSC device performance, different concentrations of CN in CB were explored and the results of this study are reported in Figure 5.17. A progressive increase in JSC and fill factor is observed at increasing CN concentration, reaching a maximum for active layer solutions of CB + 5% CN, where an optimal PCE of 3.07% is found. A further increase of CN concentration leads to a decay of PCE.

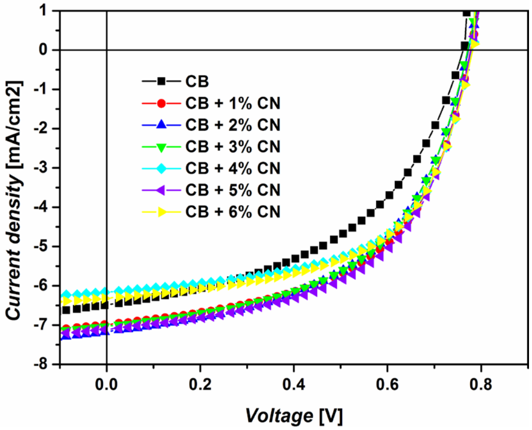

Figure 5.17 J-V curves of P2c:PC_{61}BM devices with active layer processed from CB solutions containing increasing amount of CN.

5.3.3.5 Optimization of P2d:PC_{61}BM devices

In line with the optimization procedure employed for all the polymers presented so far, the performance of P2d:PC_{61}BM devices was also investigated. In particular, the fullerene content was firstly varied and the PSC performance was monitored (Figure 5.18).

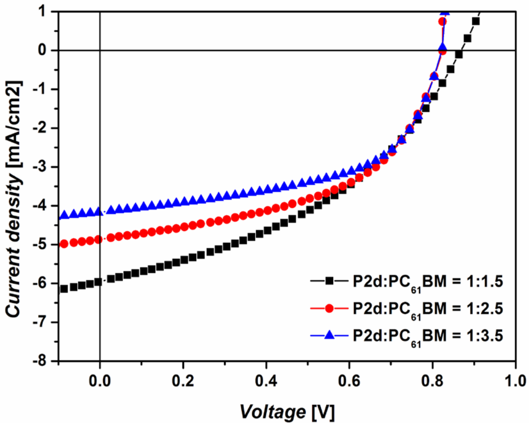

Figure 5.18 J-V curves of P2d:PC_{61}BM devices at varying polymer:PC_{61}BM ratio. The active layer blend concentration is 18 mg/mL for all devices.

A significant decrease in J_{SC} is found by increasing the amount of PC_{61}BM in the active layer blend, ascribable to the proportional decrease in the amount of light-absorbing phase (the conjugated polymer) where exciton generation occurs.

The optimization of the active layer blend concentration led to a maximum PCE of 2.22% for 20 mg/mL solution concentrations. A further increase of the active layer blend concentration would result in a sharp decrease of PCE, likely due to the emergence of resistances within the active layer that are detrimental to charge transport (Figure 5.19).

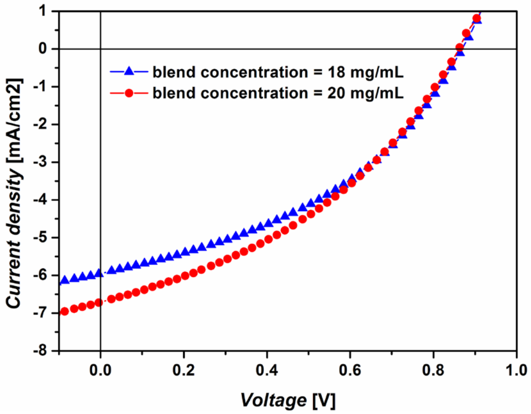

Figure 5.19 J-V curves of P2c:$PC_{61}BM$ devices at varying active layer blend concentration. The polymer:$PC_{61}BM$ ratio is 1:1.5 for both devices.

High boiling-point solvent additives were also tested in this system, as shown in Figure 5.20 where J-V curves of active layers processed from different solvent systems are presented.

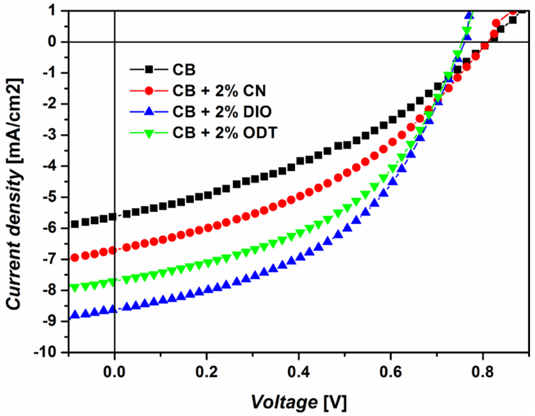

Figure 5.20 J-V curves of P2d:$PC_{61}BM$ devices with active layer processed from different solvent systems.

Even though all solvent additives appear to yield an improvement in PCE of devices mainly resulting from increased J_{SC}, the best PSC performance are obtained for active layer blend solutions containing DIO.

The optimization of the concentration of DIO in the active layer blend solution led to a maximum PCE of 3.04% for a solvent system comprising CB and 1% by vol. DIO (Figure 5.21).

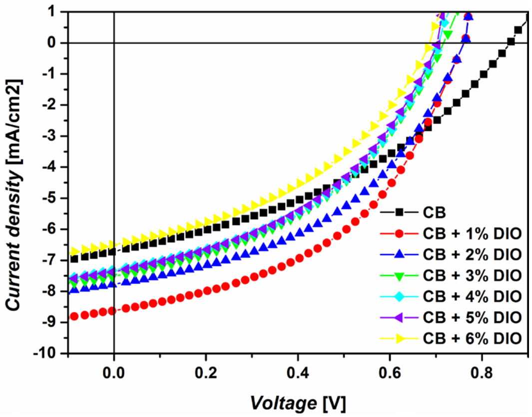

Figure 5.21 J-V curves of P2d:$PC_{61}BM$ devices with active layer processed from CB solutions containing increasing amount of DIO.

5.3.4 Performance comparison of BHJ PSC devices

The J-V output characteristics of the optimized BHJ devices presented in the previous Sections are shown in Figure 5.22 for all polymer systems. The corresponding PV parameters for optimized P1 and P2a-d PSC devices are summarized in Table 5.2.

Table 5.2 Summary of main parameters for optimized P1 and P2a-d BHJ PSC devices.

	Polymer: $PC_{61}BM$	Blend conc.	Solvent system	V_{OC} (V)	J_{SC} (mA/cm^2)	FF	PCE (max) (%)
P1	1:2.5	20 mg/mL	CB	0.87	-6.69	0.46	2.70 (2.74)
P2a	1:1.5	20 mg/mL	CB + 1% DIO	0.71	-7.70	0.53	2.88 (2.94)
P2b	1:2.5	18 mg/mL	CB	0.75	-3.66	0.48	1.32 (1.36)
P2c	1:1.5	18 mg/mL	CB + 5% CN	0.78	-7.05	0.55	3.01 (3.07)
P2d	1:1.5	20 mg/mL	CB + 1% DIO	0.76	-8.46	0.47	3.01 (3.04)

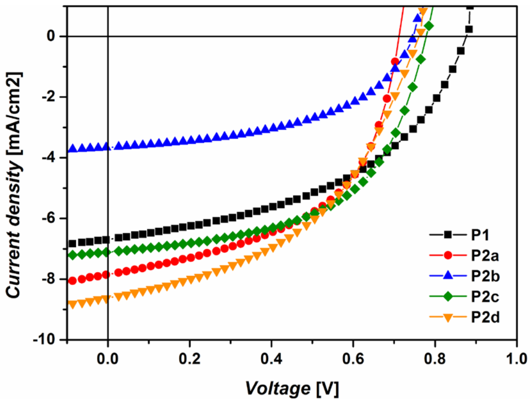

Figure 5.22 J-V curves of optimized P1, P2a, P2b, P2c and P2d PSC devices. For all devices, $PC_{61}BM$ was employed as electron-acceptor molecule.

In blend with $PC_{61}BM$, P1 and P2a-d showed maximum PCEs between 1.36% and 3.07%. The ester-functionalized polymer P1 exhibited a maximum PCE of 2.74% and did not improve after addition of high boiling-point solvent additives in the active layer blend. On the other hand, by employing DIO or CN as solvent additives, imide-functionalized polymers P2a, P2c and P2b reached maximum PCEs between 2.94% and 3.07%. Conversely, the less soluble P2b polymer, bearing octyl solubilizing chains on both the ITN and the BDT monomers (see Figure 5.1), obtained an average PCE of 1.32% and did not yield any efficiency improvement when employing solvent additives. Interestingly, P1 had the largest V_{OC} (0.87 V) and the highest HOMO energy level (-5.58 eV) of the polymer series. This suggests that device V_{OC} may be partly influenced by parameters other than the polymer HOMO, and that energy level engineering to extremely deep/stable HOMO levels may not be necessary for achieving high V_{OC}.

5.3.5 Optimization of bilayer devices

Contrary to P1 and P2a-d, the nitrile-functionalized polymer P3 did not perform as a p-type material in BHJ with $PC_{61}BM$. Instead, this polymer was found to function as an n-type material in bilayer devices. To function as a p-type donor material, the LUMO of the polymer must exhibit a minimum energy offset with the n-type acceptor molecule. Electrochemically, P3 possesses the minimum requisite 0.3 eV energy offset with the n-type molecule ($PC_{61}BM$). However, the polymer optical excited state is lower in energy than the LUMO of $PC_{61}BM$, and this energetically hinders charge separation with the n-type material.

As a result of its low energy levels, P3 polymer was tested as n-type material in bilayer devices combined with a high performing p-type polymer, poly(3-(4-n-octyl)-phenylthiophene) (POPT) (Figure 5.23).[51,52]

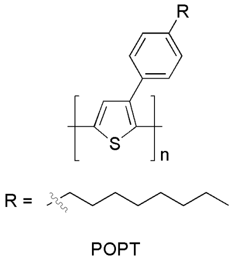

Figure 5.23 Molecular structure of poly(3-(4-n-octyl)-phenylthiophene) - POPT.

The optimization of the bilayer devices was performed by firstly analyzing the effect of the polymer solution concentration on the PSC device performance. As shown in Figure 5.24, where the J-V characteristics of the P3/POPT bilayer devices are presented as a function of solution concentration, significantly different PV behaviours are found at increasing POPT concentration.

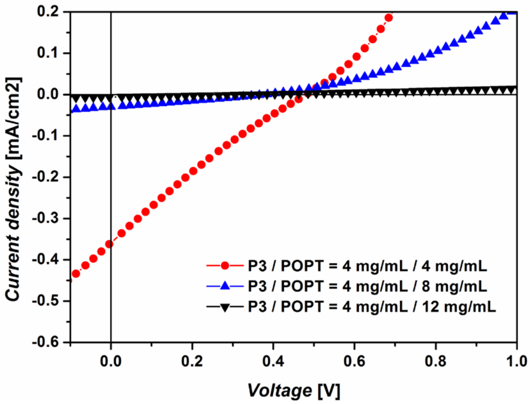

Figure 5.24 J-V curves of P3/POPT bilayer devices at varying P3/POPT ratio.

In particular, a very poor PV behaviour is observed for POPT solution concentrations above 4 mg/mL with very modest PCEs (< 10-3%). Conversely, by employing the same solution concentrations for both P3 and POPT (4 mg/mL), a maximum PCE of 0.04% is achieved.

In an attempt to further boost the PCE of P3/POPT bilayer devices, thermal annealing at 120 °C was performed at increasing annealing times (Figure 5.25).

A dramatic increase in J_{SC} and fill factor is observed upon thermal annealing on bilayer devices, leading to a maximum PCE of 0.28% after 45 min of exposure to high-temperature.

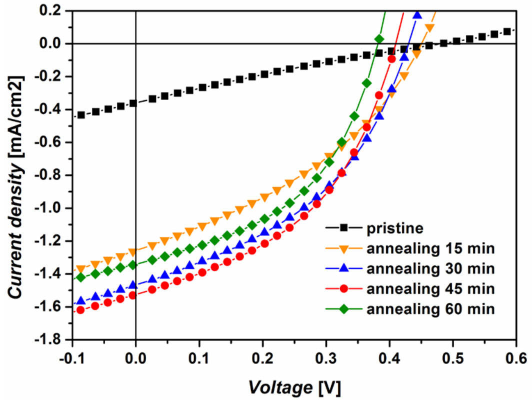

Figure 5.25 J-V curves of P3 (4 mg/mL)/POPT (4 mg/mL) bilayer devices after increasing thermal annealing (120 °C) time.

This one-order-of-magnitude increase of PCE may be attributed to morphological rearrangements occurring at the interface between the p-type and n-type materials, where exciton dissociation and charge generation take place.

5.4 CONCLUSIONS AND FUTURE WORK

The characterization and PSC device performance of a series of new ITN-based donor-acceptor co-polymers were presented in this Chapter. These co-polymers possessed different electron-withdrawing substituents on the ITN co-monomer, namely an ester, an imide and a nitrile functionality.

We were able to show that the electron-withdrawing character of functional groups can strongly influence the polymer electronic behavior, where the ester and imide based polymers behaved as p-type materials and the nitrile-based polymer exhibited an n-type character.

After an extensive optimization of device parameters, bulk-heterojunction PSCs were fabricated with PCEs up to 3.1% using an imide-functionalized ITN co-polymer blended with $PC_{61}BM$. A maximum V_{OC} of 0.87 V was reported for BHJ devices comprising the ester-functionalized ITN co-polymer in blend with $PC_{61}BM$. In addition, optimized bilayer devices were also fabricated with PCEs approaching 0.3% by employing the nitrile-functionalized ITN co-polymer as the n-type material coupled to POPT functioning as the p-type material.

A greater understanding of the role of the p-type/n-type materials interface will be gained through further studies on the morphology of the active layer of these PSC devices.

The three ITN-based acceptor monomers introduced here are promising building blocks for a new generation of low band gap PSC polymers with strong quinoidal character. These new monomers, along with an understanding of the effect of electron-withdrawing substituents on PSC polymer properties, may help to guide the future design of acceptor monomers to be used in high-performing low band-gap co-polymers.

5.5 REFERENCES

1. C.J. Brabec, S. Gowrisanker, J.J.M. Halls, D. Laird, S. Jia, and S.P. Williams "Polymer-Fullerene Bulk-Heterojunction Solar Cells." Adv. Mater. 2010, 22, 3839-3856.
2. W.Z. Cai, X. Gong, and Y. Cao "Polymer solar cells: Recent development and possible routes for improvement in the performance." Sol. Energy Mater. Sol. Cells 2010, 94, 114-127.
3. G. Dennler, M.C. Scharber, and C.J. Brabec "Polymer-Fullerene Bulk-Heterojunction Solar Cells." Adv. Mater. 2009, 21, 1323-1338.
4. B. Kippelen and J.L. Bredas "Organic photovoltaics." Energy Environ. Sci. 2009, 2, 251-261.
5. F.C. Krebs "Polymer solar cell modules prepared using roll-to-roll methods: Knife-over-edge coating, slot-die coating and screen printing." Sol. Energy Mater. Sol. Cells 2009, 93, 465-475.
6. B.C. Thompson and J.M.J. Fréchet "Organic photovoltaics - Polymer-fullerene composite solar cells." Angew. Chem. Int. Ed. 2008, 47, 58-77.
7. F.C. Krebs "Fabrication and processing of polymer solar cells: A review of printing and coating techniques." Sol. Energy Mater. Sol. Cells 2009, 93, 394-412.
8. N. Espinosa, R. Garcia-Valverde, A. Urbina, and F.C. Krebs "A life cycle analysis of polymer solar cell modules prepared using roll-to-roll methods under ambient conditions." Sol. Energy Mater. Sol. Cells 2011, 95, 1293-1302.
9. Y.Y. Liang, Z. Xu, J.B. Xia, S.T. Tsai, Y. Wu, G. Li, C. Ray, and L.P. Yu "For the Bright Future-Bulk Heterojunction Polymer Solar Cells with Power Conversion Efficiency of 7.4%." Adv. Mater. 2010, 22, E135-E138.
10. Z. He, C. Zhong, X. Huang, W.Y. Wong, H. Wu, L. Chen, S. Su, and Y. Cao "Simultaneous Enhancement of Open-Circuit Voltage, Short-Circuit Current Density, and Fill Factor in Polymer Solar Cells." Adv. Mater. 2011, 23, 4636-4643.
11. H.Y. Chen, J.H. Hou, S.Q. Zhang, Y.Y. Liang, G.W. Yang, Y. Yang, L.P. Yu, Y. Wu, and G. Li "Polymer solar cells with enhanced open-circuit voltage and efficiency." Nat. Photonics 2009, 3, 649-653.
12. S. Bertho, G. Janssen, T.J. Cleij, B. Conings, W. Moons, A. Gadisa, J. D'Haen, E. Goovaerts, L. Lutsen, J. Manca, and D. Vanderzande "Effect of temperature on the morphological and photovoltaic stability of bulk heterojunction polymer: fullerene solar cells." Sol. Energy Mater. Sol. Cells 2008, 92, 753-

760.

13. D. Di Nuzzo, A. Aguirre, M. Shahid, V.S. Gevaerts, S.C.J. Meskers, and R.A.J. Janssen "Improved Film Morphology Reduces Charge Carrier Recombination into the Triplet Excited State in a Small Bandgap Polymer-Fullerene Photovoltaic Cell." Adv. Mater. 2010, 22, 4321-4324.
14. G. Griffini, J.D. Douglas, C. Piliego, T.W. Holcombe, S. Turri, J.M.J. Frechet, and J.L. Mynar "Long-Term Thermal Stability of High-Efficiency Polymer Solar Cells Based on Photocrosslinkable Donor-Acceptor Conjugated Polymers." Adv. Mater. 2011, 23, 1660-+.
15. C.H. Hsieh, Y.J. Cheng, P.J. Li, C.H. Chen, M. Dubosc, R.M. Liang, and C.S. Hsu "Highly Efficient and Stable Inverted Polymer Solar Cells Integrated with a Cross-Linked Fullerene Material as an Interlayer." J. Am. Chem. Soc. 2010, 132, 4887-4893.
16. M.A. Ruderer and P. Muller-Buschbaum "Morphology of polymer-based bulk heterojunction films for organic photovoltaics." Soft Matter 2011, 7, 5482-5493.
17. X.N. Yang, J. Loos, S.C. Veenstra, W.J.H. Verhees, M.M. Wienk, J.M. Kroon, M.A.J. Michels, and R.A.J. Janssen "Nanoscale morphology of high-performance polymer solar cells." Nano Lett. 2005, 5, 579-583.
18. D. Beljonne, J. Cornil, L. Muccioli, C. Zannoni, J.L. Bredas, and F. Castet "Electronic Processes at Organic-Organic Interfaces: Insight from Modeling and Implications for Opto-electronic Devices." Chem. Mater. 2011, 23, 591-609.
19. J.L. Bredas, J.E. Norton, J. Cornil, and V. Coropceanu "Molecular Understanding of Organic Solar Cells: The Challenges." Acc. Chem. Res. 2009, 42, 1691-1699.
20. M.D. McGehee "Overcoming recombination." Nat. Photonics 2009, 3, 250-252.
21. T.M. Clarke and J.R. Durrant "Charge Photogeneration in Organic Solar Cells." Chem. Rev. 2010, 110, 6736-6767.
22. T.W. Holcombe, J.E. Norton, J. Rivnay, C.H. Woo, L. Goris, C. Piliego, G. Griffini, A. Sellinger, J.L. Bredas, A. Salleo, and J.M.J. Frechet "Steric Control of the Donor/Acceptor Interface: Implications in Organic Photovoltaic Charge Generation." J. Am. Chem. Soc. 2011, 133, 12106-12114.
23. E. Bundgaard and F.C. Krebs "Low band gap polymers for organic photovoltaics." Sol. Energy Mater. Sol. Cells 2007, 91, 954-985.

24. A. Facchetti "pi-Conjugated Polymers for Organic Electronics and Photovoltaic Cell Applications." Chem. Mater. 2011, 23, 733-758.

25. Y.F. Li and Y.P. Zou "Conjugated polymer photovoltaic materials with broad absorption band and high charge carrier mobility." Adv. Mater. 2008, 20, 2952-2958.

26. S.K. Pal, T. Kesti, M. Maiti, F.L. Zhang, O. Inganas, S. Hellstrom, M.R. Andersson, F. Oswald, F. Langa, T. Osterman, T. Pascher, A. Yartsev, and V. Sundstrom "Geminate Charge Recombination in Polymer/Fullerene Bulk Heterojunction Films and Implications for Solar Cell Function." J. Am. Chem. Soc. 2010, 132, 12440-12451.

27. R. Mondal, S. Ko, J.E. Norton, N. Miyaki, H.A. Becerril, E. Verploegen, M.F. Toney, J.L. Bredas, M.D. McGehee, and Z.N. Bao "Molecular design for improved photovoltaic efficiency: band gap and absorption coefficient engineering." J. Mater. Chem. 2009, 19, 7195-7197.

28. M.D. Perez, C. Borek, S.R. Forrest, and M.E. Thompson "Molecular and Morphological Influences on the Open Circuit Voltages of Organic Photovoltaic Devices." J. Am. Chem. Soc. 2009, 131, 9281-9286.

29. K. Vandewal, K. Tvingstedt, A. Gadisa, O. Inganas, and J.V. Manca "Relating the open-circuit voltage to interface molecular properties of donor:acceptor bulk heterojunction solar cells." Phys. Rev. B: Condens. Matter Mater. Phys. 2010, 81,

30. M.C. Scharber, D. Wuhlbacher, M. Koppe, P. Denk, C. Waldauf, A.J. Heeger, and C.L. Brabec "Design rules for donors in bulk-heterojunction solar cells - Towards 10 % energy-conversion efficiency." Adv. Mater. 2006, 18, 789-+.

31. S. Yamamoto, A. Orimo, H. Ohkita, H. Benten, and S. Ito "Molecular Understanding of the Open-Circuit Voltage of Polymer:Fullerene Solar Cells." Adv. Energy Mater. 2011, Early View, DOI: 10.1002/aenm.201100549.

32. N. Blouin, A. Michaud, D. Gendron, S. Wakim, E. Blair, R. Neagu-Plesu, M. Belletete, G. Durocher, Y. Tao, and M. Leclerc "Toward a rational design of poly(2,7-carbazole) derivatives for solar cells." J. Am. Chem. Soc. 2008, 130, 732-742.

33. P.L.T. Boudreault, A. Najari, and M. Leclerc "Processable Low-Bandgap Polymers for Photovoltaic Applications." Chem. Mater. 2011, 23, 456-469.

34. P.M. Beaujuge and J.M.J. Fréchet "Molecular Design and Ordering Effects in πi-Functional Materials for Transistor and Solar Cell Applications." J. Am. Chem. Soc. 2011, 133, 20009-20029.

35. J.H. Hou, H.Y. Chen, S.Q. Zhang, G. Li, and Y. Yang "Synthesis, Characterization, and Photovoltaic Properties of a Low Band Gap Polymer Based on Silole-Containing Polythiophenes and 2,1,3-Benzothiadiazole." J. Am. Chem. Soc. 2008, 130, 16144-+.

36. L.J. Huo, J.H. Hou, S.Q. Zhang, H.Y. Chen, and Y. Yang "A Polybenzo[1,2-b:4,5-b ′]dithiophene Derivative with Deep HOMO Level and Its Application in High-Performance Polymer Solar Cells." Angew. Chem. Int. Ed. 2010, 49, 1500-1503.

37. H. Meng and F. Wudl "A robust low band gap processable n-type conducting polymer based on poly(isothianaphthene)." Macromolecules 2001, 34, 1810-1816.

38. H. Meng, D. Tucker, S. Chaffins, Y.S. Chen, R. Helgeson, B. Dunn, and F. Wudl "An unusual electrochromic device based on a new low-bandgap conjugated polymer." Adv. Mater. 2003, 15, 146-149.

39. J.L. Bredas, A.J. Heeger, and F. Wudl "Towards Organic Polymers with Very Small Intrinsic Band-Gaps .1. Electronic-Structure of Polyisothianaphthene and Derivatives." J. Chem. Phys. 1986, 85, 4673-4678.

40. H. Neugebauer, C. Kvarnstrom, C. Brabec, N.S. Sariciftci, R. Kiebooms, F. Wudl, and S. Luzzati "Infrared spectroelectrochemical investigations on the doping of soluble poly(isothianaphthene methine) (PIM)." J. Chem. Phys.1999, 110, 12108-12115.

41. Q.Q. Shi, H.J. Fan, Y. Liu, J.M. Chen, L.C. Ma, W.P. Hu, Z.G. Shuai, Y.F. Li, and X.W. Zhan "Side Chain Engineering of Copolymers Based on Bithiazole and Benzodithiophene for Enhanced Photovoltaic Performance." Macromolecules 2011, 44, 4230-4240.

42. C. Piliego, T.W. Holcombe, J.D. Douglas, C.H. Woo, P.M. Beaujuge, and J.M.J. Fréchet "Synthetic Control of Structural Order in N-Alkylthieno[3,4-c]pyrrole-4,6-dione-Based Polymers for Efficient Solar Cells." J. Am. Chem. Soc. 2010, 132, 7595-7597.

43. J.M. Szarko, J.C. Guo, Y.Y. Liang, B. Lee, B.S. Rolczynski, J. Strzalka, T. Xu, S. Loser, T.J. Marks, L.P. Yu, and L.X. Chen "When Function Follows Form: Effects of Donor Copolymer Side Chains on Film Morphology and BHJ Solar Cell Performance." Adv. Mater. 2010, 22, 5468-5472.

44. Personal communication from the research group of Prof. Fréchet. 2011.

45. N.C. Cates, R. Gysel, J.E.P. Dahl, A. Sellinger, and M.D. McGehee "Effects of Intercalation on the Hole Mobility of Amorphous Semiconducting Polymer Blends." Chem. Mater. 2010, 22, 3543-3548.

46. N.C. Cates, R. Gysel, Z. Beiley, C.E. Miller, M.F. Toney, M. Heeney, I. Mcculloch, and M.D. McGehee "Tuning the Properties of Polymer Bulk Heterojunction Solar Cells by Adjusting Fullerene Size to Control Intercalation." Nano Lett. 2009, 9, 4153-4157.

47. C.V. Hoven, X.D. Dang, R.C. Coffin, J. Peet, T.Q. Nguyen, and G.C. Bazan "Improved Performance of Polymer Bulk Heterojunction Solar Cells Through the Reduction of Phase Separation via Solvent Additives." Adv. Mater. 2010, 22, E63-E66.

48. J.K. Lee, W.L. Ma, C.J. Brabec, J. Yuen, J.S. Moon, J.Y. Kim, K. Lee, G.C. Bazan, and A.J. Heeger "Processing additives for improved efficiency from bulk heterojunction solar cells." J. Am. Chem. Soc. 2008, 130, 3619-3623.

49. J.S. Moon, C.J. Takacs, S. Cho, R.C. Coffin, H. Kim, G.C. Bazan, and A.J. Heeger "Effect of Processing Additive on the Nanomorphology of a Bulk Heterojunction Material." Nano Lett. 2010, 10, 4005-4008.

50. J. Peet, J.Y. Kim, N.E. Coates, W.L. Ma, D. Moses, A.J. Heeger, and G.C. Bazan "Efficiency enhancement in low-bandgap polymer solar cells by processing with alkane dithiols." Nat. Mater. 2007, 6, 497-500.

51. T.W. Holcombe, C.H. Woo, D.F.J. Kavulak, B.C. Thompson, and J.M.J. Frechet "All-Polymer Photovoltaic Devices of Poly(3-(4-n-octyl)-phenylthiophene) from Grignard Metathesis (GRIM) Polymerization." J. Am. Chem. Soc. 2009, 131, 14160-14161.

52. C.H. Woo, T.W. Holcombe, D.A. Unruh, A. Sellinger, and J.M.J. Frechet "Phenyl vs Alkyl Polythiophene: A Solar Cell Comparison Using a Vinazene Derivative as Acceptor." Chem. Mater. 2010, 22, 1673-1679.

image in next page:

details from M. K. Čiurlionis "Summer", 1907.

>6

STUDY OF STABILITY AND DEGRADATION OF MATERIALS FOR ORGANIC LUMINESCENT SOLAR CONCENTRATORS

6.1 INTRODUCTION

Thin-film organic-based luminescent solar concentrators (OLSCs) represent a promising technology to improve power conversion efficiency of photovoltaic systems inexpensively.[1-4]

A typical thin-film OLSC consists of a luminescent organic dye dissolved into a thin film of a transparent matrix material deposited onto a glass plate. The luminescent species absorb the incident solar light and isotropically re-emit it red-shifted. A large part of the emitted photons is trapped in the OLSC plate by total internal reflection and wave-guided towards the edges, where high efficiency solar cells are placed. Ideally, the energy of photons emitted by the luminescent organic dye should match that of the band gap of the attached solar cells, to ensure high quantum yield and optimal power conversion efficiency.[5-8] Together with power conversion efficiency of devices, a major challenge for OLSC deployment is the photostability of the luminescent dye and the polymer matrix.

Poly(methyl methacrylate) (PMMA) has proven to be a very good candidate to be used as polymeric carrier matrix as it is highly transparent over a wide wavelength range, it possesses a high refractive index and it is easily processable. However, this polymer still presents some limitations related to its environmental stability upon exposure to light. It is known from the literature[9] that the photo-degradation of PMMA at room temperature involves photolysis of the macromolecular structure resulting in the random scission of the polymer backbone by a radical process. In particular, three major reactions are reported to occur during this process, namely random homolytic scission of main-chain carbon-carbon bonds, photolysis of the ester side-groups and photo-dissociation of the methyl side-groups. The effect of alkyl side group dimension was also reported to have an effect on the photo-stability of poly(alkyl methacrylate)s.[10] In particular, it was found that UV-irradiated PMMA undergoes slower photo-oxidation and destruction of ester groups with respect to other poly(alkyl methacrylate)s. This result was attributed to oxygen diffusion into the polymer bulk, made easier by the longer alkyl chains in the ester group in poly(butyl methacrylate) and poly(hexyl methacrylate) than in PMMA that yield higher flexibility and higher mobility of the macrochains.

Together with the environmental stability of the carrier matrix, the interactions between the polymer matrix, the luminescent species and light must also be taken into account when the stability of OLSC devices is considered.

In an early study on perylene-dye-doped PMMA sheets,[11] the effect of OLCS preparation method on device stability to UV light was investigated. By means of FTIR analysis it was demonstrated that thermally polymerized OLSC films exhibited higher stability with respect to films casted from solvent. This finding was confirmed by measurements of the optical density of the perylene dye, that appeared to be more prone to degradation when dispersed in solvent-casted

PMMA.

In a later work by the same group,[12] a different approach to improve the stability of the OLSC devices was explored making use of copolymers of styrene and methyl-methacrylate (MMA) to fabricate the carrier matrix. It was shown that by incorporating a commercial fluorescent dye into a poly(styrene-co-methyl methacrylate) matrix, a better photo-stability was observed compared with PMMA alone. In particular, the half-life of the dye in the copolymer matrix was proven to be more than five times longer than in the PMMA matrix as observed by field performance tests.

In addition to optimizing the matrix materials to obtain the most suitable transparent carrier, the methods used to cast and cure the polymer matrix can have an effect on OLSC stability. In a recent study by Kinderman et al.,[13] it was shown that better OLSC stability could be achieved by using dye-doped PMMA coatings on glass plates instead of dye-doped bulk PMMA samples. This result was attributed to the presence of additives in the bulk PMMA samples, which were not present in the polymer coatings. In addition, the UV-curing step needed for the polymerization of the monomer was also thought to be responsible for the photo-oxidative degradation of the luminescent species resulting in poorer environmental stability of bulk PMMA matrix compared with PMMA coatings.

The effect of oxygen on the degradation of polymer-dissolved perylene-based dyes was evaluated by monitoring the fluorescence intensity during exposure to laser pulses in the visible spectrum (532 nm).[14] Photo-oxidation was shown to be the main mechanism responsible for the photo-degradation of the OLSC device. On the other hand, samples exposed to laser pulses in anaerobic conditions underwent partially reversible photo-reduction. As a way to extend the lifetime of devices, authors recommended the fabrication of devices in an oxygen-free environment or the incorporation of additives such as oxygen quenchers or triplet state quenchers to suppress photo-oxidation of the OLSC.

As a further way of improving OLSC device stability, the incorporation of luminescent perylimide dyes into an inorganic glass fabricated by means of the sol-gel technique was studied.[15] It was found that OLSC devices produced in this way showed improved stability compared to conventional OLSC based on dye-doped transparent polymer matrices. In particular, these systems exhibited 65 % of their initial fluorescence after exposure to the equivalent of five years of outdoor weathering. These results were complemented by a Montecarlo analysis on the optical efficiency of the fabricated OLSC devices, resulting in a predicted 20 % optical efficiency for this system.

As evidenced by the studies presented so far, OLSC device stability appears highly dependent on the choice of the host matrix and by its fabrication method. In particular, the modifications of the host matrix and its interactions with the luminescent species are responsible for the variations on device performance observed during prolonged exposure to light. Together with polymer matrix degradation, a major contribution to the performance decline in the illuminated OLSC device is given by the relatively limited photo-stability of the luminescent dye, particularly when exposed to UV light.[16,17] Although a number of organic dyes showing high fluorescence quantum yield combined with relatively good photo-stability have been presented in the literature,[18-20] the reduction of absorption intensity and the fluorescence quenching of the dye molecule following interaction with light remains a critical aspect. In particular, the majority of the studies on OLSC degradation have mainly focused on the evaluation of device performance during prolonged exposure to outdoor light or during laboratory tests (laser or UV light),[13,21-23] but very little is known about the degradation mechanisms of the luminescent species occurring after irradiation. However, a clear understanding of the degradation behavior of light-exposed dye molecules at the molecular level is required in order to develop strategies to lengthen OLSC life-time.

In this Chapter, we report a study on the photo-degradation of a thin-film OLSC consisting of a model organic luminescent perylene-based dye dissolved in a PMMA matrix, deposited onto a glass slide. The OLSC was exposed in air to high-energy UV-light and its photostability was characterized by means of FTIR, UV-vis and photoluminescence spectroscopy during irradiation time. The behavior of each material constituting the OLSC device was monitored (PMMA alone, luminescent dye alone and combination of the two) and a degradation mechanism for the dye molecule was proposed. In addition, the role of the organic dye molecule in the degradation of PMMA was analyzed and the effect of the state of aggregation of the organic dye on its photo-stability was clarified.

The ultimate goal of this study was to analyze the behavior of the organic dye in strongly radicalic conditions.

6.2 EXPERIMENTAL

6.2.1 Materials

All materials from commercial sources employed in this study were used as received, without further purification. Poly(methyl methacrylate) (PMMA) was used as the material for the carrier matrix. PMMA was dissolved in chloroform prior to deposition of the thin film onto glass substrates. A perylene-based fluorescent dye (Lumogen F Red 305, purchased from BASF) was used as the fluorescent species in the thin-film OLSC (see Figure 6.1). Chloroform (Sigma-Aldrich) was used as solvent in all tests. Microscope slides (1 mm thick, purchased from Thermo Scientific) were used as rigid transparent substrates for the fabrication of the thin-film OLSC.

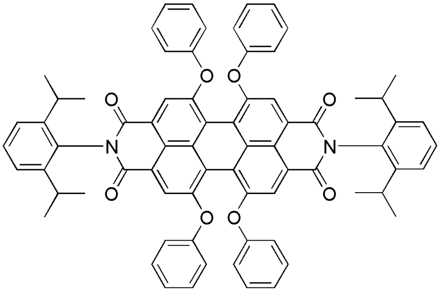

Figure 6.1. Molecular structure of the organic dye employed in this work (Lumogen F Red 305 by BASF).

6.2.2 Instrumentation

Fourier-transform infrared spectroscopy, UV-Vis spectroscopy and fluorescence spectroscopy were performed on solid state samples deposited onto NaCl, KBr or glass/quartz substrates by spin-coating (WS-400B-NPP Spin-Processor, Laurell Technologies Corp.) at 1200 RPM for 40 sec. The thickness of the solid state samples was adjusted by varying the concentration of the spin-coating solution so that signal saturation could be avoided in FTIR analysis and so that absorbance levels smaller than unity could be ensured in UV-vis analysis. The thickness of the UV-Vis solid state samples was values of absorbance Infrared spectra were recorded at room temperature in transmission mode on a Nicolet 760 – FTIR Nexus Spectrophotometer controlled by OMNIC software. Spectra were obtained using 128 scans and a 2 cm^{-1} resolution. UV-VIS absorption spectra were recorded at room temperature in transmission mode by means of a Jasco V-570 UV-VIS-NIR Spectrophotometer. Fluorescence emission spectra were recorded at room temperature on a Jasco FP-6600 Spectrofluorometer.

For the degradation studies, all samples were irradiated in air by means of a high-power UV-lamp (Mercury vapor lamp GR.E. 500 W, Helios Italquartz) providing UV-light with an emission peak centered at 254 nm. Samples were collected at different UV-irradiation times.

Proton nuclear magnetic resonance (^{1}H-NMR) spectra were recorded on a Bruker AC 400 NMR Spectrometer. All samples for ^{1}H-NMR analysis were dissolved in $CDCl_3$.

Differential scanning calorimetry (DSC) analyses were performed on solid state samples using a DSC/823e-Mettler Toledo differential scanning calorimeter. Scan rate was 10 K/min.

6.3 RESULTS AND DISCUSSION

The photodegradation study was performed by subsequently exposing each material constituting the thin-film OLSC to UV-light in air at increasing irradiation times and by monitoring the modifications occurring to each OLSC component during exposure by means of spectroscopic techniques. The polymer matrix (PMMA) and the organic dye (Lumogen F Red 305, from here on referred to as LR305) were first studied individually and then combined together in a thin film, so as to form the active material of the OLSC.

6.3.1 Polymer matrix

The material constituting the carrier matrix in an OLSC should satisfy a number of prerequisites for optimal operation. Firstly, the matrix should be highly transparent in the UV-vis spectral range in order not to interfere with photons that can be absorbed and re-emitted by the dye. Furthermore, the matrix should possess a high refractive index in order to ensure efficient light trapping via total internal reflection. Good photo-stability is also desired so as to guarantee long lifetime of devices. Finally, material cost should be minimized in order to make this technology attractive to market. With the purpose of meeting these requirements, PMMA was chosen in this work as the material for the polymer carrier matrix. PMMA has a high refractive index of about 1.5, it is a transparent polymer in the visible range and in a good portion of the UV range, it is a low-cost material, and it shows better photo-stability compared to other transparent polymeric materials.[2] The photo-stability of the polymer matrix was investigated during irradiation with UV-light by means of UV-vis spectroscopy and FTIR spectroscopy.

6.3.1.1 UV-vis absorption spectroscopy

The normalized UV-vis absorption spectrum of pristine PMMA is shown in Figure 6.2. PMMA presents a low absorption intensity throughout the entire visible spectral range. In contrast, a significantly high absorption peak can be observed in the deep UV range, centered at around 200 nm. This absorption peak may lead to degradation of the material following UV-light exposure, as the UV source employed for the degradation studies reported in this work presents a strong emission peak centered at 254 nm, which is therefore partially absorbed by PMMA.

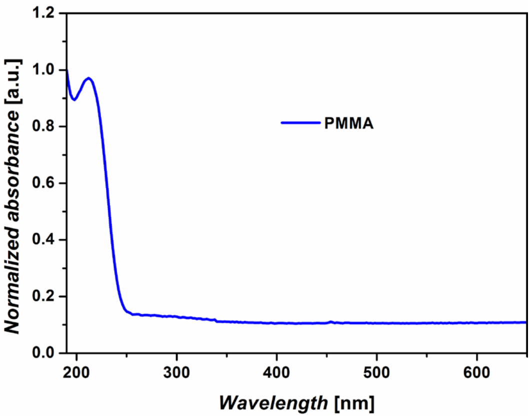

Figure 6.2. UV-vis spectrum of poly(methyl methacrylate) (PMMA).

Changes in the UV-vis absorption spectrum of the material were monitored during the photo-aging process. In the experiments, UV-vis spectra were collected every hour up to a maximum exposure time of 10 h. However, only spectra of samples degraded up to 5 h are presented in this work as this exposure time is long enough to highlight the main degradation pathways occurring to the material. In addition, significantly longer exposure times lead to complete destruction of the material.

The UV-vis spectra of PMMA films at increasing UV-exposure times are shown in Figure 6.3.

UV-irradiation of PMMA films leads to a gradual increase of absorption intensity in the 200 nm - 400 nm range. Such an increase of absorbance can be explained by the formation of unsaturated groups resulting from the scission of the ester side-group in PMMA combined with the formation of carbonyl groups resulting from the interaction of PMMA film with high energy light.[10,24]

In particular, a sharp increase in the absorption intensity of the peak centered at 235 nm is observed after 1 h of UV-light exposure accompanied by a blue shift of the same peak of about 15 - 20 nm. On the other hand, a gradual decrease in absorbance is reported for longer exposure times. Such a decrease in absorbance for exposure times longer than 1 h may be attributed to partial loss of material during irradiation.

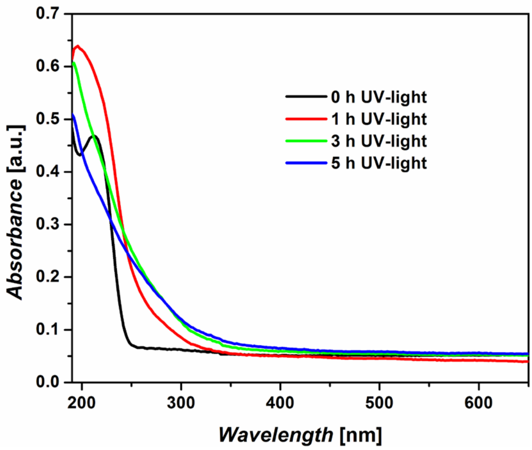

Figure 6.3. UV-vis absorption spectra of PMMA after 0 h, 1 h, 3 h, 5 h exposure to UV-light.

6.3.1.2 Fourier-transform infrared spectroscopy

FTIR spectroscopy was employed to monitor the photo-degradation process of polymer films during UV-irradiation time. After prolonged exposure to UV-light, substantial modifications to the IR spectrum of the polymer were observed. In order to identify the changes occurring during irradiation, the main IR absorption bands for pristine PMMA were identified and are reported in Table 6.1.[10,24]

Table 6.1 Frequencies and assignments of main IR bands for pristine PMMA.

Wavenumber [cm^{-1}]	Assignment
3100-2800	CH_3/CH_2 str. (asym, sym)
1731	C=O str.
1485	CH_2 bend.
1242	C-O-C str.
1192	C-O str. asym
1149	C-O str. sym
754	C-O bend.

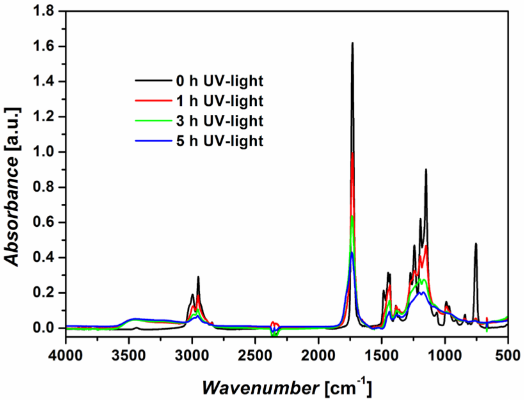

Figure 6.4. FTIR spectra of PMMA after 0 h, 1 h, 3 h and 5 h exposure to UV-light.

The evolution of the FTIR spectra in the entire IR region during the degradation process is presented in Figure 6.4, where the FTIR spectra of pristine PMMA and PMMA exposed to UV-light for 1 h, 3 h and 5 h are shown.

Significant modifications in the FTIR spectra may be observed already after 1h of UV light exposure in the whole IR region. A general reduction of all peak intensities is found in the entire spectrum. In addition, the appearance of new signals ascribable to the formation of new species can be observed at around 3500 cm^{-1} and in the carbonyl region (1850-1650 cm^{-1}), adjacent to the main carbonyl peak (C=O str.) centered at 1731 cm^{-1}. In addition, by increasing the UV-exposure time, a large and complex absorption band is formed between 1500 cm^{-1} and 1000 cm^{-1}.

In order to better clarify the changes in the FTIR spectra of degraded samples, a more detailed analysis of each characteristic IR region of PMMA is now presented. In particular, the hydroxyl/hydroperoxide stretching region, the methyl/methylene stretching region, the region around the carbonyl stretching band and the C-O-C stretching region will be successively considered. Figure 6.5 shows the FTIR spectra of PMMA films in the 3800 – 2600 cm^{-1} region, characteristic of stretching vibrations associated to hydroxyl/hydroperoxide groups (3800 – 3200 cm^{-1}) and to methyl/methylene groups (3200 – 2600 cm^{-1}). In the methyl/methylene region of the spectrum of pristine PMMA three main peaks and a shoulder can be distinguished, centered at 2995 cm^{-1}, 2950 cm^{-1}, 2840 cm^{-1} and 3025 cm^{-1}, respectively. These peaks can be attributed to the following methyl and methylene group vibrations:[10] sym CH_3-O, asym α-CH_3, sym α-CH_3, sym CH_2.

In degraded PMMA films these peaks can still be observed, although slightly shifted in frequency. In particular, after 5 h UV-exposure a 5 cm^{-1} shift to higher frequencies is observed for the symmetric α-CH_3 and CH_2 stretching vibrations, while an 18 cm^{-1} red-shift is found for the asym α-CH_3 stretching vibration with a progressive disappearance of the shoulder at 3025 cm^{-1}. In addition, by increasing

UV-exposure time these signals exhibit increasingly lower intensity compared to pristine polymer. This decrease in intensity may be attributed to gradual disappearance of methyl and methylene groups due to UV-irradiation, although partial loss of material during the degradation process may also have occurred. However the decrease of FTIR absorption intensity of methyl/methylene groups can be due not only to degradation resulting from side groups abstraction, but also to oxidation. In particular, oxidation products formed during exposure of the polymer films to UV light may undergo further photolysis leading to the formation of volatile low molecular weight products.[10,25]

In the 3800 – 3200 cm^{-1} region, a progressive increase in absorption intensity is observed with irradiation time. In particular, a new broad band appears with a peak centered at around 3500 cm^{-1}. Such a broad band is typical for free (non-associated) and hydrogen-bonded hydroxyl/hydroperoxide groups, which cannot be easily distinguished and that may form during the degradation process as by-products.[10,25]

The FTIR spectra of PMMA films in the carbonyl region at different UV-light exposure times are shown in Figure 6.6. A significant decrease of the absorption intensity of the main carbonyl peak (1731 cm^{-1}) is observed upon UV-irradiation time, suggesting photolysis and elimination of the ester group from the PMMA main chain. Concurrently, the development of carbonyl shoulders at 1700-1650 and 1750-1850 cm^{-1} is also observed. This positive change in the carbonyl region may indicate the formation of oxidation products resulting from the photo-oxidative degradation process. In particular, the high frequency region of the carbonyl peak (1750–1850 cm^{-1}) may be attributed to the formation of carboxylic and ester groups, whereas the low frequency portion (1700–1650 cm^{-1}) can be associated to the formation of aliphatic ketones and aldehydes.[10,25]

The overall modifications of the carbonyl band leading to variations in the total amount of carbonyl groups in PMMA can be explained by considering the occurrence of two distinct competitive processes during UV-exposure: decomposition of the polymer with destruction or abstraction of the ester group and oxidation with formation of new oxidised species at the end or inside the polymer chains.[25] As shown in Figure 6.7 where the spectra obtained from subtraction of pristine polymer spectrum from 1 h and 3 h degraded sample spectra are presented, the decrease in the main carbonyl peak occurring upon UV-exposure is accompanied by a progressive increase in the carbonyl shoulders associated to the formation of new oxidized species.

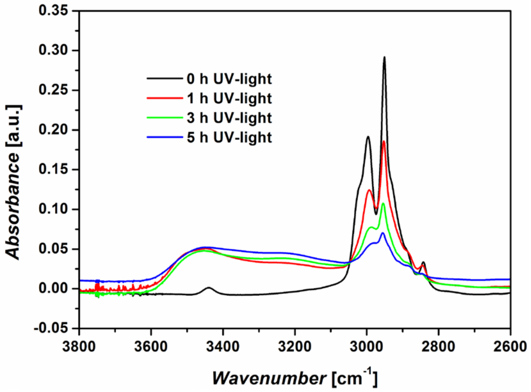

Figure 6.5. FTIR spectra of PMMA after 0 h, 1 h, 3 h and 5 h exposure to UV-light in the 3800-2600 cm^{-1} region.

The modifications occurring in the 1300-1000 cm^{-1} region characteristic of the stretching vibrations of C-O-C bonds can also be used to monitor the degradation process of PMMA. In particular, a change in the amount of these groups should be clearly noticeable in FTIR spectra of degraded samples. As shown in Figure 6.8 the absorption peak at 1240 cm^{-1} shows a significant decrease during UV irradiation accompanied by a broadening of the peaks and by the development of more complex features in the 1300-1100 cm^{-1} range. These modifications to the signals attributed to the asymmetric stretching vibration of C-O-C bonds may be ascribed to destructive reactions occurring to side groups of PMMA during UV exposure.[10,25]

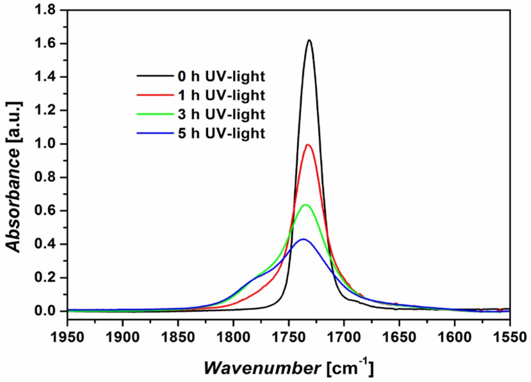

Figure 6.6 FTIR spectra of PMMA after 0 h, 1 h, 3 h and 5 h exposure to UV-light in the 1900-1600 cm^{-1} region.

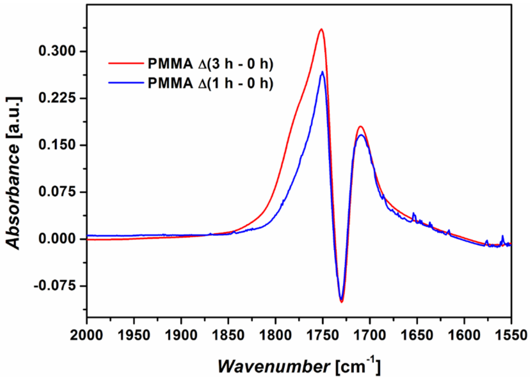

Figure 6.7 FTIR subtraction spectra in the carbonyl region. Spectra were obtained by subtracting the FTIR spectrum of pristine PMMA from 1 h and 3 h UV-light exposed samples, respectively.

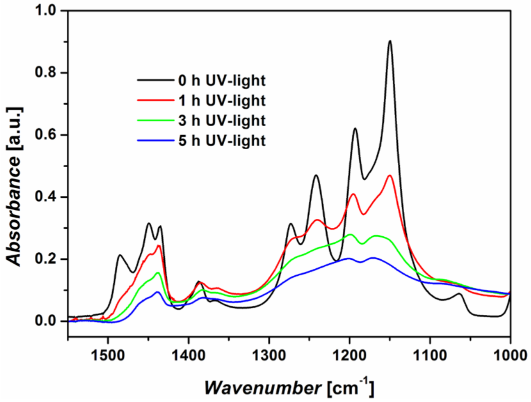

Figure 6.8 FTIR spectra of PMMA after 0 h, 1 h, 3 h and 5 h exposure to UV-light in the 1500-1000 cm^{-1} region.

6.3.2 Organic luminescent dye

Luminescent species dissolved in the carrier matrix absorb incident light and isotropically re-emit it at longer wavelengths. Total internal reflection within the polymer matrix ensures wave-guiding of the light emitted by the organic dye towards the edges of the OLSC device where solar cells are placed. Ideally the energy of the emitted photons should be slightly higher than the band gap of the attached solar cells so as to yield near-unity conversion efficiency. Therefore, organic dyes suitable for OLSC technology should exhibit high luminescent quantum yield (LQY) together with high solubility in the polymeric matrix and in organic solvents. The LQY is partly dependent on the Stokes shift of the organic dye, i.e. on the difference in wavelength between its absorption and emission peak maxima. The organic luminescent dye employed in this work exhibits a rather high

Stokes shift (~ 40 nm), as shown in Figure 6.9 where its absorption and emission spectra are presented.

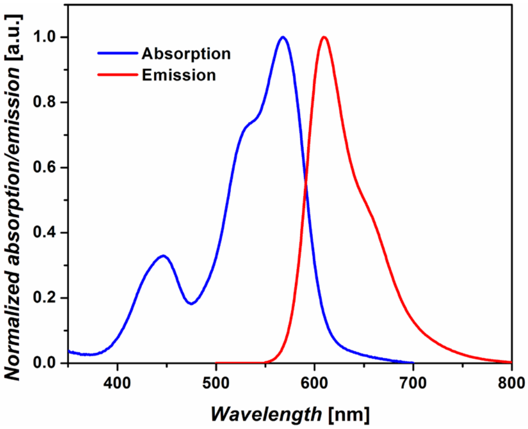

Figure 6.9. Normalized absorption and emission spectra of the organic dye molecule employed in this work (LR305).

Similarly to what carried out for the PMMA studies, the photo-stability of the organic dye was investigated by monitoring the modifications occurring to UV-vis, fluorescence and FTIR spectra upon exposure to UV-light.

6.3.2.1 UV-vis absorption spectroscopy

Figure 6.10 presents the UV-vis absorption spectrum of LR305 in the solid state. The molecule presents a high absorption intensity in the UV portion of the spectrum (190 nm – 350 nm), with two distinct peaks centered at 194 nm and 283 nm.

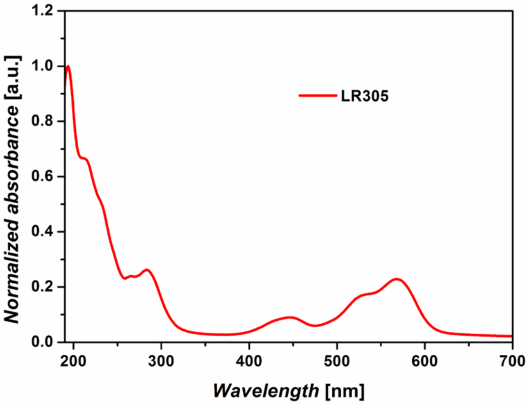

Figure 6.10. UV-vis absorption spectrum of the organic dye molecule LR305.

The high absorption intensity found at 194 nm may suggest that LR305 can potentially act as UV-absorber when combined to the polymeric carrier matrix, thus leading to stabilization of PMMA. This aspect will be discussed more in detail in Section 6.3.4.

In the visible region (350 nm – 700 nm), two main absorption bands can be distinguished: a broad higher-intensity absorption band at longer wavelengths with a peak centered at 568 nm and a lower-intensity absorption band centered at 445 nm. In order to clarify the origin of each of these absorption bands, the LR305 absorption spectrum was compared to the UV-vis spectrum of a perylene-di-imide derivative (PDI) that shows a similar molecular structure to LR305, but does not exhibit lateral substituents attached to the perylene core (see Figure 6.11).

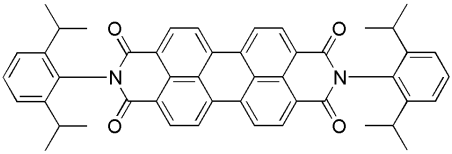

Figure 6.11. Molecular structure of the perylene di-imide derivative (PDI) considered for UV-vis spectra comparisons.

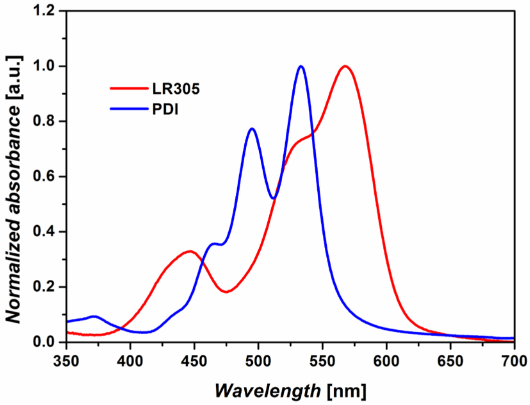

Figure 6.12. UV-vis spectra of LR305 and PDI in the visible region (350 nm - 700 nm).

As shown in Figure 6.12 where the absorption spectra of LR305 and PDI in the visible region are presented, PDI shows a single complex absorption band in the range 350 – 700 nm, which can be attributed to a single absorbing group. On the other hand, in the same region LR305 exhibits two distinct peaks (445 nm and 568 nm) that can be associated to two different absorbing groups. Accordingly, the longer-wavelength broader absorption band in LR305 may be assigned to the absorption of the perylene core as a similar composite peak is also found in the UV-vis spectrum of PDI. Conversely, the peak centered at 445 nm may be attributed to the absorption of the lateral phenyl groups, not present in PDI.

The degradation process of LR305 was investigated by monitoring the modifications occurring to the UV-vis spectra of the dye at increasing UV-irradiation time, as shown in Figure 6.13.

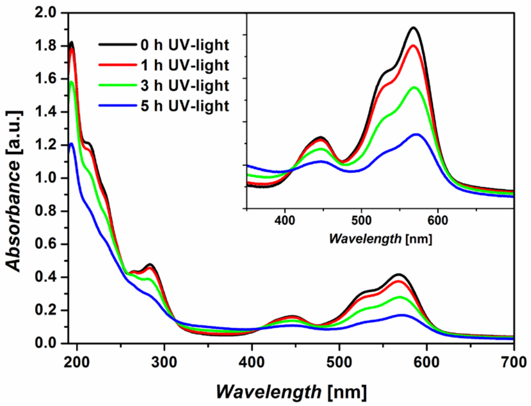

Figure 6.13. UV-vis absorption spectra of LR305 after 0 h, 1 h, 3 h and 5 h of UV-irradiation. The inset shows a close-up of the absorption spectra in the visible range 350 – 700 nm.

A general decrease of intensity is observed for all absorption bands at increasing UV-exposure time. In addition, a 5 nm red-shift is found for the main absorption peak after 5 h of exposure to UV-light (568 – 573 nm). Longer exposure times lead to a further decrease in absorption intensity together with a more pronounced red-shift of the main perylene core absorption peak (data not shown).

In order to highlight differences in the modifications occurring to the main absorption peaks of LR305 (445 nm and 568 nm) upon UV-exposure, their intensities were calculated and compared as a function of irradiation time (Figure 6.14). During the first 5 h of irradiation, the intensities of both the signal attributed to the absorption of lateral substituents (445 nm) and the one attributed to perylene core absorption (568 nm) decrease in a similar fashion, suggesting that the degradation rate is comparable for the two groups. However, for longer exposure times, the shorter-wavelength absorption peak starts to exhibit a slightly faster decrease in absorption intensity with respect to the longer-wavelength absorption peak. This observation may indicate that the degradation process initiates with disruption of the lateral substituents attached to the perylene core, although a more detailed discussion on this topic will be presented in Section 6.3.4.

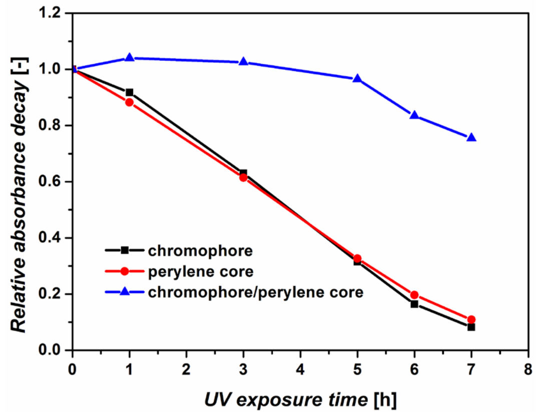

Figure 6.14. Relative absorbance decay of absorption peaks attributed to lateral substituents (445 nm) and perylene core (568 nm). The ratio between the intensities is also shown.

6.3.2.2 Fluorescence spectroscopy

Emission spectra of LR305 thin films deposited onto quartz substrates by spin coating were examined by fluorescence spectroscopy.

As already discussed in Section 6.3.2.1, the dye molecule shows two main absorption bands in the visible spectrum, with peaks centered at 445 nm and 568 nm, respectively. The shorter-wavelength peak was attributed to lateral groups absorption while the longer-wavelength peak to the absorption of the perylene core of the molecule.

Theoretically, the excitation wavelength λ_{exc} employed in fluorescent emission studies should be the same as the absorption peak wavelength (in this case 445 nm and 568 nm) to maximize the emitted signals. However, during experiments part of the monochromatic light used to excite the fluorescent molecule is reflected by the sample and recorded by the detector, thus appearing in the emission spectrum as a false emission peak. Therefore, in order to prevent the presence of a false emission peak centered at 568 nm resulting from light reflection by the sample, in the region of the perylene core absorption λ_{exc} was set to 540 nm (wavelength at which a shoulder is observed in the UV-vis spectrum). In addition, excitation at λ_{exc} = 445 nm was also performed to take into account the contribution to light absorption given by the lateral chromophores.

Figure 6.15 shows the normalized fluorescence spectra of LR305 resulting from excitation at 445 nm and at 540 nm, respectively. Both spectra exhibit a maximum centered at 609 nm and are perfectly overlapping with each other, confirming that a single group (the perylene core) is responsible for the emission process of the dye molecule.

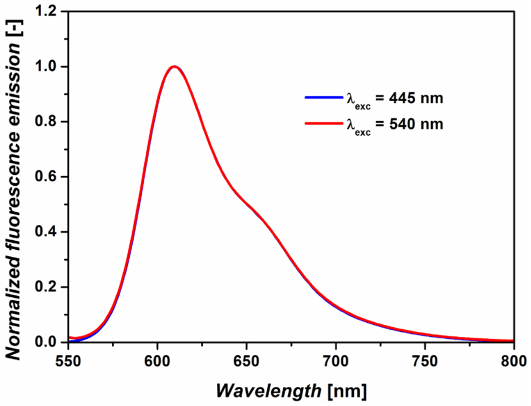

Figure 6.15. Normalized fluorescent emission spectra of pristine LR305 resulting from excitation with 445 nm and 540 nm monochromatic light.

During experimental analysis, the intensity of the emission spectrum of the dye excited at λ_{exc} = 445 nm was found to be lower than that obtained by 540 nm light excitation. This finding may be attributed to the difference in relative absorption intensity between the two main absorption peaks in the UV-vis spectra, being lower for the shorter-wavelength absorption peak.

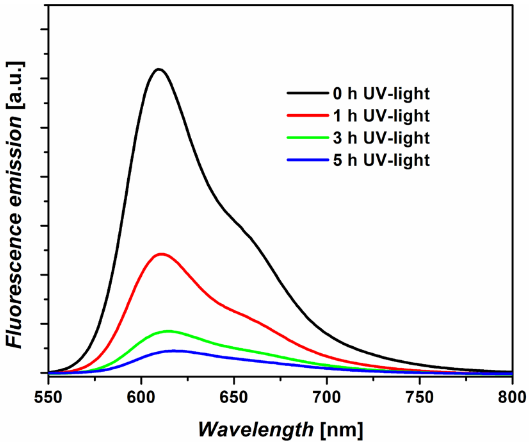

Figure 6.16. Fluorescence emission spectra of LR305 for λ_{exc} = 445 nm at 0 h, 1 h, 3 h, 5 h UV-exposure time.

In order to evaluate the effect of UV-exposure on the fluorescent emission of the dye, fluorescence spectra at increasing UV-irradiation times were collected. Figure 6.16 presents the emission spectra for λ_{exc} = 445 nm. As shown in the plot, the emission intensity decreases at increasing UV-light exposure. In addition, a 9 nm red-shift of the emission peak is observed. These results are in agreement with those found on LR305 UV-vis absorption spectra, where a comparable red-shift of the absorption peak was reported.

Similar trends were also found for the emission spectrum obtained at λ_{exc} = 540 nm (data not shown).

6.3.2.3 Fourier-transform infrared spectroscopy

FTIR spectroscopy was used to monitor the modifications occurring to the dye molecule upon UV-exposure. Figure 6.17 presents the FTIR spectrum of LR305 thin film.

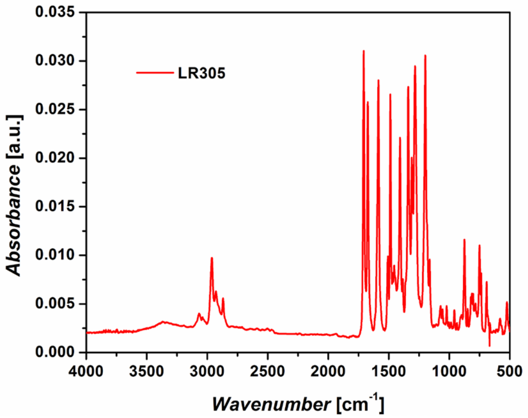

Figure 6.17. FTIR spectrum of pristine LR305.

The FTIR spectrum of the dye presents well defined features in the C-H stretching region, where signals associated to C-H aromatic (3100 – 3000 cm^{-1}) and aliphatic (3000 – 2800 cm^{-1}) stretching vibrations can be clearly recognized. The region between 1800 cm^{-1} and 1000 cm^{-1} includes a complex set of peaks related to the stretching vibrations of carbon bonds and CH deformations (CH_2 and CH_3 bending and wagging). In the range 1000 – 650 cm^{-1}, the out-of-plane region can be distinguished.[26,27]

In order to identify the characteristic vibrations responsible for the signals appearing in the IR spectrum of LR305, comparisons between the FTIR spectrum of the dye and simpler molecules with known FTIR spectra were carried out. A first comparison was performed between LR305 and PDI (see Figure 6.11), as also done during the UV-vis analysis discussed earlier. The molecular structures of the two molecules (Figure 6.1 and Figure 6.11) present a number of similarities. In particular, the same aliphatic groups are observed. Accordingly, the C-H aliphatic region (3000 – 2800 cm^{-1}) of the FTIR spectrum of LR305 and PDI (shown in Figure 6.18) exhibit a similar structure with three narrow peaks centered at 2962 cm^{-1}, 2928 cm^{-1} and 2870 cm^{-1} characterized by comparable relative intensities.

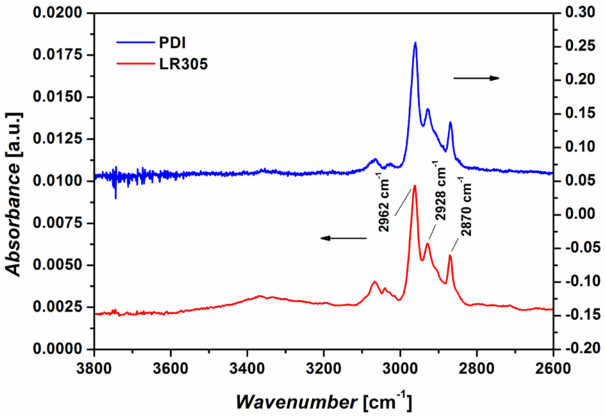

Figure 6.18. FTIR spectra of LR305 and PDI in the 3800 - 2600 cm^{-1} region.

Conversely, some differences between the two spectra can be observed in the aromatic C-H stretching region (3200 – 3000 cm^{-1}). A more defined aromatic C-H stretching band is found in the FTIR spectrum of LR305 which may be attributed to a larger amount of aromatic C-H bonds present in LR305 compared to PDI responsible for those signals. This difference may be explained by considering the presence of four additional lateral substituents in the LR305 molecule, which are indeed four aromatic rings.

The comparison between LR305 and PDI was extended to the 1800 – 1000 cm^{-1} region (Figure 6.19), where some differences can be clearly observed. As the two molecules possess the same perylene core, it is expected that the main differences emerging from their FTIR spectra be ascribable to vibrations of the bonds relative to the lateral substituents, which are not present in PDI.

In the carbonyl region (1800 – 1650 cm^{-1}) two narrow peaks can be observed in both spectra. These signals may therefore be assigned to in-phase and out-of-phase vibrations of C=O bonds, which are present in both molecules. The peak centered at 1586 cm^{-1} found in the LR305 spectrum may be assigned to the stretching vibrations of C=C bonds in the perylene core. An equivalent peak is also observed in the PDI spectrum, as expected. One peak centered at 1487 cm^{-1} is found in the LR305 spectrum, which is not observed in the PDI spectrum. Accordingly, this signal may be assigned to the stretching vibrations of C=C bonds in the lateral aromatic rings, only present in LR305.

Although with some differences in their relative intensities, the peaks at 1408 cm^{-1}, 1385 cm^{-1}, 1361 cm^{-1} and 1340 cm^{-1} can be observed in both spectra. As these peaks are related to single bond stretching vibrations, they could be attributed both to C-C stretching and C-N stretching.

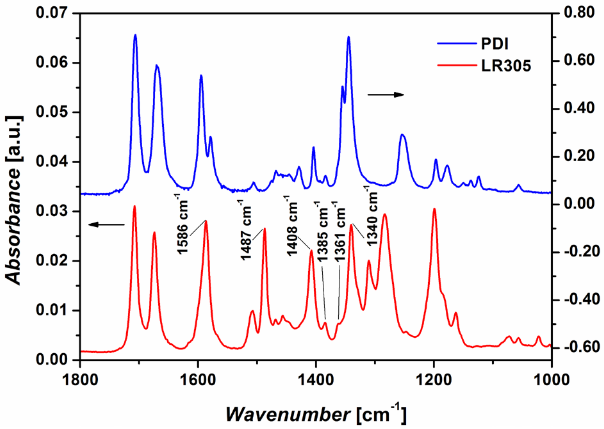

Figure 6.19. FTIR spectra of LR305 and PDI in the 1800 - 1000 cm^{-1} region.

It is worth noticing that a small contribution to the 1586 cm^{-1} FTIR signal can also be given by the C=C stretching vibrations of the lateral substituents, as evident by comparing the FTIR spectrum of LR305 with that of diphenyl-ether (DPE, Figure 6.20), a simple molecule in which identification of FTIR peaks can be performed more easily. The FTIR spectra of the two molecules in the 1700-1400 cm^{-1} region is shown in Figure 6.21. Indeed, a low-intensity peak is also observed in the DPE spectrum at 1590 cm^{-1}.

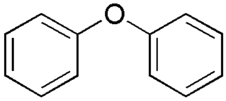

Figure 6.20. Molecular structure of diphenyl-ether (DPE).

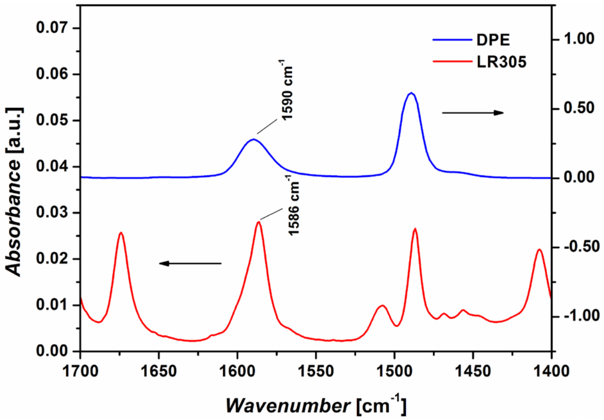

Figure 6.21. FTIR spectra of LR305 and DPE in the 1700 – 1400 cm^{-1} region.

A comparison of FTIR spectra of LR305 and PDI in the out-of-plane region (1000 – 650 cm^{-1}) is presented in Figure 6.22.

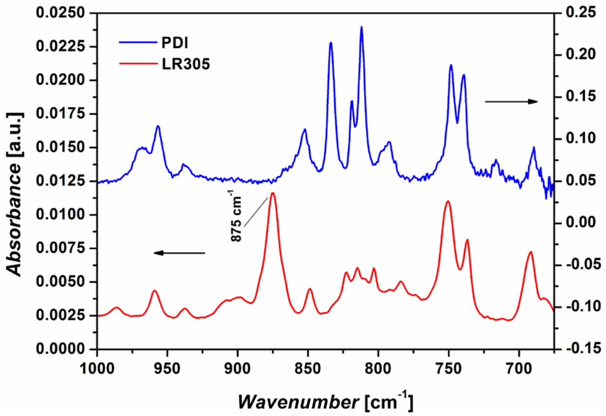

Figure 6.22. FTIR spectra of LR305 and PDI in the 1000 – 650 cm^{-1} region.

As shown in the plots, the main difference arising from the two spectra is represented by the presence of an absorption peak centered at 875 cm^{-1} in the LR305 spectrum, which is not observed in PDI. The assignment of this peak was possible on the basis of a further comparison between LR305 and DPE in the out-of-plane region (Figure 6.23).

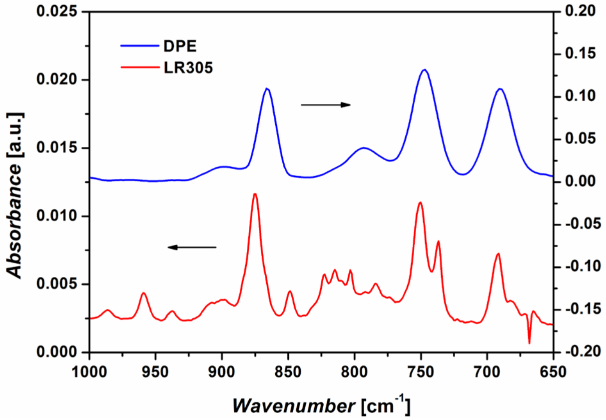

Figure 6.23. FTIR spectra of LR305 and DPE in the 1000 – 650 cm^{-1} region.

In particular, both LR305 and DPE show a sharp single peak around 880 – 850 cm^{-1}. Quantum chemical calculations were employed[28] to study this system and this peak was assigned to the breathing of the benzene ring of DPE. Since no such peak is found in the PDI spectrum (see Figure 6.22), this signal is expected to be due to vibrations of bonds not present in PDI. Accordingly, it was attributed to the breathing of the lateral benzene rings attached to the perylene core in the LR305 molecule.

The modifications to the FTIR spectrum of LR305 upon UV-exposure were analyzed in order to evaluate the photo-stability of the dye molecule. In particular, three main absorption peaks were monitored during the degradation process. The peaks centered at 1586 cm^{-1} and 1340 cm^{-1} were elected as markers of the behavior of the perylene core, while the peak assigned to the lateral ring breathing (875 cm^{-1}) was chosen as the indicator of the modifications occurring to the lateral substituents. The evolution of the FTIR spectra of the dye molecule at increasing UV-light exposure time is shown in Figure 6.24, where a focus on the C-H stretching region (3200 – 2800 cm^{-1}) is presented.

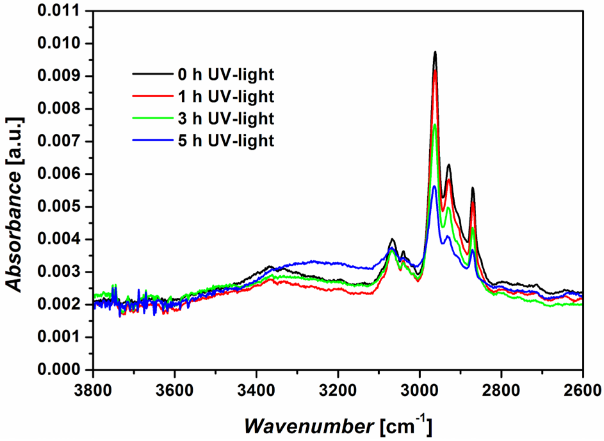

Figure 6.24. FTIR spectra of LR305 at 0 h, 1 h, 3 h, 5 h UV-exposure time in the 3200 - 2800 cm^{-1} region.

The prolonged exposure to UV-light yields a progressive decrease in absorption intensity in the entire C-H stretching region, including both aromatic (3200 – 3000 cm^{-1}) and aliphatic (3000 – 2800 cm^{-1}) bonds. In addition, a new absorption band seems to appear in the range 3400 – 3100 cm^{-1} with a peak centered at about 3350 cm^{-1}. This new feature may be due to the formation of hydroxyl species occurring during the photo-oxidation process, although absorption of moisture by the sample upon UV-irradiation may have also occurred.

In the 1800 – 1600 cm^{-1} carbonyl region (Figure 6.25), a similar decrease of absorption intensity is observed. In addition, the appearance of a wide band centered at around 1775 cm^{-1} is reported, whose intensity progressively increases upon exposure to UV-light. This band may be assigned to stretching vibrations of C=O bonds originating from the formation of new oxidized species appearing during irradiation.

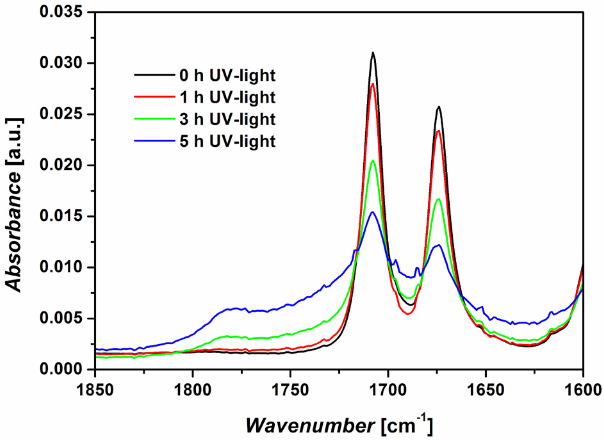

Figure 6.25. FTIR spectra of LR305 at 0 h, 1 h, 3 h, 5 h UV-exposure time in the 1850 - 1600 cm^{-1} region.

Figure 6.26 presents the evolution of FTIR spectra of LR305 in the 1650 – 1000 cm^{-1} region upon UV-irradiation. A general decrease in absorption intensity can be observed in this region, accompanied by a broadening of the absorption bands that increases with UV-light exposure time.

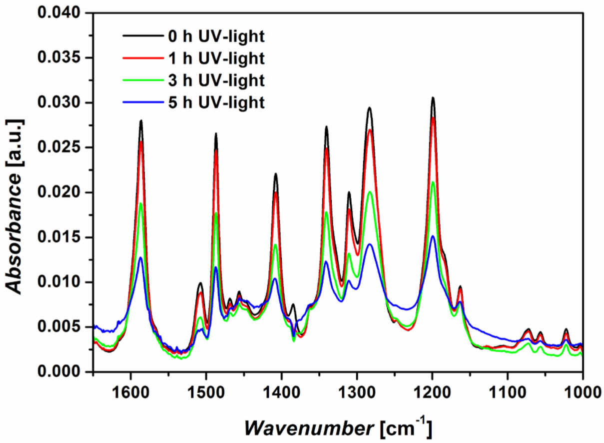

Figure 6.26. FTIR spectra of LR305 at 0 h, 1 h, 3 h, 5 h UV-exposure time in the 1650 - 1000 cm^{-1} region.

The appearance of more complex features in this region may be related to the formation of degraded species upon UV-irradiation that lead to additional IR signals compared to the pristine dye molecule.

A similar behavior was found in the out-of-plane region of the IR spectrum, where no relevant peaks appear to form upon exposure to UV-light (Figure 6.27).

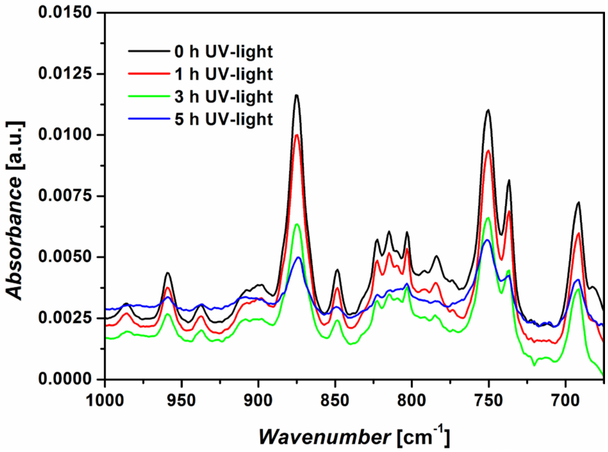

Figure 6.27. FTIR spectra of LR305 at 0 h, 1 h, 3 h, 5 h UV-exposure time in the 1000 - 675 cm^{-1} region.

In order to better analyze the modifications occurring to the FTIR spectra of LR305 during exposure to UV-light, absorption intensities of characteristic peaks of the dye molecule were measured. In particular the signal assigned to the ring breathing (875 cm^{-1}) was monitored and compared to signals attributed to characteristic vibrations of the perylene core, namely the peak centered at 1586 cm^{-1} (C=C stretching) and the peak centered at 1340 cm^{-1} (C-C/C-N stretching). The relative absorbance decay of these peaks is presented in Figure 6.28 as a function of UV-exposure time.

As shown in the plot, the rate of disappearance of the peak associated to the lateral phenyl ring breathing appears only slightly faster than the decay of the signals attributed to the perylene core, suggesting that the degradation process may affect more easily the lateral substituents than the perylene core. On the contrary, a substantially similar absorbance decay is observed for C-C/C-N bond vibrations (1340 cm^{-1}) compared to the lateral ring breathing (875 cm^{-1}). These results are in agreement with the observations reported previously on the evolution of UV-vis absorption spectra of the dye molecule during UV-irradiation.

A further analysis on the modifications occurring to the organic dye molecule dissolved in the polymeric carrier matrix is needed to clarify the effect of dye degradation on the behavior of the actual OLSC film. This analysis is presented in the next section.

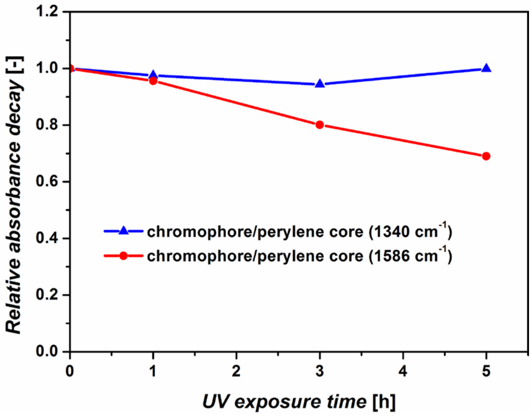

Figure 6.28. Relative absorbance decay over UV-exposure time of FTIR absorption peaks in LR305 associated with bond vibrations in the lateral chromophore substituents (875 cm^{-1}) and in the perylene core (1586 cm^{-1} and 1340 cm^{-1}).

6.3.3 Thin-film organic luminescent solar concentrator

In order for the photo-luminescence properties of the organic dye to be optimized during OLSC device operation, the dye needs to be mixed in relatively low concentrations in a transparent carrier matrix, which is most commonly a polymeric material such as PMMA. When this solution is deposited as thin film, the dye particles are uniformly distributed in the free volume of the polymeric binder. Self-absorption is therefore significantly reduced, as photons emitted by the dye molecule have a low probability to hit and be absorbed by an adjacent dye molecule.

The OLSC thin films analyzed in this Section were obtained by spin-coating a rigid transparent substrate (quartz or glass slide) with a solution of PMMA and LR305 in $CHCl_3$ solvent. In the photo-degradation studies on the OLSC thin-film (from here on referred to as OLSC-TF), PMMA concentration was set at 10 wt. % to $CHCl_3$ while the dye concentration was set at 6 wt. % to PMMA.

Photo-degradation studies on OLSC-TF were carried out by means of fluorescence emission, UV-vis and FTIR spectroscopy. The results obtained from these analyses were then compared to those obtained from the studies presented earlier on the polymer matrix and the organic dye.

6.3.3.1 UV-vis absorption spectroscopy

The solid-state UV-vis absorption spectrum of OLSC-TF is shown in Figure 6.29. Similarly to what found for the dye-only (LR305) absorption spectrum (see Figure 6.10), two different absorption peaks are observed.

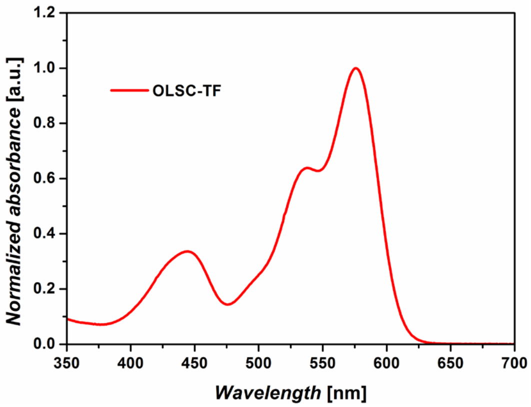

Figure 6.29. Normalized UV-vis absorption spectrum of the OLSC thin film (OLSC-TF).

The shorter-wavelength absorption peak centered at 445 nm is attributed to the absorption of the lateral substituents of the dye molecule, as reported earlier for LR305. The longer-wavelength absorption peak is associated to the absorption of the perylene core of the dye molecule. This peak exhibits an 8 nm red-shift compared to the same peak in the LR305 UV-vis spectrum (568 nm vs 576 nm, respectively).

The evolution of the UV-vis absorption spectra of OLSC-TF at increasing UV-exposure times is shown in Figure 6.30. As also reported for LR305, the absorption intensities in the UV-vis spectra progressively decrease at increasing irradiation times. In addition, a 5 nm blue-shift is observed for the higher energy absorption peak after 5 h of UV-exposure.

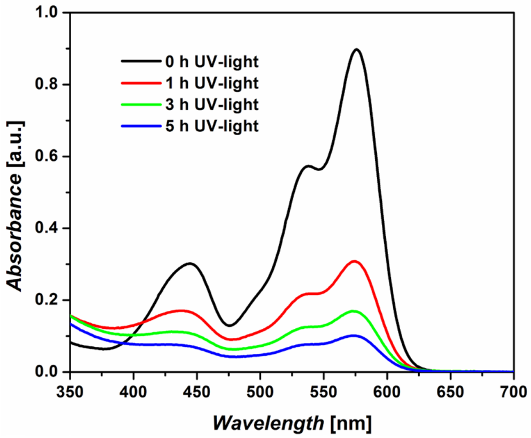

Figure 6.30. UV-vis absorption spectra of OLSC-TF at 0 h, 1 h, 3 h, 5 h UV-exposure time.

The relative intensities of the two main absorption peaks in OLSC-TF were calculated and their trend was monitored over UV-exposure time, in order to highlight differences in the rate of disappearance of the two main peaks characteristic of the two absorbing species in the dye molecule (lateral substituents and perylene core).

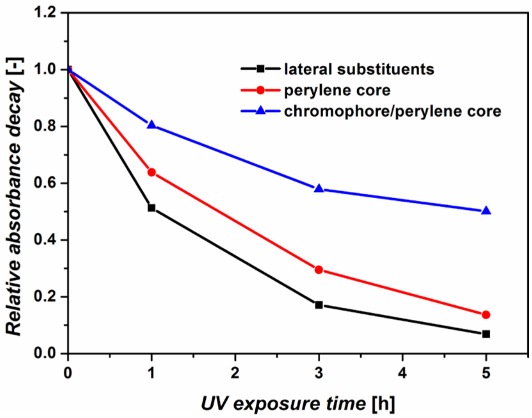

Figure 6.31. Normalized absorbance decay over UV-exposure time of UV-vis absorption peaks attributed to absorption of lateral substituents (shorter-wavelength UV-vis absorption peak) and perylene core absorption (longer-wavelength UV-vis absorption peak). The ratio between their intensities is also shown.

The intensity of the signal associated to the absorption of the lateral substituents of the dye molecule in OLSC-TF (shorter-wavelength absorption peak) appears to undergo a significantly faster decrease upon UV-exposure compared to the perylene core absorption (longer-wavelength absorption peak). In particular, a 50% relative intensity decrease is found for the shorter-wavelength absorption peak already after 1 h of UV-exposure compared to a 30% decrease observed for the longer-wavelength absorption peak. This result may indicate that the degradation process of the dye molecule is more marked on the lateral substituents than on the perylene core.

A similar trend was observed in LR305 thin films although for longer UV-exposure times, suggesting that the dye molecule may exhibit different UV-exposure responses depending on the system in which the organic dye is incorporated (dye-only LR305 or OLSC-TF). A more detailed discussion on this aspect will be presented in Section 6.3.4.

6.3.3.2 Fluorescence spectroscopy

Similarly to what discussed in Section 4.3.2.2 for LR305, fluorescence emission spectra of OLSC-TF were collected at different excitation wavelengths, namely λ_{exc} = 445 nm and λ_{exc} = 540 nm and are presented in Figure 6.32.

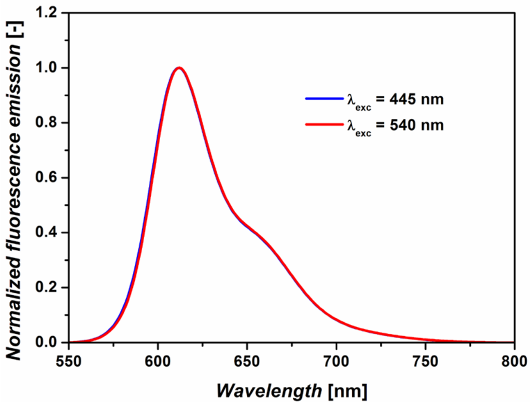

Figure 6.32. Normalized fluorescent emission spectra of OLSC-TF resulting from excitation with 445 nm ad 540 nm monochromatic light.

The same features are observed in both spectra (λ_{exc} = 445 nm and λ_{exc} = 540 nm), with a sharp single emission peak centered at 612 nm. Therefore also in the case of dye molecule dissolved in polymer matrix (OLSC-TF) the emission phenomenon is independent on the excitation wavelength and carried-out by a single molecular group within the organic dye (the perylene core).

In order to monitor the evolution of fluorescence emission during UV-irradiation, emission spectra were collected at increasing exposure times and are presented in Figure 6.33. The same experimental conditions as for the LR305 system were employed during analysis, in order to allow comparisons and highlight differences in the degradation behavior.

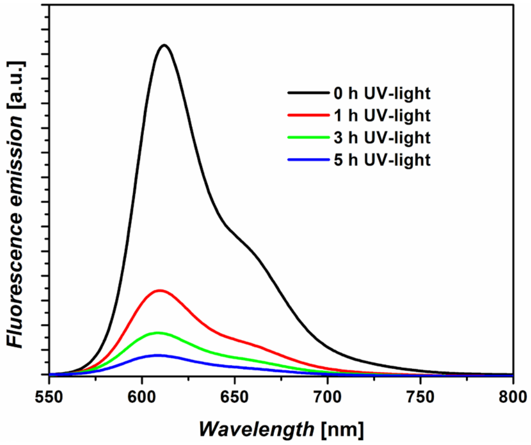

Figure 6.33. Fluorescence emission spectra of OLSC-TF for λ_{exc} = 445 nm at 0 h, 1 h, 3 h, 5 h UV-exposure time.

A decrease of the emission intensity is observed upon exposure to UV-light. In addition, a 5 nm blue-shift of the emission peak is observed after 5 h UV-exposure.

These results are in contrast with those found on LR305 emission spectra, where a red-shift of the emission peak was reported. This difference may be correlated to a different effect of UV-light on the dye molecule that appears to be more invasive in the case of OLSC-TF, where the dye molecule is mixed within the polymeric binder. Similar trends were also found for the emission spectrum obtained at λ_{exc} = 540 nm (data not shown). A more detailed comparison between LR305 and OLSC-TF spectra will be presented in Section 6.3.4.

6.3.3.3 Fourier-transform infrared spectroscopy

The identification of the FTIR absorption signals ascribable to the organic-dye molecule in OLSC-TF samples was performed by comparing OLSC-TF with PMMA FTIR spectra, as presented in Figure 6.34.

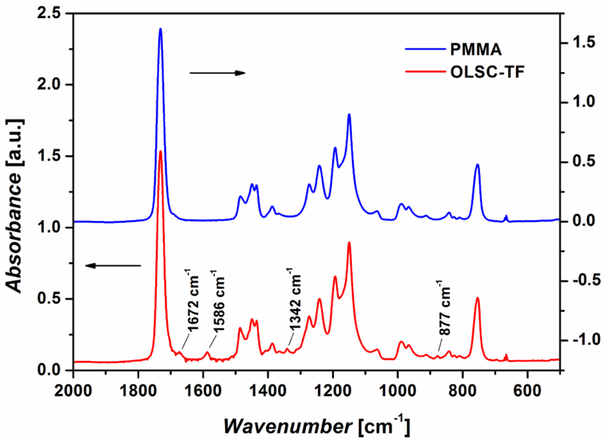

Figure 6.34. FTIR spectra of OLSC-TF and PMMA in the 2000 – 500 cm^{-1} region.

A series of absorption peaks can be identified and assigned to specific bond vibrations on the basis of the analysis on FTIR spectra already performed on LR305 (see Section 6.3.2.3). In particular, a first absorption band is observed at 1672 cm^{-1} and it is attributed to the lower energy C=O stretching vibration of the dye molecule. The stretching vibrations of the C=C bonds of the perylene core are responsible for the peak at 1586 cm^{-1}. Stretching vibrations of the dye molecule can be observed at 1342 cm^{-1}. Finally, the signal attributed to the breathing of the lateral rings can be found at 877 cm^{-1}.

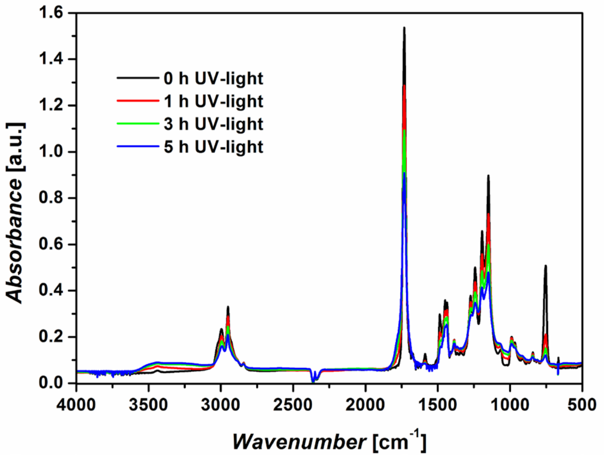

Figure 6.35. FTIR spectra of OLSC-TF after 0 h, 1 h, 3 h, 5 h exposure to UV-light.

These peaks appear at the same frequencies in both LR305 and OLSC-TF samples, indicating that no chemical interactions occur between the organic dye and the polymer matrix.

These four peaks were monitored during exposure to UV-light in order to examine the effect of degradation on the organic dye molecule when dissolved in PMMA matrix (Figure 6.35).

The prolonged exposure of OLSC-TF to UV-light leads to an increase of the FTIR signals in the 3600-3200 cm^{-1} region accompanied by the appearance of two bands in the carbonyl region adjacent to the main peak (1731 cm^{-1}), as also found in the degradation of PMMA (see Figure 6.6 and Figure 6.7). In addition, a general decrease of the absorption peaks associated to PMMA bond vibrations is observed. The peaks attributed to bond vibrations in the dye molecule exhibit a progressive decrease of intensity at increasing UV-exposure time, as also reported for the dye-only films. However, different rates of intensity decay are observed, as discussed more in detail in the next Section. A similar trend is also found for PMMA, which appears to undergo a slower degradation when mixed with LR305.

6.3.4 The role of the organic dye in the degradation of OLSC thin films

In the previous Sections, the modifications occurring to each OLSC component during exposure to UV-light were monitored by means of spectroscopic techniques to highlight potential degradation pathways. In this Section, a comparison on the results obtained from that analysis is presented, aiming at clarifying the role of the organic dye in the photo-degradation of the OLSC device. In particular, two aspects are analyzed in detail.

Firstly, the effect of the presence of the dye molecule in the polymer matrix on the photo-degradation of PMMA is evaluated by comparing FTIR spectra of degraded PMMA with degraded OLSC-TF, as different degradation rates for PMMA were observed in these two cases.

Subsequently, the role of the aggregation state of the dye molecule on its photo-stability was analyzed by comparing spectroscopic results obtained from dye-only (LR305) and OLSC-TF films.

6.3.4.1 The organic dye as UV-absorber

The modifications occurring to PMMA when exposed to UV-light were presented in Section 6.3.1 and Section 6.3.3, where the degradation study was carried-out on both PMMA-only films and dye-doped PMMA films. The spectroscopic analysis showed the occurrence of faster modifications on PMMA-only films compared to OLSC-TF films upon UV-exposure, suggesting that the presence of the dye molecule in PMMA may help to reduce the PMMA degradation process. Indeed, both PMMA-only and dye-doped PMMA films were deposited in the same conditions and present comparable thicknesses as the absorption intensities found in the FTIR spectra are comparable.

As shown in Figure 6.36, where a comparison between the FTIR spectra of PMMA and OLSC-TF after 5 h exposure to UV-light is presented, signals ascribable to similar degradation species forming during UV-exposure can be observed in both spectra.

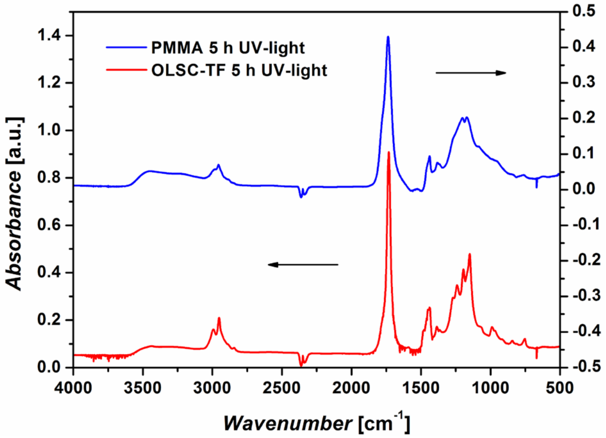

Figure 6.36. FTIR spectra of PMMA and OLSC-TF after 5 h UV-exposure.

However, significantly different relative intensities are found for the FTIR bands characteristic of PMMA bond vibrations, being much lower in the case of PMMA-only films. In addition, much more severe modifications are observed in the PMMA-only film compared to the dye-doped PMMA film.

Figure 6.37 shows the normalized intensity decay of FTIR absorption peaks assigned to C-H stretching (2950 cm^{-1}), C=O stretching (1731 cm^{-1}) and C-O-C stretching (1150 cm^{-1}) vibrations in PMMA compared to the same signals as found in OLSC-TF. For all characteristic vibrations, a much sharper decrease is found in PMMA-only films than in dye-doped PMMA films. In particular, a 70% decrease of intensity is found after 5 h UV exposure for C=O stretching signals in PMMA films, together with a decrease of over 90% for both C-H stretching and C-O-C stretching absorption peaks. Conversely, dye-doped PMMA films exhibit a much slower rate of peak intensity decrease over irradiation time, with a maximum observed for C-O-C stretching signals that lose 60% of their initial intensity (compared to more than 95% loss in PMMA-only films).

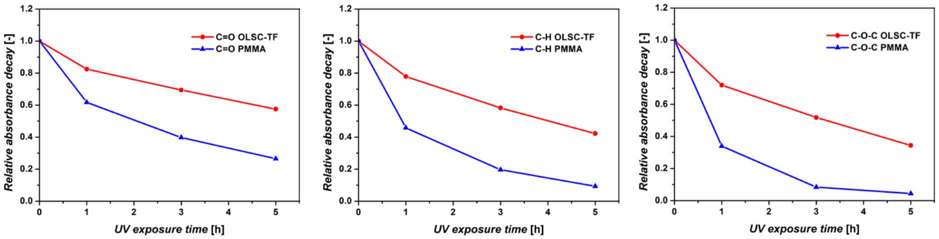

Figure 6.37.Normalized absorbance decay of stretching vibrations relative to C-H (2950 cm^{-1}), C=O (1731 cm^{-1}) and C-O-C (1150 cm^{-1}) bonds in PMMA-only and OLSC-TF films.

These results may suggest that the organic dye acts as a protective agent on the PMMA film. As shown in Figure 6.38, where a comparison between UV-vis absorption spectra of PMMA and LR305 is presented, the organic dye exhibits a strong absorption intensity in the UV region of the spectrum. The high-energy photons absorbed by the dye molecule in this region may be converted by the dye into lower energy photons (as evident from the dye fluorescence spectrum) or may lead to non-radiative electronic relaxations. These processes may prevent these high-energy photons from interacting with the polymeric matrix, thus reducing the density of high-energy photons that can be absorbed by the matrix. A lower degradation rate may therefore be observed for dye-doped PMMA thin films, resulting from the UV-absorbing action of the organic dye molecule.

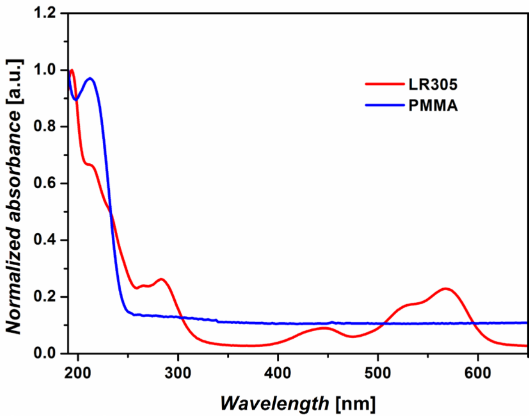

Figure 6.38.UV-vis absorption spectra of PMMA and LR305.

6.3.4.2 The role of the state of aggregation of the organic dye on its stability

The results presented in the previous Sections have yielded two main conclusions on the photo-stability of the organic dye molecule. As a first outcome, different rates of FTIR intensity decay were found for signals attributed to the lateral substituents of the dye molecule compared to its perylene core. In particular, a sharper decrease was observed for the absorption bands associated to vibrations of the lateral substituents. This observation may suggest a degradation mechanism of the organic dye initiating with the disruption of the lateral substituents attached to the perylene core in the dye molecule, the former appearing to be more prone to photo-degradation. In order to support the proposed degradation mechanism, a further analysis was carried-out on UV-vis absorption spectra of both LR305 and OLSC-TF samples. In particular absorption spectra of UV-exposed samples were subtracted from the pristine UV-vis spectrum, so that the absorption spectrum of degraded species forming during UV-irradiation could be highlighted and studied.

The subtraction spectra of OLSC-TF samples at increasing UV-exposure time normalized to their absorption maximum are presented in Figure 6.39, where the UV-vis spectrum of pristine OLSC-TF is also shown for ease of reference. A blue-shift of the absorption peaks in the subtraction spectra can be observed, increasing upon UV-exposure. In particular, the peak associated to the perylene core absorption (576 nm) undergoes a blue shift of about 18 nm while a 27 nm blue-shift is observed for the peak associated to the absorption of the lateral substituents (445 nm). These blue-shifts may be due to a decrease of electron delocalization in the dye molecule upon UV-exposure which may result in an absorption band-gap increase.

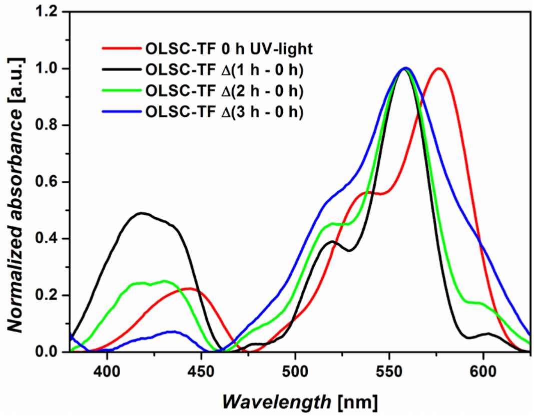

Figure 6.39.UV-vis subtraction spectra of OLSC-TF samples at increasing UV-exposure time. Each subtraction spectrum was obtained by subtracting the spectrum of degraded sample from the spectrum of the pristine sample.

In addition, a progressive decrease of the 445 nm peak intensity is observed upon UV-exposure. Such a decrease further supports the hypothesis of a degradation mechanism of the dye molecule involving the abstraction of the lateral substituents from the perylene core, as already found from FTIR analysis results discussed earlier. In order to confirm these trends, UV-vis subtraction spectra of dye-only samples (LR305) were also calculated (data not shown), but no meaningful tendencies were observed. This result may indicate that the organic dye exhibits different levels of photo-stability depending on its state of aggregation, namely when exposed as dye-only film (LR305) or when included in a polymeric matrix (OLSC-TF). Indeed, evidences of the occurrence of the proposed mechanism deemed responsible for the organic dye degradation were found in both LR305 (dye-only) and OLSC-TF samples, although different degradation rates were observed. In particular, significantly faster modifications to the spectroscopic characteristics of the organic dye were found in OLSC-TF compared to LR305 films. Figure 6.40 presents a plot of the relative intensities of FTIR peaks assigned to vibrations of lateral substituents (ring breathing at 877 cm^{-1}) and perylene core (stretching vibrations at 1586 cm^{-1}) for LR305 and OLSC-TF samples. Two different degradation rates can clearly be observed, with a considerably faster decay in OLSC-TF samples. These results suggest that the lateral substituents in the dye molecule undergo a much faster degradation compared to the perylene core when the organic dye molecule is dissolved into a polymeric carrier (OLSC-TF sample). Indeed, after 5h UV-exposure the intensity of the signal attributed to the ring breathing (877 cm^{-1}) exhibits a 70% decrease with respect to the perylene core (1586 cm^{-1}) in OLSC-TF thin films. Conversely, in dye-only films only a 30% decrease is observed.

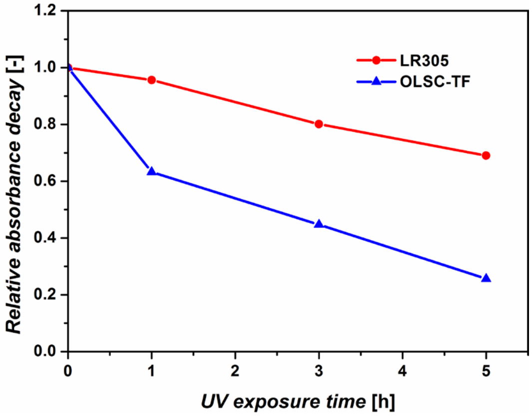

Figure 6.40. Normalized absorbance decay over UV-exposure time of FTIR absorption peaks associated with organic dye bond vibrations of lateral substituents (875 cm^{-1}) and perylene core (1586 cm^{-1}) for LR305 and OLSC-TF samples.

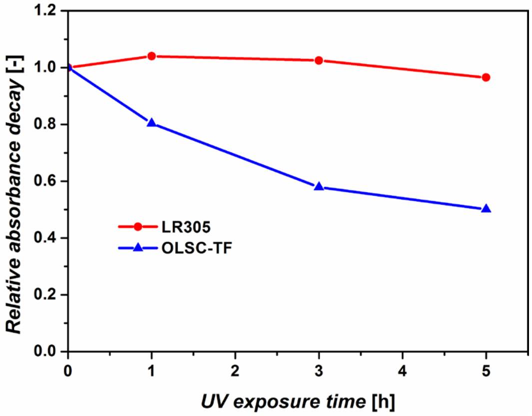

Figure 6.41. Normalized absorbance decay over UV-exposure time of UV-vis absorption peaks associated with lateral substituents (shorter-wavelength peak) and perylene core (longer-wavelength peak) absorption for LR305 and OLSC-TF samples.

An even sharper difference between LR305 and OLSC-TF can be observed from UV-vis spectra, as shown in Figure 6.41 where the normalized relative decay of UV-vis absorption peaks associated with lateral substituents (shorter-wavelength peak) and perylene core (longer-wavelength peak) absorption is presented for both LR305 and OLSC-TF samples.

The intensities of both the signal attributed to absorption of lateral substituents (445 nm) and the one attributed to perylene core absorption (568 nm) decrease in a similar fashion in LR305 up to a UV-exposure time of 5 h, suggesting that the degradation rate is comparable for the two absorbing species. Only for longer UV-irradiation times, the shorter-wavelength absorption peak was found to exhibit a slightly faster decrease in absorption intensity with respect to the longer-wavelength absorption peak (see Section 6.3.2.1). On the contrary, significant differences are observed in the rate of degradation of the dye in OLSC-TF samples. After 5 h of UV-exposure, a 50% decrease in the ratio between shorter- and longer-wavelength UV-vis absorption peaks is found in OLSC-TF samples, indicating a much faster decay of the lateral substituents with respect to the perylene core of the organic dye. A much faster degradation process is therefore observed when the organic dye is dissolved in a polymeric matrix (OLSC-TF), as opposed to the relative photo-stability of dye-only films (LR305).

In order to further clarify the reasons of dye photo-stability in LR305 films, calorimetric analyses were carried-out on LR305 samples via DSC. Figure 6.42 shows the DSC scans obtained from pristine and 5 h UV-irradiated LR305 thin films. A glass transition (T_g) at 150 °C is observed in pristine LR305 (Figure 6.42a), together with a crystallization phenomenon (T_C) occurring at 260 °C and a sharp endothermic peak (T_m) centered at about 390 °C ascribable to a melting process.

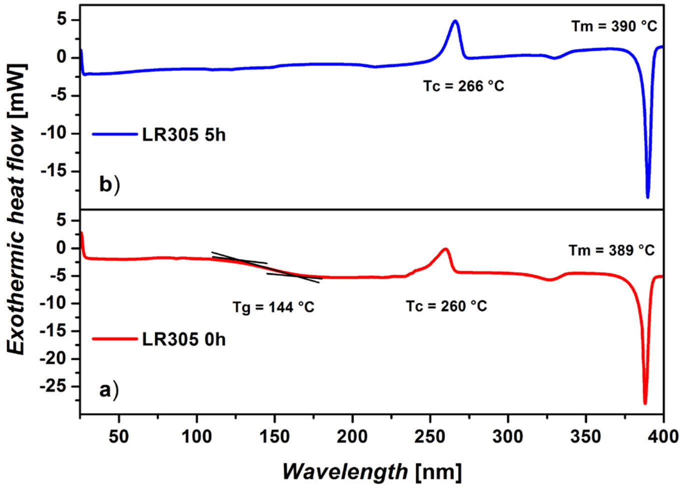

Figure 6.42. DSC scans on 0 h (a) and 5 h (b) UV-exposed LR305 thin film samples.

The presence of an intense melting peak indicates the semi-crystalline nature of the organic dye with a relatively high portion of crystalline domains. Conversely, the glass transition is indicative of the existence of amorphous portions in the material, which appear to crystallize at around 250 °C. The semi-crystalline nature of the dye may contribute to the stability of dye-only films towards UV-light. In order to verify this hypothesis, a DSC scan on dye-only films after 5 h UV-exposure was also performed, as shown in Figure 6.42b. The DSC trace of degraded LR305 samples exhibits similar features as those observed in the pristine film. In particular, an exothermic crystallization peak and an endothermic melting peak are found. In addition, the glass transition temperature appears to be shifted to higher temperatures, although it cannot be clearly distinguished. UV-exposure seems therefore to cause a physical degradation of the organic dye, mainly affecting its amorphous phase. Conversely, no chemical modifications to the organic dye molecule after UV-exposure are observed from the DSC scan, as no appearance of transitions ascribable to new chemical species formed during UV-exposure is reported.

A further insight into the photo-stability of dye-only films was given by analyzing LR305 samples through ^{1}H-NMR spectroscopy. Figure 6.43 presents ^{1}H-NMR spectra of pristine and 5 h UV-irradiated LR305 samples. No significant differences between ^{1}H-NMR spectra for pristine (Figure 6.43a) and degraded (Figure 6.43b) LR305 samples are observed. In particular, the relative intensities of aromatic (δ 7.0 ÷ 7.5) and aliphatic (δ 1.2 ÷ 1.1) hydrogen atoms do not appear to change with UV-exposure time, further confirming the hypothesis of a relatively high photo-stability of dye-only films.

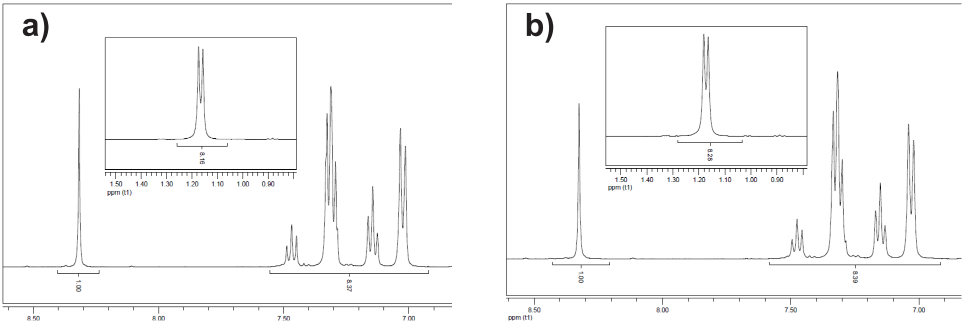

Figure 6.43. ^{1}H-NMR spectra of 0 h (a) and 5 h (b) UV-exposed LR305 thin film samples.

6.4 CONCLUSIONS AND FUTURE WORK

A spectroscopic study on the photo-degradation of a thin-film OLSC was presented in this Chapter. The OLSC consisted of a model organic luminescent dye dissolved in a PMMA matrix, deposited onto a rigid transparent substrate. The photo-stability of each material constituting the thin-film OLSC was monitored upon exposure to UV-light in order to highlight the contribution to OLSC degradation given by each OLSC component.

The results of this work showed a substantial instability of PMMA thin-films that appeared to undergo severe degradation upon exposure to UV-light, with formation of oxidized species. These results are in agreement with recent literature reports on the same system.[10,25]

The photo-stability of PMMA appeared to be improved by addition of the organic luminescent dye, as a significantly lower degradation rate was observed in dye-doped PMMA films compared to PMMA-only films. This result was attributed to the UV-absorbing properties of the organic dye that may prevent high-energy photons from interacting with the polymeric matrix, thus effectively reducing the degradation rate of PMMA thin films.

Significant modifications to the molecular structure of the organic dye were observed after UV-irradiation and a degradation mechanism was proposed, initiating with the disruption of the lateral substituents attached to the perylene core of the dye molecule. Indeed, the former were found to be more prone to photo-degradation than the central core. The proposed degradation mechanism was evident both in dye-only films and in OLSC films, although different degradation rates were observed for these two systems. In particular, significantly faster modifications to the spectroscopic characteristics of the organic dye were found in OLSC films compared to dye-only films. This result was correlated to the different state of aggregation of the dye molecule in the two systems. In particular the poorer photo-stability of the organic dye in OLSC films was attributed to the decrease in crystallinity of the dye molecule following dissolution in a polymeric matrix. Indeed, the amorphous phase of the dye, present in higher amounts in OLSC films, may undergo a faster degradation, thus leading to rapid destruction of the dye molecule. Conversely, due to higher crystallinity, dye-only films are able to exhibit relatively high stability to UV-exposure.

Further tests in controlled atmosphere (O_2, N_2) will be conducted in order to elucidate the role of oxygen in the photo-degradation of OLSC thin films.

In addition, potential stabilization techniques such as the use of highly transparent protective coatings or the use of stabilizing additives will be explored in order to enhance the lifetime of OLSC devices. As a preliminary study, the compatibility of commercial stabilizing agents (Hindered Amine Light Stabilizers) with the organic dye and the polymeric matrix was tested and showed promising results.

6.5 REFERENCES

1. M.J. Currie, J.K. Mapel, T.D. Heidel, S. Goffri, and M.A. Baldo "High-efficiency organic solar concentrators for photovoltaics." Science 2008, 321, 226-228.
2. B.S. Richards and A. Shalav "The role of polymers in the luminescence conversion of sunlight for enhanced solar cell performance." Synthetic Met. 2005, 154, 61-64.
3. B.C. Rowan, L.R. Wilson, and B.S. Richards "Advanced Material Concepts for Luminescent Solar Concentrators." Ieee J. Sel. Top. Quantum Electron. 2008, 14, 1312-1322.
4. W.G.J.H. van Sark, K.W.J. Barnham, L.H. Slooff, A.J. Chatten, A. Buchtemann, A. Meyer, S.J. McCormack, R. Koole, D.J. Farrell, R. Bose, E.E. Bende, A.R. Burgers, T. Budel, J. Quilitz, M. Kennedy, T. Meyer, C.D.M. Donega, A. Meijerink, and D. Vanmaekelbergh "Luminescent Solar Concentrators - A review of recent results." Opt. Express 2008, 16, 21773-21792.
5. G. Smestad, H. Ries, R. Winston, and E. Yablonovitch "The Thermodynamic Limits of Light Concentrators." Sol. Energy Mater. 1990, 21, 99-111.
6. P.F. Scudo, L. Abbondanza, R. Fusco, and L. Caccianotti "Spectral converters and luminescent solar concentrators." Sol. Energy Mater. Sol. Cells 2010, 94, 1241-1246.
7. K. Yoshioka, K. Koizumi, and T. Saitoh "Simulation and fabrication of flat-plate concentrator modules." Sol. Energy Mater. Sol. Cells 2003, 75, 373-380.
8. D.J. Farrell and M. Yoshida "Operating regimes for second generation luminescent solar concentrators." Prog. Photovolt: Res. Appl. 2012, 20, 93-99.
9. B. Ranby and J.F. Rabek "Photodegradation, Photo-oxidation and Photostabilization of Polymers: Principles and Applications.", John Wiley & Sons Ltd, 1975.
10. H. Kaczmarek, A. Kaminska, and A. van Herk "Photooxidative degradation of poly(alkyl methacrylate)s." Eur. Polym. J. 2000, 36, 767-777.
11. A.F. Mansour, M.G. El Shaarawy, S.M. El Bashir, M.K. El Mansy, and M. Hammam "Optical study of perylene dye doped poly(methyl methacrylate) as fluorescent solar collector." Polym. Int. 2002, 51, 393-397.
12. A.F. Mansour, H.M.A. Killa, S.A. El Wanees, and M.Y. El Sayed "Laser dyes doped with poly(ST-Co-MMA) as fluorescent solar collectors and their field performance." Polym. Test. 2005, 24, 519-525.
13. R. Kinderman, L.H. Slooff, A.R. Burgers, N.J. Bakker, A. Buchtemann, R.

Danz, and J.A.M. van Roosmalen "I-V performance and stability study of dyes for luminescent plate concentrators." J. Sol. Energy Eng.-T. ASME 2007, 129, 277-282.

14. N. Tanaka, N. Barashkov, J. Heath, and W.N. Sisk "Photodegradation of polymer-dispersed perylene di-imide dyes." Appl. Opt. 2006, 45, 3846-3851.
15. R. Reisfeld, D. Shamrakov, and C. Jorgensen "Photostable Solar Concentrators Based on Fluorescent Glass-Films." Sol. Energy Mater. Sol. Cells 1994, 33, 417-427.
16. A.A. Earp, T. Rawling, J.B. Franklin, and G.B. Smith "Perylene dye photodegradation due to ketones and singlet oxygen." Dyes Pigm. 2010, 84, 59-61.
17. A.A. Earp, J.B. Franklin, and G.B. Smith "Absorption tails and extinction in luminescent solar concentrators." Sol. Energy Mater. Sol. Cells 2011, 95, 1157-1162.
18. S.M. Reda "Stability and photodegradation of phthalocyanines and hematoporphyrin doped PMMA as solar concentrators." Sol. Energy 2007, 81, 755-760.
19. G. Seybold and G. Wagenblast "New Perylene and Violanthrone Dyestuffs for Fluorescent Collectors." Dyes Pigm. 1989, 11, 303-317.
20. P.A. Cahill "Toward red-emitting, radiation tolerant chromophores." Radiat. Phys. Chem. 1993, 41, 351-363.
21. M.G. El Shaarawy, S.M. El Bashir, M. Hammam, and M.K. El Mansy "Bent fluorescent solar concentrators (BFSCs): Spectroscopy, stability and outdoor performance." Curr. Appl. Phys. 2007, 7, 643-649.
22. M. Hammam, M.K. El Mansy, S.M. El Bashir, and M.G. El Shaarawy "Performance evaluation of thin-film solar concentrators for greenhouse applications." Desalination 2007, 209, 244-250.
23. A.F. Mansour "Optical efficiency and optical properties of luminescent solar concentrators." Polym. Test. 1998, 17, 333-343.
24. T. Caykara and O. Guven "UV degradation of poly(methyl methacrylate) and its vinyltriethoxysilane containing copolymers." Polym. Degrad. Stab. 1999, 65, 225-229.
25. H. Kaczmarek and H. Chaberska "The influence of UV irradiation and support type on surface properties of poly(methyl methacrylate) thin films." Appl. Surf. Sci. 2006, 252, 8185-8192.
26. Bellamy L.J. "The infra-red spectra of complex molecules.", Third edition,

Springer, 1975.

27. Socrates G. “Infrared and Raman characteristic group frequencies.”, Third edition, John Wiley and Sons, Chichester - England 2001.
28. Personal communication from the research group of Prof. Del Zoppo. Calculations performed with Firefly QC package. 2011.

image in next page:

details from M. K. Čiurlionis “The City (I)“, 1908.

>7

FABRICATION AND TESTING OF WORKING DEVICES: AN OVERVIEW OF MATERIALS AND METHODS

7.1 INTRODUCTION

In this Chapter, a comprehensive overview of the main experimental methods followed in this work to produce working devices is presented. In particular details are given on all materials, fabrication procedures and electrical characterization methods employed for standard bulk-heterojunction polymer solar cells, inverted-type bulk heterojunction polymer solar cells and thin-film organic luminescent solar concentrators.

7.2 BULK-HETEROJUNCTION POLYMER SOLAR CELLS

In this Section, experimental details on the fabrication of the BHJ polymer solar cells studied in this work will be presented, including aspects related to their electrical characterization. In particular, two distinct solar cell device architectures will be discussed: standard-type and inverted-type BHJ devices.

7.2.1 Standard device architecture

In the most studied polymer solar cells, devices are typically fabricated by simple solution processing of the active layers followed by evaporation of metallic back electrodes, to produce devices with a so-called "standard" architecture where electrons flow from the transparent electrode (anode) to the back electrode (cathode) (Figure 7.1).

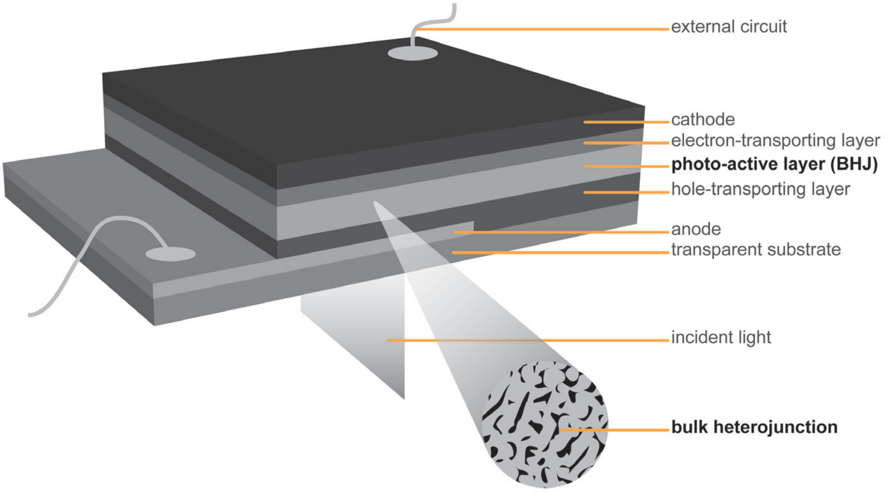

Figure 7.1 Schematization of a standard BHJ PSC device architecture.

A standard geometry is extremely convenient when devices are to be prepared on a laboratory scale, as it represents a suitable standardized platform to investigate materials properties and efficiency.

In Chapter 4 and Chapter 5 this type of architecture was employed to study stability and efficiency of PSC devices and in this Section an overview on device preparation and testing will be given.

7.2.1.1 The ITO-glass substrate

In this work all devices were fabricated on pre-patterned ITO-coated glass substrates, having a surface resistivity $R = 20\ \Omega\square^{-1}$ (supplied by Thin Film Devices, Inc.). Patterning of the ITO surface is necessary in order to avoid short-circuits resulting from electrical connections between front and back electrodes that may occur when contacting the evaporated metallic back electrode. Prior to use, the substrates were cleaned by ultrasonication in 2% Hellmanex soap water for 20 min, and then subjected to successive ultrasonication in de-ionized water (20 min), acetone (20 min) and isopropyl alcohol (20 min). At the end of the cleaning process, the substrates were dried under a stream of nitrogen to eliminate residual solvent on the ITO surface.

7.2.1.2 The PEDOT:PSS layer

In order to improve the surface roughness of the ITO film and to stabilize the electrical contact between the transparent anode and the photoactive layer, a thin film of hole-conducting poly(3,4-ethylenedioxythiophene):poly(styrenesulfonate) PEDOT:PSS (Baytron PH) (Figure 7.2) was spin-coated onto the UV-ozone treated ITO-glass substrates.

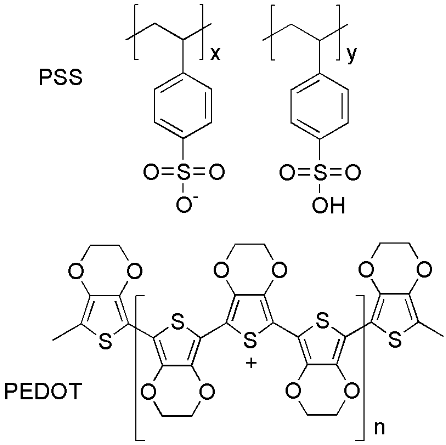

Figure 7.2. Molecular structure of poly(3,4-ethylenedioxythiophene):poly(styrenesulfonate) PEDOT:PSS.

UV-ozone treatement was performed in order to improve the wettability of the ITO thin-film by PEDOS:PSS and was performed in a UV-ozone cleaner for 30 min. The filtered PEDOT:PSS aqueous dispersion (0.45 mm syringe-filters) was spin-coated onto the ITO-glass substrates at 4000 RPM for 40 s followed by baking at 140 °C for 15 min in air, so that complete evaporation of the water could be ensured.

All substrates were then moved to a nitrogen-filled glove box to perform all the following fabrication steps.

7.2.1.3 The photoactive layer

In the most successful PSC devices, the photoactive layer is composed of a blend of a p-type conjugated polymer and an n-type fullerene derivative, forming the so called donor–acceptor bulk heterojunction (BHJ).[1,2]

In order to produce such BHJ, solutions of polymers and fullerene derivatives need to be prepared. Most of the p-type polymers studied in this PhD thesis were dissolved in a solution of a chlorinated solvent (typically chlorobenzene or o-dichlorobenzene) at a concentration of 15 mg/mL. The same solvent was employed for the n-type fullerene solutions, although a significantly higher solid concentration was used (40 mg/mL) due to the very good solubility of $PC_{61}BM$ and $PC_{71}BM$ in chlorinated solvents. To ensure complete dissolution of the solid material, the as-prepared solutions were magnetic-stirred overnight at a suitable temperature (typically 110 °C).

In order to eliminate undesirable solid particles in the solution that may spoil the resulting thin film, all solutions (both polymer and fullerene) were passed through a 0.45 μm polytetrafluoroethylene (PTFE) syringe-filter prior to mixing for the preparation of the blend solutions. When employed, high boiling-point solvent additives (1,8-octanedithiol - ODT, 1,8-diodooctane - DIO, 1,8-dibromooctane - DBO and 1-chloronaphthalene - CN) were added to the respective blend solutions in varying volume concentrations and stirred overnight before spin-coating. During device optimization, different concentrations for the blend solutions and different polymer:acceptor ratios were tested in order to obtain the optimized process conditions.

The polymer:fullerene active layer blend solutions prepared as presented above were spin-coated onto the PEDOT:PSS-covered ITO-glass substrates at 1200 RPM for 40 sec followed by 1 sec (for chlorobenzene solutions) or 4 sec (for o-dichlorobenzene solutions) at 2000 RPM, to produce thin films of varying thicknesses (typically in the order of 100 nm). A longer high rotational-speed spinning time was required for o-dichlorobenzene solutions to achieve dry active layer thin films due to the higher boiling point of this solvent compared to chlorobenzene (180 °C vs. 130 °C, respectively).

7.2.1.4 The metallic back electrode

To complete the PSC device fabrication process, a metallic back electrode needs to be applied on the active layer thin film.

In this work, the evaporated cathode consisted of a bilayer thin film of Ca (20 nm) and Al (100 nm), deposited by thermal evaporation under high vacuum (~ 10^{-7} Torr). The deposition rate was 1 Å/sec for the Ca layer and 4 Å/sec for the Al layer, respectively. To avoid gradients in layer thickness, the samples were rotated during the deposition process. Typically, it took about 20 min to deposit the complete back electrode.

A shadow mask was employed to define the active device area, which was measured to be 0.03 cm^2. In particular, the layout of the shadow mask afforded eight independent devices on each ITO-glass substrate.

When performed, thermal annealing was carried out by placing the complete device on a temperature controlled hot-plate in N_2 atmosphere with the active layer facing up.

A photograph showing typical PSC BHJ devices prepared according to the fabrication procedure detailed in this Section is presented in Figure 7.3.

7.2.1.5 Device testing

The performance of the as-prepared PSC BHJ devices was measured by collecting their current-voltage (J-V) curves under illumination. In particular, a Keithley 2400 source-measure unit was employed under AM 1.5G solar illumination at 100 mW cm^{-2} (1 sun) using a Thermal-Oriel 150 W solar simulator. The calibration of the solar simulator was performed by means of a NREL certified silicon photocell. In order to collect the J-V characteristics of the PSC devices, voltage scans were performed between - 0.2 V and 1.0 V with 10 mV steps on the illuminated device and the current response of devices was recorded.

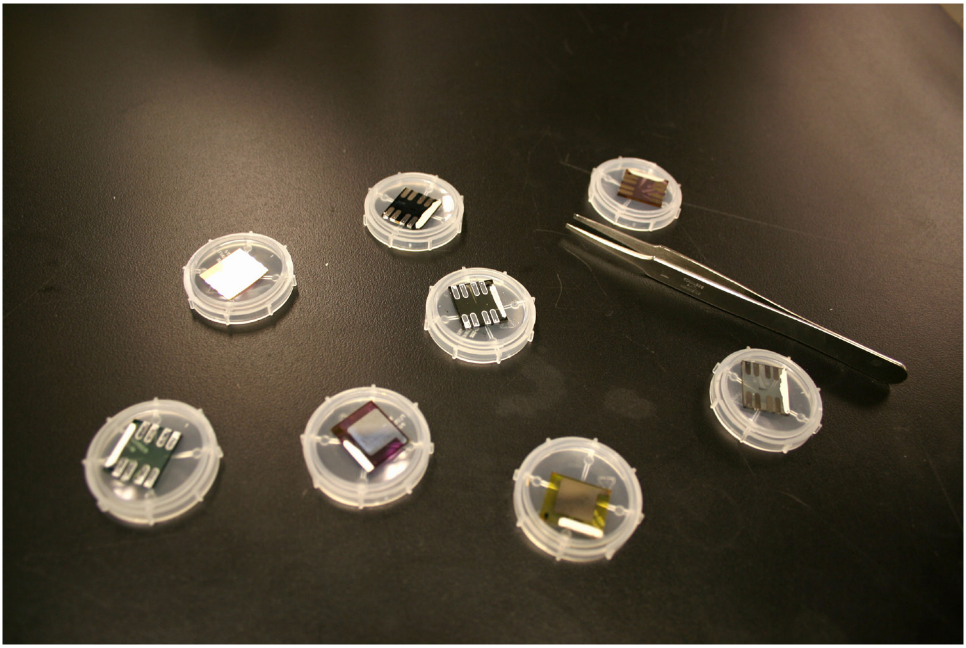

Figure 7.3 Photograph showing a set of typical standard PSC BHJ devices prepared in this work.

7.2.2 Inverted device architecture

Although a standard device geometry may be convenient when preparing devices on a laboratory scale, such a device architecture may present some drawbacks when large scale production is considered mainly due to the vacuum processing steps required for back electrode deposition. As a way to overcome these problems, the so-called "inverted" device geometry was introduced, allowing the use of solution-processed rather than vacuum-processed metallic back electrodes.[3,4] As shown in Figure 7.4, in this device architecture the transparent electrode works as a cathode, where electron collection takes place. Conversely, the back electrode is responsible for the extraction of holes, thus behaving as anode.

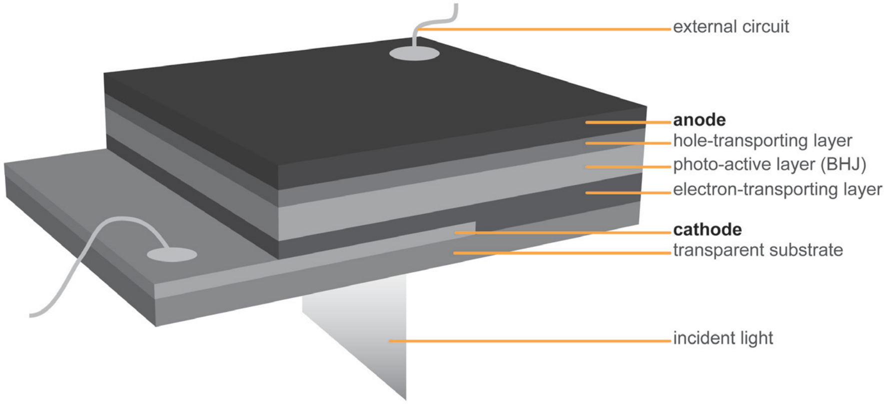

Figure 7.4 Schematization of an inverted PSC device architecture.

In this Section, preliminary results on device processing and testing of inverted PSC structures fabricated in this PhD work are presented. It is worth noticing that all fabrication steps presented in the following Sections were completely performed in air, in order to demonstrate the possibility of producing working PSC devices without the need of any special apparatus for atmosphere control (e.g. oxygen-free environment).

7.2.2.1 The ITO-glass substrate

Similarly to what described in Section 7.2.1, ITO-covered glass substrates (25 mm x 50 mm x 1.1 mm, ITO thickness = 100 nm, supplied by Delta Technologies Ltd.) were thoroughly cleaned and dried for 20 min on a 100 °C hot-plate prior to deposition of the active layers. Both patterned and non-patterned ITO-covered glass substrates were employed in this work to study the effect of ITO patterning on PSC device performance. When performed, patterning of the ITO thin films was carried-out by chemically etching a defined area of the ITO film by means of an aqua regia solution (HNO_3/HCl = 25%/75%) under magnetic stirring. An area of the ITO-covered glass was masked with common adhesive tape and the unmasked area of the film was immersed in the aqua regia solution for 5 min until complete ITO etching was achieved.

7.2.2.2 The electron transporting layer

Simple ITO is not well suited as an electron collecting electrode in typical polymer:fullerene inverted-type systems due to non-optimized work-function and energy levels alignment. In order to overcome these problems and improve electron extraction, n-type metal oxides are usually deposited onto the ITO film. Among these, titanium oxide (TiO_X), cesium carbonate (Cs_2CO_3) and zinc oxide (ZnO) have been successfully tested.[5-7]

In this work, a low-temperature-annealed sol-gel derived ZnO layer was prepared to be used as electron transporting layer in inverted PSC devices. The ZnO precursor was prepared according to literature[7] by dissolving zinc acetate dihydrate (4.5 mmol) and monoethanolamine (4.5 mmol) in 2-methoxyethanol (0.1 mol) (Figure 7.5).

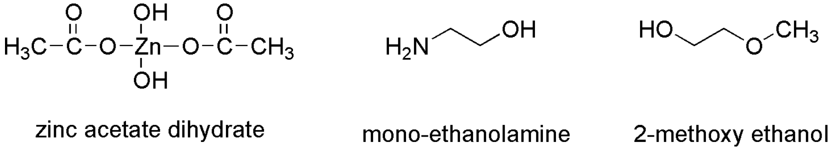

zinc acetate dihydrate

mono-ethanolamine

2-methoxy ethanol

Figure 7.5 Molecular structures of zinc acetate dihydrate, mono-ethanolamine and 2-methoxyethanol.

The sol precursor was maintained under magnetic stirring (600 RPM) overnight to allow for the hydrolysis reaction to occur.

The ZnO precursor solution was spin-coated onto the ITO-glass substrates at 1200 RPM for 40 sec and 2000 RPM for 1 sec. The obtained thin films were annealed on a hot plate for 1 h at 150 °C in air. These processing conditions were selected after analyzing the morphological features of ZnO films annealed for 1 h at both 150 °C and 200 °C by means of atomic force microscopy (AFM). As shown in Figure 7.6, no significant differences were observed in the morphology of 150 °C- and 200°C-annealed ZnO films. In particular, the root mean square (RMS) roughness of the two samples appeared to be comparable (0.36 nm and 0.30 nm for 150 °C- and 200 °C-annealed ZnO films, respectively) and so did their thickness (34 nm for 150 °C annealing and 23 nm 200 °C annealing).

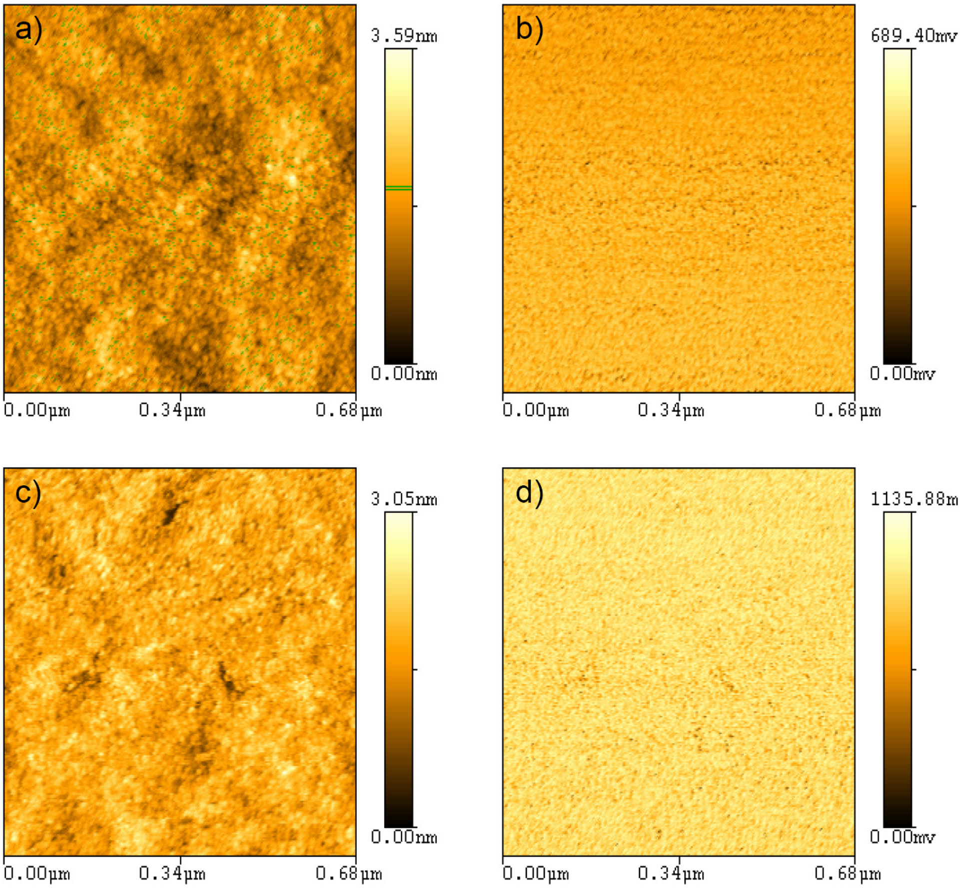

Figure 7.6. Atomic force microscopy topography (a, c) and phase images (b, d) of spin-coated ZnO thin films annealed for 1 h at (a, b) 150 °C and (c, d) 200 °C.

Since no particular differences were observed in the morphological features of the two films and in accordance with the photovoltaic results presented in the literature on similar systems,[7] higher temperature annealing (200 °C) was employed in this work for PSC device fabrication.

7.2.2.3 The photoactive layer

As also presented in Section 7.2.1, a BHJ system was employed for the fabrication of inverted PSC devices. In particular, poly(3-hexylthiophene) (P3HT) (Rieke Metals) was chosen as the p-type conjugated polymer and [6,6]-phenyl-C_{61}-butyric acid methyl ester ($PC_{61}BM$) (Nano-C) was selected as the n-type acceptor molecule. A solution of P3HT in chlorobenzene (23 mg/mL) was prepared and magnetic-stirred overnight at 110 °C. Separately, a chlorobenze solution of $PC_{61}BM$ (40 mg/mL) was also prepared and allowed to stir overnight at the same temperature, so that complete dissolution could be achieved.

In order to eliminate undesirable solid particles in the solution that may spoil the resulting thin film, all solutions (both polymer and fullerene) were passed through a 0.45 μm PTFE syringe-filter prior to mixing for the preparation of the blend solutions. Two different blend solution concentrations were analyzed, namely 14 mg/mL and 28 mg/mL, while the P3HT:$PC_{61}BM$ ratio was set to 1:0.8, according to literature.[8]

The as-prepared polymer:fullerene active layer blend solutions were spin-coated onto the ZnO-covered ITO-glass substrates at 1200 RPM for 40 sec followed by 1 sec at 2000 RPM, to produce thin films with typical thicknesses of about 150-200 nm.

After photoactive layer deposition, thermal annealing was performed by placing the substrates on a hot-plate at 140 °C for 10 min with the active layer facing up. The active layer thin film underwent a change in color upon thermal annealing from dark red to purple, indicating a red-shift of the absorption spectrum resulting from improved π–π stacking of the polymer chains in the thin solid film.

7.2.2.4 The hole transporting layer

As hole transporting layer, a PEDOT:PSS (Sigma Aldrich) water dispersion was used. The PEDOT:PSS water dispersion typically possesses a high surface tension, while the photoactive layer typically presents a relatively low surface energy. These characteristics result in poor wetting of the photoactive layer by the PEDOT:PSS dispersion, with detrimental implications in device functioning. To overcome this problem, additives may be included in the PEDOT:PSS dispersion to lower its surface tension.[3,4,9,10]

To this end, a commercial nonionic surfactant (Triton® X100, from here on referred to as X100, Figure 7.7) supplied by Sigma Aldrich was employed in this work in conjunction with PEDOT:PSS to improve wettability of the active layer.

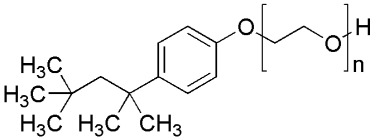

Figure 7.7. Molecular structure of Triton® X100 (X100).

In particular, a PEDOT:PSS/X100 (100/1 wt. %) was prepared and allowed to magnetic-stir at ambient temperature for 4 h prior to deposition.

The X100-modified PEDOT:PSS dispersion was deposited onto the thermally-annealed photoactive layer by spin-coating (1 sec at 2000 RPM followed by 40 sec at 4000 RPM). In order to ensure complete removal of water from the film after spin-coating, the substrates were placed face-up on a hot-plate at 140 °C for 15 min.

7.2.2.5 The metallic back electrode

One of the main advantages of the inverted device architecture is that vacuum deposition of the metallic back electrode can be avoided. In this type of design, the back electrode is deposited onto the hydrophilic PEDOT:PSS layer rather than on the oleophilic photoactive layer, as done for standard-type PSC devices. This difference allows the use of organic solvent-based conductive pastes as back electrode.

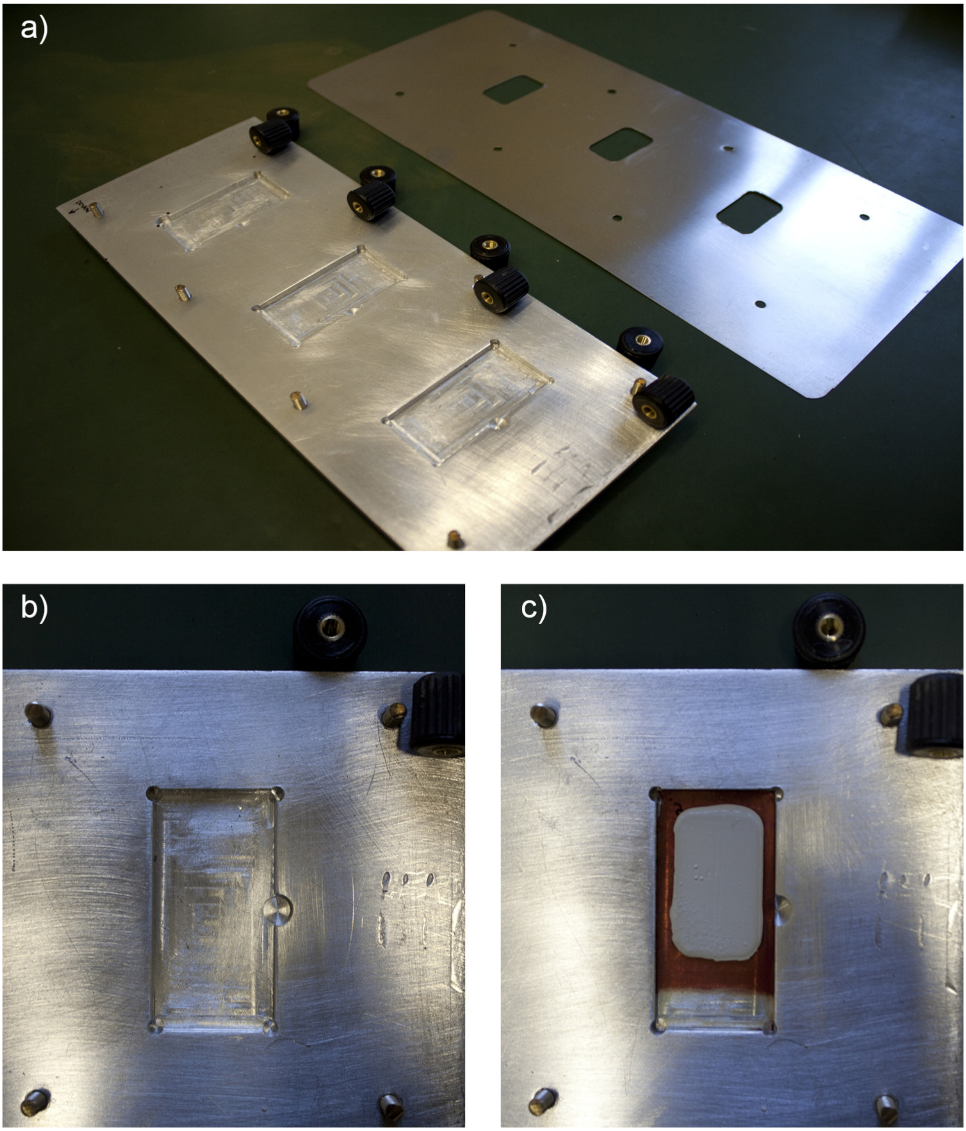

Figure 7.8 Experimental blade-coating set-up used in this work for application of the metallic back electrode in inverted PSC devices: a) sample holder, b) close-up of the slot for substrate positioning and c) completed PSC device positioned in the slot.

In this work, PV410 Silver Conductor paste (DuPont) was applied as back electrode on the PEDOT:PSS layer by blade-coating. The deposition of PV410 was carried-out by using a home-built blade-coating apparatus shown in Figure 7.8. This set-up comprises a stainless steel substrate holder that is able to accommodate three substrates at a time. In addition, patterned stainless steel foils (200 mm thick) are used as shadow masks.

The silver paste was applied on each substrate through these shadow masks, each defining a device active area of 3.6 cm^2.

After deposition, the substrates were annealed on a hot plate at 140 °C for 15 min to allow complete curing of the silver paste and guarantee optimal performance.

A photograph showing typical inverted PSC BHJ devices prepared according to the fabrication procedure detailed in this Section is presented in Figure 7.9.

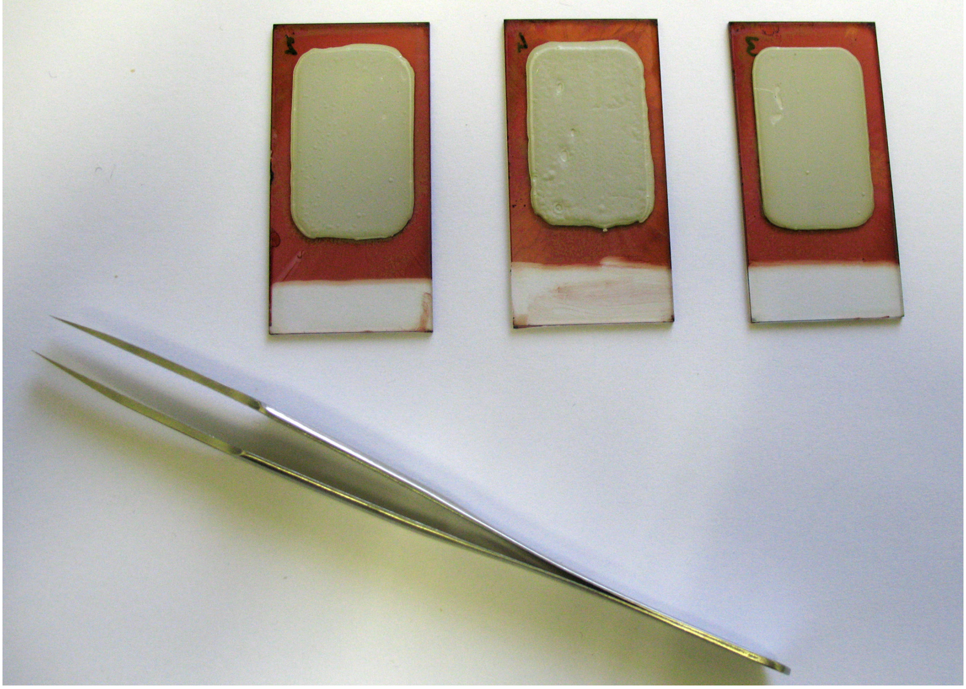

Figure 7.9 Photograph showing a set of typical inverted PSC BHJ devices prepared in this work.

7.2.2.6 Device testing

Similarly to what performed on the standard PSC devices (Section 7.2.1), the performance of the as-prepared inverted PSC BHJ devices was measured by collecting their J-V curves under illumination. In particular, a Keithley 2612 source-measure unit was employed under AM 1.5G solar illumination at 100 mW cm^{-2} (1 sun) using an Abet Technologies 150 W solar simulator whose power output was monitored by means of a power-meter with thermopile sensor (Ophir).

In order to collect the J-V characteristic curves of the PSC devices, voltage scans were performed between -0.2 V and 0.8 V with 10 mV steps on the illuminated device and the current response of devices was recorded. All testing was carried-out in air by employing the apparatus shown in Figure 7.10.

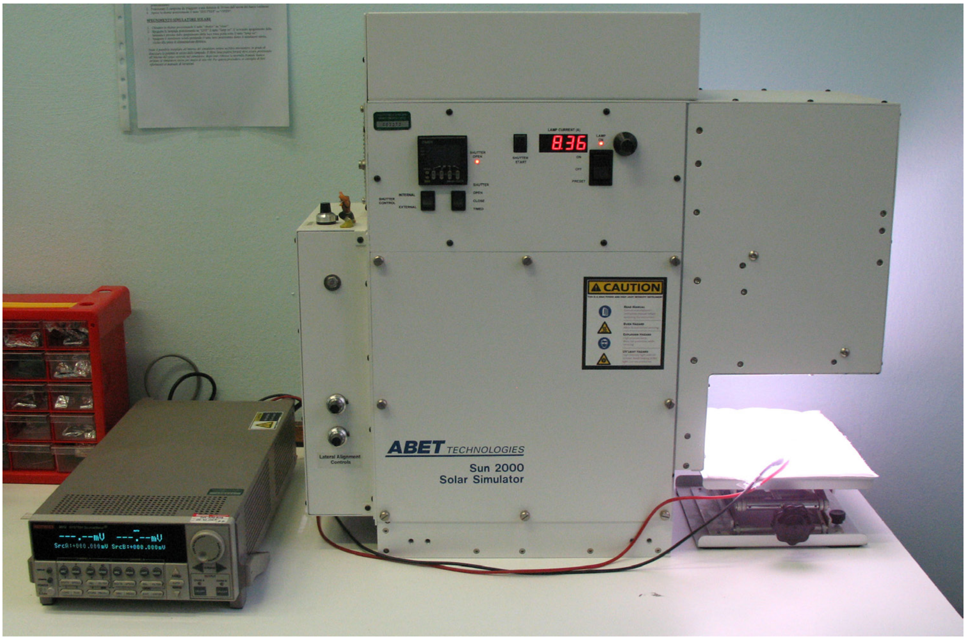

Figure 7.10. Photograph showing the I-V testing apparatus used in this work, comprising a solar simulator and a source-measure unit connected to the device-under-test by means of crocodile clips.

A thorough optimization of inverted-type BHJ PSC device efficiency can be carried-out by independently studying the effect of different device parameters on device performance. In this work, a preliminary study was conducted on the effects on device efficiency of the concentration of the P3HT:PC$_{61}$BM active layer blend solution and of ITO-etching. The results of these preliminary studies are presented in the next Sections.

7.2.2.7 Effect of the concentration of the photoactive-layer blend solution

As detailed in Section 7.2.2.3, two different concentrations of the active-layer blend solution were analyzed in this work, namely 14 mg/mL and 28 mg/mL. The effect of this parameter on PSC performance was studied on PSC devices with non-etched ITO layer, so that the etching effect could be evaluated separately in further studies.

The J-V curves of 14 mg/mL and 28 mg/mL devices are shown in Figure 7.11.

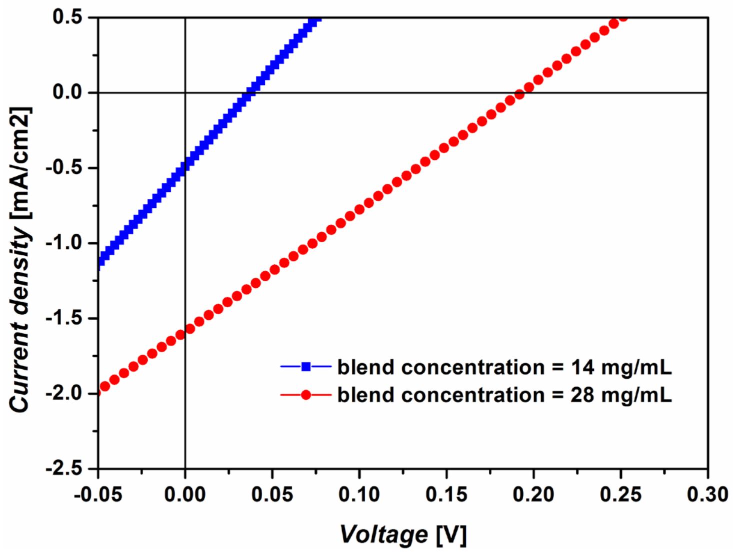

Figure 7.11 J-V curves of P3HT:PC61BM (1:0.8) inverted BHJ PSC devices with active-layer blend concentration of 14 mg/mL and 28 mg/mL in chlorobenzene.

Although a rather poor photovoltaic response is observed for both devices, characterized by low values of fill factor and V_{OC}, a significant increase in JSC is observed by increasing the blend concentration from 14 mg/mL to 28 mg/mL. As shown in Table 7.1, where the main photovoltaic parameters are shown for these devices, the J_{SC} undergoes a three-fold increase when the blend concentration is increased from 14 mg/mL to 28 mg/mL (from - 0.44 mA/cm^2 to - 1.53 mA/cm^2). This current improvement, together with a significant increase in V_{OC}, is the main responsible for the one-order-of-magnitude increase in device efficiency from 0.004% to 0.075%.

Table 7.1 Summary of average photovoltaic parameters for inverted BHJ PSC devices as a function of active layer blend concentration. The P3HT:PC_{61}BM ratio is 1:0.8 for all cases. No ITO etching was performed on these devices.

Blend concentration	V_{OC} (V)	J_{SC} (mA/cm^2)	FF	PCE (PCE_{max}) (%)
18 mg/mL	0.03	- 0.44	0.24	0.004 (0.005)
28 mg/mL	0.19	- 1.53	0.26	0.075 (0.078)

The generally low performance found in both devices may be ascribed to two possible causes. On the one side, degradation pathways may have occurred and negatively affected the performance of the PSC device, as the entire fabrication process was carried-out in ambient air. On the other side, possible short-circuits within the device generating from the electrical connection created between the two electrodes when the back electrode is connected to the measuring unit (by means of crocodile clips). Indeed, part of the silver layer may scratch and get into contact with the underlying layers down to the ITO thin film. This problem arises from the fact that these cells where fabricated without properly patterning the ITO layer by chemical etching. This effect is analyzed more in detail in the next Section.

7.2.2.8 Effect of ITO etching

In order to highlight the importance of patterning the ITO layer to avoid short-circuits within the device under test, ITO-etched inverted P3HT:$PC_{61}BM$ PSC devices were tested and compared to the non-etched devices.
The J-V curves for these devices are presented in Figure 7.12, while the main device parameters are shown in Table 7.2.

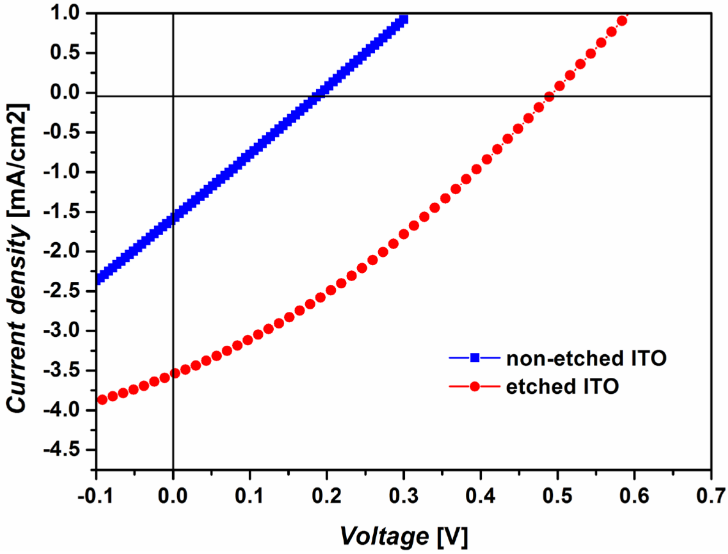

Figure 7.12 J-V curves of P3HT:$PC_{61}BM$ (1:0.8) inverted BHJ PSC devices with and without etched ITO layer. The blend concentration is for both devices 28 mg/mL.

Table 7.2 Summary of average photovoltaic parameters for inverted BHJ PSC devices with and without etching of the ITO layer. The P3HT:$PC_{61}BM$ ratio and active layer blend concentration are for all devices 1:0.8 and 28 mg/mL, respectively.

ITO etching	V_{OC} (V)	J_{SC} (mA/cm^2)	FF	PCE (PCE_{max}) (%)
NO	0.19	- 1.53	0.26	0.075 (0.078)
YES	0.47	- 3.16	0.33	0.49 (0.55)

While the non-etched device is characterized by low V_{OC} and fill factor, significant improvements are observed when ITO-patterning is performed. In particular, a large increase in V_{OC} is observed up to a value of approximately 0.5 V which is in line with values reported in the literature for similar BHJ systems.[8] In addition, the J_{SC} also improves significantly, leading to a maximum device efficiency approaching 0.6%.

Although this value of device PCE is still much lower than state of the art P3HT:PC_{61}BM device efficiencies which exhibit PCEs in the order of 5%,[11] the preliminary work carried-out in this PhD project demonstrates that perfectly working PSC devices can be relatively easily fabricated in air without the use of any vacuum step such as the thermal evaporation of the metallic back electrode. Therefore large and complex laboratory apparatuses can be avoided to some extent and techniques more easily scalable to industrial level can be used as an alternative to fabricate working PSC devices.

In particular, reasonable values of device efficiencies could be achieved by deposition of the metallic electrode via blade coating and a good level of reproducibility could be obtained.

Further work will need to be carried-out on PSC device fabrication and assembly, with particular emphasis on the optimization of device performance and environmental stability.

7.3 THIN-FILM ORGANIC LUMINESCENT SOLAR CONCENTRATORS

In this Section, details on the materials used for organic luminescent solar concentrator (OLSC) and on their fabrication steps are presented. In addition, preliminary results on photovoltaic tests performed on working devices are also reported.

7.3.1 Polymer matrix

Poly(methyl-methacrylate) - PMMA represents an ideal host material for OLSC construction mainly due to its high transparency, suitable refractive index and because of the ease of incorporation of organic fluorophores into the material.
The structures of poly(methyl-methacrylate) is shown in Figure 7.13, while its UV-vis absorption spectrum is presented in Figure 7.14.

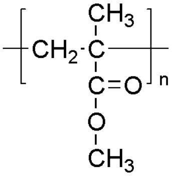

$$\left[CH_2-C(CH_3)(COOCH_3) \right]_n$$

Figure 7.13 Molecular structure of poly(methyl-methacrylate).

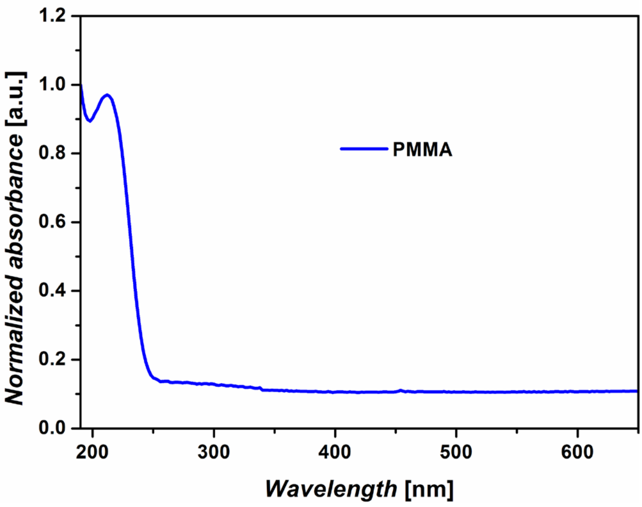

Figure 7.14 UV-vis absorption spectrum of poly(methyl-methacrylate) - PMMA.

As presented in Chapter 2, PMMA in OLSC technology can either be employed as a dye-doped bulk plate or as a dye-doped thin-film deposited onto a transparent substrate such as glass. In this work, thin-film OLSC were fabricated and studied, as it was proposed that this configuration may reduce reabsorption losses by allowing the re-emitted photons to be trapped mainly in the undoped substrate and spend a large proportion of their path inside of it.[12-14]

7.3.2 Organic luminescent dye

Luminescent species dissolved in the carrier matrix absorb incident light and isotropically re-emit it at longer wavelengths. Ideally the energy of the emitted photons should be slightly higher than the band gap of the attached solar cells so as to yield near-unity conversion efficiency. In this work, a commercially available organic dye was employed (Lumogen F Red 305, by BASF, from here on referred to as LR305), presenting a perylene-based structure (see Figure 7.15).

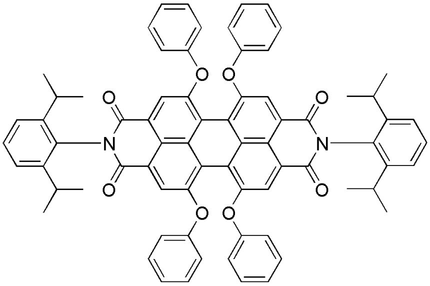

Figure 7.15. Molecular structure of Lumogen F Red 305.

This dye exhibits high luminescent quantum yield (LQY > 90%, as given by the supplier) together with high solubility in the PMMA polymeric matrix as well as in common organic solvents.

The LQY is partly dependent on the Stokes shift of the organic dye, i.e. on the difference in wavelength between its absorption and emission peak maxima. The organic luminescent dye employed in this work exhibits a rather high Stokes shift (~ 40 nm), as shown in Figure 7.16 where the normalized absorption and emission spectra are presented.

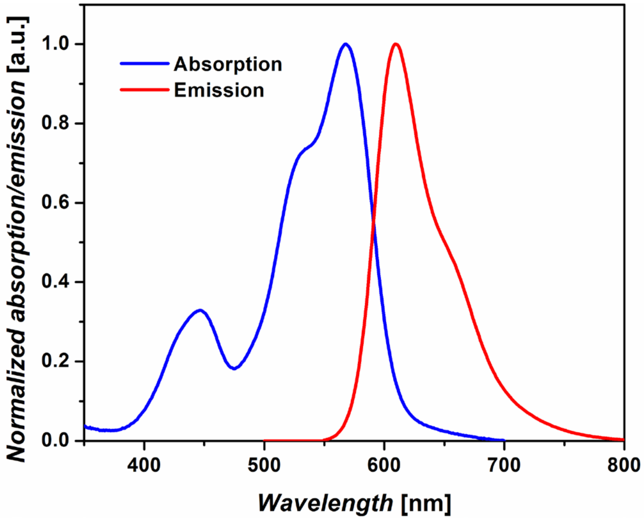

Figure 7.16 Normalized absorption and emission spectra of the organic dye molecule employed in this work (LR305).

7.3.3 Solar cells

In this work, the silicon solar cells to be coupled to the OLSC thin films were fabricated by Silonex Inc. (SLSD-71N400) and presented the following outer dimensions: 25.4 mm (width) x 2.5 mm (height) x 1.0 mm (thickness), with a photo-active area of 45.2 mm^2. The silicon solar cells were provided cabled, so that electrical testing could be easily carried-out.

The main motivations for choosing this type of cells were their size, suitable for mounting on the edges of a glass-based OLSC (typical edge dimensions of 25 mm x 1 mm) and their commercial availability. A photograph showing several of these cells is shown in Figure 7.17.

According to manufacturer's specifications, these cells present a typical sensitivity spectral range spanning from 400 nm to 1100 nm, with a peak sensitivity reported at 930 nm, where a maximum spectral response of 0.55 A/W is found. The spectral response (SR) at a given wavelength is defined as:

$$SR(\lambda) = \frac{J_{ph}(\lambda)}{I(\lambda)} \qquad \text{(Equation 7.1)}$$

where $J_{ph}(\lambda)$ [units A/m^2] is the total photogenerated short-circuit current density at a given wavelength λ and $I(\lambda)$ [units W/m^2] is the spectral irradiance of the incident light.

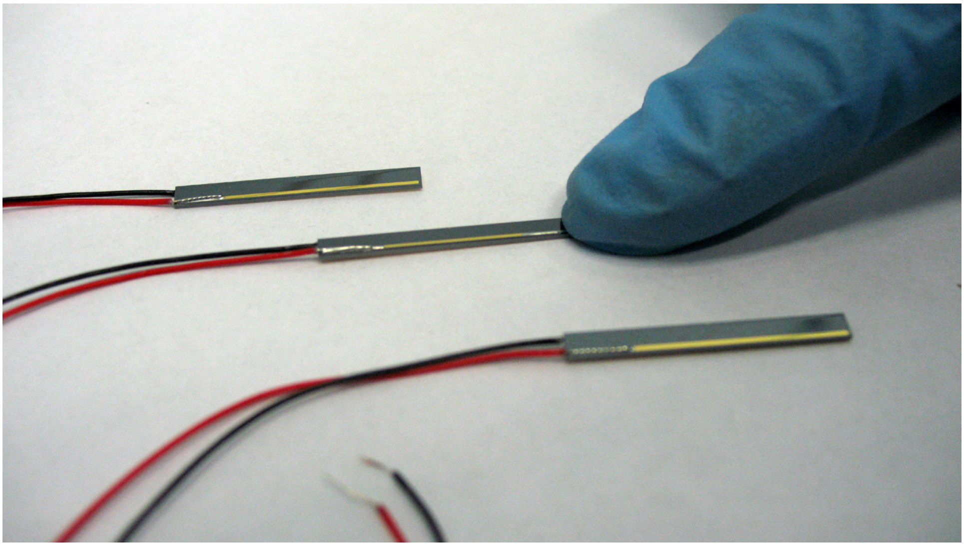

Figure 7.17. Photograph showing three of the silicon cells employed for OLSC device fabrication.

The characteristic I-V curve for a typical solar cell employed in this work, tested under AM 1.5G simulated sunlight, is shown in Figure 7.18 where the dark characteristic curve is also shown for reference.

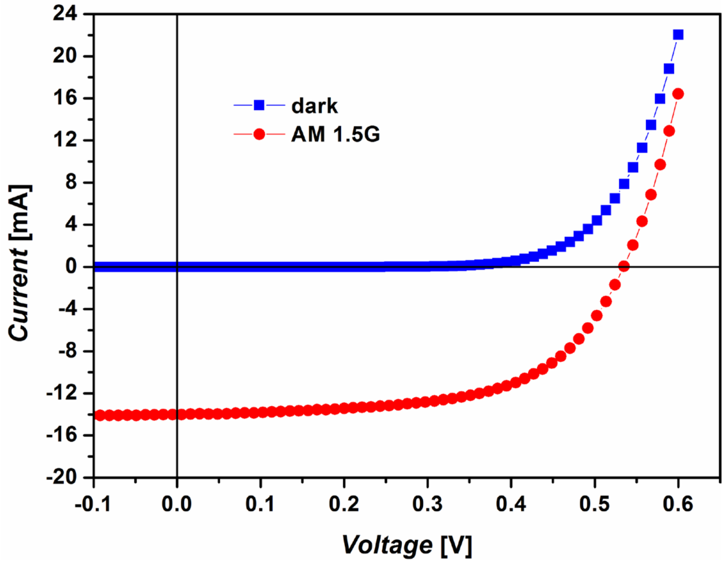

Figure 7.18. Dark and illuminated current-density (I-V) curve of a representative silicon solar cell employed in this work.

The solar cells tested in this work presented an average I_{SC} of - 14 mA, an average V_{OC} of 0.55 V, an average FF of 58%, resulting in an average PCE of 9.5%.

7.3.4 Bonding material

In order to guarantee optimal performance, solar cells must be optically matched to the edges of the glass-substrate where the OLSC thin film is deposited on. In addition, they must also be firmly held and able to withstand normal handling during testing. One way to provide both good optical coupling and mechanical support for the PV cells is to permanently glue them to the edge of the OLSC thin film glass substrate by means of a polymeric adhesive.

In this work, the bonding was performed by means of a commercial hotmelt thermosoftening polyurethane adhesive (Krystalflex PE399, by Huntsman Polyurethanes) 0.5 mm thick, which was cut into small strips the same size as the OLSC glass substrate edge (typically 25 mm x 1 mm), as shown in Figure 7.19.

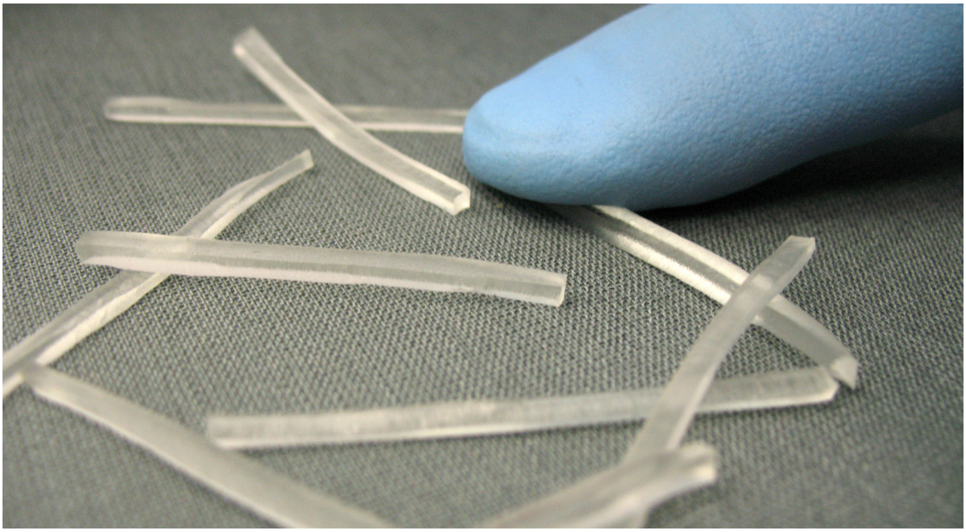

Figure 7.19. Photograph showing strips of the hotmelt polyurethane adhesive employed in this work as solar cell-OLSC bonding material.

When heated above its softening temperature (80 °C¸ 140 °C), the polyurethane adhesive undergoes melting and becomes transparent, thus matching its refractive index (n = 1.49) to the refractive index of glass.

7.3.5 OLSC device assembly

All thin-film OLSC devices fabricated and tested in this work were fabricated on glass substrates. Firstly, solid PMMA chips were dissolved in chloroform under magnetic stirring. After complete dissolution was achieved (2 h), the organic luminescent dye was added to the solution and allowed to dissolve completely (3 h under magnetic stirring). During device optimization, different concentrations of PMMA in chloroform and different concentrations of dye in PMMA were tested in order to obtain the optimized process conditions, and the experiments were repeated multiple times to ensure data reproducibility.

The solutions of dye-doped PMMA in chloroform were spin-coated onto glass substrates (1200 RPM, 40 sec) and allowed to dry out in air before further processing to form the thin-film OLSC. A photograph showing a set of thin-film OLSCs used in this work is presented in Figure 7.20.

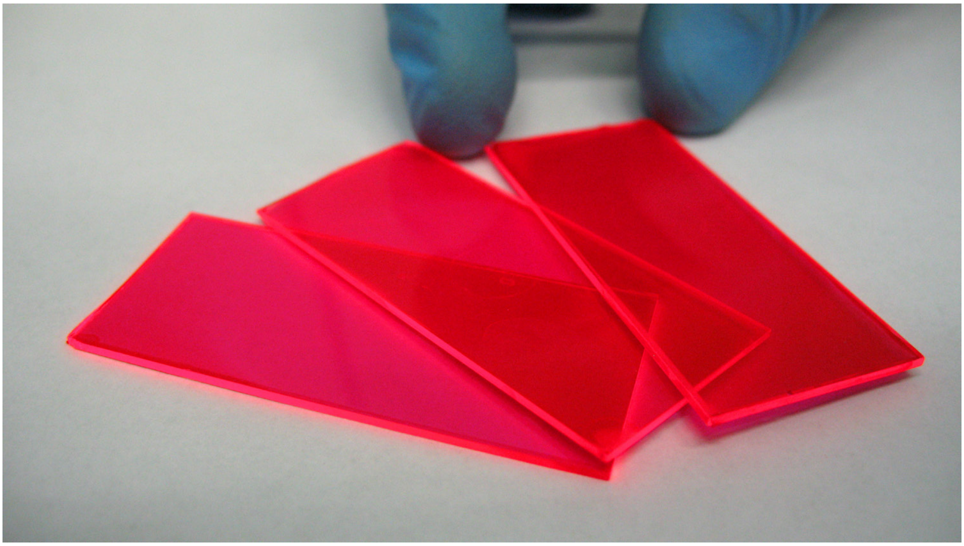

Figure 7.20. Photograph showing a set of OLSC thin films deposited onto glass substrate.

Such thin-film OLSCs were then coupled to a Si solar cell so that one edge of the rigid glass substrate was connected to the photoactive area of the PV cell.

In order to perform the bonding process, the silicon solar cell was positioned face-up on a 130 °C hot-plate and the polyurethane adhesive film was subsequently placed on the solar cell photoactive face. Once softening of the polyurethane film was achieved (approximately 5 min at 130 °C), one edge of the OLSC glass substrate was manually pressed onto the adhesive film for about 1 min to ensure a good optical contact with the solar cell. The OLSC system was then allowed to cool down to room temperature so that hardening of the polyurethane could be achieved. This ensured firm bonding between the solar cell and the thin-film OLSC and good handling resistance.

During the bonding process, particular care was taken in ensuring perfect 90° alignment between the solar cell plane and the OLSC plane to prevent losses of light travelling from the luminescent plate to the solar cell and avoid inaccuracies in the I-V tests. In particular, a steel square was used as a guide during the press-curing process, so that good heat transfer could be ensured between the hot plate and the polyurethane adhesive together with excellent control of the overall planarity of the system (Figure 7.21).

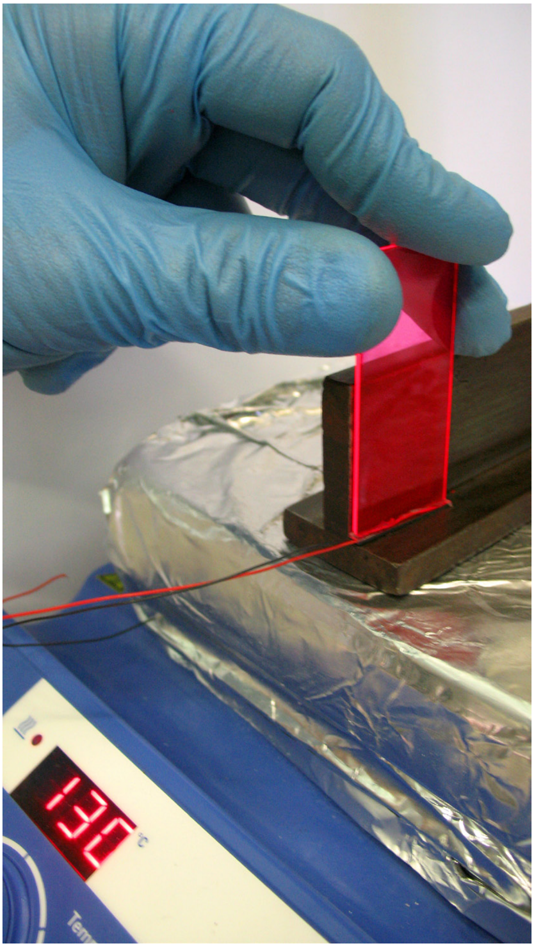

Figure 7.21. Photograph showing the bonding process, where the glass-based OLSC thin film is attached to a silicon solar cell by means of a polyurethane adhesive by press-curing at 130 °C.

7.3.6 OLSC device testing

The current-voltage (I-V) curves of the illuminated OLSC/solar cell systems (from here on referred to as OLSC device) were collected by means of a Keithley 2612 source-measure unit under AM 1.5G solar illumination at 100 mW/cm^2 (1 sun) (Abet Technologies 150 W solar simulator). I-V testing was carried-out by performing scans between - 0.2 V and 0.6 V with 10 mV steps on the illuminated device and by recording the current response. The solar simulator power output was monitored by means of a power-meter with thermopile sensor (Ophir). The electrical connection between the PV cells and the source-measure unit was performed by means of crocodile clips. A photograph of the I-V testing apparatus is shown in Figure 7.9.

The OLSC performance was evaluated by comparing the photovoltaic response of the illuminated PV cell with that of the OLSC device (including PV cell bonded to the OLSC thin film).

The I-V curve of a typical OLSC device under solar light illumination is shown in Figure 7.22, where the I-V curve of a typical silicon solar cell is also reported for comparison.

By connecting the OLSC thin film to the silicon solar cell, a significant increase in PCE is reported, mainly resulting from an increase in short-circuit current ISC. This clearly indicates that the addition of the OLSC thin film to the solar cell allows a larger amount of photons to be harvested and subsequently directed towards the solar cell. These photons can be converted by the attached solar cell into electrical charges, thus improving the efficiency of the simple solar cell.

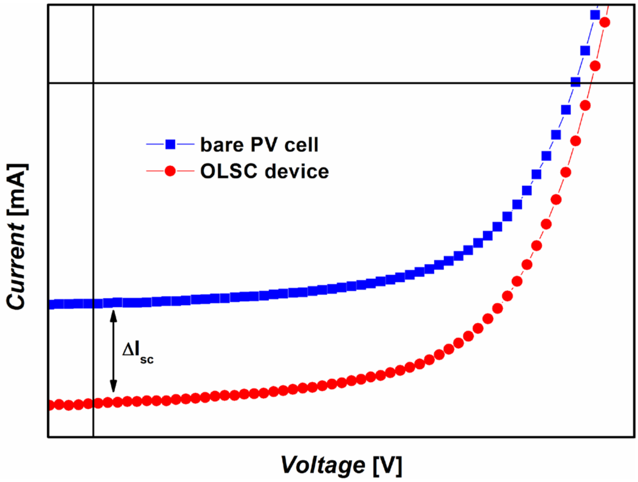

Figure 7.22. I-V curves of a representative OLSC device and of a silicon solar cell. DISC represents the difference in short-circuit current between OLSC device and PV cell.

In order to estimate the efficiency of OLSC devices, two different approaches were used. A first estimate was given by calculating the absolute power conversion efficiency of the OLSC device $\eta_{\mathrm{ABS}}^{(\mathrm{OLSC})}$, according to the following equation:[15,16]

$$\eta_{\mathrm{ABS}}^{(\mathrm{OLSC})} = \mathrm{FF}^{(\mathrm{OLSC})} \frac{(\mathrm{I}_{\mathrm{SC}}^{(\mathrm{OLSC})} / \mathrm{A}^{(\mathrm{OLSC})})\mathrm{V}_{\mathrm{OC}}^{(\mathrm{OLSC})}}{\mathrm{P}_{\mathrm{IN}}} \qquad \text{(Equation 7.2)}$$

where $\mathrm{FF}^{(\mathrm{OLSC})}$, $\mathrm{I}_{\mathrm{SC}}^{(\mathrm{OLSC})}$, $\mathrm{V}_{\mathrm{OC}}^{(\mathrm{OLSC})}$, $\mathrm{A}^{(\mathrm{OLSC})}$ are the fill factor, the short-circuit current, the open-circuit voltage and the active area of the OLSC device, where $\mathrm{A}^{(\mathrm{OLSC})}$ = 13.45 cm^2.

This parameter represents the actual efficiency of the OLSC device and takes into account the contribution to photon absorption of the surface area of the OLSC thin film, thus allowing comparisons between OLSC devices with different OLSC thin film dimensions and equal solar cell type.

As shown in Figure 7.22, the incorporation of an OLSC thin film to a solar cell leads to an efficiency gain ($\Delta\eta$) mainly resulting from an increase in I_{SC}. This $\Delta\eta$ can be calculated as follows:

$$\Delta\eta = \frac{\eta_{\mathrm{REL}}^{(\mathrm{OLSC})} - \eta^{(\mathrm{CELL})}}{\eta^{(\mathrm{CELL})}} = \frac{\mathrm{FF}^{(\mathrm{OLSC})}}{\mathrm{FF}^{(\mathrm{CELL})}} \frac{\mathrm{I}_{\mathrm{SC}}^{(\mathrm{OLSC})}}{\mathrm{I}_{\mathrm{SC}}^{(\mathrm{CELL})}} \frac{\mathrm{V}_{\mathrm{OC}}^{(\mathrm{OLSC})}}{\mathrm{V}_{\mathrm{OC}}^{(\mathrm{CELL})}} - 1 \approx \frac{\mathrm{I}_{\mathrm{SC}}^{(\mathrm{OLSC})}}{\mathrm{I}_{\mathrm{SC}}^{(\mathrm{CELL})}} - 1 \qquad \text{(Equation 7.3)}$$

where $\eta^{(\mathrm{CELL})}$ is the power conversion efficiency of the solar cell calculated as:

$$\eta^{(\mathrm{CELL})} = \mathrm{FF}^{(\mathrm{CELL})} \frac{(\mathrm{I}_{\mathrm{SC}}^{(\mathrm{CELL})} / \mathrm{A}^{(\mathrm{CELL})})\mathrm{V}_{\mathrm{OC}}^{(\mathrm{CELL})}}{\mathrm{P}_{\mathrm{IN}}} \qquad \text{(Equation 7.4)}$$

and $\eta_{\mathrm{REL}}^{(\mathrm{OLSC})}$ is the relative power conversion efficiency of the OLSC device calculated as:

$$\eta_{\mathrm{REL}}^{(\mathrm{OLSC})} = \mathrm{FF}^{(\mathrm{OLSC})} \frac{(\mathrm{I}_{\mathrm{SC}}^{(\mathrm{OLSC})} / \mathrm{A}^{(\mathrm{CELL})})\mathrm{V}_{\mathrm{OC}}^{(\mathrm{OLSC})}}{\mathrm{P}_{\mathrm{IN}}} \qquad \text{(Equation 7.5)}$$

where $\mathrm{A}^{(\mathrm{CELL})}$ is the active area of the silicon solar cell ($\mathrm{A}^{(\mathrm{CELL})}$ = 45.2 mm^2).

The relative power conversion efficiency of the OLSC device $\eta_{\mathrm{REL}}^{(\mathrm{OLSC})}$ gives a measure of the power conversion efficiency of the solar cell after coupling with the OLSC thin film. Therefore, by calculating the efficiency gain $\Delta\eta$ defined in Equation 7.3 it is possible to evaluate the variation of the photovoltaic properties of the illuminated solar cell after addition of the OLSC thin film. In particular, for positive values of $\Delta\eta$, the use of an OLSC device yields a positive efficiency gain.

In order to ensure reproducibility during measurements, I-V tests on each condition were performed on three different devices, and for each device, I-V measurements were repeated five times. Therefore, each tested condition was defined by averages of 15 measured values. In addition, during testing each OLSC device was placed onto a white mat cloth that acted as a distributed Bragg back-reflector, so that losses due to light exiting the back of the illuminated OLSC device could be limited.

A thorough optimization of OLSC device efficiency can be performed by independently studying the effect of different device parameters on device performance. In this work, a preliminary parametric study was conducted on the effects on OLSC device efficiency of the concentration of the organic luminescent dye in the OLSC thin film and of the thickness of the OLSC thin film. The results of these parametric studies are presented in the next Sections.

7.3.6.1 Effect of the concentration of the organic dye in the OLSC thin film

The concentration of the organic dye with respect to PMMA in the OLSC thin film was systematically varied from 2% wt. to 12% wt. at constant PMMA concentration in solution (10% vol. in $CHCl_3$) and the resulting performance of the OLSC device was evaluated in terms of photovoltaic response. The thickness of the OLSC thin film (5 mm), measured by optical profilometry (Microfocus, UBM), was found to be independent on dye concentration, as expected.

Firstly, bare silicon solar cells were tested in order to obtain the photovoltaic parameters needed as reference in the studies of the OLSC devices. In particular, a set of twenty-one solar cells was analyzed for this study, divided into seven groups of three solar cells each. Each group was assigned to a specific dye concentration. After testing, each solar cell was coupled to an OLSC thin film with a given dye concentration, and the I-V characteristics of the resulting OLSC devices were collected under simulated sunlight.

The variations of $\Delta\eta$ and $\eta_{ABS}^{(OLSC)}$ at increasing organic dye concentration are presented in Figure 7.23, where the corresponding I-V curves are also reported.

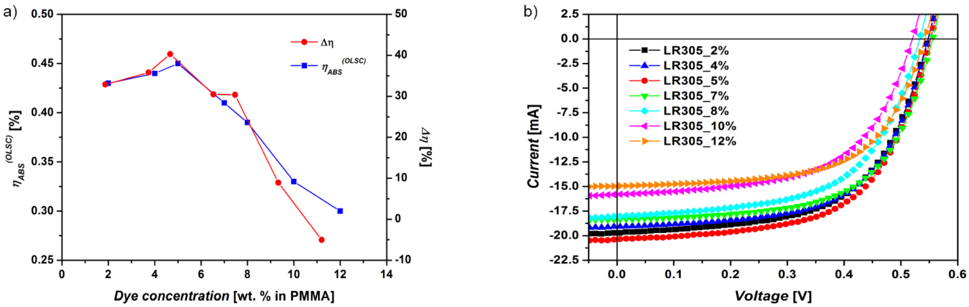

Figure 7.23. (a) Variation of $\Delta\eta$ and $\eta_{ABS}^{(OLSC)}$ at increasing organic dye concentration; (b) I-V curves of OLSC devices at increasing dye concentration in PMMA matrix.

While the fill factor and the V_{OC} of the OLSC devices do not vary significantly at increasing dye concentration, a maximum is found for I_{SC} for a dye concentration of 5%. Accordingly, a maximum of $\Delta\eta$ and $\eta_{ABS}^{(OLSC)}$ is also found for this concentration value. These trends can be better clarified by examining the photovoltaic parameters of the OLSC devices at increasing dye concentration, which are summarized in Table 7.3.

Table 7.3 Summary of main photovoltaic parameters for OLSC devices as a function of organic dye concentration.

	$V_{OC}^{(OLSC)}$ [V]	$FF^{(OLSC)}$	$I_{SC}^{(OLSC)}$ [mA]	$\eta^{(OLSC)}_{REL}$ [%]	$\Delta\eta$ [%]	$\eta^{(OLSC)}_{ABS}$ [%]
LR305_2%	0.55	58.09	- 18.42	13.00 ± 0.24	32.89	0.43 ± 0.01
LR305_4%	0.55	60.33	- 18.42	13.47 ± 0.50	35.81	0.44 ± 0.02
LR305_5%	0.55	59.05	- 18.95	13.58 ± 1.33	40.29	0.45 ± 0.04
LR305_7%	0.54	59.08	- 17.57	12.47 ± 1.38	30.48	0.41 ± 0.05
LR305_8%	0.53	58.11	- 17.59	12.00 ± 0.24	30.37	0.39 ± 0.01
LR305_10%	0.52	58.27	- 14.85	9.96 ± 0.74	8.94	0.33 ± 0.02
LR305_12%	0.52	58.96	- 13.29	9.14 ± 1.48	- 5.05	0.30 ± 0.05

Both $\Delta\eta$ and $\eta_{ABS}^{(OLSC)}$ increase for dye concentrations up to 5%, where a maximum efficiency gain of 40.29% is found. For the same dye concentration the absolute OLSC device efficiency $\eta_{ABS}^{(OLSC)}$ reaches a maximum value of 0.45%. For higher dye concentrations, the performance of the OLSC device decreases down to a minimum of $\eta_{ABS}^{(OLSC)} = 0.30\%$ for 12% LR305 in PMMA, where a negative efficiency gain $\Delta\eta$ is observed (- 5.05%).

These results may be explained by considering two distinct effects of the dye concentration on OLSC device operation. The increase of OLSC device efficiency at low dye concentrations (up to 5%) may be ascribed to a progressive increase of the amount of photons reaching the solar cell, resulting from the higher amount of luminescent species in the OLSC thin film that are responsible for the absorption of the incident light and for its re-emission. However, a further increase in the concentration of the organic dye in the OLSC thin film may lead to a progressive increase of re-absorption phenomena occurring between adjacent dye molecules, which result in a reduction of the actual number of photons reaching the solar cell.

The negative $\Delta\eta$ value found for LR305_12% (- 5.05%) clearly indicates that for such a high dye concentration the addition of an OLSC thin film is detrimental to the operation of the solar cell. In particular, a higher solar cell efficiency would be obtained by simply shining sunlight on the photoactive area of the bare PV cell.

As already stated in Chapter 2, the value of $\eta_{ABS}^{(OLSC)}$ strongly depends on different OLSC parameters, the most influent being OLSC dimensions and type of solar cells employed. For this reason, it is inappropriate to directly compare the absolute OLSC device efficiencies reported in this Section with record literature data, most of which are measured on systems employing different and more performing solar cells (e.g., GaAs, CIGS or CdTe). Conversely, it is more convenient to consider the relative efficiency increment $\Delta\eta$ which gives a measure of the increase in efficiency experienced by the solar cell when coupled to the OLSC plate.

7.3.6.2 Effect of OLSC thin film thickness

The effect of film thickness on OLSC device performance can in principle be analyzed either by varying the concentration of PMMA in the $CHCl_3$ solution or by changing the rotational speed of the spin-coating process. As changes in spin-coating speed may also lead to changes in the surface morphology of the OLSC thin film, in this work the OLSC thickness was varied by systematically changing the PMMA solution concentration. In particular, the concentration of PMMA in $CHCl_3$ was increased from 1% vol. to 20% vol.. Conversely, the concentration of the organic dye in PMMA was maintained constant and equal to 5% wt., that represents the value at which the best OLSC device efficiency was found in the previous study on dye concentration (Section 7.3.6.1). The thickness of the resulting thin films was measured by optical profilometry and varied between 100 nm and 7 mm.

Similarly to what performed in the study on organic dye concentration, bare silicon solar cells were initially tested to record the photovoltaic parameters needed as reference for the OLSC devices. Also in this study, a set of twenty-one solar cells was analyzed, divided into seven groups of three solar cells each. Each group was assigned to a specific PMMA concentration. Once I-V testing on bare solar cells was performed, OLSC devices were fabricated and then I-V tested under simulated sunlight.

Figure 7.24 shows the variation of $\Delta\eta$ and $\eta_{ABS}^{(OLSC)}$ at increasing PMMA concentration.

For ease of reference the corresponding I-V curves are also presented. By increasing the concentration of PMMA in $CHCl_3$ solution, a progressive increase in OLSC device efficiency is reported, both in terms of $\eta_{ABS}^{(OLSC)}$ and $\Delta\eta$ Such an increase is reflected in a noticeable increase in I_{SC} of OLSC devices, as apparent from Figure 7.24b. For PMMA concentrations higher than 10%, a plateau is reached where the OLSC efficiency appears to be essentially independent on PMMA concentration.

This behavior can be clarified by considering the dependence of both $\eta_{ABS}^{(OLSC)}$ and $\Delta\eta$ on the thickness of the OLSC thin film. As shown in Table 7.4, where measured thicknesses of the OLSC thin films studied in this Section are presented together with the main photovoltaic parameters of the corresponding OLSC devices, the progressive increase of PMMA concentration in $CHCl_3$ solution leads to a gradual increase in the OLSC thin film thickness. However, for PMMA concentrations higher than 10%, no significant changes are found in OLSC thin film thickness.

Accordingly, a plateau is observed in Figure 7.24a for $\eta_{ABS}^{(OLSC)}$ and $\Delta\eta$ at PMMA concentrations higher than 10% vol. in PMMA, indicating that constant OLSC thin film thickness results in constant OLSC device performance, provided that the organic dye concentration is also constant.

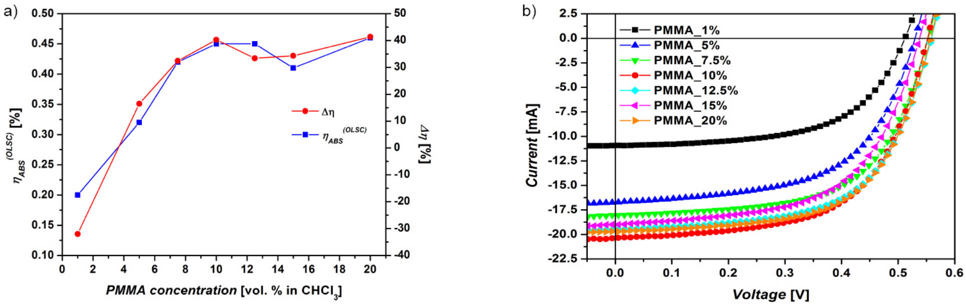

Figure 7.24. (a) Variation of $\Delta\eta$ and $\eta_{ABS}^{(OLSC)}$ at increasing organic PMMA concentration; (b) I-V curves of OLSC devices at increasing PMMA concentration.

Table 7.4 Summary of OLSC thin film thicknesses and main photovoltaic parameters for OLSC devices as a function of PMMA concentration.

PMMA	Thick. [μm]	$V_{OC}^{(OLSC)}$ [V]	$FF^{(OLSC)}$	$I_{SC}^{(OLSC)}$ [mA]	$\eta_{REL}^{(OLSC)}$ [%]	$\Delta\eta$ [%]	$\eta_{ABS}^{(OLSC)}$ [%]
1%	0.1±0.02	0.51	57.29	-9.27	5.94±1.66	-32.03	0.20±0.05
5%	0.3±0.05	0.51	55.02	-15.64	9.81±1.51	16.50	0.32±0.05
7.5%	3.5±0.09	0.55	59.47	-17.64	12.74±0.76	32.45	0.42±0.02
10%	5.0±0.07	0.55	59.06	-18.95	13.58±1.33	40.29	0.45±0.04
12.5%	6.0±0.10	0.56	59.66	-18.45	13.59±1.21	33.40	0.45±0.04
15%	6.0±0.09	0.53	57.81	-18.31	12.51±0.54	34.30	0.41±0.02
20%	7.0±0.13	0.55	59.37	-19.28	14.03±1.08	41.37	0.46±0.04

It is worth noticing that in this work only OLSC thin film thicknesses up to 7 mm were analyzed, mainly due to limitations caused by the deposition technique employed to fabricate the OLSC devices. Indeed, spin-coating is typically used to achieve film thicknesses in the range of 10 nm – 10 µm, while for significantly thicker films other deposition techniques may be more suitable. In line with this observation, further studies will be carried-out to better explore the effect of film thickness on OLSC device performance by using different deposition methods such as blade coating.

7.4 REFERENCES

1. Y.Y. Liang, Z. Xu, J.B. Xia, S.T. Tsai, Y. Wu, G. Li, C. Ray, and L.P. Yu "For the Bright Future-Bulk Heterojunction Polymer Solar Cells with Power Conversion Efficiency of 7.4%." Adv. Mater. 2010, 22, E135-E138.
2. Z. He, C. Zhong, X. Huang, W.Y. Wong, H. Wu, L. Chen, S. Su, and Y. Cao "Simultaneous Enhancement of Open-Circuit Voltage, Short-Circuit Current Density, and Fill Factor in Polymer Solar Cells." Adv. Mater. 2011, 23, 4636-4643.
3. F.C. Krebs "Polymer solar cell modules prepared using roll-to-roll methods: Knife-over-edge coating, slot-die coating and screen printing." Sol. Energy Mater. Sol. Cells 2009, 93, 465-475.
4. F.C. Krebs, J. Fyenbo, and M. Jorgensen "Product integration of compact roll-to-roll processed polymer solar cell modules: methods and manufacture using flexographic printing, slot-die coating and rotary screen printing." J. Mater. Chem. 2010, 20, 8994-9001.
5. W. Gaynor, J.Y. Lee, and P. Peumans "Fully Solution-Processed Inverted Polymer Solar Cells with Laminated Nanowire Electrodes." Acs Nano 2010, 4, 30-34.
6. H. Oh, J. Krantz, I. Litzov, T. Stubhan, L. Pinna, and C.J. Brabec "Comparison of various sol-gel derived metal oxide layers for inverted organic solar cells." Sol. Energy Mater. Sol. Cells 2011, 95, 2194-2199.
7. Y.M. Sun, J.H. Seo, C.J. Takacs, J. Seifter, and A.J. Heeger "Inverted Polymer Solar Cells Integrated with a Low-Temperature-Annealed Sol-Gel-Derived ZnO Film as an Electron Transport Layer." Adv. Mater. 2011, 23, 1679-1683.
8. J.Y. Kim, S.H. Kim, H.H. Lee, K. Lee, W.L. Ma, X. Gong, and A.J. Heeger "New architecture for high-efficiency polymer photovoltaic cells using solution-based titanium oxide as an optical spacer." Adv. Mater. 2006, 18, 572-576.
9. F.C. Krebs "Fabrication and processing of polymer solar cells: A review of printing and coating techniques." Sol. Energy Mater. Sol. Cells 2009, 93, 394-412.
10. K. Norrman, M.V. Madsen, S.A. Gevorgyan, and F.C. Krebs "Degradation Patterns in Water and Oxygen of an Inverted Polymer Solar Cell." J. Am. Chem. Soc. 2010, 132, 16883-16892.
11. W.Z. Cai, X. Gong, and Y. Cao "Polymer solar cells: Recent development and possible routes for improvement in the performance." Sol. Energy Mater.

Sol. Cells 2010, 94, 114-127.

12. M. Graetzel, C. Jorgensen, K. Kalyanasundaram, J. Kiwi, R. Reisfeld, H. Tributsch, R. Reisfeld, and C. Jorgensen "Luminescent solar concentrators for energy conversion. Solar Energy Materials." In: "Springer Berlin / Heidelberg, 1982, p. 1-36.
13. R. Reisfeld, D. Shamrakov, and C. Jorgensen "Photostable Solar Concentrators Based on Fluorescent Glass-Films." Sol. Energy Mater. Sol. Cells 1994, 33, 417-427.
14. R. Reisfeld "New developments in luminescence for solar energy utilization." Opt. Mater. 2010, 32, 850-856.
15. L.H. Slooff, E.E. Bende, A.R. Burgers, T. Budel, M. Pravettoni, R.P. Kenny, E.D. Dunlop, and A. Buchtemann "A luminescent solar concentrator with 7.1% power conversion efficiency." Phys. Status Solidi-RRL 2008, 2, 257-259.
16. W.G.J.H. van Sark, K.W.J. Barnham, L.H. Slooff, A.J. Chatten, A. Buchtemann, A. Meyer, S.J. McCormack, R. Koole, D.J. Farrell, R. Bose, E.E. Bende, A.R. Burgers, T. Budel, J. Quilitz, M. Kennedy, T. Meyer, C.D.M. Donega, A. Meijerink, and D. Vanmaekelbergh "Luminescent Solar Concentrators - A review of recent results." Opt. Express 2008, 16, 21773-21792.

image in next page:

details from M. K. Čiurlionis "Fairy Tale (Fairy Tale of the Kings)", 1909.

>8

CONCLUSIONS AND FUTURE WORK

8.1 POLYMER SOLAR CELLS

8.1.1 Photo-chemical stability of p-conjugated polymers

A study was carried out on the photo-chemical stability of a model p-conjugated polymer (poly(3-hexyl-thiophene) - P3HT) used in PSC devices. The results obtained from this study showed that:

- the polymer exhibits substantial instability to photo-oxidative degradation when exposed as thin solid film to simulated sunlight in air;
- significant modifications to the chemical structure of P3HT occur as a result of its photo-instability;
- a two-step degradation mechanism can be invoked, involving side-chain scission with formation of carbonyl species and aperture of the thiophene ring with formation of thioesters;
- higher polymer regioregularity enhances polymer photo-stability, likely because of the presence of a higher degree of crystallinity in the polymer;
- the addition of multi-walled carbon nanotubes (MWCNT) to P3HT slows down considerably the degradation rate of the polymer, likely due to the radical scavenging properties of MWCNT.

These findings contribute to increase the molecular understanding on the photo-degradation behavior of P3HT and give suggestions on potential routes for improving its stability.

8.1.2 Morphological stability of high-efficiency PSC devices

The synthesis and characterization of a series of photocrosslinkable low-bandgap conjugated polymers for use in BHJ PSCs was presented, in the attempt to improve long-term morphological stability of devices, while preserving high efficiency. The results of this work showed that:

- incorporation of these photocrosslinked polymers with fullerene derivatives in optimized BHJ devices leads to thermally-stable highly-efficient PSC devices. In particular, it was demonstrated that after 72 h of thermal annealing at 150 °C, a stable PCE of 4.7% was obtained in devices containing photocrosslinked polymer and $PC_{71}BM$ in the active layer, mainly due to preservation of an optimal BHJ morphology following photocrosslinking;
- careful control of the crosslinking moiety content in the conjugated polymer is critical to achieve optimal device performance;
- the type of fullerene molecule appears to influence the morphological

stability of the photo-active layer. In particular, photocrosslinked $PC_{71}BM$ devices outperform $PC_{61}BM$ devices both in efficiency and thermal stability, suggesting that in addition to increased light absorption with respect to $PC_{61}BM$, $PC_{71}BM$ may be able to provide morphological stability of the active layer at high temperature;
- surface analysis via AFM corroborates the trends observed from the photovoltaic tests.

These findings provide important guidelines for the design and development of PSC materials with high efficiency and improved morphological stability.

8.1.3 Efficient PSC devices incorporating new low-bandgap conjugated polymers

The characterization and PSC device performance of a series of new isothianaphthene (ITN)-based low-bandgap co-polymers was presented. These co-polymers possessed different electron-withdrawing substituents on the ITN acceptor co-monomer, namely an ester, an imide and a nitrile functionality. The results of this work showed that:

- the electron-withdrawing character of functional groups present on the acceptor co-monomer can strongly influence the polymer electronic behavior. In particular, ester and imide based polymers behave as p-type materials, while the nitrile-based polymer exhibits an n-type character;
- extensive optimization of device parameters allows to fabricate $PC_{61}BM$-based BHJ PSC devices with power conversion efficiencies as high as 2.7% and 3.1%, using ester- and imide-based ITN co-polymer, respectively;
- optimized bilayer devices can be fabricated with PCEs approaching 0.3% by employing the nitrile-functionalized ITN co-polymer as the n-type material coupled to POPT functioning as the p-type material.

These findings demonstrate that the electronic nature of conducting co-polymers can be systematically controlled by simply altering the electron withdrawing functionalities on the acceptor co-monomer. The new monomers presented in this study, along with an understanding of the effect of electron-withdrawing substituents on PSC polymer properties, may help to guide the future design of acceptor monomers to be used in high-performing low bandgap co-polymers.

8.1.4 Processing of inverted PSC devices

A preliminary study on inverted PSCs was carried-out aimed at exploring novel processing techniques compatible with large-scale production of PSC devices. As alternative to thermal evaporation, an Ag paste was used as metallic back-electrode, deposited onto the device by blade-coating. Both device fabrication and testing were completely performed in ambient air and PCEs in the order of 0.5% were achieved on large area (3.6 cm^2) PSC devices.

These results demonstrate the possibility of producing working PSC devices in air with no need of vacuum processing steps.

8.1.5 Suggestions for future work

According to the results on photo-stability, MWCNTs appear to be promising candidates for improving P3HT lifetime. Further studies can be conducted in order to clarify this aspect and to explore the potential use of MWCNT as alternative n-type material in BHJ organic photovoltaics.

In the attempt to attain better photostability of the p-type polymer, appropriate protective chemical additives may be employed, such as hindered amine light stabilizers, radical scavengers, oxygen scavengers, UV-absorbers.

In addition, protective coatings may be applied on the PSC device. These coatings need to exhibit very low permeability to oxygen and water as well as good mechanical resistance to allow sufficient protection of the device photo-active layer. A potentially attractive technique to prepare this type of coatings is the sol-gel technology.

Finally, further studies on the potential use of novel processing techniques to fabricate inverted PSC devices can be carried-out. Among these, screen printing, ink-jet printing and doctor blading represent promising approaches to study the photovoltaic response of the actual PSC device on both rigid and flexible substrates.

8.2 ORGANIC LUMINESCENT SOLAR CONCENTRATORS

8.2.1 Photo-chemical stability of organic materials for OLSCs

A study on the photo-chemical stability of a thin-film OLSC device was presented, consisting of a perylene-based luminescent organic dye dissolved into a polymeric matrix (PMMA). The results of the degradation study showed that:

- the host matrix (PMMA) exhibits substantial instability to photo-oxidative degradation, with formation of oxidized species following exposure to UV-light in air;
- the photo-stability of PMMA appears to improve by addition of the organic luminescent dye, as a significantly lower degradation rate is observed in dye-doped PMMA films compared to PMMA-only films. This result may be attributed to the UV-absorbing properties of the organic dye that may prevent high-energy photons from interacting with the polymeric matrix, thus effectively reducing the degradation rate of PMMA thin films;
- significant modifications to the molecular structure of the organic dye are observed upon UV-irradiation;
- a degradation mechanism for the dye molecule can be invoked, initiating with the disruption of the lateral substituents attached to the perylene core of the dye molecule, as they were found to be more prone to photo-degradation than the central core;
- degradation of the organic dye are observed both in dye-only films and in OLSC films, although different degradation rates are found for these two systems. In particular, significantly faster modifications to the spectroscopic characteristics of the organic dye are found in OLSC films compared to dye-only films. This result may be correlated to the different state of aggregation of the dye molecule in the two systems.

These findings lead to a deeper understanding of the degradation behavior of light-exposed OLSC materials and may help to develop efficient strategies to lengthen OLSC lifetime.

8.2.2 Efficiency of OLSC devices

A preliminary parametric study on the efficiency of a working OLSC device coupled to a c-Si solar cell tested under simulated sunlight was presented. Device parameters such as the organic dye concentration and the thickness of the thin-film OLSC were analyzed and successively optimized. The results showed that a maximum efficiency gain of over 40% can be achieved after the integration of the c-Si solar cell with the OLSC thin-film as a results of careful control of device parameters.

These findings provide useful guidelines for the fabrication of efficient OLSC devices.

8.2.3 Suggestions for future work

In order to elucidate the effect of oxygen in the photo-degradation process of the OLSC thin films, further tests in controlled atmosphere (O_2, N_2) can be conducted. In addition, degradation studies of the integrated OLSC device (OLSC thin film, bonding agent and c-Si solar cell) can be carried-out in milder irradiation conditions, such as for instance in a weather-o-meter set-up.

Furthermore, potential stabilization techniques such as the use of highly transparent protective coatings or the use of stabilizing additives may be explored in order to enhance the lifetime of OLSC devices.

Another approach to lengthen device lifetime is represented by the use of hybrid structures to form modified glasses to incorporate fluorophores via the sol-gel technique. Different parameters characteristic of the sol-gel technique can be tuned to achieve desired properties, such as for instance the modulation of the refractive index of the host matrix. This parameter in particular may be also beneficial to reduction of escape-cone losses, thus leading to improved OLSC device efficiency. To this end, further tests also need to be performed on other device parameters, such as for instance the geometric factor (OLSC top surface to solar cell active area) to optimize the performance of the OLSC device.

Finally, the incorporation of quantum dots in the host matrix may represent a promising strategy to minimize fluorophore degradation.

>>

APPENDIX A:
LIST OF SYMBOLS AND ABBREVIATIONS

AFM	Atomic Force Microscopy
AM 1.5G	Air Mass 1.5 Global solar spectral irradiance
$A^{(CELL)}$	Active area of solar cell
$A^{(LSC)}$	Top surface area of the LSC
$A^{(OLSC)}$	Top surface area of the OLSC
BDT	Benzo[1,2-*b*:4,5-*b′*]dithiophene
BHJ	Bulk heterojunction
CB	Chlorobenzene
CN	1-chloronaphthalene
CV	Cyclic voltammetry
C_{60}	Buckminsterfullerene
DBO	1,8-dibromooctane
DCB	*o*-dichlorobenzene
DIO	1,8-diiodooctane
DPE	Di-phenyl-ether
DSC	Differential Scanning Calorimetry
$\Delta\eta$	Efficiency gain of OLSC device
E_g	Energy bandgap
$\eta^{(LSC)}{}_{ABS}$	Absolute power conversion efficiency of LSC
$\eta^{(OLSC)}{}_{ABS}$	Absolute power conversion efficiency of OLSC
$\eta^{(OLSC)}{}_{REL}$	Relative power conversion efficiency of OLSC
FF	Fill factor
$FF^{(OLSC)}$	Fill factor of OLSC device
FTIR	Fourier Transform Infrared Spectroscopy
GPC	Gel Permeation Chromatography
HALS	Hindered amine light stabilizer
HOMO	Highest occupied molecular orbital
I_{SC}	Short circuit current
$I^{(OLSC)}{}_{SC}$	Short circuit current of OLSC device
ITN	Isothianaphthene
ITO	Indium-Tin Oxide
J_{SC}	Short circuit current density
LSC	Luminescent solar concentrator
LUMO	Lowest unoccupied molecular orbital
LR305	Lumogen® F Red 305
MMA	Methyl methacrylate
MWCNT	Multi-walled carbon nanotubes
ODT	1,8-octanedithiol
OLSC	Organic luminescent solar concentrator
OLSC-TF	Organic luminescent solar concentrator thin film
OPV	Organic photovoltaics

P3HT	Poly(3-hexyl thiophene)
PCE	Power conversion efficiency
$PC_{61}BM$	[6,6]-phenyl-C_{61}-butyric acid methyl ester
$PC_{71}BM$	[6,6]-phenyl-C_{71}-butyric acid methyl ester
PDI	Perylene-diimide
PEDOT:PSS	Poly(3,4-ethylenedioxythiophene): poly(styrene sulfonate)
PITN	Poly(isothianaphthene)
PMMA	Poly(methyl methacrylate)
POPT	Poly(3-(4-n-octyl)-phenylthiophene)
PSC	Polymer solar cell
PV	Photovoltaics
T_C	Crystallization temperature
T_g	Glass transition temperature
T_m	Melting temperature
TPD	Thieno[3,4-c]pyrrole-4,6-dione
V_{OC}	Open circuit voltage
$V^{(OLSC)}{}_{OC}$	Open circuit voltage of OLSC device
XL	Crosslinking

>>

APPENDIX B:
LIST OF PUBLICATIONS AND COMMUNICATIONS

- Articles in international journals with referee
  - **G. Griffini**, S. Turri, M. Levi, “Degradation and stabilization of poly(3-hexylthiophene) thin films for photovoltaic applications”, Polymer Bulletin, 2011, 66, 211-222.
  - **G. Griffini**, J.D. Douglas, C. Piliego, T.W. Holcombe, S. Turri, J.M.J. Fréchet, J.L. Mynar, “Long-term thermal stability of high-efficiency polymer solar cells based on photocrosslinkable donor-acceptor conjugated polymers”, Advanced Materials, 2011, 23, 1660-1664.
  - T.W. Holcombe, J.E. Norton, J. Rivnay, C.H. Woo, L. Goris, C. Piliego, **G. Griffini**, A. Sellinger, J. Brédas, A. Salleo, J.M.J. Fréchet, “Steric control of the donor/acceptor interface: implications in organic photovoltaic charge generation”, Journal of the American Chemical Society, 2011, 133, 12106-12114.
- International conference proceedings
  - **G. Griffini**, J. D. Douglas, C. Piliego, T. W. Holcombe, S. Turri, J. L. Mynar, J. M. J. Fréchet, “Polymer solar cells with long-term thermal stability and high efficiency based on photocrosslinkable donor-acceptor conjugated polymers”, Proceedings of the 26th European Photovoltaic Solar Energy Conference and Exhibition - EU PVSEC 2011, 05-09 Settembre 2011, Hamburg (DE), pp. 218-220.
- National conference proceedings
  - **G. Griffini**, S. Turri, M. Levi, “Degrado e stabilizzazione di polimeri coniugati per applicazioni fotovoltaiche”, Atti del 10° Convegno Nazionale AIMAT, 5-8 Settembre 2010, Capo Vaticano (IT), pp 337-340.
- Communications at international conferences
  - **G. Griffini**, J. D. Douglas, C. Piliego, T. W. Holcombe, S. Turri, J. L. Mynar, J. M. J. Fréchet, “Thermally stable high-efficiency polymer solar cells based on photocrosslinkable donor-acceptor conjugated polymers”, 3rd Hybrid and Organic Photovoltaics Conference - HOPV2011, 15-18 Maggio 2011, Valencia (ES) (*oral communication*).
  - C.Piliego, **G. Griffini**, J.D. Douglas, T.W. Holcombe, J.L. Mynar, J.M.J. Fréchet, “Long-term thermal stability in high-efficiency polymer solar cells based on photocrosslinkable donor-acceptor conjugated polymers”, 4th International Symposium on Flexible Organic Electronics - ISFOE11, 10-13 Luglio 2011, Thessaloniki (GR) (*oral communication*).

  - **G. Griffini**, S. Turri, M. Levi, "Degradation and stabilization techniques of conjugated polymers for photovoltaic applications", European Energy Conference 2010, 20-23 Aprile 2010, Barcelona (ES) (*poster presentation*).
  - J. D. Douglas, **G. Griffini**, C. Piliego, T. W. Holcombe, S. Turri, J. M. J. Fréchet, J. L. Mynar, "Long-term thermal stability of high-efficiency polymer solar cells based on photocrosslinkable donor-acceptor conjugated polymers", ACS Division of Polymeric Materials: Science and Engineering (PMSE), Spring Meeting 2012, San Diego (USA) March 2012. Submitted (*oral communication*).
  - **G. Griffini**, M. Levi, S. Turri "Stabilization strategies of thin-film organic luminescent solar concentrators", European Energy Conference 2012, Maastricht (NL) March 2012. (*poster presentation*).
- Communications at national conferences
  - **G. Griffini**, S. Turri, M. Levi, "Celle solari polimeriche: durabilità e degrado", PV TECH 2009 – HIGH TECH EXPO 2009, Milan (IT) (*invited talk*).
  - **G. Griffini**, "Materiali organici per la tecnologia fotovoltaica: stato dell'arte e prospettive di sviluppo", Zero Emission Rome 2011, 14-16 Settembre 2011, Roma (IT) (*invited talk*).
  - M. Levi, **G. Griffini**, L. Brambilla, M. Del Zoppo, S. Turri, "Photodegradation of a thin-film organic luminescent solar concentrator: a spectroscopic study", VIII Convegno Nazionale INSTM Scienza e Tecnologia dei Materiali, 26-29 Giugno 2011, Aci Castello (IT). (*poster presentation*).

The following articles were published on international journals:

Polym. Bull. (2011) 66:211–222
DOI 10.1007/s00289-010-0323-9

ORIGINAL PAPER

Degradation and stabilization of poly(3-hexylthiophene) thin films for photovoltaic applications

Gianmarco Griffini · Stefano Turri · Marinella Levi

Received: 25 March 2010 / Revised: 3 June 2010 / Accepted: 10 June 2010 /

Abstract Polymer-based solar cells (PSC) represent a promising technology in the field of photovoltaics, although they still suffer from poor environmental stability. Poly(3-hexylthiophene) (P3HT) is one of the most commonly employed electron-donor materials for the preparation of the photo-active layer of PSC and it is known to undergo degradation when exposed to light. In this work, the degradation of P3HT was studied by irradiating polymer films by means of simulated sunlight. The results of this study highlighted a remarkable instability of P3HT. Substantial modifications of the infrared as well as of the UV–Vis spectra of the polymer were reported and a degradation pathway was suggested, in agreement with recent literature results. In order to stabilize the structure, two additives were evaluated namely a standard Hindered Amine Light Stabilizer (HALS) and Multi-Walled Carbon Nanotubes (MWCNT). The addition of MWCNT appeared to significantly reduce the rate of degradation.

Keywords Poly(3-hexylthiophene) · Photovoltaic · Degradation · Stabilization · Multiwall carbon nanotube

Introduction

Polymer-based solar cells (PSC) represent nowadays a possible alternative to more traditional silicon-based photovoltaic technology [1]. Indeed, the light weight of the materials used as well as the opportunity of employing flexible substrates for their fabrication open up the possibility for new applications such as large-area non-planar devices. However, PSC still show limited power conversion efficiencies and

---

G. Griffini · S. Turri (✉) · M. Levi
Dipartimento di Chimica, Materiali e Ingegneria Chimica "Giulio Natta", Politecnico di Milano,
Piazza Leonardo da Vinci 32, 20133 Milan, Italy
e-mail: stefano.turri@polimi.it

suffer of relatively poor environmental stability which limits their operational lifetime compared to inorganic-based photovoltaic technology [2].

Although environmental stability of PSC still represents a challenge towards PSC deployment on industrial scale, significant progresses in terms of manufacture and demonstration have been recently made. In particular roll-to-roll manufacturing processes based on all printing techniques have been employed to fabricate devices on flexible substrates with inverted cell geometry [3, 4] and with ITO-free fabrication steps [5, 6]. In addition, the relative stability towards degradation of encapsulated large area PCS has been demonstrated through round robin and inter-laboratory studies on devices fabricated on flexible substrates using full roll-to-roll processing techniques [7]. Recently, field studies involving the fabrication of flexible PSC modules in ambient conditions through full roll-to-roll processes have also been presented [8] and the integration of PSC modules into commercial products has been shown [9].

In the most efficient PSC prototypes [10], the photoactive layer is typically made of a blend of an electron-acceptor and an electron-donor material, where the latter is constituted by a semiconducting conjugated polymer. Among the most commonly employed electron-donor materials, poly(3-hexylthiophene) (P3HT) is receiving a great deal of attention, due to its good electrical and mechanical properties as well as its ability to be easily processed in solution of common organic solvents [11]. Furthermore, P3HT appears to be more environmentally stable than other semiconducting conjugated polymers, but also devices based on this material are susceptible to chemical degradation. In particular, the interaction of oxygen, water and light with the materials constituting the active polymer layer and the metallic electrode leads to a decay of the photovoltaic performances over time [12, 13]. Nevertheless, the fabrication of air stable PSC has been reported on an inverted device geometry where the active layer is constituted by a bulk heterojunction of zinc oxide nanoparticles and poly-(3-carboxydithiophene) (P3CT) [14].

In addition to the stability in the complete PSC devices, the photo-degradation of the active conjugated polymer still represents a challenge. Indeed, P3HT stability towards light still appears to be poor and the mechanisms underlying its degradation have to be fully clarified, especially in the solid state.

One of the first studies on the stability of P3HT towards light was carried out by Abdou and Holdcroft [15]. In their work, P3HT in chloroform solution containing dissolved molecular oxygen was irradiated by UV and visible light. Degradation of the polymer was observed and two degradation pathways were proposed. The first involved the photosensitized formation of singlet oxygen $O_2(^1\Delta_g)$ by the triplet state of P3HT causing formation of endoperoxide species which would lead in turn to reduction of π-conjugation and polymer photobleaching. The second involved free-radical attack of photosensitized trace amounts of transition-metal salts to the lateral alkyl chain leading to chain scission and formation of carbonyl and hydroxyl adducts as well as crosslinking. Based on these observations, in a later work by the same group [16] a mechanism accounting for the solid state behaviour of P3HT was subsequently proposed. However, no suggestions were given on possible ways to decrease the degradation rate.

A similar free-radical mechanism was suggested for the thermo-oxidative degradation of poly(3-octylthiophene) (P3OT) in the solid state [17] with formation of a ketonic group in the α-carbon position of the alkyl side chain of the polymer. The effect of stabilizers on the degradation of P3OT was also studied, by employing different classes of stabilizers, namely primary antioxidants, secondary antioxidants, antioxidants reacting with nonoxygenated radicals, metal deactivators, and light stabilizers in the form of radical scavengers. However, no clear positive effects on the degradation rate of P3OT were observed by FTIR and SEC analyses. This was attributed to the high sensitivity of hydrogen abstraction from the α-carbon position of P3OT which could lead to a radical site in every alkyl group of the polymer.

In the work by Caronna et al. [18] the photodegradation of poly(3-butylthiophene) (P3BT) in the solid state was studied in different environmental conditions, namely air, nitrogen and oxygen. No degradation was observed in nitrogen atmosphere while two degradation products were isolated and identified after irradiation in air. Their formation was attributed to the reaction of singlet oxygen with the polymer conjugated chain, the former generated by energy transfer from the excited state of the polymer to molecular oxygen. In addition two compounds were found to decrease the rate of polymer oxidation, namely *N*-hexadecyl-*N*-methylaniline and 1-phenyldodecan-1-one. Their stabilizing action was attributed to their ability to act as light screen thereby protecting the polymer from photo-oxidation.

The poly[2-methoxy-5-(3′,7′-dimethyloctyloxy)-1,4-phenylenevinylene] (MDMO-PPV) system in solid state was studied by Chambon et al. [19, 20] through photo- and thermal-oxidation. Infrared spectroscopy allowed to monitor the formation of ester, formate and carboxylic acid species and a degradation route was suggested involving radical oxidation of the polymer. The study was extended to the blend constituted by methano-fullerene[6,6]-phenyl C61-butyric acid methyl ester (PCBM) and MDMO-PPV. It was found that the addition of PCBM to MDMO-PPV results in a decrease of degradation rate of MDMO-PPV in blended film. This effect was attributed to radical scavenging properties of PCBM.

In a recent work by Manceau et al. [21] the accelerated photo-oxidative degradation of P3HT in the solid state was studied in the presence of air. On the basis of infrared spectroscopy results and chemical derivatization treatments, a degradation mechanism was proposed involving the radical oxidation of the hexyl side-chain and the sulphur atom of thiophene ring. Based on a previous work by the same group [22], it was also confirmed that singlet oxygen does not appear to be the main intermediate in the degradation process of P3HT. On the other hand, no suggestions were made on possible ways to decrease the degradation rate.

In the present work, a study was presented on the photo-oxidative degradation of P3HT in the solid state under simulated sunlight. A degradation mechanism was proposed confirming what reported in the literature for accelerated experiments [21]. Furthermore, the addition of two compounds to P3HT was studied, namely a Hindered Amine Light Stabilizer (HALS) and Multi-Walled Carbon Nanotubes (MWCNT), and the effect of their addition to the stabilization of P3HT was investigated.

Experimental

Poly(3-hexylthiophene) (P3HT) was purchased from Rieke Metals Inc. (type 4002, regioregularity 94%) and was used as received. Chloroform (Sigma–Aldrich) was used as solvent in all tests. Multi-walled Carbon Nanotubes (MWCNT—average diameter 9.5 nm, average length 1.5 µm, purity >95%) were purchased from NanoCyl and used as received, without any further purification. The Hindered Amine Light Stabilizer additive (TINUVIN®292) was purchased from CIBA and used as received.

Infrared spectroscopy and UV–Vis spectroscopy were performed on thin film samples ($\sim$200 nm) deposited on NaCl, KBr and glass substrates by spin coating (WS-400B-NPP, Laurell Technologies Corp.). The thickness of the samples was measured by profilometry. Infrared spectra were recorder in transmission mode on a Nicolet 760–FTIR Spectrophotometer controlled by OMNIC software. Spectra were obtained using 32 scans and a 4 cm^{-1} resolution. UV–Vis absorption spectra were recorded in transmission mode on solid state samples deposited onto glass substrates by means of a Jasco V-570 UV–Vis-NIR Spectrophotometer.

All samples were irradiated in air by means of a Class A solar simulator (Xenon short arc lamp 150 W, Abet Technologies) with AM1.5G (ASTM 927-91) spectral distribution and a power output of about 2,200 W/m^2 (approximately 2 suns). The solar simulator power output was monitored by means of a powermeter with thermopile sensor (Ophir). Samples were collected at different irradiation times.

The molecular weight of the samples was determined through Gel Permeation Chromatography (GPC—Waters 410) using THF as eluent and polystyrene standards.

^{1}H-NMR spectra were recorded on a Bruker AC 300 NMR Spectrometer. All samples for ^{1}H-NMR were dissolved in $CDCl_3$.

DSC analyses were performed on solid state samples using a DSC/823e-Mettler Toledo differential scanning calorimeter. Scan rate was 20 K/min.

Results and discussion

The molecular weights of the polymer samples were measured by gel permeation chromatography in THF. At different irradiation times the molecular weight of the polymer was determined in order to monitor modifications of the macromolecular chain length occurring after exposure to light. The pristine polymer gave values of $\bar{M}_n = 3.0 \times 10^4$ and $\bar{M}_w = 7.0 \times 10^4$, respectively. By increasing the exposure time of the cast polymer films, no significant variation of $\bar{M}_n$ and $\bar{M}_w$ was observed even after 200 h of exposure to simulated sunlight. On the other hand, a progressively higher amount of insoluble material was formed with increasing exposure time. This trend reflects the fact that the GPC analysis is limited to soluble material as it is carried-out in solution. Insoluble moieties containing degradation products, which were not found in the pristine polymer but only in degraded samples, are filtered-out before elution of the sample into the GPC and are thus excluded from the analysis.

All polymer samples were also analyzed by solution ^{1}H-NMR spectroscopy. As far as the pristine polymer is concerned, one sharp band centred at δ 6.98 was observed in the ^{1}H-NMR. This band is attributed to the thiophene proton and denotes the HT–HT regioregular structure of the polymer [23]. This regioregular structure was confirmed by the ^{1}H-NMR spectrum in the α- and β-methylene proton region, where only the signals corresponding to HT linkage were present (Fig. 1a).

As far as the spectra from irradiated samples are concerned, no modifications to the P3HT ^{1}H-NMR spectrum were observed even after 100 h of exposure (Fig. 1b). The reason for that might be the fact that also in this case the analysis is carried out on polymer solution, thus insoluble moieties formed during irradiation are excluded from the analysis.

Calorimetric measurements were carried out through DSC on all polymer samples in order to monitor the thermal transitions following irradiation. According to what reported in the literature [24], an endothermic transition was observed from a crystalline to a liquid crystalline state at a temperature of 220–240 °C (peak maximum 237 °C) for the pristine polymer. By means of calorimetric experiments, changes in the degree of crystallinity $X = \Delta H/\Delta H^0$ at increasing exposure times were also monitored, where ΔH is the actual enthalpy of fusion of the polymer and ΔH^0 is the enthalpy of fusion of the ideal crystal, taken as 99 J/g [25]. As it can be seen from Table 1, a very small variation in the degree of crystallinity of the polymer can be observed at increasing irradiation times.

The solid-state UV–Vis absorption spectrum of the pristine P3HT is shown in Fig. 2, where also the spectrum of 24 h irradiated P3HT is reported. The pristine polymer shows a maximum peak at 520 nm and two shoulders at 550 and 600 nm, respectively. After irradiation, a progressive decrease of the absorption intensity of the polymer was observed associated to a blue shift of the absorption band. These

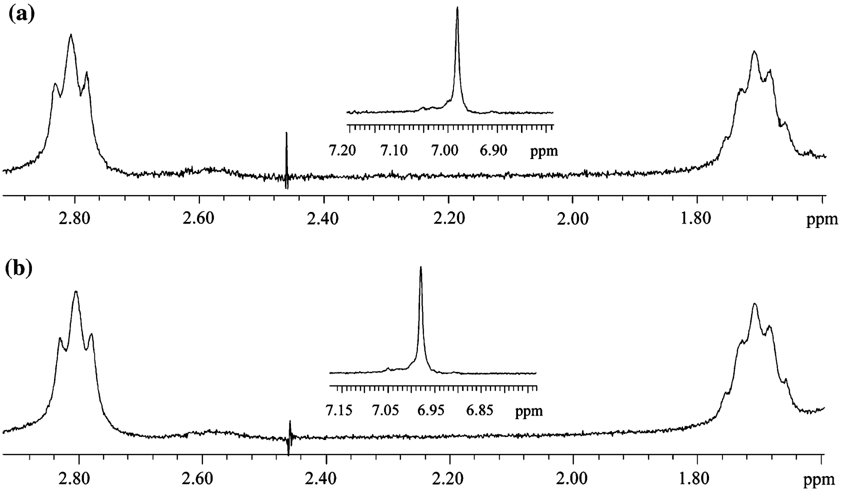

Fig. 1 Expanded ^{1}H-NMR spectra in the methylene region for pristine P3HT (**a**) and 100 h irradiated P3HT (**b**). Aromatic region is also shown in the *insets*

Table 1 Variation of degree of crystallinity of P3HT during exposure to simulated sunlight

Exposure time (h)	*X* (%)
0	21.4
48	19.8
96	19.9

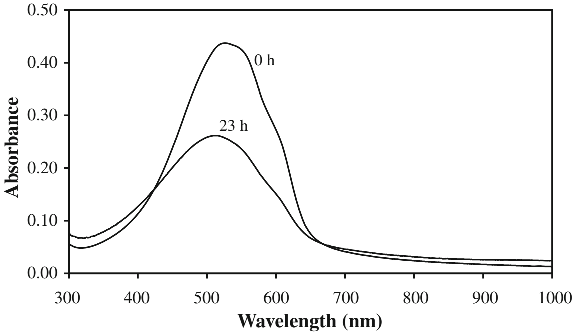

Fig. 2 UV–Vis absorption spectra of P3HT as a function of irradiation time (0 h, 24 h)

modifications can be attributed to the photobleaching of the polymer resulting from a reduction of the conjugation length. These observations are consistent with what reported in the literature [21] at longer exposure times.

Fourier-Transform infrared spectroscopy was used to monitor the kinetics of the photooxidation process. After irradiation, significant modifications of the IR spectra of the polymer were observed. In order to identify the changes occurring during irradiation, the main IR absorption bands for the pristine polymer have been identified and are reported in Table 2 [23].

A progressive decrease of absorption intensity was observed for various functional groups. In particular, the intensity of the absorption bands related to alkyl groups, aromatic C–H and thiophene ring rapidly decreased. As an example, Fig. 3 shows the progressive disappearance of the characteristic bands assigned to alkyl groups. As it can be noted, after approximately 50 h of exposure to simulated sunlight, the intensity of the peaks is decreased down to less than 50% of the original value.

In addition to the aforementioned trend, the simultaneous appearance of other absorption bands was reported. Several features appeared in the carbonyl region, as shown in Fig. 4, where different maxima can be distinguished upon irradiation. In the same graph, the disappearance of the band assigned to the thiophene ring stretching at 1,510 cm^{-1} (see Table 2) during exposure to simulated sunlight can be observed.

According to what reported above, Fig. 5 shows the time-dependent evolution of absorption intensity of different characteristic IR bands during irradiation. In order to make comparisons easier, normalized absorption intensities are reported.

Table 2 Frequencies and assignments of main IR bands for pristine P3HT

Wavenumber (cm^{-1})	Assignment
3,055	C–H (aromatic) str
2,955	CH_3 asym str
2,925	CH_2 asym str
2,855	CH_2 sym str
1,510	Thiophene ring str
1,454	
820	C–H bend thiophene ring

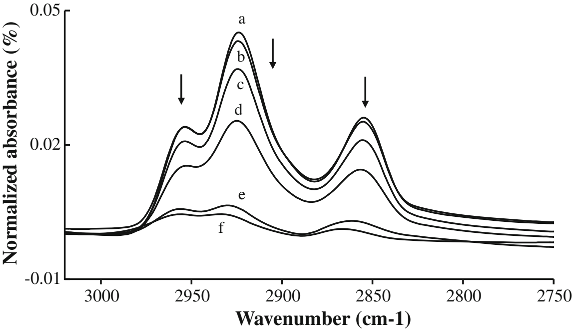

Fig. 3 Variation of FTIR spectra of P3HT spin-coated films in the aliphatic region as a function of irradiation time (*a*: 0 h; *b*: 6 h; *c*: 24 h; *d*: 48 h; *e*: 72 h; *f*: 100 h)

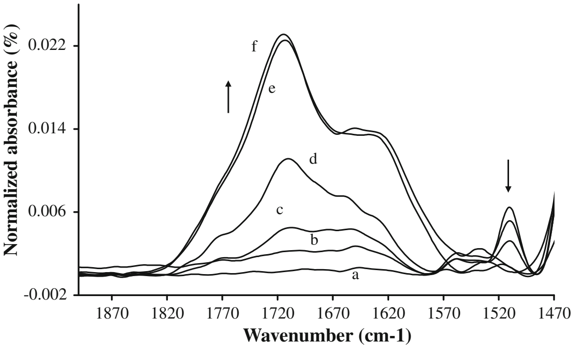

Fig. 4 Variation of FTIR spectra of P3HT spin-coated films in the carbonyl region as a function of irradiation time (*a*: 0 h; *b*: 6 h; *c*: 24 h; *d*: 48 h; *e*: 72 h; *f*: 100 h)

As shown in the graph, a decrease of intensity for signals attributed to alkyl groups and thiophene ring is observed accompanied by the appearance of new bands which may be assigned to carbonyl species and thioesters [21].

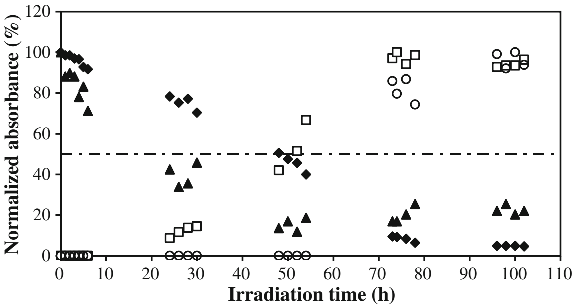

Fig. 5 Variation of normalized absorption intensity of characteristic groups in P3HT as a function of irradiation time: (*filled diamond*) alkyl groups in the range 3,000–2,800 cm^{-1}; (*filled triangle*) thiophene ring at 1,510 cm^{-1}; (*open square*) carbonyl groups at 1,715 cm^{-1}; (*open circle*) thioesters at 620 cm^{-1}

After about 50 h of exposure to simulated sunlight, the original absorption intensity is reduced by almost 50% for both alkyl groups and thiophene ring. At the same time, signals assigned to C=O stretching of carbonyl species and S=O stretching of thioesters progressively appear.

These trends may be attributed to modifications occurring to the macromolecular structure caused by a two-fold mechanism. On one side (Scheme 1), oxidations on the alkyl side-chain may occur resulting from the attack of oxygen to the carbon in α-position to the thiophene ring, which may lead to the formation of carbonyl species (1,715 cm^{-1}) since it is recognized that the carbon atom of a methylene in α-position to an unsaturated species is characterized by reduced C–H bond energy, thus representing a preferential site for radical attack [26].

On the other side (Scheme 2), modifications of the polymer backbone may occur leading to the opening of the thiophene ring. In particular bands assigned to thioesters (620 cm^{-1}), sulfoxides (1,050 cm^{-1}), dialkyl sulphones (1,150 cm^{-1}) and sulphones (1,190 cm^{-1}) were detected in the IR spectra of irradiated samples.

Considering what found so far, P3HT seems to show a remarkable instability towards photo-oxidation under simulated sunlight. In order to reduce the degradation rate of the polymer, potential stabilizing additives were therefore employed in this work. In particular two substances were chosen, one belonging to the class of Hindered Amine Light Stabilizers (HALS) and the other being Multi-Walled Carbon Nanotubes (MWCNT). The former was chosen because of its known ability to act as a radical scavenger in plastics and coatings technology. The latter was selected because it may act both as a radical scavenger [20] and quencher of excited

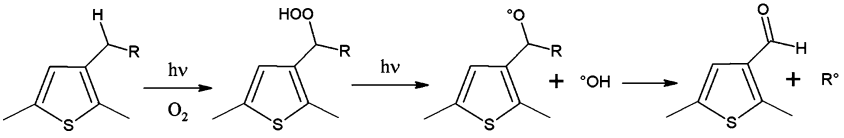

Scheme 1 Mechanism of photo-oxidation of lateral alkyl chain in P3HT

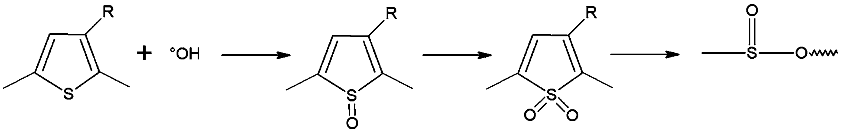

Scheme 2 Mechanism of photo-oxidation of polymer backbone in P3HT

states, and moreover it can be an efficient electron-acceptor photovoltaic component.

The HALS (5 wt%) was added to a solution of P3HT in chloroform (20 mg/mL), dissolved by magnetic stirring and then spin coated onto NaCl, KBr and CaF_2 substrates for FTIR analysis.

As far as the MWCNT system is concerned, a homogeneous dispersion of MWCNT in chloroform was prepared by ultrasonication for 90 min. The desired volume of the MWCNT dispersion was then added to a P3HT solution in chloroform (20 mg/mL) and a further 60 min ultrasonication was performed. The final concentration of the P3HT-MWCNT dispersion (20 mg/mL P3HT in chloroform—1 wt% MWCNT) was prepared by distillation of chloroform under vacuum and magnetic stirring. The dispersion was eventually spin coated onto NaCl, KBr and CaF_2 substrates for FTIR analysis.

The stabilizing effects of the two additives were monitored by means of FTIR. Figure 6 shows the changes of normalized absorption intensity of IR bands in the alkyl group region as a function of irradiation time The trend of neat P3HT is also reported, for reference.

No significant effects on the degradation rate of P3HT were reported after the addition of HALS to P3HT. On the other hand, a clear reduction in the degradation rate was observed when MWCNT were added. In particular, after about 100 h of exposure to simulated sunlight, a decrease of only 50% with respect to the original absorption intensity is observed in the case of P3HT-MWCNT blends. The same absorption intensity is reached after only 50 h of irradiation for neat P3HT and P3HT-HALS system.

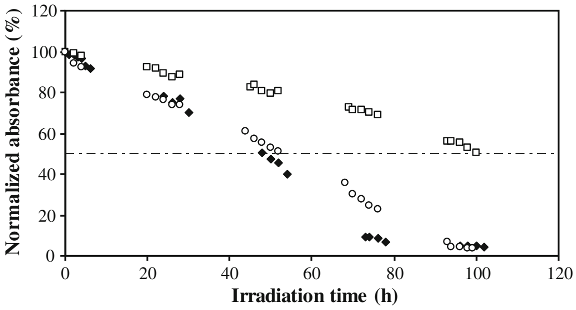

Fig. 6 Variation of normalized absorption intensity of the alkyl group IR signals as a function of irradiation time: (*filled diamond*) pure P3HT; (*open circle*) P3HT-HALS system; (*open square*) P3HT-MWCNT system

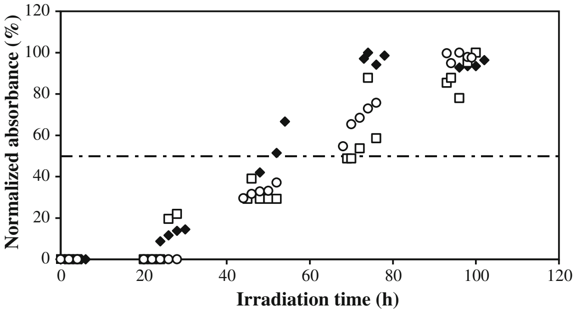

Fig. 7 Variation of normalized absorption intensity of IR signals related to carbonyl group as a function of irradiation time: (*filled diamond*) pure P3HT; (*open circle*) P3HT-HALS system; (*open square*) P3HT-MWCNT system

The time-dependent variation of normalized absorption intensity of IR bands related to carbonyl groups (1,715 cm^{-1}) during irradiation is reported in Fig. 7.

In this case both the presence of HALS and MWCNT appear to slightly slow down the degradation rate of P3HT. Moreover, the formation of carbonyl species appears to be slower for the P3HT-MWCNT system than for the P3HT-HALS one, according to the trend reported in Fig. 6. Similar trends were observed for the disappearance of IR signal assigned to the thiophene ring (1,510 cm^{-1}) and for the formation of the band assigned to thioesters (620 cm^{-1}).

The stabilizing effect of carbon nanotubes observed through FTIR in the P3HT-MWCNT blend might be explained by the radical scavenging properties of MWCNT which allow for a reduction of the degradation rate of P3HT. Similar results were actually observed on another system, namely poly[2-methoxy-5-(3′,7′-dimethyloctyloxy)-1,4-phenylenevinylene] (MDMO-PPV) blended with methano-fullerene [6,6]-phenyl C61-butyric acid methyl ester ([60] PCBM), suggesting that also PCBM can act as radical scavenger when mixed with P3HT and exposed to light [20].

The reduced stabilizing effect reported in the P3HT-HALS system could be attributed to the induction time needed by HALS molecules to activate and act as photo-stabilizers. Clearly, this induction time appears to be longer than the degradation rate of the neat polymer.

Conclusions

The results obtained from this work underline a substantial instability of P3HT to photooxidation following exposure to simulated sunlight. Modifications of the chemical structure of the polymer are observed, which corroborate the hypothesis of a degradation mechanism involving side-chain scission with formation of carbonyl species and aperture of the thiophene ring with formation of thioesters [11].

As a way to reduce photo-degradation rate, two substances were added to P3HT, namely a HALS and MWCNT, and the photo-chemical behaviour of these two new blends was investigated through FTIR.

While no significant effects were observed in the P3HT-HALS system, the addition of MWCNT to P3HT appeared to reduce significantly the degradation kinetics of the polymer, due to a radical scavenging effect of MWCNT. As a result, MWCNT might represent a good electron-acceptor candidate to improve photostability of organic solar cells.

References

1. Po R, Maggini M, Campioni N (2010) Polymer solar cells: recent approaches and achievements. J Phys Chem C 114:695–706
2. Jørgensen M, Norrman K, Krebs FC (2008) Stability/degradation of polymer solar cells. Sol Energy Mater Sol Cells 92:686–714
3. Krebs FC, Gevorgyan SA, Alstrup J (2009) A roll-to-roll process to flexible polymer solar cells: model studies, manufacture and operational stability studies. J Mater Chem 19:5442–5451
4. Krebs FC, Tromholt T, Jørgensen M (2010) Upscaling of polymer solar cell fabrication using full roll-to-roll processing. Nanoscale 1. doi:10.1039/b9nr00430k
5. Krebs FC (2009) All solution roll-to-roll processed polymer solar cells free from indium-tin-oxide and vacuum coating steps. Org Electron 10:761–768
6. Krebs FC, Norrman K (2010) Using light-induced thermocleavage in a roll-to-roll process for polymer solar cells. ACS Appl Mater Interfaces 2:877–887
7. Krebs FC, Gevorgyan SA, Gholamkhass B, Holdcroft S, Schlenker C, Thompson ME, Thompson BC, Olson D, Ginley DS, Shaheen SE, Alshareef HN, Murphy JW, Youngblood WJ, Heston NC, Reynolds JR, Jia S, Laird D, Tuladhar SM, Dane JGA, Atienzar P, Nelson J, Kroon JM, Wienk MM, Janssen RAJ, Tvingstedt K, Zhang F, Andersson M, Inganäs O, Lira-Cantu M, de Bettignies R, Guillerez S, Aernouts T, Cheyns D, Lutsen L, Zimmermann B, Würfel U, Niggemann M, Schleiermacher HF, Liska P, Grätzel M, Lianos P, Katz EA, Lohwasser W, Jannon B (2009) A round robin study of flexible large-area roll-to-roll processed polymer solar cell modules. Sol Energy Mater Sol Cells 93:1968–1977
8. Krebs FC, Jørgensen M, Norrman K, Hagemann O, Alstrup J, Nielsen TD, Fyenbo J, Larsen K, Kristensen J (2009) A complete process for production of flexible large area polymer solar cells entirely using screen printing—first public demonstration. Sol Energy Mater Sol Cells 93:422–441
9. Krebs FC, Nielsen TD, Fyenbo J, Wadstrøm M, Pedersen MS (2010) Manufacture, integration and demonstration of polymer solar cells in a lamp for the “Lighting Africa” initiative. Energy Environ Sci 3:512–525
10. Park SH, Roy A, Beaupré S, Cho S, Coates N, Moon JS, Moses D, Leclerc M, Lee K, Heeger AJ (2009) Bulk heterojunction solar cells with internal quantum efficiency approaching 100%. Nat Photonics 3:297–303
11. Roncali J (1992) Conjugated poly(thiophenes): synthesis, functionalization, and applications. Chem Rev 92:711–738
12. Norrman K, Gevorgyan SA, Krebs FC (2009) Water-induced degradation of polymer solar cells studied by $H_2^{18}O$ labeling. ACS Appl Mater Interfaces 1:102–112
13. Petersen MH, Gevorgyan SA, Krebs FC (2008) Thermocleavable low band gap polymers and solar cells therefrom with remarkable stability toward oxygen. Macromolecules 41:8986–8994
14. Krebs FC (2008) Air stable polymer photovoltaics based on a process free from vacuum steps and fullerenes. Sol Energy Mater Sol Cells 92:715–726
15. Abdou MSA, Holdcroft S (1993) Mechanisms of photodegradation of poly(3-alkylthiophenes) in solution. Macromolecules 26:2954–2962
16. Abdou MSA, Holdcroft S (1995) Solid-state photochemistry of π-conjugated poly(3-alkylthiophenes). Can J Chem 73:1893–1901
17. Ljungqvist N, Hjertberg T (1995) Oxidative degradation of poly(3-octylthiophene). Macromolecules 28:5993–5999
18. Caronna T, Forte M, Catellani M, Meille SV (1997) Photodegradation and photostabilization studies of poly(3-butylthiophene) in the solid state. Chem Mater 9:991–995

19. Chambon S, Rivaton A, Gardette JL, Firon M, Lutsen L (2006) Aging of a donor conjugated polymer: photochemical studies of the degradation of poly[2-methoxy-5-(3′,7′-dimethyloctyloxy)-1,4-phenylenevinylene]. J Polym Sci A Polym Chem 45:317–331
20. Chambon S, Rivaton A, Gardette JL, Firon M (2007) Photo- and thermal degradation of MDMO-PPV:PCBM blends. Sol Energy Mater Sol Cells 91:394–398
21. Manceau M, Rivaton A, Gardette JL, Guillerez S, Lemaître N (2009) The mechanism of photo- and thermooxidation of poly(3-hexylthiophene) (P3HT) reconsidered. Polym Degrad Stab 94:898–907
22. Manceau M, Rivaton A, Gardette JL (2008) Involvement of singlet oxygen in the solid-state photochemistry of P3HT. Macromol Rapid Commun 29:1823–1827
23. Chen TA, Wu X, Rieke RD (1995) Regiocontrolled synthesis of poly(3-alkylthiophenes) mediated by Rieke zinc: their characterization and solid-state properties. J Am Chem Soc 117:233–244
24. Hugger S, Thomann R, Heinzel T, Thurn-Albrecht T (2004) Semicrystalline morphology in thin films of poly(3-hexylthiophene). Colloid Polym Sci 282:932–938
25. Malik S, Nandi AK (2002) Crystallization mechanism of regioregular poly(3-alkyl thiophene)s. J Polym Sci B Polym Phys 40:2073–2085
26. Berkowitz J, Ellison GB, Gutman D (1994) Three methods to measure RH bond energies. J Phys Chem 98:2744–2765

ADVANCED MATERIALS
www.advmat.de

Materials Views
www.MaterialsViews.com

Long-Term Thermal Stability of High-Efficiency Polymer Solar Cells Based on Photocrosslinkable Donor-Acceptor Conjugated Polymers

Gianmarco Griffini, Jessica D. Douglas, Claudia Piliego, Thomas W. Holcombe, Stefano Turri, Jean M. J. Fréchet, and Justin L. Mynar**

Solution-processable polymer-based organic photovoltaics (OPVs) have attracted considerable attention over the past two decades because of the many advantages they can provide: low-cost fabrication, flexible devices, and light-weight construction.[1] In the most successful OPV device architectures, the photoactive layer is composed of a blend of a p-type conjugated polymer and an n-type fullerene derivative, forming the so-called donor–acceptor bulk heterojunction (BHJ).[2]

Recently, the long-term stability of OPV devices has been recognized as an important area of research, both in academia and industry.[3] Concerning this issue, a number of studies have demonstrated the detrimental effects of oxygen and moisture on device operation,[4] and attempts have been made to elucidate the degradation mechanism of the photoactive organic layer.[5] In addition to chemical degradation pathways, achieving and maintaining an effective BHJ morphology within the active layer is critical for sustaining high OPV performance. In optimized BHJs, phase separation of the electron donor and the electron acceptor domains should be on the same length-scale as the exciton diffusion length, facilitating efficient exciton harvesting.[6] Furthermore, a 3D bicontinuous network of the donor and acceptor materials is necessary for productive charge extraction from the device.[7]

Although an optimized BHJ morphology can be attained by means of several processing techniques,[8] the peak-performance morphology only represents a metastable state, which cannot usually be maintained over long operation times. In fact, most BHJ systems show poor stability and often undergo macrophase segregation of the blend components, especially after prolonged exposure to heat.[9] Considering that normal OPV device operation may subject the active layer to large temperature fluctuations, improving the robustness of the BHJ with respect to thermal stability is critical.[10]

Several studies have reported on the morphological evolution and thermal stability of the active layer in standard BHJ systems such as blends of poly(3-hexylthiophene) (P3HT):[6,6]-phenyl-C$_{61}$-butyric acid methyl ester (PC$_{61}$BM) or poly[2-methoxy-5-(3',7'-dimethyloctyloxy)-1,4-phenylenevinylene] (MDMO-PPV):PC$_{61}$BM. In such systems, phase segregation in the active layer occurs upon thermal annealing, resulting first in an improvement followed by a quick decline in device performance, particularly at high temperatures.[11–13] In order to improve the thermal stability of these OPV devices, different strategies have been presented, which include the use of diblock copolymer compatibilizers,[14] the use of fullerene-attached diblock copolymers,[15] and the use of both thermally crosslinkable acceptor[16] and donor[17] materials within the active layer. Recently, our group synthesized a library of photocrosslinkable P3HT copolymers containing some light-sensitive bromoalkyl substituents for use as p-type materials in BHJ devices. Utilizing these materials, it was shown that even after two days of annealing at an elevated temperature of 150 °C, the devices containing the photocrosslinked polymer within the active layer were able to retain their initial power conversion efficiency (PCE). This result was attributed to the stabilizing effect of the photocrosslinked polymer on the nanoscale morphology of the active layer.[18] In contrast to thermal crosslinking, photocrosslinking does not interfere with the thermal treatments that are often needed during device optimization; thus, this process allows for morphology optimization with independent control of crosslinking and thermal annealing.

Although BHJ devices based on the P3HT:PC$_{61}$BM blend represent a benchmark in the OPV literature, new p-type polymers have been synthesized in an effort to improve device efficiencies.[19] In particular, the copolymerization of electron-rich and electron-poor monomers, constituting the so-called donor–acceptor (D–A) approach, has proven to be an effective strategy to obtain low-bandgap polymers with optical and electronic properties that can be tuned via synthetic control of the electron-rich and electron-poor units. Using this strategy, reports have demonstrated PCEs approaching 7–8%, after systematic optimization of appropriate device parameters.[20] However, the thermal stability of OPVs based on D–A polymers has yet to be investigated in detail: no example of long-term thermally stable devices based on this class of high-efficiency p-type polymers has been reported to date.

G. Griffini, J. D. Douglas, Dr. C. Piliego, T. W. Holcombe,
Prof. J. M. J. Fréchet, Dr. J. L. Mynar
Departments of Chemistry and Chemical Engineering
University of California
Berkeley, Berkeley, CA 94720-1460, USA
E-mail: frechet@berkeley.edu; jmynar@gmail.com
G. Griffini, J. D. Douglas, Dr. C. Piliego, T. W. Holcombe,
Prof. J. M. J. Fréchet, Dr. J. L. Mynar
Materials Science Division
Lawrence Berkeley National Laboratory
Berkeley, CA 94720, USA
G. Griffini, Prof. S. Turri
Department of Chemistry
Materials and Chemical Engineering "Giulio Natta"
Politecnico di Milano, Piazza Leonardo da Vinci 32, 20133 Milan, Italy

DOI: 10.1002/adma.201004743

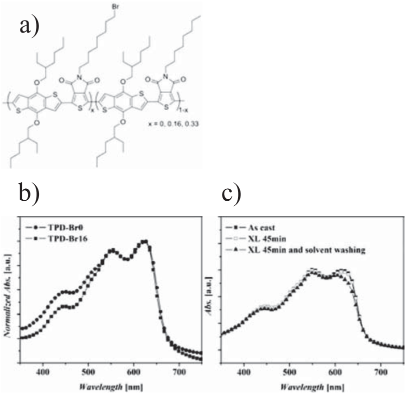

Figure 1. a) Molecular structure of the polymers used in this study. b) Normalized absorption spectra of polymer films without Br substituents (TPD-Br0) and with 16% Br substituents (TPD-Br16) in the polymer chain. c) Absorption spectra of TPD-Br16 polymer films pristine (as cast), after 45 min of UV-irradiation (photocrosslinking (XL) 45 min), and after UV-irradiation and solvent washing (XL 45 min and solvent washing).

Herein, we report the first study on the thermal stability of OPV devices based on D–A copolymers. Through a new synthetic pathway, we have developed a photocrosslinkable derivative of the thieno[3,4-*c*]pyrrole-4,6-dione (TPD)-based polymer that was recently reported.[20c,e] The new polymer contains TPD repeat units with a terminal, primary bromide functionality appended to the octyl solubilizing group (TPD-Br) (see **Figure 1**a), thereby allowing for photocrosslinking of the polymer in devices. By synthetically tuning the number of Br units in the polymer and by employing UV-mediated photocrosslinking, OPV devices with high PCE and excellent thermal stability were fabricated. Devices employing copolymers with varying amounts of Br units were tested: 0% Br-units (TPD-Br0), 16% Br-units (TPD-Br16), and 33% Br-units (TPD-Br33). The best OPV performance after annealing was obtained with photocrosslinked TPD-Br16. In contrast to the sharp PCE decrease observed for TPD-Br0 devices, the annealed OPVs based on photocrosslinked TPD-Br16 demonstrated remarkable long-term thermal stability. After 72 h of thermal annealing at 150 °C, an average PCE of 4.6% ± 0.1% was obtained with a short circuit current density (J_{SC}) of 10.1 mA cm^{-2}, an open circuit voltage (V_{OC}) of 0.85 V, and a fill factor (*FF*) of 54%. The maximum PCE obtained was as high as 4.7%. To the best of our knowledge, this represents the highest PCE reported thus far, for OPV systems subjected to long-term thermal annealing at high temperature.

The normalized UV-vis absorption spectra of the as-cast TPD-Br16 and TPD-Br0 polymers are shown in Figure 1b. Both polymers exhibit three maxima between 400 nm and 700 nm, in accordance with previous reports.[20c,e] Furthermore, no major differences can be observed between the absorption spectra of the two polymers, indicating that the addition of Br units to the polymer does not significantly affect its optical properties. Figure 1c shows the UV-vis absorption spectra of TPD-Br16 films as-cast and after photocrosslinking. After 45 min of UV irradiation, the polymer film becomes resistant to solvent washing. With thermal annealing, no solvent resistance is observed.[18] The absorption intensity at 550 nm after UV-irradiation and washing with solvent differs by less than 4% from the absorption intensity of the as-cast film, indicating that photocrosslinking has occurred. In addition, no major differences in the absorption spectra of as-cast and photocrosslinked films are observed, indicating that the photocrosslinking process does not significantly affect the optical properties of the solid state polymer. A similar trend was observed for the TPD-Br33 film (see Supporting Information). On the other hand, TPD-Br0 polymer containing no Br units does not undergo photocrosslinking when irradiated with UV light as evidenced by low resistance to solvent washing.

The performance of the corresponding OPV devices was investigated using the indium tin oxide (ITO)/poly(3,4-ethylenedioxythiophene) (PEDOT):poly(styrenesulfonate) (PSS)/polymer:[6,6]-phenyl-C_{71}-butyric acid methyl ester ($PC_{71}BM$)/Ca/Al device architecture. After optimization of TPD-Br16 and TPD-Br33 device parameters, *ortho*-dichlorobenzene (*o*-DCB) was chosen as the solvent for the active layer blend deposition. In addition, these devices do not contain high-boiling-point solvent additives,[21] as they did not yield any improvement to the performance of the TPD-Br16 and TPD-Br33 OPV devices. $PC_{71}BM$ was employed as the n-type material because it was found to yield higher device performance compared to $PC_{61}BM$ during device optimization (see Supporting Information).

The thermal stability of TPD-Br16 devices is shown in **Figure 2**a, where the performances of both photocrosslinked (TPD-Br16 XL) and non-photocrosslinked (TPD-Br16 no XL) devices are shown. For comparison, the thermal stability of TPD-Br0 devices is also shown. The average device parameters at 0 h and 72 h annealing are listed in **Table 1**. An optimal polymer:$PC_{71}BM$ wt.-ratio of 1:2 was found for both TPD-Br0 and TPD-Br16 polymer systems (see Supporting Information for details on device fabrication). The initial performance of TPD-Br16 no XL devices (5.6% PCE) is comparable to that of TPD-Br0 devices (5.2% PCE), suggesting that the introduction of a terminal alkyl-bromine functionality on the solubilizing group of TPD does not detrimentally affect the optical properties of the polymer and the PV performance of the OPV devices at this incorporation ratio. On the other hand, TPD-Br16 XL devices show a significantly lower initial PCE (3.3%) with respect to both TPD-Br0 and TPD-Br16 no XL. This can be attributed to the effect of crosslinking on the π-stacking of the polymer chains, affecting the electronic properties of the polymer and the OPV device performance.[20c] However, a striking difference is observed between TPD-Br16 XL and the other two devices upon exposure to heat: while both TPD-Br0 and TPD-Br16 no XL devices undergo a sharp decrease in performance upon thermal annealing over time, TPD-Br16 XL devices show an increase in PCE, which stabilizes after 24 h of annealing. A PCE as high as 4.6% was obtained for the crosslinked polymer after 72 h of annealing at 150 °C. This

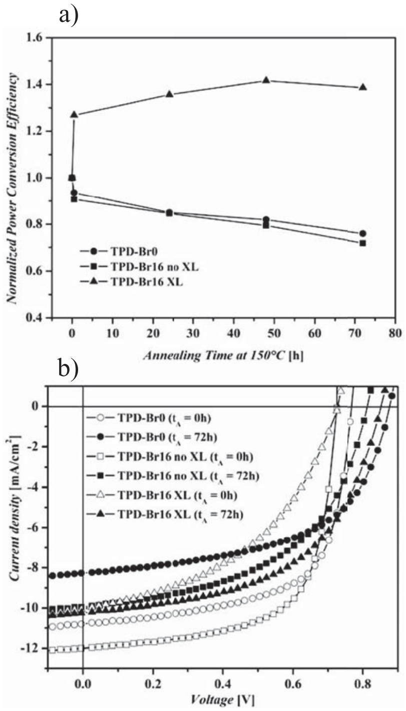

Figure 2. a) Normalized PCEs of TPD-Br0 (●), non-photocrosslinked TPD-Br16 (no XL ■), and photocrosslinked TPD-Br16 (XL ▲) devices during long-term thermal annealing at 150 °C with $PC_{71}BM$ as n-type material. The efficiency of each device was normalized to its initial efficiency (at annealing time 0 h). The same blend concentration (24 mg mL^{-1} in dichlorobenzene) and polymer:$PC_{71}BM$ ratio (1:2) was used for all devices. b) Current–voltage (*J–V*) curves of the best OPV devices before (open symbols, t_A = 0 h) and after (full symbols, t_A = 72 h) long-term thermal annealing (t_A).

represents the first demonstration of long-term thermally stable OPV devices based on a D–A polymer.

The evolution of device performance with annealing time for the three systems reported in Figure 2a can be better understood by analyzing the *J–V* output characteristics recorded at annealing times 0 h and 72 h at 150 °C (see Figure 2b). An increase in the V_{OC} is observed for all devices after 72 h of annealing at high temperature. This increase may be related to a change in the energy of the interfacial charge-transfer states between the polymer and fullerene caused by morphological rearrangement of the fullerene molecules adjacent to the polymer chains after annealing.[22] However, both TPD-Br0 and TPD-Br16 no XL devices undergo a significant decrease in their short-circuit current density and fill factor during annealing, which results in a sharp decrease in PCE with respect to the initial values. Conversely, the J_{SC} of TPD-Br16 XL devices remains constant, even after 72 h of annealing at 150 °C, while the fill factor increases about 18% compared to its initial value. This indicates that photocrosslinking has allowed for an optimal morphology of the active layer to be preserved throughout the entire annealing process, thus leading to remarkable long-term thermal stability of these devices. Similar trends were found for TPD-Br33 devices, although lower PCEs with respect to TPD-Br16 were observed for both the non-photocrosslinked and the photocrosslinked systems (see Supporting Information). This indicates that judicious control of the TPD-Br content in the polymer is necessary to ensure optimal PV performances.

Table 1. Characteristic photovoltaic parameters for TPD-Br0:$PC_{71}BM$ and TPD-Br16:$PC_{71}BM$ devices.

	XL[a]	Annealing time t_A [h]	J_{SC} [mA cm^{-2}]	V_{OC} [V]	*FF* [%]	PCE (PCE_{max}) [%]
TPD-Br0	–	0	−10.6	0.76	64	5.2 (5.3)
TPD-Br0	–	72	−8.2	0.87	55	3.9 (4.1)
TPD-Br16	–	0	−11.7	0.73	66	5.6 (5.7)
TPD-Br16	–	72	−9.6	0.81	51	4.0 (4.2)
TPD-Br16	+	0	−10.0	0.73	45	3.3 (3.3)
TPD-Br16	+	72	−10.1	0.85	53	4.6 (4.7)

[a] Active layers not subjected (–) and subjected (+) to crosslinking under UV irradiation prior to cathode deposition.

In order to clarify the effect of photocrosslinking on the morphology of the active layer, atomic force microscopy (AFM) was performed on both TPD-Br16 no XL and TPD-Br16 XL films (see **Figure 3**). Before thermal annealing, the non-photocrosslinked TPD-Br16 active layer film (Figure 3a,b) shows a well-developed interpenetrating network and a finer nanoscale morphology compared to the photocrosslinked film (Figure 3e,f). The surface root-mean-square (RMS) roughness before annealing is 2.5 nm and 2.1 nm for non-photocrosslinked and photocrosslinked films, respectively. After annealing at 150 °C for 72 h, a very rough surface morphology is observed on the non-photocrosslinked film (Figure 3c,d), resulting in a value of RMS roughness as high as 34.9 nm. This significant morphology change may yield poor contact between the active layer and the electrode, as well as unfavorable conditions for charge separation and transport. Accordingly, a significant decrease in device performance is observed for the TPD-Br16 no XL device after annealing. On the other hand, a finer morphology is observed for the photocrosslinked film after annealing (Figure 3g,h), which is correlated to the increase in device PCE. Only a slight increase in RMS roughness is observed for this film (up to 3.0 nm), suggesting that photocrosslinking allows for the preservation of a well-developed interpenetrating donor/acceptor network that can be maintained, even after 72 h of annealing at 150 °C.

It is worth mentioning that during device optimization, each polymer was also tested in BHJ devices with $PC_{61}BM$

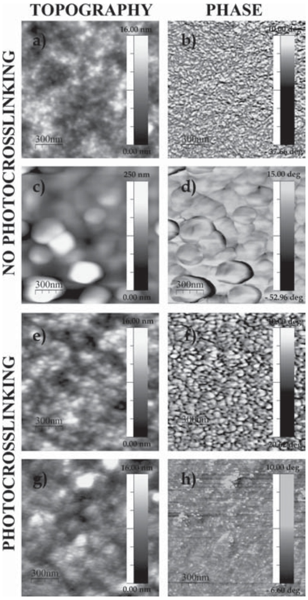

Figure 3. AFM (1.5 μm × 1.5 μm) topography and phase images of TPD-Br16:PC$_{71}$BM active layers (1:2 wt:wt). The top four images are for the non-crosslinked films (TPD-Br16 no XL), prior to (a,b) and after (c,d) 72 h of thermal annealing at 150 °C. The bottom four images are for the crosslinked devices (TPD-Br16 XL), prior to (e,f) and after (g,h) 72 h of thermal annealing at 150 °C.

(see Supporting Information). As opposed to BHJs containing photocrosslinked polymer and PC$_{71}$BM, devices containing photocrosslinked polymer and PC$_{61}$BM showed a peak PCE after 30 min of annealing at 150 °C that was not maintained after longer annealing times. Additionally, AFM analysis revealed the formation of aggregates in both photocrosslinked and non-photocrosslinked active layers after 72 h of annealing at 150 °C, although a rougher surface was found for non-photocrosslinked films (see Supporting Information). We speculate that the different behavior found for polymer:PC$_{61}$BM blends compared to polymer:PC$_{71}$BM blends may be related to the different sizes of these fullerene molecules (1.67 vs 1.92 nm)[23] and their movement during the annealing process. Thermal annealing appears to allow the smaller PC$_{61}$BM molecules to diffuse within the crosslinked polymer network, initially improving the performance but ultimately leading to formation of larger aggregates, whereas this effect is not observed with PC$_{71}$BM. Due to steric bulkiness, the larger PC$_{71}$BM molecules may be confined into the polymer network, thus inhibiting the formation of large aggregates. This result may indicate that, in addition to increased light absorption with respect to PC$_{61}$BM, PC$_{71}$BM is able to provide morphological stability of the active layer at high temperature. Further investigations to clarify these observations are underway.

In summary, the first photocrosslinkable donor–acceptor conjugated polymer for use in BHJ organic solar cells was developed. After 72 h of thermal annealing at 150 °C, a stable PCE of 4.6% was obtained in devices containing photocrosslinked polymer in the active layer. This represents the highest performance reported thus far for thermally stable OPV devices. Careful control of the crosslinking moiety content in the polymer was found to be critical in order to achieve optimal device performance. The results of this study provide important guidelines for the design and development of OPV materials with long-term thermal stability and high efficiency.

Supporting Information

Supporting Information is available from the Wiley Online Library or from the author.

Acknowledgements

This work is part of the "Plastics Electronics" program at Lawrence Berkeley National Laboratory and was supported by the Director, Office of Science, Office of Basic Energy Sciences, Materials Sciences and Engineering Division, of the U.S. Department of Energy under Contract No. DE-AC02-05CH11231 (all experimental work). G.G. thanks Fondazione Banca del Monte di Lombardia; T.W.H. thanks the National Science Foundation, and J.D.D. thanks the Natural Sciences and Engineering Research Council of Canada for research fellowships. The authors thank Dr. Jill Millstone and Claire Woo for helpful discussions.

Received: December 27, 2010

---

[1] a) C. J. Brabec, S. Gowrisanker, J. J. M. Halls, D. Laird, S. Jia, S. P. Williams, *Adv. Mater.* **2010**, *22*, 3839; b) G. Dennler, M. C. Scharber, C. J. Brabec, *Adv. Mater.* **2009**, *21*, 1323; c) B. Kippelen, J. L. Brédas, *Energy Environ. Sci.* **2009**, *2*, 251; d) B. C. Thompson, J. M. J. Fréchet, *Angew. Chem. Int. Ed.* **2008**, *47*, 58; e) F. C. Krebs, J. Fyenbo, M. Jørgensen, *J. Mater. Chem.* **2010**, *20*, 8994; f) F. C. Krebs, T. D. Nielsen, J. Fyenbo, M. Wadstrøm, M. S. Pedersen, *Energy Environ. Sci.* **2010**, *3*, 512.

[2] a) G. Yu, J. Gao, J. C. Hummelen, F. Wudl, A. J. Heeger, *Science* **1995**, *270*, 1789; b) G. Yu, A. J. Heeger, *J. Appl. Phys.* **1995**, *78*, 4510.

[3] M. Jørgensen, K. Norrman, F. C. Krebs, *Sol. Energy Mater. Sol. Cells* **2008**, *92*, 686.

[4] a) F. C. Krebs, H. Spanggaard, *Chem. Mater.* **2005**, *17*, 5235; b) F. C. Krebs, K. Norrman, *Prog. Photovoltaics* **2007**, *15*, 697; c) M. O. Reese, A. J. Morfa, M. S. White, N. Kopidakis, S. E. Shaheen, G. Rumbles, D. S. Ginley, *Sol. Energy Mater. Sol. Cells* **2008**, *92*, 746; d) A. Seemann, H. J. Egelhaaf, C. J. Brabec, J. A. Hauch, *Org. Electron.* **2009**, *10*, 1424.

[5] a) M. Manceau, S. Chambon, A. Rivaton, J. L. Gardette, S. Guillerez, N. Lemaitre, *Sol. Energy Mater. Sol. Cells* **2010**, *94*, 1572; b) M. O. Reese, A. M. Nardes, B. L. Rupert, R. E. Larsen, D. C. Olson, M. T. Lloyd, S. E. Shaheen, D. S. Ginley, G. Rumbles, N. Kopidakis,

Adv. Funct. Mater. **2010**, *20*, 3476.; c) A. Rivaton, S. Chambon, M. Manceau, J. L. Gardette, N. Lamaitre, S. Guillerez, *Polym. Degrad. Stab.* **2010**, *95*, 278.

[6] S. K. Pal, T. Kesti, M. Maiti, F. Zhang, O. Inganäs, S. Hellström, M. R. Andersson, F. Oswald, F. Langa, T. Österman, T. Pascher, A. Yartsev, V. Sundström, *J. Am. Chem. Soc.* **2010**, *132*, 12440.

[7] a) W. L. Ma, C. Y. Yang, X. Gong, K. Lee, A. J. Heeger, *Adv. Funct. Mater.* **2005**, *15*, 1617; b) X. Yang, J. Loos, *Macromolecules* **2007**, *40*, 1353.

[8] J. Peet, M. L. Senatore, A. J. Heeger, G. C. Bazan, *Adv. Mater.* **2009**, *21*, 1521.

[9] a) S. Bertho, G. Janssen, T. J. Cleij, B. Conings, W. Moons, A. Gadisa, J. D'Haen, E. Goovaerts, L. Lutsen, J. Manca, D. Vanderzande, *Sol. Energy Mater. Sol. Cells* **2008**, *92*, 753; b) B. Paci, A. Generosi, V. Rossi Albertini, R. Generosi, P. Perfetti, R. de Bettignies, C. Sentein, *J. Phys. Chem. C* **2008**, *112*, 9931.

[10] a) D. Di Nuzzo, A. Aguirre, M. Shahid, V. S. Gevaerts, S. C. J. Meskers, R. A. J. Janssen, *Adv. Mater.* **2010**, *22*, 4321; b) M. Helgesen, M. Bjerring, N. C. Nielsen, F. C. Krebs, *Chem. Mater.* **2010**, **22**, 5617.

[11] B. Conings, S. Bertho, K. Vandewal, A. Senes, J. D'Haen, J. Manca, R. A. J. Janssen, *Appl. Phys. Lett.* **2010**, *96*, 163301.

[12] a) X. N. Yang, J. Loos, S. C. Veenstra, W. J. H. Verhees, M. M. Wienk, J. M. Kroon, M. A. J. Michels, R. A. J. Janssen, *Nano Lett.* **2005**, *5*, 579; b) X. N. Yang, J. K. J. van Duren, R. A. J. Janssen, M. A. J. Michels, J. Loos, *Macromolecules* **2004**, *37*, 2151.

[13] K. Sivula, C. K. Luscombe, B. C. Thompson, J. M. J. Fréchet, *J. Am. Chem. Soc.* **2006**, *128*, 13988.

[14] K. Sivula, Z. T. Ball, N. Watanabe, J. M. J. Fréchet, *Adv. Mater.* **2006**, *18*, 206.

[15] S. Miyanishi, Y. Zhang, K. Tajima, K. Hashimoto, *Chem. Commun.* **2010**, *46*, 6723.

[16] M. Drees, H. Hoppe, C. Winder, H. Neugebauer, N. S. Sariciftci, W. Schwinger, F. Schaffler, C. Topf, M. C. Scharber, Z. G. Zhu, R. Gaudiana, *J. Mater. Chem.* **2005**, *15*, 5158.

[17] S. Miyanishi, K. Tajima, K. Hashimoto, *Macromolecules* **2009**, *42*, 1610.

[18] B. J. Kim, Y. Miyamoto, B. W. Ma, J. M. J. Fréchet, *Adv. Funct. Mater.* **2009**, *19*, 2273.

[19] a) E. Bundgaard, F. C. Krebs, *Sol. Energy Mater. Sol. Cells* **2007**, *91*, 954; b) H. Y. Chen, J. H. Hou, S. Q. Zhang, Y. Y. Liang, G. W. Yang, Y. Yang, L. P. Yu, Y. Wu, G. Li, *Nat. Photonics* **2009**, *3*, 649; c) Y. F. Li, Y. P. Zou, *Adv. Mater.* **2008**, *20*, 2952.

[20] a) L. J. Huo, J. H. Hou, S. Q. Zhang, H. Y. Chen, Y. Yang, *Angew. Chem. Int. Ed.* **2010**, *49*, 1500; b) Y. Y. Liang, Z. Xu, J. B. Xia, S. T. Tsai, Y. Wu, G. Li, C. Ray, L. P. Yu, *Adv. Mater.* **2010**, *22*, E135; c) C. Piliego, T. W. Holcombe, J. D. Douglas, C. H. Woo, P. M. Beaujuge, J. M. J. Fréchet, *J. Am. Chem. Soc.* **2010**, *132*, 7595; d) Y. Zhang, S. K. Hau, H. L. Yip, Y. Sun, O. Acton, A. K. Y. Jen, *Chem. Mater.* **2010**, *22*, 2696; e) Y. P. Zou, A. Najari, P. Berrouard, S. Beaupre, B. R. Aich, Y. Tao, M. Leclerc, *J. Am. Chem. Soc.* **2010**, *132*, 5330.

[21] a) C. V. Hoven, X. D. Dang, R. C. Coffin, J. Peet, T. Q. Nguyen, G. C. Bazan, *Adv. Mater.* **2010**, *22*, E63; b) J. K. Lee, W. L. Ma, C. J. Brabec, J. Yuen, J. S. Moon, J. Y. Kim, K. Lee, G. C. Bazan, A. J. Heeger, *J. Am. Chem. Soc.* **2008**, *130*, 3619.

[22] a) K. Vandewal, K. Tvingsted, A. Gadisa, O. Inganäs, J. V. Manca, *Phys. Rev. B* **2010**, *81*, 125204; b) M. D. Perez, C. Borek, S. R. Forrest, M. E. Thompson, *J. Am. Chem. Soc.* **2009**, *131*, 9281.

[23] T. Kawauchi, J. Kumaki, A. Kitaura, K. Okoshi, H. Kusanagi, K. Kobayashi, T. Sugai, H. Shinohara, E. Yashima, *Angew. Chem. Int. Ed.* **2008**, *47*, 515.

JACS
JOURNAL OF THE AMERICAN CHEMICAL SOCIETY
ARTICLE
pubs.acs.org/JACS

Steric Control of the Donor/Acceptor Interface: Implications in Organic Photovoltaic Charge Generation

Thomas W. Holcombe,[†] Joseph E. Norton,[#] Jonathan Rivnay,[^] Claire H. Woo,[‡,§] Ludwig Goris,[^,∇] Claudia Piliego,[§] Gianmarco Griffini,[§,○] Alan Sellinger,[^] Jean-Luc Brédas,[#] Alberto Salleo,[^] and Jean M. J. Fréchet*,[†,‡,§,∥]

[†]Department of Chemistry, and [‡]Department of Chemical Engineering, University of California Berkeley, Berkeley, California 94720-1460, United States
[§]Materials Sciences Division, Lawrence Berkeley National Laboratory, Berkeley, California 94720, United States
[∥]King Abdullah University of Science and Technology, Thuwal, Saudi Arabia 23955-6900
[^]Department of Materials Science and Engineering, Stanford University, Stanford, California 94305, United States
[#]Center for Organic Photonics and Electronics and School of Chemistry and Biochemistry, Georgia Institute of Technology, Atlanta, Georgia 30332, United States
[∇]Institute for Materials Research (IMO), Hasselt University, Diepenbeek, Belgium
[○]Department of Chemisty, Politecnico di Milano, 20133 Milan, Italy

Ⓢ *Supporting Information*

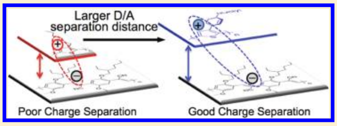

ABSTRACT: The performance of organic photovoltaic (OPV) devices is currently limited by modest short-circuit current densities. Approaches toward improving this output parameter may provide new avenues to advance OPV technologies and the basic science of charge transfer in organic semiconductors. This work highlights how steric control of the charge separation interface can be effectively tuned in OPV devices. By introducing an octylphenyl substituent onto the investigated polymer backbones, the thermally relaxed charge-transfer state, and potentially excited charge-transfer states, can be raised in energy. This decreases the barrier to charge separation and results in increased photocurrent generation. This finding is of particular significance for nonfullerene OPVs, which have many potential advantages such as tunable energy levels and spectral breadth, but are prone to poor exciton separation efficiencies. Computational, spectroscopic, and synthetic methods were combined to develop a structure−property relationship that correlates polymer substituents with charge-transfer state energies and, ultimately, device efficiencies.

■ INTRODUCTION

State-of-the-art solution processable organic photovoltaic (OPV) devices generally rely on fullerene derivatives as both the electron acceptor and the electron transporter.[1] Fullerene:polymer blends, termed bulk heterojunctions (BHJs), hold record efficiencies around 8%.[2] Although these devices have provided exceptional growth for the field of OPVs and have demonstrated rapid performance improvement over the past two decades, alternative n-type materials[3] and device architectures[4] could lead to "break-through" technological and basic science advances. Currently, the best nonfullerene OPV device efficiencies hover around 2%.[5] To move beyond fullerene-based OPVs, a greater understanding of charge generation in organic photovoltaics is critical.

Fullerenes provide several potential advantages over polymers and nonfullerene small molecules in photovoltaic applications: they possess high molecular symmetry,[6] are strongly polarizable, and present triply degenerate LUMO levels.[7] Conjugated polymers and planar small molecules are less symmetric, often have well-defined charge-transport axes,[8] and are generally not as highly polarizable overall; conjugated polymers have a dielectric constant of ca. 3[9a] versus fullerenes with a dielectric constant of ca. 4.[9b] These properties of fullerenes generally facilitate charge separation and the generation of free carriers.

Because OPVs require a donor/acceptor interface to separate the photoexcited state (Frenkel-type excitons),[10] it is important to understand the thermodynamics of charge separation at this interface.[1d,11] The relative free energy of charge separation (ΔG_{CS}^{rel}) for several donor materials combined with a fullerene acceptor has previously been estimated by the abbreviated Weller equation $\Delta G_{CS}^{rel} = E_s - |(\mathrm{HOMO}_{\mathrm{donor}} - \mathrm{LUMO}_{\mathrm{acceptor}})|$, where the difference between the singlet excited state energy (E_s) and the relative band offsets provided good agreement with measured short-circuit current (J_{sc}).[12] Although values for ΔG_{CS}^{rel} calculated from this equation correlated with the observed J_{sc} for several devices,[12,13] other factors such as active layer absorption breadth, optical density, morphology, as well as charge-carrier mobility and electrode choice are all known to critically affect J_{sc} in addition to ΔG_{cs}. A brief description of how

Received: April 8, 2011
Published: June 20, 2011

morphology can specifically impact charge separation is presented in the Supporting Information, and it is discussed with reference to the current investigation. Notably, the abbreviated Weller equation does not include the lattice polarization energy or Coulomb attraction terms, as these are not easily measured.[14] Toward expanding our understanding of charge generation in OPVs, we must explore factors beyond the thermodynamics of charge separation as estimated from bulk electronic properties.

For instance, charge generation depends not only on the donor and acceptor material state energies, but also on the specific molecular environment at the donor/acceptor (D/A) interface and on the kinetics of exciton separation/recombination.[15,11] Akin to a chemical reaction, exciton separation to yield free charges can proceed via more than one mechanism. In some cases, no "reaction intermediates" are observed, whereas in other cases there is a spectroscopically observable "geminate pair" or charge transfer (CT) state. Probing the parameters that control the mechanism of charge generation, particularly for nonfullerene devices, is of great importance to the field of OPVs. Studies show that this electron−hole (e−h) pair is sensitive to applied electric field and, intriguingly, to hydrostatic pressure: an externally applied field during device operation is known to increase the current extracted from the device; when the bias is applied opposite ("reverse") to the voltage generated under illumination, free carriers are quickly removed from the active layer, and the dipolar geminate pair is driven to separate.[16] External pressure on the system is believed to have the opposite effect on the geminate pair, decreasing the intermolecular distance at the D/A interface, and leading to increased radiative recombination of the CT state with a lower energy, implying a more stable, deeply trapped intermediate.[17]

Our work toward understanding charge generation started from a structural point of view, and we drew inspiration from studies reported by Granstrom et al. in 1998.[18] In that publication, poly[3-(4-*n*-octyl)-phenylthiophene] (POPT) was shown to produce the most photocurrent in any OPV device at the time, a notable achievement with the common electron acceptor material poly[2-methoxy-5-(2′-ethylhexyloxy)-1,4-(1-cyanovinylene)phenylene] (CNPPV). Motivated by that research, we reported studies in which (POPT) outperformed poly(3-hexylthiophene) (P3HT) in both bilayer devices with CNPPV[5b] and BHJ devices with the newer acceptor material 4,7-bis(2-(1-(2-ethylhexyl)-4,5-dicyanoimidazol-2-yl)vinyl)benzo[*c*][1,2,5]-thiadiazole (EV-BT).[5c] Our first report focused on the inconsistency between expected and realized performance values for OPV devices with the acceptor CNPPV, specifically the almost double short-circuit current density (J_{sc}) for POPT devices despite reduced optical density as compared to P3HT; however, very little was understood at that time about why better performance was achieved with POPT instead of P3HT. In our second report, we utilized EV-BT to make progress toward elucidating the physical properties that governed the OPV performance parameters of these nonfullerene devices. For example, reverse bias analysis suggested a tighter binding of the geminate pair at the P3HT:EV-BT interface; that is, a lower-energy CT state provided a deeper energetic well (a trapped intermediate) for partially separated charges. We suspected that the octylphenyl content of POPT played a critical role at the D/A interface, potentially facilitating geminate pair separation.

To shed light on how using an alkylphenyl side group enhances J_{sc} as compared to a simple alkyl side group, we investigated analogous material combinations with different substitution and acceptor materials. Beyond correlating structure to performance on the basis of multiple device comparisons, more direct methods to investigate the CT states were necessary to draw a fitting conclusion. Herein, we utilize a combination of computational and spectroscopic methods, as well as tailored synthesis and extensive device engineering, to understand how modifying thiophene substitution from alkyl to octylphenyl on two otherwise identical backbones, polythiophene and polyquarterthiophene, leads to a greater understanding of the effects that side group interactions at D/A interfaces have on charge generation. Structural control of the D/A interface may prove to be a powerful tool for tuning charge separation dynamics, and we

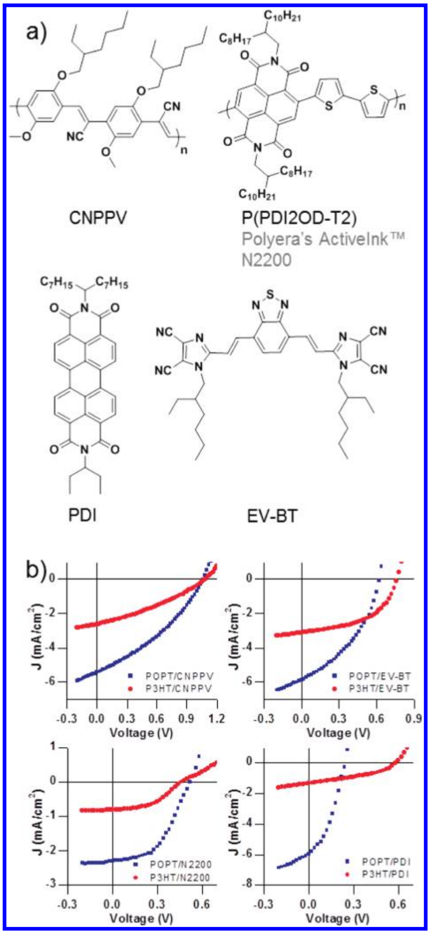

Figure 1. (a) Structures of P3HT and POPT, (b) the structures of four different acceptors (two polymers and two small molecules) that are tested in a head-to-head comparison between P3HT and POPT. (c) $J-V$ curves for the devices corresponding to the acceptor components in (a).

Table 1. PV Output Characteristics of POPT versus P3HT Devices, and Maximum Efficiencies for Optimized Device Systems[a]

device active layer	J_{sc} [mA/cm^2]	V_{oc} [V]	FF	PCE [%]
POPT/CNPPV	−5.44	1.06	0.35	2.00
P3HT/CNPPV	−2.63	1.08	0.33	0.93
POPT:EV-BT	−5.70	0.62	0.40	1.41
P3HT:EV-BT	−2.81	0.77	0.51	1.11
POPT/N2200	−2.50	0.52	0.47	0.61
P3HT/N2200	−0.80	0.46	0.46	0.17
POPT:PDI	−5.70	0.24	0.37	0.51
P3HT:PDI	−1.70	0.57	0.41	0.39

[a] Symbol "/" indicates a bilayer device, while symbol ":" indicates a BHJ device. Devices were optimized first on the basis of thickness (solvent choice and solution concentration) and then on the basis of annealing conditions (various temperatures and times).

provide a seminal example of how steric effects can improve charge separation in organic photovoltaics.

■ RESULTS

Both P3HT and POPT were synthesized via the GRIM polymerization method.[5b] The structure of POPT consists of phenyl groups covalently bound to the polythiophene backbone as part of the solubilizing substituent. This functionality increases the ionization potential (deepens the HOMO level) to −5.5 eV from −5.2 eV as compared to P3HT. Additionally, the optical properties are shifted toward a broader spectral response while maintaining similar charge-transport properties.[5b] The energetic changes result in an excited state that is lower in energy (and the electron affinity is also more exothermic) in POPT as compared to P3HT; thus, POPT is thermodynamically less likely to undergo exciton separation with a given acceptor, as compared to P3HT (when a normal Marcus regime can be invoked). Contrary to thermodynamic expectations, however, POPT yielded more efficient charge separation as a donor material in PV cells with polymeric and small molecule acceptors, such as CNPPV and EV-BT, respectively.[5b,c] In particular, the considerably and recurrently higher J_{sc} prompted an in-depth investigation combining device fabrication, theoretical modeling, and advanced spectroscopy to gain insight into these systems. The following results exploit observed differences in performance caused by the presence of phenyl substituents to better understand the charge separation process. By expanding our data set beyond the two systems already reported,[5b,5c] we aim to probe the universality of this design strategy for improving charge generation in nonfullerene OPVs.

Four acceptors were utilized with POPT and P3HT in head-to-head comparisons: CNPPV, EV-BT, *N*-(1-hexylheptyl)-*N*′-(1-ethylpropyl)perylene-3,4,9,10-tetracarboxylic diimide (PDI),[19] and poly{[*N*,*N*′-bis(2-octyldodecyl)-naphthalene-1,4,5,8-bis(dicarboximide)-2,6-diyl]-*alt*-5,5′-(2,2′-bithiophene) (Polyera ActiveInk N2200),[20] Figure 1a (see the Supporting Information for device fabrication details). In most cases, both bilayer and bulk heterojunction devices were compared, provided that an orthogonal solvent system was found to allow the fabrication of bilayers; here, we report the device architecture that demonstrated the higher efficiencies for each acceptor material. Polymer−polymer solar cells performed better in the bilayer device architecture, whereas polymer−small molecule solar cells were better in the BHJ architecture. On the basis of individually optimized devices in all four comparisons, POPT consistently outperforms P3HT (Table 1 and Figure 1b). While the V_{oc} and FF of the POPT and P3HT devices are comparable in most cases, the J_{sc} values of POPT devices are at least twice those of P3HT devices, leading to the higher overall efficiencies of POPT devices. It should be noted that the P3HT/N2200 device results are consistent with two recent reports that demonstrated N2200 in a BHJ device with P3HT yields ~0.2% efficiency.[21] Additionally, the kink observed for the P3HT/N2200 device may be due to similar effects discussed in prior work.[16b] The effect of morphology on J_{sc}, generally and in the cases of POPT/CNPPV and P3HT/CNPPV devices, is discussed in the Supporting Information.

To generalize the effect of interfacial steric interactions on charge generation, we expanded the scope of this study beyond POPT and P3HT to another polymer backbone, polyquarterthiophene. We synthesized poly(3,3-di(4-*n*-octyl)phenylquarterthiophene) PQT-OP and compared it to poly(3,3-didodecylquarterthiophene) PQT-DD (Table 2 and Figure 2). Independently optimized devices with CNPPV, EV-BT, and PDI were consistently found to perform nearly twice as well with PQT-OP than PQT-DD, due largely to an increase in J_{sc}. The V_{oc} values for PQT-based devices with the same

Table 2. PV Output Characteristics of PQT-OP versus PQT-DD Devices[a]

device active layer	J_{sc} [mA/cm^2]	V_{oc} [V]	FF	PCE [%]
PQT-OP/CNPPV	−2.43	1.18	0.39	1.12
PQT-DD/CNPPV	−1.51	1.20	0.38	0.69
PQT-OP/EV-BT	−2.68	0.95	0.48	1.22
PQT-DD/EV-BT	−1.48	0.98	0.43	0.62
PQT-OP:PDI	−3.33	0.63	0.42	0.88
PQT-DD:PDI	−2.18	0.66	0.34	0.49

[a] Reported are maximum efficiencies for individually optimized device systems. A "/" indicates a bilayer device, while a ":" indicates a BHJ device.

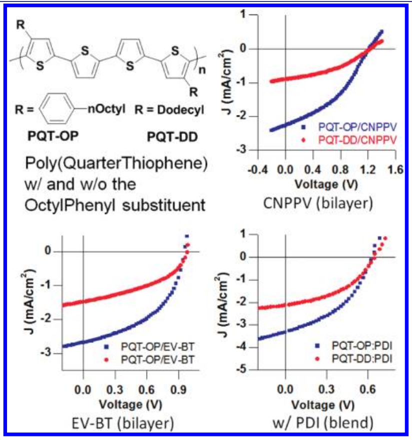

Figure 2. PQT polymer structures and a comparison of individually optimized devices. Devices were optimized first on the basis of thickness (solvent choice and solution concentration) and then on annealing conditions (various temperatures and times).

acceptor material were greater than for the polythiophene-based; however, there were no significant V_{oc} differences between the phenyl and alkyl PQT derivatives. This lends credence to the hypothesis that interfacial interactions could play a role that rivals the importance of the materials state energies.[22,23] The CT state energy, whatever its physical structure, has already been strongly correlated with V_{oc}.[22] It is worth noting that PQT-OP provides PDI-based devices with the highest performance to date. These data supported our hypothesis that the effect of this substituent could be generalized to other systems, as this is the same trend that was observed for POPT as compared to P3HT.

These experimental results are in contradiction with predictions based on a simple comparison of the donor polymer state energies. The larger ionization potential (lower HOMO level) of POPT as compared to P3HT (−5.5 vs −5.2 eV) in combination with a smaller bandgap should thermodynamically result in a lower J_{sc} based on the abbreviated Weller equation. However, octylphenyl devices produce significantly increased J_{sc} values as compared to devices utilizing the alkyl analogues. Morphological and light absorption parameters were ruled out in previous studies as the dominant factor in this kind of comparison, through a careful examination of device output parameters during optimization and analysis (such as reverse-bias analysis), as well as characterization of the films by AFM.[5b,c] Examination of the PQT polymers provided similar results. PQT-OP has a slightly larger ionization potential (IP) and a similar optical gap as compared to PQT-DD; PQT-OP and PQT-DD have IPs of −5.4 versus −5.3 eV, respectively, and optical gaps of approximately 1.9−2.0 eV (with absorption onsets of 640 and 620 nm). Again, devices using the octylphenyl-containing donor polymers consistently produce a substantially greater J_{sc}. These data clearly confirm that the material state energies and optical properties are not the only factors affecting the charge generation efficiencies in these systems. More importantly, we hypothesize that the molecular interactions at the D/A interface are a determining factor in these devices. Modeling of the D/A interface has recently predicted that the molecular configurations[23] and environment at this interface are critical in the charge-generation process, and here we aim to correlate theory with a benchmark physical test system.[15,24]

Because the highest performing devices utilized POPT and P3HT in combination with CNPPV (Table 1, Figure 1) as the component materials, these systems were characterized in more detail to understand how their structural properties influence interfacial interactions and, ultimately, charge generation. The component materials were first analyzed using a computational description of their molecular geometries. Modeling at the Density Functional Theory (DFT) B3LYP/6-31G(d,p) level of theory provided optimized geometries of the neutral ground states for (isolated) hexamers of the relevant species (Figure 3). Two POPT conformations were explored: the first structure allows the phenyl rings to participate in conjugation with the thiophene backbone (Figure 3b, POPT-*unconstrained*), and the second structure forces the phenyl rings to twist perpendicular to the backbone (Figure 3c, POPT-*perp*). POPT-*perp* minimizes conjugation between the pendant phenyl ring of the side group and the thiophene ring of the polymer backbone but maximizes conjugation along the backbone (see Supporting Information, Figure S1). The neutral ground-state geometries were also calculated for P3HT (Figure 3a) and CNPPV (Figure 3d), where the alkyl chains were modeled as methyl groups. The calculations show that the backbone of POPT is strictly planar only when the phenyl rings are forced out of plane with respect to the backbone, minimizing steric or electronic interactions between the thiophene and phenyl groups.

Vertical transition energies of the polymers can be qualitatively described from those of the oligomers by a Kuhn-type dependence on $1/N$ where N is the number of double bonds along the shortest path connecting the terminal carbon atoms of the molecular backbone.[25] The electronic structures for oligomers of increasing length were calculated, and a Kuhn fit of the data was used to extrapolate the $S_0 \rightarrow S_1$ transition energies of the extended polymers. The plots for the two POPT structures, P3HT, and CNPPV are presented in Figure 4. The best agreement between theory and experiment, that is, where the optical bandgap (E_g^{opt}) for POPT equals 1.8 eV, occurs when the polymer backbone is planar, suggesting that the phenyl groups of polymer side chains prefer to orient perpendicular to the backbone in thin films. The results for P3HT and CNPPV are also in good agreement with experiment.

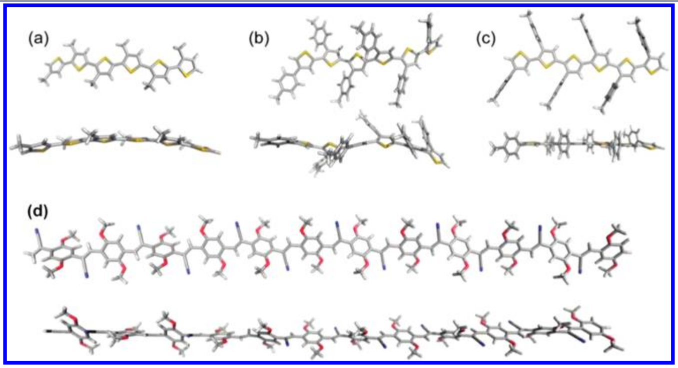

Figure 3. B3LYP/6-31G(d,p)-optimized neutral ground-state structures of the hexamers of (a) P3HT, (b) POPT-*unconstrained*, (c) POPT-*perp*, and (d) CNPPV shown from the top-view (top) and side-view (bottom).

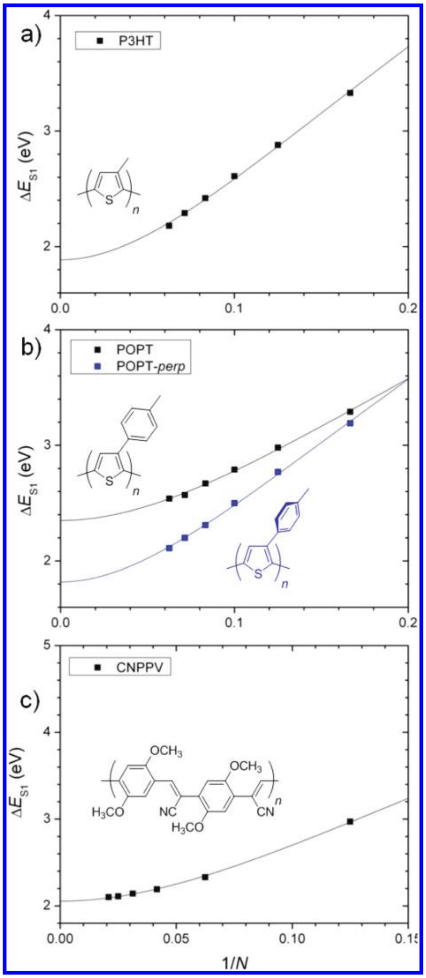

Figure 4. Vertical S0 → S1 transition energies of (a) P3HT and (b) POPT-*unconstrained* and POPT-*perp* where the phenyl group is constrained to be perpendicular to the polymer backbone (c) CNPPV. *N* is the number of double bonds along the backbone.

The presence of two dominant conformations of POPT is supported empirically by two-dimensional grazing incidence X-ray scattering (2D GIXS) measurements. Figure 5a shows the 2D GIXS pattern and the in-plane line scan of the POPT sample, while Figure 5b illustrates the schematic of solid-state packing for POPT. The presence of two peaks at 3.8 and 5.1 Å suggests that there are two different $\pi-\pi$ packing distances in the POPT thin film. Importantly, these two different $\pi-\pi$ packing distances arise from the two major conformations for the phenyl rings relative to the POPT backbone: the $\pi-\pi$ packing distance of 3.8 Å correlates to the phenyl ring oriented parallel with the backbone, while the $\pi-\pi$ stacking distance of 5.1 Å correlates to a POPT-*perp* orientation where the phenyl ring is twisted perpendicular to the backbone and causes an increase in separation between adjacent polymers. It should also be noted that the peak broadening observed in the GIXS pattern may be an indication that the phenyl ring can adopt varying degrees of rotation between the parallel and perpendicular conformations. The packing parameters of POPT and several phenyl-substituted polythiophenes have been studied in-depth elsewhere.[26] GIXS data of PQT-OP also evidence two dominant conformations for the phenyl ring, resulting in $\pi-\pi$ spacings of 5.1 and 3.9 Å (Supporting Information, Figure S2). The relative scattering intensity of the two $\pi-\pi$ spacings in PQT-OP is reversed from that of POPT. This reversal in PQT-OP can be attributed to the lack of substituents on two of the four thiophenes in the polymer repeat unit, thereby favoring the tighter $\pi-\pi$ spacing at 3.9 Å. Detailed GIXS data for P3HT[27] and PQT-DD[28] have been analyzed previously, and backbone spacings of 3.8 and 4.2 Å were reported, respectively. CNPPV derivatives are known to be relatively amorphous; however, weak diffraction signals between 4 and 5 Å have been observed.[29] X-ray scattering is limited to the investigation of regular periodicity present in a bulk material, and it is not appropriate for the study of polymer blend or bilayer interfaces. However, as the D/A interface in these material systems was our primary focus, we turned to computational analysis to develop a model interface for the charge separation event.

Model dimer configurations were constructed from best-fit planes of polythiophene/CNPPV separated at distances (*R*) between 4 and 5 Å in 0.2 Å increments (Figure 5d). To construct CT states from these dimers, charges were constrained to each molecule using the constrained density functional theory (C-DFT) method implemented in NWChem Version 4.6.[30] A conductor polarizable continuum model (CPCM) with $\varepsilon = 4$ was used to approximate polarization effects expected in organic solid-state systems. Given the limitations of the theoretical approach, we are mainly interested in the relative CT-state energies, which are plotted in Figure 5c. The model dimer configuration of POPT-*perp* is predicted to have the highest CT state energy followed by the P3HT and then the POPT-*unconstrained* configurations. PQT-OP model calculations require many more nuclei at the interface, which is beyond the scope of the present work.

To verify our calculations of the CT state energies in these D/A systems, we used spectroscopic techniques to experimentally observe their CT states. Sensitive photocurrent measurements, via Fourier transform photocurrent spectroscopy (FTPS),[22,24b] can extract the weak sub-bandgap external quantum efficiency, and photothermal deflection spectroscopy (PDS) can detect sub-bandgap absorption. These tools have previously been used to investigate charge-transfer states.[31] A recent and very significant FTPS study suggests that the CT state, sometimes called a CT exciton, is very efficiently split into free charge carriers at room temperature in P3HT:PCBM and MDMO-PPV:PCBM devices.[32] Spectral evidence and device studies of various D/A systems suggest that these CT states determine the V_{oc} of the PV cell and act as an intermediate in the generation and recombination of free charge carriers.[22,24b] Consequently, spectroscopic techniques rooted in sub-bandgap absorption are considered a good indicator

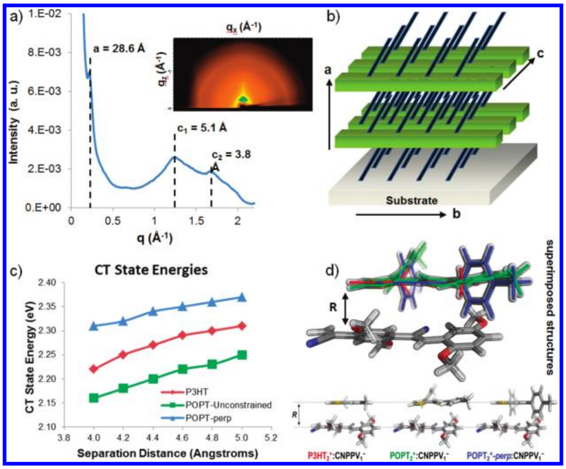

Figure 5. (a) An X-ray line scan taken parallel to the substrate surface showing peaks at *d* spacing equal to 28.6, 5.1, and 3.8 Å corresponding to the "*a*" distance and two different "*c*" distances, respectively, taken from the 2D GIXS pattern of POPT on Si substrate (inset). (b) Schematic of the polymer packing relative to the substrate, with corresponding labels to the peaks indicated in (a). (c) CT-state energies for the D/A systems illustrated in (d), estimated at the C-DFT B3LYP/6-31G(d,p) level. (d) Physical representation of dimers of POPT and P3HT with a single repeat unit of CNPPV, both superimposed and side-by-side.

of the presence of such CT states and of the maximum V_{oc} that can be expected with a given D/A combination.

Here, PDS spectra were obtained by detecting the mirage effect in a transparent, inert medium (Fluorinert) with a probe HeNe laser beam. Nonradiative heating associated with absorption of a monochromatic pump beam causes the mirage effect to occur. PDS was used in this investigation to support our hypothesis that molecular orientation of the phenyl groups affects the CT state energy. PDS measurements were performed on drop cast and spun cast films of POPT and P3HT blended with CNPPV. We underline here that bilayer films do not provide enough interfacial surface area to produce good signal-to-noise ratios; in addition, the molecular level interface is not expected to change upon going from the bilayer to BHJ morphology, vide infra, and see extended discussion in the Supporting Information. Figure 6 shows the PDS spectra of the homopolymers and the polymer blends under investigation; spectra are scaled to absolute values of the absorption coefficient by matching the signal near the absorption edge to that from the UV−vis spectra of the same films.

Blends of both P3HT and POPT with CNPPV produce nonadditive absorptions that are attributed to the presence of CT states at the D/A interfaces. For P3HT:CNPPV (1:1 wt/wt), a CT state absorption is present at 1.26 eV. For POPT, however, there are two sub-bandgap peaks attributed to CT states, one at 1.17 eV and one at 1.50 eV, possibly indicating two distinct interfacial configurations. These peak maxima are extracted by fitting an exponential for the band edge and Gaussian curves for the CT peaks in the sub-bandgap regions. The results of the calculations presented in Figure 5c are qualitatively in agreement with the observed PDS absorption peaks, in that the P3HT:CNPPV blend has a CT state energy that resides between the two POPT:CNPPV CT state energies. (We note that, in addition to the intrinsic limitations of the methodologies, the difference in energy between theory and experiment may be due in part to the fact that the physical size of the CT state (e.g., the extent that the CT exciton is delocalized) could be larger than what was considered in the calculations.) To verify that the energies of these CT states remain unchanged with film morphology and film thickness, POPT:CNPPV (1:1) films were compared as both drop cast and spun cast from 1,2-dichlorobenzene (Supporting Information, Figure S3). While the CT state peak positions do not change, the relative intensity of the sub-bandgap absorption to the UV−vis absorption is enhanced in the spun cast film, likely a result of finer scale phase segregation that leads to greater D/A interfacial surface area and increased relative sub-bandgap absorption.

PDS measurements were also performed to probe the CT state energies of the PQT-based polymers blended with CNPPV. The PQT-DD:CNPPV (1:1 wt/wt) shows little nonadditive sub-bandgap absorption, while PQT-OP presents two sub-bandgap absorption peaks at 1.25 and 1.56 eV. The higher energy CT state peak is significantly less intense for PQT-OP as compared to POPT (Supporting Information, Figure S4); the reason for this is discussed below. It should be noted that our first attempts to obtain a clean PDS signal from PQT polymers were difficult until we discovered that residual palladium from the cross-coupling polymerization led to an erroneous mirage effect and dramatically increased background signal (Figure S5).

■ DISCUSSION

A thermodynamic driving force for charge generation, that is, exciton dissociation leading to charge separation, is present at the interface between the donor/acceptor (D/A) materials in an

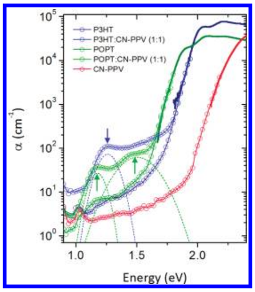

Figure 6. Absorption spectra of P3HT, POPT, and blends with CN-PPV. Thick solid lines are UV−vis absorption spectra of the homopolymers; symbols are the PDS absorption spectra of drop cast films. The arrows indicate the sub-bandgap features attributed to CT states in the blend systems. P3HT:CNPPV peak maximum at 1.26 eV, while POPT:CNPPV possesses two peaks at 1.17 and 1.50 eV.

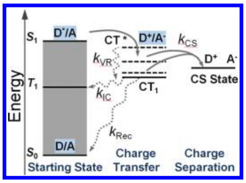

Figure 7. A diagram of possible electron flow pathways at the D/A interface, relative to potential energy (adapted from ref 11). CT state energies (ground-state solid black, excited-state dashed black) are shown in relation to the D/A singlet excited state (S_1), triplet state (T_1), and ground state (S_0). Competing energetic pathways and rates are also depicted: vibrational relaxation of the CT state (k_{VR}), intersystem crossing of the CT state to the donor triplet state (k_{IC}), recombination of the CT state to the ground state (k_{Rec}), and finally charge separation (k_{CS}). In addition to thermodynamics considerations, the kinetics of these processes will determine the charge separation behavior for each photovoltaic system.

OPV active layer. Photon absorption by either the donor or the acceptor materials produces the opportunity for charge-carrier generation: in the case of "donor" excitation, the system decreases in potential energy from the singlet excited state (E_s) by transferring an electron from donor to acceptor, and in the case of "acceptor" excitation, by transferring a hole from acceptor to donor. For simplicity, the process is generally discussed from the viewpoint of an excited donor material. A general diagram depicting charge separation is presented in Figure 7.

Although a thermodynamic driving force helps to generate free charges, the immediate physical separation of the electron and hole does not necessarily lead directly to free charges. The low dielectric constant of the active layer can produce a Coulomb trap for a partially separated exciton at the D/A interface. This state is usually referred to as a charge-transfer (CT) state. The CT state may either recombine to the initial ground states of the donor and acceptor materials or undergo further separation into free charges. It is broadly debated whether an intermediate CT state is requisite to charge separation,[11,32] and it is more recently debated whether this separation/generation can occur from lowest-lying CT_1 states.[32] It was also recently reported that a modest thermodynamic driving force of 0.1 eV leads to reasonable quantum yields of photocurrent with fullerene-based devices, based on commonly measured material properties, which supports our previous finding with POPT/CNPPV.[34] The contention surrounding the lowest-lying CT states is that they can be bound (vs the charge-separated states) by more energy than thermally available from k_BT (where k_B is the Boltzmann constant); thus, it is postulated that excess energy released during partial exciton dissociation could create higher-lying (excited) CT states (CT*), which are more likely to escape the Coulomb trap.[33c] However, strictly discussing the thermodynamics of charge separation ignores the important kinetic considerations of this process.

The efficiency of the charge separation (CS) process indeed depends on kinetic factors. Given that there is greater potential energy stored in the singlet exciton than a charge transfer exciton, and the possibility that sub-bandgap absorption produces excited CT* states that may relax down to CT_1, two rates are of critical importance: the rate of charge separation (k_{CS}) and the rate of vibrational relaxation of an excited CT state down to CT_1 (k_{VR}); see Figure 7. If $k_{CS} > k_{VR}$, then the electron is expected to readily escape the Coulomb potential and proceed to the CS state. If $k_{VR} > k_{CS}$, then relaxation to the CT_1 state leads to a more tightly bound (lower energy) intermediate. The electron can still escape from this state;[32] however, other processes start to compete with charge separation: if either the donor or the acceptor material possesses a triplet level (T_1) below the CT_1 state, intersystem crossing leads to long-lived metastable triplets. Also, the CT_1 state for some systems can radiatively or vibrationally decay to the ground state S_0.[16c,35] For these reasons, the kinetics of CS must be considered when parsing the charge-generation process.

In this work, OPV devices comparing POPT to P3HT and PQT-OP to PQT-DD were fabricated and analyzed. POPT and PQT-OP possess phenyl groups covalently bound to the polymer backbone as part of the solubilizing substituents. This functionality decreases the thermodynamic driving force for charge separation (vide supra), but both POPT and PQT-OP produced remarkably higher J_{sc} relative to their alkyl analogs. All relevant PV characteristics are summarized in Tables 1 and 2. Further, X-ray scattering data evidenced that both POPT and PQT-OP may adopt planar-with- and perpendicular-to-the-backbone conformations for the pendant phenyl rings. CT state energies for model dimer configurations were calculated and are plotted in Figure 5c: POPT-*perp* is predicted to have the highest CT state energy, while the CT state energy for P3HT lies between those of the POPT-*perp* and POPT-*unconstrained* conformations. Finally, experimental spectroscopic evidence of charge-transfer states at the interface with the acceptor CNPPV, gathered via PDS for all four donor polymers, is consistent with the relative values predicted by the model dimer calculations.

With an out-of-plane twist of the phenyl rings, the separation distance between POPT and the acceptor molecule would likely increase as steric repulsion from the phenyl rings hinders backbone−backbone interaction. PDS data confirm the presence of two distinct features in the sub-bandgap regime, which could be a direct result of these two dominant conformations at the D/A interface, as it has been explained in the previous section. Because these conformationally dependent states are both involved as intermediates in the charge-generation process, the corresponding geminate pairs would overcome different energetic barriers to split into free charges. We postulate that a twisted phenyl ring

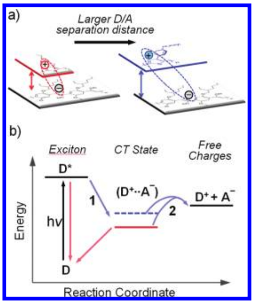

Figure 8. (a) Cartoon of how steric interactions can lead to an increase in backbone spacing, a decrease in the Coulomb binding force, and destabilization of the geminate pair. (b) Schematic of how the change depicted in cartoon (a) leads to a different energy landscape with increased charge separation probability in POPT, as the CT state is considered an intermediate trapped in an energetic well.

conformation of POPT (POPT-*perp*) is beneficial for charge generation, as an intermediate with increased potential energy is more likely to fully separate into free charges (Figure 8). FTPS measurements could lead to a quantitative description of the quantum yields for these two states, and this is the focus of future work.

This study also generated two additional significant and supportive findings. PDI-based acceptors have garnered much attention as alternative n-type materials to replace fullerenes;[3a] here, we produce the highest efficiency devices with this acceptor to date, despite tremendous efforts with alternative approaches toward higher efficiency.[3a,13a,19] This is just another indication that control over the interfacial geometry at the molecular level can lead to much improved device performance, as a complementary tool to morphology and state energy control. Additionally, the photovoltaic performance with the high mobility n-type polymer ActiveInk N2200 demonstrates that POPT outperforms P3HT both in our laboratories and as compared to two very recent reports.[21]

Combining all of the data, analysis, and literature context, we have synthesized and proposed a general design principle for improved charge separation in nonfullerene OPVs: tuning the D/A interfacial interaction through steric control to facilitate photocurrent generation. Regardless of whether charge separation happens from a relaxed CT_1 state or an excited CT state, increasing the steric bulk at the D/A interface likely decreases the Coulomb binding strength exerted on the geminate pair. We postulate that the phenyl ring pendant to POPT and PQT-OP provides an almost ideal interaction distance between the charge carrying components of the D/A interface, and this leads to two of the best nonfullerene devices to date. The higher energy of the intermediate CT state, with a lower activation barrier to free carrier generation, improves photocurrent generation and provides the key to the observed phenomenon (Figure 8). This effect was not limited to one donor polymer or one acceptor material, but rather it was general for two donors and four acceptors (four polymers and two small molecules), for a total of seven material combinations. All of these material combinations yielded optimized devices with the phenyl containing polymeric substituents producing substantially greater photocurrents, and overall power conversion efficiencies, than the alkyl analogues.

■ CONCLUSIONS

We have utilized computational modeling, PDS spectroscopy and tailored synthetic design to probe the importance of steric interactions at the donor/acceptor interface in nonfullerene OPV devices. By introducing the octylphenyl substituent onto the investigated polymer backbones, the thermally relaxed charge-transfer state, and potentially excited charge-transfer states, are likely raised in energy, as evidenced by PDS. This decreases the barrier to charge separation, and assuming we have controlled properly for changes in morphology by thoroughly optimizing each materials/device system, it could be the source of increased photocurrent generation. The design principle was shown to be general across two polythiophene backbones and with four different acceptors, two polymers and two small molecules. Additionally, the lower energy PDS onset for POPT-based devices with CNPPV (1.17 eV) versus the onset for PQT-OP with CNPPV (1.26 eV) is reflected in the V_{oc} of these devices. The combined data from POPT and PQT-OP devices and their materials analyses suggest that controlling the steric interaction at the D/A interface could be a general design principle toward improving charge generation in nonfullerene OPVs.

■ ASSOCIATED CONTENT

Ⓢ **Supporting Information.** Experimental, device fabrication, and characterization details. This material is available free of charge via the Internet at http://pubs.acs.org.

■ AUTHOR INFORMATION

Corresponding Author

frechet@berkeley.edu

■ ACKNOWLEDGMENT

This work was supported by the Center for Advanced Molecular Photovoltaics (Award No. KUS-C1-015-21), supported by King Abdullah University of Science and Technology (KAUST), and the U.S. Department of Energy under Contract No. DE-AC02-05CH11231 (synthesis and some device characterization work). T.W.H., C.H.W., and J.R. thank the National Science Foundation for graduate research fellowships. We gratefully acknowledge Polyera Inc. and Paul Armstrong for providing the Active Ink N2200 and PDI, respectively, used in this study. Paul Armstrong and Yoshi Miyamoto are thanked for assistance with device optimization. We also thank David Kavulak and Barry Thompson for helpful discussions.

■ REFERENCES

(1) (a) Boudreault, P. T.; Najari, A.; Leclerc, M. *Chem. Mater.* **2011**, *23*, 456–459. (b) He, Y. J.; Chen, H. Y.; Hou, J. H.; Li, Y. F. *J. Am. Chem. Soc.* **2010**, *132*, 1377–1382. (c) Piliego, C.; Holcombe, T. W.; Douglas, J. D.; Woo, C. H.; Beaujuge, P. M.; Frechet, J. M. J. *J. Am. Chem. Soc.* **2010**, *132*, 7595–7597. (d) Thompson, B. C.; Frechet, J. M. J. *Angew. Chem., Int. Ed.* **2008**, *47*, 58–77.

(2) Chen, H. Y.; Hou, J. H.; Zhang, S. Q.; Liang, Y. Y.; Yang, G. W.; Yang, Y.; Yu, L. P.; Wu, Y.; Li, G. *Nat. Photonics* **2009**, *3*, 649–653.

(3) (a) Anthony, J. E. *Chem. Mater.* **2010**, *23*, 583–590. (b) Brunetti, F. G.; Gong, X.; Tong, M.; Heeger, A. J.; Wudl, F. *Angew. Chem., Int. Ed.* **2010**, *49*, 532–536. (c) Shin, R. Y. C.; Kietzke, T.; Sudhakar, S.; Dodabalapur, A.; Chen, Z. K.; Sellinger, A. *Chem. Mater.* **2007**, *19*, 1892–1894.

(4) Lee, M. R.; Eckert, R. D.; Forberich, K.; Dennler, G.; Brabec, C. J.; Gaudiana, R. A. *Science* **2009**, *324*, 232–235.

(5) (a) McNeill, C. R.; Abrusci, A.; Zaumseil, J.; Wilson, R.; McKiernan, M. J.; Burroughes, J. H.; Halls, J. J. M.; Greenham, N. C.; Friend, R. H. *Appl. Phys. Lett.* **2007**, *90*, 1935061–3. (b) Holcombe, T. W.; Woo, C. H.; Kavulak, D. F. J.; Thompson, B. C.; Frechet, J. M. J. *J. Am. Chem. Soc.* **2009**, *131*, 14160–14161. (c) Woo, C. H.; Holcombe, T. W.; Unruh, D. A.; Sellinger, A.; Frechet, J. M. J. *Chem. Mater.* **2010**, *22*, 1673–1679. (d) Zhou, E.; Cong, J.; Wei, Q.; Tajima, K.; Yang, C.; Hashimoto, K. *Angew. Chem., Int. Ed.* **2011**, *50*, 2799–2803.

(6) The fullerene structure is a truncated icosohedron.

(7) Kanai, Y.; Grossman, J. C. *Nano Lett.* **2007**, *7*, 1967–1972 and references therein.

(8) Wöll, C. *Physical and Chemical Aspects of Organic Electronics: From Fundamentals to Functioning Devices*; Wiley-VCH: Weinheim, 2008.

(9) (a) Knipper, M.; Parisi, J.; Coakley, K.; Waldauf, C.; Brabec, C. J.; Dyakonov, V. *Z. Naturforsch., A* **2007**, *62*, 490–494. (b) Mihailetchi, V. D.; Koster, L. J. A.; Blom, P. W. M.; Melzer, C.; de Boer, B.; van Duren, J. K. J.; Janssen, R. A. J. *Adv. Funct. Mater.* **2005**, *15*, 795–801.

(10) (a) Sariciftci, N. S.; Smilowitz, L.; Heeger, A. J.; Wudl, F. *Science* **1992**, *258*, 1474–1476. (b) Halls, J. J. M.; Walsh, C. A.; Greenham, N. C.; Marseglia, E. A.; Friend, R. H.; Moratti, S. C.; Holmes, A. B. *Nature* **1995**, *376*, 498–500.

(11) Bredas, J. L.; Norton, J. E.; Cornil, J.; Coropceanu, V. *Acc. Chem. Res.* **2009**, *42*, 1691–1699.

(12) Ohkita, H.; Cook, S.; Astuti, Y.; Duffy, W.; Tierney, S.; Zhang, W.; Heeney, M.; McCulloch, I.; Nelson, J.; Bradley, D. D. C.; Durrant, J. R. *J. Am. Chem. Soc.* **2008**, *130*, 3030–3042.

(13) (a) Shoaee, S.; Clarke, T. M.; Huang, C.; Barlow, S.; Marder, S. R.; Heeney, M.; McCulloch, I.; Durrant, J. R. *J. Am. Chem. Soc.* **2010**, *132*, 12919–12926. (b) Clarke, T. M.; Ballantyne, A. M.; Nelson, J.; Bradley, D. D. C.; Durrant, J. R. *Adv. Funct. Mater.* **2008**, *18*, 4029–4035.

(14) Morteani, A. C.; Sreearunothai, P.; Herz, L. M.; Friend, R. H.; Silva, C. *Phys. Rev. Lett.* **2004**, *92*, 2474021–4.

(15) Beljonne, D.; Cornil, J.; Muccioli, L.; Zannoni, C.; Bredas, J. L.; Castet, F. *Chem. Mater.* **2011**, *23*, 591–609.

(16) (a) Marsh, R. A.; Hodgkiss, J. M.; Friend, R. H. *Adv. Mater.* **2010**, *22*, 3672–3676. (b) Ooi, Z. E.; Tam, T. L.; Sellinger, A.; deMello, J. C. *Energy Environ. Sci.* **2008**, *1*, 300–309. (c) Veldman, D.; Ipek, O.; Meskers, S. C. J.; Sweelssen, J.; Koetse, M. M.; Veenstra, S. C.; Kroon, J. M.; van Bavel, S. S.; Loos, J.; Janssen, R. A. J. *J. Am. Chem. Soc.* **2008**, *130*, 7721–7735.

(17) Schmidtke, J. P.; Friend, R. H.; Silva, C. *Phys. Rev. Lett.* **2008**, *100*, 1574011–4.

(18) Granstrom, M.; Petritsch, K.; Arias, A. C.; Lux, A.; Andersson, M. R.; Friend, R. H. *Nature* **1998**, *395*, 257–260.

(19) Rajaram, S.; Armstrong, P. B.; Kim, B. J.; Frechet, J. M. J. *Chem. Mater.* **2009**, *21*, 1775–1777.

(20) Yan, H.; Chen, Z. H.; Zheng, Y.; Newman, C.; Quinn, J. R.; Dotz, F.; Kastler, M.; Facchetti, A. *Nature* **2009**, *457*, 679–686.

(21) (a) Fabiano, S.; Chen, Z.; Vahedi, S.; Facchetti, A.; Pignataro, B.; Loi, M. A. *J. Mater. Chem.* **2011**, ASAP. (b) Moore, J. R.; Albert-Seifried, S.; Rao, A.; Massip, S.; Watts, B.; Morgan, D. J.; Friend, R. H.; McNeill, C. R.; Sirringhaus, H. *Adv. Energy Mater.* **2011**, *1*, 230–240.

(22) Vandewal, K.; Tvingstedt, K.; Gadisa, A.; Inganas, O.; Manca, J. V. *Nat. Mater.* **2009**, *8*, 904–909.

(23) (a) Yi, Y. P.; Coropceanu, V.; Bredas, J. L. *J. Am. Chem. Soc.* **2009**, *131*, 15777–15783. (b) Yi, Y.; Coropceanu, V.; Bredas, J. L. *J. Mater. Chem.* **2011**, *21*, 1479–1486.

(24) (a) Huang, Y. S.; Westenhoff, S.; Avilov, I.; Sreearunothai, P.; Hodgkiss, J. M.; Deleener, C.; Friend, R. H.; Beljonne, D. *Nat. Mater.* **2008**, *7*, 483–489. (b) Vandewal, K.; Tvingstedt, K.; Gadisa, A.; Inganas, O.; Manca, J. V. *Phys. Rev. B* **2010**, *81*, 1252041–8.

(25) Gierschner, J.; Cornil, J.; Egelhaaf, H. J. *Adv. Mater.* **2007**, *19*, 173–191.

(26) Fell, H. J.; Samuelsen, E. J.; Mardalen, J.; Andersson, M. R. *Synth. Met.* **1995**, *69*, 283–284.

(27) Verploegen, E.; Mondal, R.; Bettinger, C. J.; Sok, S.; Toney, M. F.; Bao, Z. A. *Adv. Funct. Mater.* **2010**, *20*, 3519–3529.

(28) Thompson, B. C.; Kim, B. J.; Kavulak, D. F.; Sivula, K.; Mauldin, C.; Frechet, J. M. J. *Macromolecules* **2007**, *40*, 7425–7428.

(29) (a) Chen, S. A.; Chang, E. C. *Macromolecules* **1998**, *31*, 4899–4907. (b) Chen, S. H.; Su, C. H.; Su, A. C.; Chen, S. A. *J. Phys. Chem. B* **2004**, *108*, 8855–8861.

(30) (a) Wu, Q.; Van Voorhis, T. *J. Chem. Theory Comput.* **2006**, *2*, 765–774. (b) Wu, Q.; Van Voorhis, T. *J. Phys. Chem. A* **2006**, *110*, 9212–9218. (c) Wu, Q.; Van Voorhis, T. *Phys. Rev. A* **2005**, *72*, 0245021–4. (d) Valiev, M.; Bylaska, E. J.; Govind, N.; Kowalski, K.; Straatsma, T. P.; Van Dam, H. J. J.; Wang, D.; Nieplocha, J.; Apra, E.; Windus, T. L.; de Jong, W. *Comput. Phys. Commun.* **2010**, *181*, 1477–1489.

(31) (a) Goris, L.; Haenen, K.; Nesladek, M.; Wagner, P.; Vanderzande, D.; De Schepper, L.; D'Haen, J.; Lutsen, L.; Manca, J. V. *J. Mater. Sci.* **2005**, *40*, 1413–1418. (b) Goris, L.; Poruba, A.; Hod'akova, L.; Vanecek, M.; Haenen, K.; Nesladek, M.; Wagner, P.; Vanderzande, D.; De Schepper, L.; Manca, J. V. *Appl. Phys. Lett.* **2006**, *88*, 0521131–3.

(32) Lee, J.; Vandewal, K.; Yost, S. R.; Bahlke, M. E.; Goris, L.; Baldo, M. A.; Manca, J. V.; Van Voorhis, T. *J. Am. Chem. Soc.* **2010**, *132*, 11878–11880.

(33) (a) Clarke, T. M.; Durrant, J. R. *Chem. Rev.* **2010**, *110*, 6736–6767. (b) Deibel, C.; Strobel, T.; Dyakonov, V. *Adv. Mater.* **2010**, *22*, 4097–4111. (c) Zhu, X. Y.; Yang, Q.; Muntwiler, M. *Acc. Chem. Res.* **2009**, *42*, 1779–1787.

(34) Zhou, Y.; Tvingstedt, K.; Zhang, F. L.; Du, C. X.; Ni, W. X.; Andersson, M. R.; Inganas, O. *Adv. Funct. Mater.* **2009**, *19*, 3293–3299.

(35) Loi, M. A.; Toffanin, S.; Muccini, M.; Forster, M.; Scherf, U.; Scharber, M. *Adv. Funct. Mater.* **2007**, *17*, 2111–2116.